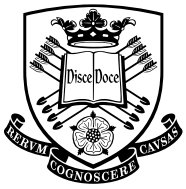

The University Of Sheffield.

THE ADHESION AND MECHANICAL BEHAVIOUR OF DIFFERENT ELASTOMERS

by:

Alessandra Petroli

Thesis submitted in partial fulfilment of the requirements for the degree of Doctor of Philosophy

The University of Sheffield
Faculty of Science
Department of Physics and Astronomy

October, 2018

THE ADHESION AND MECHANICAL BEHAVIOUR OF DIFFERENT ELASTOMERS

Alessandra Petroli

Thesis submitted in partial fulfilment of the requirements for the degree of Doctor of Philosophy

The University of Sheffield
Faculty of Science
Department of Physics and Astronomy

October, 2018

To Mario Petroli and Mark Tice,
a chi non ha potuto e a chi non ha voluto.

(Italian saying not translatable into English: dedication is to two people, who for reasons beyond academic ability were unable to obtain a PhD degree. I am eternally grateful for their patience and help with this thesis).

Abstract

This work was focused on the physical removal of small particles from plastic surfaces, in collaboration with Teknek, a company that develops cleaning solutions and that provided some of the materials like reference surfaces and some elastomers (cleaning materials).

Atomic force microscopy was used to find the adhesion force between colloidal probes made of different materials and different types of surfaces to verify which surface has the greatest or lowest adhesion. Colloidal probes were chosen as example of contaminant particles to be removed: the surface that shows the greatest adhesion toward a colloidal probe is the one that would retain the contaminant.

Adhesion test was done on samples provided by Teknek: it was found that, for these samples, roughness is the main factor that modifies adhesion. Qualitative explanation of how roughness could influence adhesion is provided considering the different scales of roughness and surface features. Characterization of samples hydrophobicity/hydrophilicity cannot exclude a contribution of the capillary force in enhancing adhesion.

Some laboratory made samples made of polydimethylsiloxane were synthesised to verify if bulk properties can influence adhesion. Adhesion test revealed that the Young's modulus and the crosslinking density do not change adhesion in the studied conditions. Viscoelasticity was seen only in two samples and it is known that it allows adhesion to be dependent on the crack speed and a new strategy is proposed for crack speed calculation from experimental data. It was found that calculated crack speeds follow the expected behaviour toward the energy release rate, however this method also allowed to have a look at the microscale detachment process letting the conclusion that also at this scale, polydimethylsiloxane behaviour is comparable to that seen at the macroscale, with mainly polymer elongation and

Abstract

'regular' movement of the contact line before the minimum of the force-indentation curve, and fingering detachment processes after it.

Acknowledgements

I would like to thank my supervisor, Prof. Mark Geoghenan, for allowing me to come back to research and satisfy my old desire of attending a PhD program. I really appreciated his encouragements especially when I felt I should have never seen the end of this work and I would have liked to stop everything. I also would like to thank my co-supervisor, Prof. Ashley Cadby for mathematical, or better, statistical suggestions for data elaboration and Prof. Ed Daw for his wise suggestions in difficult situations. Thanks are also owed to Sheila Hamilton, technical manager of Teknek for providing materials for this project and allowing me to remain in contact with the industrial world. I would like to thank Dr Zhenyu (Jason) Zhang, Dr Francesca Quacquarelli and Dr Ana Lorena Morales-García for instructing me in the use different kinds of atomic force microscopies and introducing different types of experiments that could be done with them. I cannot forget the help received from Dr Becca Savage and Dr Nic Mullin every time there was something wrong with the atomic force microscopies and I thank them for being always present and available when necessary. I am also pleased to have found a competent and precise support from the Asylum Research staff as well as from Paweł Hermanowicz (for his program AtomicJ). I am thankful to Dr Renato Buzio for the discussion about his method of calculating the contact radius. I would like to thank Dr Emanuele D'Angelo (Department of Industrial Chemistry – University of Bologna), Dr Vincent Verney (ICCF – Institute de Chieme de Clermont-Ferrand) and Prof. Marcello Romagnoli (Department of Engineering – University of Modena) for time and support for the DMA analysis. I appreciate the work done by Mattias Ansorg in creating and allowing people to use this well-done thesis template. My thanks to Mario Petroli for the mathematical support, discussions and explanations about the contact physics and computer assistance.

Acknowledgements

I am grateful to the members of the Polymer Physics group who were involved in the project: Prof Jamie Hobbs, Dr Mike Weir, Dr Andy Parnell, Dr Sarah Canning, Dr Tom Kennelly, Dr Rita La Spina, Dr Amy Hall, Dr Thomas Kennelly, Dr Chris Clarkson, Dr Fabio Pontecchiani, Dr Richard Webb and Dr Steve Collins. A special thanks to Dr Maryam Raftari, Dr Youmna Mouhamad, Elisa Laera, Dr Latifah Alfhaid and Dr Wala G. Dizayee for their friendship and the enrichment that derives from the exchange of experiences and cultures.

My warm thanks to all friends in Sheffield that made my experience unforgettable: Dr Christian Berretta, Dr Mauro Nicolao, Omolara Plang, Mark Tice, Dr Ikechukwu E. Onyenwe, Dr Anthony C. Ezeribe, Dr Loredana Saccone and Mengshu Yao.

I would like to express appreciation for the support of Dr Ciro Polizzi, Salvatore Spatola, Dr Stefano Cerini, Dr Fabrizio Tarterini, Dr Tiziana Benelli, Dr Laura Mazzocchetti, Dr Micaela Vannini and Dr Grazia Totaro, for their precious helps in last (terrible) period of data elaboration and writing-up. In addition, I would like to thank Luigi D'Andrea, Dr Manuela Mandrone, Dr Andrea Milelli, Dr Alessandro Lombi, Prof. Francesco Scagnolari, Prof. Elisabetta Salatelli, Prof. Carla Boga, Luca Zuppiroli, Dr Rita Mazzoni, Prof. Maria Cristina Cassani, Prof. Elisabetta Venuti, Prof. Silvia Bordoni, Arianna Rivalta, Beatrice Berti, Dr Tommaso Salzillo and Marina Grandini for the support at work in this particularly uncomfortable period.

I cannot forget to thank Prof. Vincenzo Giulio Albano and Prof. Magda Monari, supervisors of Bachelor's and Master's theses, for introducing me to field of science.

Last but not least, a special thanks to my family who supported me in this experience from the beginning to the end.

Nomenclature

a	Contact radius
$\bar{a}$	Dimensionless contact radius
a_{T}	WLF shift factor
A_{H}	Hamaker constant
α	Polarizability
β	Dissipative function constant
β_1	Angle
c_1 , c_2 , c_3	Generic coefficients
c^g , c^S	WLF shift factor constants
Cu	Copper
$\Gamma_i(Re)$	Imaginary part of the hydrodynamic function
γ , $\Delta\gamma$	Surface energy or surface tension, work of adhesion
γ^{d}	Surface energy dispersion contribution
γ^{p}	Surface energy polar contribution
γ_{lv}	Liquid-vapour interfacial tension
γ_{sl}	Solid-liquid interfacial tension
γ_{sv}	Solid-vapour interfacial tension
γ_{12}	Interfacial energy
d	Distance over which the Dugdale potential acts
D	Derivative parameter
D	Distance between the tip apex and the surface
DMT	Derjaguin, Muller and Toporov (contact mechanic theory)
Δ	AFM head displacement
ΔV	Voltage difference
δ	Elastic displacement or indentation
$\bar{\delta}$	Dimensionless displacement or indentation

Nomenclature

$\hat{\delta}$	Phase lag
δ_c	Cantilever deflection
δ_m	Elastic displacement of the cantilever
δ_p	Piezo-actuator displacement
E	Young's modulus
E^*	Reduced Young's modulus
E'	Storage modulus
E''	Loss modulus
ε	Strain
ε_0	Vacuum permittivity
ε_r	Relative permittivity
f	Crosslinker functionality
F	Force
$\bar{F}$	Dimensionless adhesion force
F_{adh}	Adhesion force
$F_{adh\ Bradley}$	Adhesion force according to the Bradley model
$F_{adh\ DMT}$	Adhesion force according to the DMT model
$F_{adh\ JKR}$	Adhesion force according to the JKR model
$F_{adh\ PR}$	Adhesion force roller-particle
$F_{adh\ PS}$	Adhesion force roller-substrate
F_{cap}	Capillary force
F_{elec}	Electrostatic force
F_S	Surface force
F_{vdW}	Van der Waals forces
ϕ	Interaction energy
φ_2	Volume fraction
Φ	Dissipative function
g	Correction factor
G	Shear modulus
η	Viscosity
h	Distance

Nomenclature

h_0	Distance over which the Dugdale potential acts
$\hbar$	Reduced Planch's constant
H	Energy release rate
I	Integrative parameter
I	First ionization potentials
JKR	Johnson Kendall and Roberts (contact mechanics theory)
k_{B}	Boltzmann constant
k_{c}	Spring constant of the cantilever
k_{ref}	Spring constant of the reference cantilever
K	Compression modulus
L	Cantilever length
λ	Peak to peak distance
m	Ratio between the total distance over which all forces act and the contact radius
m_{c}	Cantilever mass
m_{c}^{*}	Cantilever effective mass
m_f	Final mass
m_i	Initial mass
m_{sw}	Mass in the swollen state
m_{t}	Cantilever tip mass
M	Known mass
M_c	Molecular weight
μ_{M}	Transition parameter
μ_{T}	Tabor parameter
n	Crosslink density, dissipative function exponent
n_i	Fraction of surface made of the chemical i
N	Number of points in an AFM image of a surface
ν	Poisson coefficient
v	Crack speed

Nomenclature

v^*	Characteristic speed
ν_1 , ν_2	Orbiting frequency of electrons of atom 1 and 2, respectively
O	Contact point along the z axis
p	Pressure distribution
p_0	Pressure distribution at the origin O
$p_0^{'}$	Addition pressure in JKR model
P	Proportional parameter
P	Pressure
P_{sat}	Saturation vapour pressure
PC	Polycarbonate
PDMS	Polydimethylsiloxane
PET	Polyethylene terephthalate
PI	Polyimide
PP	Polypropylene
PS, PS-DVB	Polystyrene divinylbenzene
PU	Polyurethane
q	Quality factor
Q	Degree of swelling
Q_1 , Q_2	Electric charge
r	Distance of a point of a surface from the origin O
r_f	Ratio between actual and nominal contact areas of contact
r_1	Azimuthal radius, radius of hemispherical asperity
r_2	Meridional radius, radius of hemispherical asperity
R	Gas constant
R	Radius of a spherical body
R^*	Reduced radius
R_a	Arithmetic roughness
R_{ku}	Kurtosis of roughness distribution
R_p	Maximum profile peak height
R_{rms} , R_q	RMS roughness

Nomenclature

R_{sk}	Skewness of roughness distribution
R_t	Maximum height profile
R_v	Maximum profile valley depth
ρ_f	Density of the fluid surrounding the cantilever
ρ_p	Polymer density
ρ_s	Solvent density
S	Point on the surface of a body
σ	Stress
σ_0	Attractive interaction of the Dugdale potential
t	Time
t_c	Cantilever thickness
T	Temperature
T_1, T_2	Distant points
T_g	Glass transition temperature
T_S	Glass transition temperature plus 50 K
θ_C	Contact angle of a heterogeneous surface
θ_{CW}	Contact angle in an intermediate condition between the pure Cassie-Baxter and the pure Wenzel regimes
θ_W	Contact angle according to the Wenzel equation
θ_Y	Contact angle according to the Young equation
u	Dipole moment
u_{ind}	Induced dipole moment
u_z	Normal elastic displacement of surface point
U_E	Stored elastic strain energy
U_P	Potential energy
U_S	Surface energy
U_T	Total free energy
V	Volume
V_f	Final volume
V_m	Molar volume
V_{sw}	Volume in the swollen state

Nomenclature

w	Cantilever width
$w(h)$	Potential
w_{vdW}	Van der Waals energy
W_{ext}	Extractable fraction
χ	Flory-Huggins polymer-solvent interaction parameter
z_0	Interatomic equilibrium distance
z_i	Distance of the profile height of depth from the mean height
Z_{err}	Voltage difference between the setpoint and the actual cantilever position
Z_{v}	Correction voltage for the vertical position
ω	Angular frequency
ω_{0c} , ω_{1c}	Cantilever resonance frequency

Table of contents

Table of contents

Table of contents

1 Foreword

Non ho mai incontrato un uomo così ignorante dal quale non abbia potuto imparare qualcosa.

(Never have I met a man so ignorant that nothing could be learned from him)

[attributed to Galileo Galilei, 1564-1642]

To stick different materials together can be considered as a primordial research of human beings. To create a new item very often requires the necessity to assemble different smaller parts in a way they can work harmoniously and properly together to perform a new task as required. Joints can be mechanical or adhesive: very often both types of connections are used in the same item. Even if in the story of humanity attention was mainly paid on developing mechanical joints, the adhesive joints were and are equally important and used as well. For instance the use of glue obtained from resin to stick together the stone part with the shaft of hatchets or to let coloured pigment adhere to the walls of a cave (Chauvet cave in Vallon-Pont-d'Arc in the Ardèche) in the Upper Palaeolithic era. A relatively recent example can be found in remains of the Roman architecture: we know the engineering rules used by Romans for the construction of their buildings, however we do not know how they were able to create their 'glue' or concrete. And their concrete or 'pozzolana' is very long-lasting, more than the modern ones. More recently, with the Industrial Revolution and the development of products with increasingly better performances and resistances, adhesion and cohesion of different parts or materials have become of primary importance and are important challenges to tackle. Still more difficult is the development of adhesive joints that can change their properties according to specific conditions (for example as some tapes that develop strong adhesion after some time, to let the user adjust or remove it during the application or in a short time after the application without damages of the surfaces; or some surface treatments that can allow a surface to modify its adhesive properties according to

properties of the surrounding environment, like for example pH). However, it is probably at microscale that adhesion becomes intriguing, with a history that starts much earlier than human beings, when cells developed different types of mechanisms to adhere to each other and to create all the complex structures and organisms that we know, we are part of, and probably we do not know completely and in detail yet. A history that is still continuing with the development of highly specialised living beings as the study case of gecko's feet.

However, unlike the mechanical joints, adhesion began to be studied only in the recent centuries and it is still a work-in-progess field, because of the complexity of the mechanisms involved, which are physical and molecular in origin and thus still difficult to study, to fully understand and to be organised in a (possibly comprehensive) theory. Nevertheless, in the last decades, progresses in fundamental physics and chemistry in understanding adhesion mechanisms are significant and let researches develop new technological materials, with micro/nanoscale or molecular organization. Together with these materials, also new processes and new guidelines are being developed to ensure a suitable environment for the production of these materials, with particular attention given to avoid contaminations that can be crucial in guaranteeing the desired performances of these material themselves. And maybe, also a cleaning process can be a matter of adhesion....

1.1 Thesis outline

This thesis is organized into two introductory chapters, two results chapters and final conclusions. The introductory chapters will deal with the background and all the information useful for the data presentation and discussion of the following chapters. The first introductory chapter will deal about the framework of this research, the background and the state-of-art of the topics necessary for the following chapters. The second introductory chapter is related to the experimental part, with description of samples, used equipment and an outline of methods used in data analysis. The first chapter related to data will show results about

fundamental physics of adhesion on model materials, while the following chapter will present results of analysis related to a specific product issue. The final chapter will summarise common results and hypotheses about future work.

2 Theoretical concepts and background

This chapter will introduce the theoretical background of this project: the aim is to present the state-of-art of theories regarding fields related to the project, not only as introduction but also to let readers understand choices done in the experimental and results sections. However, because this project requires the knowledge of different fields, from chemistry to physics, and some of them in a detailed way, it is quite challenging to create a chapter that should be easily readable and exhaustive at the same time. For that reason, some parts will be less developed than others, limiting the effort to the relevant concepts for the following sections. For the same reason, this chapter will follow a particular order: it will begin with a short description of the background and the objectives of the project, then it will quickly describe the scientific formulation of it, to move on a general description of the main characteristics and properties of polymers. More attention will be paid to elastomers, a particular kind of polymer that plays a relevant role in the project. Then, a description of surfaces and their interactions is presented, followed by the description of adhesion forces. A quite long and detailed section will deal with the different models of the mechanics of adhesion, starting from the classic ones until the proposed models for viscoelastic systems. A short section will describe what is reported in literature about the influence of crosslink density on adhesion on elastomers, especially focusing on data regarding the elastomer used in this work. A special section will deal with the effect of surface roughness on the previously presented properties: the aim of this is to highlight how roughness can also drastically change them. Finally, coming back to polymers, an introduction of the most used polymer network and its routes of synthesis will be presented.

2.1 Background and objectives

The aim of this project is to study interfacial adhesion between mainly polymeric materials and particles and to investigate how adhesion is influenced by both

surface features and bulk properties of those materials. This will be done both on commercial surfaces and laboratory made samples: in this way it is possible to connect practical and fundamental science to get a larger and more comprehensive insight in the field of adhesion. Commercial surfaces were provided by Teknek, that is a partner of this project, while the other samples were synthesized directly in our laboratory.

The interest in knowing interfacial adhesion between surfaces and particles is related to the study of particles detachment for cleaning issue. The 'art of cleaning' is quite important both in the industrial and research processes, however there are different methods that can be used to obtain a clean product. Which method may be used it is a matter of the types of products and of the contaminants to remove. For example, in the pharmaceutical and food industry, bacteria and micro-organisms are considered as contaminants to remove or, at least, to control; in the electronic industry, contaminants are usually particles, that can derive from previous steps of the production process; in any fields that deal with surface and interfacial properties and analyses, everything that lies on a surface and that derives from interactions with the environment is considered a contaminant (usually organic contamination like grease or formation of a layer of oxide because of the interaction with oxygen). Surely, the previous examples are not exhaustive of the wide range of existing contaminants and products, however they can suggest how different they can be and how the developed strategies for the removal of contaminants can be different. For instance, in the food and pharmaceutical industry, preservatives are used to avoid and to control contamination of products and, in some application, the use of sterile packaging is recommended, actually using both chemical and physical methods. In the electronic industry, contact cleaning is largely used [1, 2] in some cases together with non-contact cleaning as well [3, 4]. And finally, to obtain real chemically clean surfaces, usually chemical cleaning is used [5, 6].

Teknek is a worldwide leader company in cleaning products and machineries. Its technology and know-how are focused on the contact cleaning of particles: it

develops a cleaning system based on different types of polymeric rollers, each suitable for the removal of nano- and micro-particles from different kinds of surfaces. The surfaces to be cleaned varies from organic materials, as polymers, to inorganic materials, such as metals. Their technology is applied in different types of fields, and in some of them the efficient removal of particles is fundamental, as in the electronic industry.

In the most common design of Teknek's machines, the 'dirty' surface is laid on a moving layer that leads the surface toward the cleaning rollers. Cleaning rollers are the core of the cleaning system: they turn and catch particles from the surface. Over the cleaning rollers there is an adhesive roller, that removes particles from the cleaning rollers each time, so that cleaning rollers always show their uncontaminated part to the 'dirty' surface. The adhesive roller is a multi-layer roller: it is sufficient to remove the outside layer to get a new clean one. An example of the described cleaning system is shown and described in Figure 2.1.

Figure 2.1: An example of the cleaning process developed by Teknek. The pale blue surface is the surface to be cleaned (it is grey in the left part and bright in the right part after the removal of the particles); the four blue rollers in contact with the surface are the cleaning rollers and the two big white and blue rollers are the adhesive rollers. Image courtesy of Teknek.

Teknek pays a lot of attention to the development of its cleaning rollers: they must be effective and they do not have to release contaminants on the surfaces to be cleaned or to ruin them. Thus, Teknek develops different kinds of rollers: each is specific for types of surfaces and particles. So, Teknek has a practical and a posteriori knowledge about its rollers: Teknek researchers empirically know how to

modify the surface or the material of their rollers, in order to satisfy a specific issue of a customer. However, they feel important also to go into fundamental science in order to provide better solutions to their customers. That is why Teknek partially funded this research and provided some of the materials used.

However, dealing with commercial materials may be difficult because they may not correspond to specifications used to develop physical theories. For example, in surface adhesion studies, it is quite common to start from the simplest type of sample, that means a non-deformable or perfectly elastic material with a homogeneous, perfectly clean and smooth surface. This is rarely the case in commercial materials, where at least one of the previous conditions is not fulfilled. Not only: in order to find a correlation between a physical property of a material and a feature, it is often necessary to have a series of homologous materials that differ from them in only one feature, in order to surely correlate that feature with a change of the studied property. Also this may be difficult when working with commercial materials, because industrial research faces with a specific practical issue and this could demand the change of different features at the same time with respect to a previously developed material. Thus, in order to correlate results found in the analysis of commercial materials with theories and features, and, at the same time, in order to use theories' results for prediction in 'real world' or for development of commercial materials, a model material is necessary. In this project, the laboratory made material represents the model material, because it is synthesized in order to obtain samples that are the most similar to those used to develop physical theories and studies of features. Specifically, the model material is an elastomer: the choice of which type of elastomer to use is related both the commercial samples provided and the ideal networks used in physical studies. The homologous series is carried out changing a bulk property in order to see if surface properties can be related to it.

2.2 Scientific formulation of Teknek system

The part of the project related to Teknek's samples focuses on features, properties and performances of the cleaning rollers (thus means that attention will be paid on the surface to be cleaned and cleaning rollers, excluding the adhesive roller). The Teknek system can be sketched as depicted in Figure 2.2, with a particle on a surface and the cleaning roller over it. The particle will be removed from the surface if its adhesive interactions with the roller are greater than its adhesive interactions with the surface (adhesive interactions acting between two surfaces can be considered as a whole, also referred as adhesion force). That means that there are two adhesion forces that play a role in the system: the adhesion force between the particle and the surface of the substrate $F_{\text{adh PS}}$, and the adhesion force between the particle and the roller, $F_{\text{adh PR}}$. The condition to be satisfied in order to remove the particle from the substrate is

$$F_{\text{adh PR}} > F_{\text{adh PS}} \tag{2.1}$$

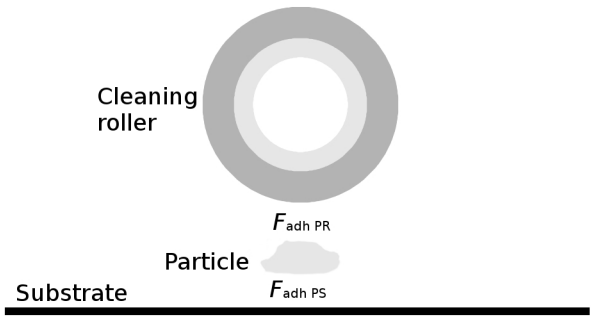

Figure 2.2: Sketch of Teknek system, consisting in the surface of a substrate, a particle to be removed and the cleaning roller. The three components are depicted as they were separated instead of being into contact for sake of clarity. The particle is disputed between the substrate and the roller: it will adhere on the surface where the adhesion force is the greatest.

In this project, colloidal probes will be used as particles and adhesion force against different substrates and rollers will be collected. This will let us know adhesion behaviour of both substrates and rollers and which roller is able to clean substrates removing specific types of particles from them.

2.3 Aim of the investigation of laboratory made samples

Laboratory made samples, that are synthesised in order to match the requirements of fundamental physics research with the aim to go into the industrial issue of Teknek, are tested with the same method of the commercial samples. Because they are 'model materials', adhesion investigation is focused on the understanding of adhesion behaviour rather than on an extensive study of adhesion performances: it means that, for example, only one type of colloidal particle is used in adhesion tests, however, adhesion test may be performed with different sets of parameters. Moreover, other tests are performed in order to verify their synthesis and to characterise their behaviour and bulk properties. And then, adhesion data are correlated with those properties and behaviour.

Results collected from adhesion studies of the rollers and the laboratory made samples will be compared in order to have a comprehensive view of adhesion – sample features and properties dependence.

2.4 Polymers: description and properties

A polymer is a long molecule formed by several repeating units, from few hundreds to several thousands. In fact, the word 'polymer' derives from a Greek word that means 'many members'. The repeating unit should not be confused with the monomer, that is the starting small molecule used for the synthesis of the polymer. Of course, the monomer and the repeating unit can be quite similar in structure: it depends on the kind of reaction used for the synthesis. However, it is quite common to use the word 'monomer' also for the designation of the repeating unit.

The repeating units can be identical or of two or three different types and can be arranged in an ordered way or not. Polymeric chains can be linear, or branched or crosslinked. According to the types of repeating units, their positions along the chain, chain types and length, the resulting polymer will show different physical and mechanical properties. For example, a particular class of polymeric material is

represented by elastomers. Elastomers, also called rubbers, are able to deform when a stress is applied without breaking and to recover their original shape when the stress is removed. That is explained by the structure: elastomers are formed by chains crosslinked with each other (actually, they can be considered as formed by a unique endless molecule). Thus, when the stress is applied, chains will be stretched, but they cannot flow each other because of the crosslinks that act as constrains. Subsequently, with the removal of the stress, chains can recover their original position and conformation, letting the sample recover its original shape. On the contrary, when a stress is applied on a polymer formed by linear chains, the sample will deform because of the stretching and the flowing of its chains; however, when the stress is removed, chains will recover their original conformations (related to the stretching) but not their original relative positions (related to the flow) and the sample will remain in a deformed state. In addition, also the productive process and the use of additives can result in polymers formed by the same repeating units but with different physical and mechanical properties. However, in this project, influences of processing and additives will be not considered, apart from being aware of those and so, because of that, conditions to minimize them as much as possible are used.

2.4.1 The glass transition temperature

The glass transition temperature, T_g, is a very important physical property of polymers. It is the temperature that defines the change from the glassy state to a softer rubbery/melt state. Below T_g, the amorphous phase of the polymer is not able to be in thermodynamic equilibrium with the temperature because there is not enough energy for chains movements: it can be described as frozen in a specific conformation. In this state, the polymer behaves as glass: it is a hard and brittle material. Above T_g, the amorphous phase of the polymer is in melt state: in this state, the polymer behaves as a viscous liquid, where chains can have freedom of movements and the polymer can be in thermodynamic equilibrium with the temperature. In this state, for example, an elastomer behaves as previously

described, while a non-crosslinked amorphous polymer behaves as a soft plastic or a viscous liquid (depending on the molecular weight) and a semi-crystalline polymer behaves as a more rigid plastic due to the crystalline domains.

It should be noted that the glass transition temperature does not have a unique value: it depends on the kinetics of the process of cooling and heating (the slower the speed of cooling is, the lower the T_g is). Actually, it is a range of temperatures in which the transition can happen. By convention, the tabulated values of T_g are referred to cooling speeds in the range of 10-20 °C/min [7].

The glass transition temperature is not directly involved in this project, but it is an important polymer property which is used for polymer characterization and is present in many formulas.

2.4.2 Mechanical properties and behaviours

In addition to the glass transition temperature, another important feature of polymers is the way they act when a stress is applied, that is their mechanical behaviour. Mechanical behaviour can range from being perfectly elastic to perfectly viscous: between these two boundaries, a mixed behaviour is observed, referred as viscoelasticity. A brief introduction is presented below, in order to let the reader better understand the following sections.

A perfectly elastic polymer is a material that shows an instantaneous strain when a stress is applied and that is able to recover its original shape when the stress is removed, so that there is not energy dissipation. In fact, energy used to deform the polymer is stored in the polymer and returned when the stress is removed so that the polymer recovers its original shape. For small deformations the strain is usually directly proportional to the applied stress. The coefficient of proportionality that relates stress to strain is called 'modulus': the type of modulus depends on the kind of applied stress. It is called 'elastic modulus' or 'Young's modulus' (usually E) when it refers to mono-axial tension or compression test or 'shear modulus' (usually G) when it refers to a shear test or 'compression modulus' (usually K) when it refers to

non-mono-axial compression test. Thus, if the mono-axial axial tension or compression is considered, σ is the applied stress (that is the ratio between the applied force and the area of application of that force) and ε is the strain, the relationship between them is:

$$\sigma = E\varepsilon \tag{2.2}$$

The elastic behaviour is often sketched as a spring, whose elastic constant is one of the previous moduli.

The three moduli are related each other by means of the Poisson coefficient, ν according to:

$$E = 3K(1 - 2\nu) = 2G(1 + \nu) \tag{2.3}$$

The Poisson coefficient is a temperature-dependent characteristic of a material and it is a measurement of volume variation when a mono-axial stress is applied. It usually ranges from 0-0.2 to 0.5 (this last value is for incompressible materials).

A perfectly viscous polymer is a material that shows a time-dependent strain when a stress is applied: the speed of deformation is directly proportional to the applied stress. In this case, when the applied stress is removed, the polymer does not recover its original shape: the energy used to deform it is totally dissipated during the deformation process. The coefficient of proportionality that relates stress to velocity of deformation is called 'viscosity', η. Thus, if σ is the applied stress and $\dot{\varepsilon}$ is the velocity of deformation, the relationship between them is:

$$\sigma = \eta\dot{\varepsilon} \tag{2.4}$$

The viscous behaviour is often sketched as a dashpot with a fluid with a viscosity η.

All the other mechanical behaviours that are in between the perfect elastic and the perfect viscous models, are referred as viscoelastic. Viscoelasticity can be linear or non-linear. In the former case, the coefficients that correlate stress with strain are only time-dependent; in the latter case they are also stress or strain-dependent. For small strain or stress, as that deals with in this project, linear viscoelasticity holds. A viscoelastic polymer partially behaves as an elastic material,

instantaneously responding to the changes of the applied stresses, and partially behaves as a viscous material, time-responding to the changes of the applied stress. Actually, it is a material that partially dissipates energy and whose behaviour depends on the velocity of the applied stress or strain. The coefficients that correlate stress and strain are actually time-dependent functions. The form of these functions depends on the specific characteristics of each material. A common way to express them is to use different combinations of parallel or in series viscous elements (dashpots) and elastic elements (springs) with different viscosities and elastic constants. Some simple examples of these combinations are a spring and a dashpot connected in series (also called 'Maxwell element'), a spring and a dashpot connected in parallel (also called 'Kelvin-Voigt element') or combinations of both of them.

An interesting case of mechanical behaviour of polymers is when an oscillatory stress or strain is applied to them. Usually, a periodic sinusoidal function of stress or strain is used, like:

$$\varepsilon(t) = \varepsilon_0 \sin(\omega t) \tag{2.5}$$

where ε_0 is the strain amplitude and ω is the frequency of the applied strain. If the polymer is perfectly elastic, it will show a sinusoidal stress in phase with the applied strain:

$$\sigma(t) = \sigma_0 \sin(\omega t) \tag{2.6}$$

If the polymer is perfectly viscous, it will show a sinusoidal stress 90° out of phase, in fact, starting from 2.4 and using 2.5, the stress function becomes:

$$\sigma(t) = \eta\dot{\varepsilon} = \eta\omega\varepsilon_0 \cos(\omega t) = \sigma_0 \sin(\omega t + \pi/2) \tag{2.7}$$

where $\sigma_0 = \eta\omega\varepsilon_0$ is the stress amplitude. If the polymer is viscoelastic, it will show an intermediate behaviour with a phase lag between the applied strain and the recorded stress lower than 90°. If $\hat{\delta}$ is the phase lag, the general function for the stress is:

$$\begin{aligned}\sigma(t) &= \sigma_0 \sin(\omega t + \hat{\delta}) = \sigma_0(\sin(\hat{\delta})\cos(\omega t) + \cos(\hat{\delta})\sin(\omega t)) \\ &= \sigma_0^{'}\sin(\omega t) + \sigma_0^{''}\cos(\omega t)\end{aligned} \tag{2.8}$$

where the components in phase and out of phase are been separated. Using 2.2, it is possible to express 2.8, for examples, in terms of E (if a mono-axial tension is considered) as in the following:

$$\sigma(t) = \varepsilon_0 E^{'}\sin(\omega t) + \varepsilon_0 E^{''}\cos(\omega t) \tag{2.9}$$

where the in phase modulus $E^{'}$ is called 'real modulus' or 'storage modulus' and the out of phase modulus $E^{''}$ is called 'imaginary modulus' or 'loss modulus'. Ideally, the storage modulus equals the Young's modulus, however the former is equal or similar to the latter only when the applied stress or strain are small and their application rate is low [8, 9]. Because this is the case of this work, the storage modulus at the lowest frequencies will be considered equivalent to the corresponding bulk modulus (because, of course, the previous mathematical presentation can be equally applied to different kinds of applied stresses or strains and so to different kinds of moduli). In any case, the ratio between the loss modulus and the storage modulus is the measurement of the phase lag, that is a measurement of viscoelasticity of the sample:

$$\tan\hat{\delta} = \frac{E^{''}}{E^{'}} \qquad \text{or} \qquad \hat{\delta} = \arctan\left(\frac{E^{''}}{E^{'}}\right) \tag{2.10}$$

The value of the phase lag is a characteristic of a material and depends on the frequency ω and the temperature of the analysis.

2.4.3 Elastomers

Elastomers are a particular type of polymers, partially introduced previously. They are able to be significantly deformed by a small stress and to recover their original shape when the applied stress is removed. This characteristic is strictly related to their crosslinked structure as aforementioned. Crosslinks act as chemical constrains that do not let chains flow if a stress is applied and let chains return in their original positions after the removal of the stress.

Thus, an elastomer can be thought as a three-dimensional network, with crosslinks connecting three or more polymer chains together. The number of chains connected to a single crosslink is defined as 'functionality': in order to have a network, this number should be greater than two, otherwise it is just a prolongation of chains.

Moreover, also the positions of the crosslinks along the chains and their three-dimensional displacement in the network can influence the mechanical behaviour of an elastomer and should be considered. Where crosslinks are located along chains is primarily a matter of the chemical reaction chosen for the synthesis of crosslinks. Some reactions can form crosslinks at any point of a chain, while others only in specific positions. An example of reaction of the former type is the radical reaction, while examples of the latter one are all those reactions that happen between specific chemical groups distributed in the polymer chain. This last type of reaction can imply the presence of two different kinds of reactive chemical groups along chains (and this means that usually the crosslink reaction is between two 'similar' polymers that differ for the nature of those chemical groups), or between two species, the polymer with a specific type of chemical group, and another molecule, called crosslinker, that is able to react with the chemical group presented along the chain and to connect more chains together. At a better glance, the difference between a so-called 'crosslinker' or a so-called 'similar polymer' is just a matter of language and usage: they are both species that are able to connect three or more chains of polymer. In any case, the word 'crosslinker' is used when the connecting species is quite chemically different from the polymer (usually it is a quite short or small molecule, quite different from the polymer). In the case of a 'similar polymer' it is usually considered as the polymer itself, because it is assumed that small changes in the chemical groups do not affect the characteristics of the chains themselves. In any case if these chemical groups are regularly distributed along chains, also the three dimensional network will try to be ordered. Usually, theories that deal with elastomers or rubbers assume that the network is regular, or better, ideal with crosslinks uniformly distributed along the chains and the

network. A particular case is when reactive chemical groups are at the ends of the polymer chains: in this case, the distance between two crosslinks is the length of the linear chain and the network can be thought as a regular 'mesh'. However, other factors usually prevent the formation of a such 'perfect' three-dimensional network, even when the reactive chemical groups are regularly distributed along the chains. For example, a very critical factor is the crosslinks reaction condition: in order to have a good network, the ends of chains and eventually the crosslinker, should be located right next to each others, but this may be very difficult to achieve, because starting linear polymers are often quite viscous, so it is difficult to mix them in an efficient manner. Moreover, during the reaction, the viscosity greatly increases until chain translations become impossible. In addition to this, linear polymer chains should be imagined like coils, because that is the most favourable conformation. Of course, this conformation can generate some imperfections in the network, such as, for example, loops (because the two ends of the same polymer chain are linked to the same crosslink), entanglements (because one chain can twist around another one, both belonging to different parts of the network) and others. In conclusion, it is impossible to synthesis an ideal polymer network, even if a good crosslinking reaction is chosen. However, if imperfections are limited, theories based on an ideal network can be still used with a good approximation.

There are three main classical theories that are used to relate macroscopic elastic behaviour (like the mechanical or swelling ones) to network structure. They are based on the assumptions that chain distribution is Gaussian, the elastic free energy of the network is the sum of chains elastic free energy and the network is ideal. What is different among these models are the boundary conditions [10]:

- in the affine model, the network deforms affinely at all length scales. It means that an applied stress at macroscopic scale acts in the same way on all crosslinks, which are not free to fluctuate, and chains, which can only deform affinely;

- In the phantom model, the crosslinks are able to fluctuate around their mean positions and chains can move freely. Only the mean crosslinks positions deform affinely with the applied stress;
- In the constrained junction fluctuation model, crosslinks are still able to fluctuate around their mean positions, but they are also limited by chains surrounding them. This model actually describes situations in between the other two, that are the limiting cases.

Because of these different boundary conditions, these three models are applied in different cases: for small deformations the affine model holds; for intermediate deformations, the constrained junction fluctuation model is well suitable; for large deformations, the phantom model applies and for very large deformations, none of them are fine, because at least one of the main assumptions does not hold. Other models have been developed, however these are the most common and regularly used.

An important parameter when a polymer network is considered is the (mean) distance between crosslinks. This is strictly related to the mechanical properties of the elastomer: short chains between crosslinks will lead to a greater Young's modulus and a lower applied stress without rupture of the sample. On the contrary, long chains will be easily deformed and will support greater strains before breaking. A common measure of this is the crosslink density: it is not a measure of the length of chains between two crosslinks, although it is related to that. In fact, it is the number of active elastic strands per unit volume of an elastomer: low crosslink densities mean that long chains connect crosslinks, while high crosslink densities are due to short chain connections. However, a relationship between the crosslink density and the (averaged) weight of the chains between crosslinks M_c exists and it is

$$M_c = \frac{\rho_p}{n} \tag{2.11}$$

where ρ_p is the polymer density and n is the crosslink density.

Crosslink density can be found from both swelling or mechanical measurements; formulas will differ for each of the aforementioned models. Swelling happens when a solvent penetrates into the polymer network: how much the sample swells depends on the length of the chains between crosslinks (or on the crosslink density) and on the type of solvent. After a certain time, when the polymer is in contact with the solvent, an equilibrium state is reached, where the mixing contribution to the free energy (that arises from the maximization of polymer-solvent interactions and so it is the driving force for the swelling of the polymer) is balanced by the elastic contribution to the free energy (that tries to avoid the swelling of the polymer, because chains prefer a lower energy state, with non elongated conformations) [11]. When equilibrium is reached, formulas let the crosslink density be related to the increased volume of the sample. In the affine model that formula is:

$$n = \frac{\ln(1-\varphi_2) + \varphi_2 + \chi\varphi_2^2}{V_m\left(\frac{2\varphi_2}{f} - \varphi_2^{1/3}\right)} \tag{2.12}$$

where V_m is the molar volume of the solvent, φ_2 is the volume fraction of the polymer in the swollen state, f is the crosslink functionality and χ is the Flory-Huggins polymer-solvent interaction parameter. In the phantom model that formula becomes:

$$n = \frac{\ln(1-\varphi_2) + \varphi_2 + \chi\varphi_2^2}{V_m\varphi_2^{1/3}\left(\frac{2}{f} - 1\right)} \tag{2.13}$$

or in its more general formula

$$n - u = \frac{\ln(1-\varphi_2) + \varphi_2 + \chi\varphi_2^2}{V_m\varphi_2^{1/3}} \tag{2.14}$$

where u is the number of junctions per unit volume. The general formula is useful in the case of non complete reactions or where the functionality of the crosslink is not known.

The Flory-Huggins polymer-solvent interaction parameter is specific for every pair of solvent and polymer. In the simplest approximation it depends only on the

temperature, but many studies have shown that it is also dependent on the volume fraction of the polymer in the swollen state, φ_2 [10, 12-15], according to the most general formula

$$\chi = c_1 + c_2\varphi_2 + c_3\varphi_2^2 \tag{2.15}$$

where the constants c_1, c_2 and c_3 are different for each polymer-solvent pair (equation 2.15 is the most general formula: often, the simplest equations with c_3 and sometimes also with c_2 equal to zero are used). This dependency is still not clear: in fact, for some polymer-solvent pairs there is a great dependence on the polymer volume fraction, while for others the Flory-Huggins interaction parameter is largely insensitive of that. It is thought that better solvents show the least dependency [16]. However, for the same polymer-solvent pairs at constant polymer volume fraction, the Flory-Huggins interaction parameter is different for a linear polymer and solvent or for a crosslinked network and solvent [12, 13].

Starting from a mechanical measurement, for each of models previously seen it is possible to calculate the change of the free energy related to a specific applied stress (for example for mono-axial tension). From the free energy it is possible to find the relative stress-strain relationship and the expression of the modulus in terms of the crosslink density. Considering again the case of the mono-axial tension, the crosslink density is:

$$n = \frac{E}{3\,\mathrm{R}\,T} \tag{2.16}$$

for the affine model or

$$n = \frac{2\,E}{3\,\mathrm{R}\,T} \quad \text{or} \quad n - u = \frac{E}{3\,\mathrm{R}\,T} \tag{2.17}$$

for the phantom model, where R is the gas constant and T is the temperature (the right-hand side equation is the generalised form). It is interesting to note that in the non generalised phantom model, the modulus is a half of that in the affine model. Relationships 2.16 and 2.17 hold only from small strains [17].

However, both the swelling and the mechanical properties are influenced by network defects, so results of these measurements take into consideration all the constraints to the swelling or to the extension of the sample, including loops or entanglements, for examples. That means that, the use of formulas from 2.12 to 2.17 in the case of non-ideal network can lead to wrong conclusions. In the case of networks with few defects, those formulas can still be used, but, in absence of another independent method for the determination of related properties, it is better to consider them in a qualitative or semi-quantitative way.

2.5 Surfaces and interfaces

In this thesis, great attention is dedicated to surfaces and interactions among them. A surface is the outer part of a condensed phase: it is the part of one phase that is exposed to another phase. Usually, in the macroscopic world, little attention is dedicated to surface and interface properties, even if they have a relevant role in everyday life (for example, in the adhesive or paint fields). In fact, materials are often characterized by means of bulk properties, which are properties of the entire phase, derived by the aggregate of atoms or molecules in that phase. Atoms and molecules that belong to the surfaces or to the first layers of the surfaces of a phase experience a different situation in comparison with those that are in the bulk. Because the molecules in bulk are surrounded by other molecules of the same type, they experience the same interactions in all the directions, while molecules at the interface are only partially in contact with molecules of the same type, and so they experience interactions only in specific directions (from molecules of the bulk and other surface molecules next to them, as depicted in Figure 2.3 for molecules in a drop). This condition confers different properties on a surface with respect to the bulk.

An interface is the boundary between two (or more) phases. Interactions among different phases happen at the interface: they can be solid-solid, solid-liquid, solid-vapour or liquid-vapour interfaces.

The first characteristic of a surface is the surface energy (and tension) that will be described in the next section, together with its connection to the work of adhesion (surface tension and surface energy are often used as synonyms: they are effectively related to the same physical property but specifically, the former is a vector, the latter is a scalar). The following section will introduce the contact angle with water as an indication of hydrophobicity or hydrophilicity. These are other important characteristics of a surface and they originate from the differences of surface energy and tension of the three media involved. In particular, hydrophilicity can play a relevant role in influencing the adhesion force, in specific environmental conditions, as will be explained in more details in the section about the capillary force.

2.5.1 Surface energy, surface tension and work of adhesion

As a result of the fact that surfaces experience a different environment in comparison to molecules or atoms in the bulk, they have energy. To understand the origin of this energy it is possible to refer to the process of surface formation, starting from a single piece of material. The formation of two complementary surfaces is due to the separation or rupture of the original piece into two smaller pieces: it implies the rupture of chemical bonds or interactions that were present at the beginning. This means that the surface formation is often an unfavourable process and that surfaces possess a higher energy due to the partial loss of bonds and interactions. Surface energy is defined as the work required to increase the surface by unit area, while surface tension as the force required to extend a liquid film by unit length and γ is the symbol used for them (from that, γ can be equivalently expressed both in $\mathrm{N/m}$ and $\mathrm{J/m^2}$). Surface energies and surface tensions in air have been tabulated for different solids and liquids.

Thus, surface energies are implied in surfaces formation starting from a single substance or two different substances initially brought into contact. In the former case it is dealt with work of cohesion, in the latter case with work of adhesion. Work

of cohesion for the formation of two unit surfaces is simply twice the surface energy of the considered substance:

$$\Delta\gamma = 2\gamma \tag{2.18}$$

where $\Delta\gamma$ is the work of cohesion. Work of adhesion between two unit surfaces is defined as the sum of the surface energies of the two substances minus the interfacial energy of both of them in contact:

$$\Delta\gamma = \gamma_1 + \gamma_2 - \gamma_{12} \tag{2.19}$$

where $\Delta\gamma$ is now the work of adhesion, γ_{12} is the interfacial energy of the two substances in contact and γ_1 and γ_2 are the surface energies in air or in vacuum of solid 1 and solid 2, respectively.

In equation 2.19, γ_{12} is specific of the interactions of material 1 with material 2 and so is often not tabulated. Luckily, different models have been developed for the calculation of $\Delta\gamma$ starting from the surface energies of the two solids, avoiding the calculation of 'mixed' term. The first step is the assumption that the surface energy of a solid or a liquid is the sum of different contributions, due to different types of acting forces. For example, if in the solid or in the liquid two different types of forces are present, say, the polar and the dispersion ones, the surface energy of the body 1 will be:

$$\gamma_1 = \gamma_1^{\mathrm{p}} + \gamma_1^{\mathrm{d}} \tag{2.20}$$

where the superscripts p and d stand for polar and dispersion, respectively (for a better description of the polar and dispersion contributions refer to the following parts of this chapter). The second step is the assumption that the work of adhesion is the sum of the geometric means of the different contributions to the surface energies of the two bodies. The first proposed model considers only the geometric mean of the dispersion contributions, because this type of contribution is always present (it corresponds to the dispersion or London forces) [18]. According to this model, the work of adhesion is:

$$\Delta\gamma = 2\sqrt{\gamma_1^{\mathrm{d}}\gamma_2^{\mathrm{d}}} \tag{2.21}$$

so, equating equation 2.21 with 2.19, the interfacial energy is:

$$\gamma_{12} = \gamma_1 + \gamma_2 - 2\sqrt{\gamma_1^d \gamma_2^d} \tag{2.22}$$

A more complete model considers also the contribution of the polar components [19], so that the work of adhesion becomes:

$$\Delta\gamma = 2\sqrt{\gamma_1^d \gamma_2^d} + 2\sqrt{\gamma_1^p \gamma_2^p} \tag{2.23}$$

and, consequently, the interfacial energy becomes:

$$\gamma_{12} = \gamma_1 + \gamma_2 - 2\sqrt{\gamma_1^d \gamma_2^d} - 2\sqrt{\gamma_1^p \gamma_2^p} \tag{2.24}$$

The choice of the model depends on the presence or absence of a strong polar contribution to the work of adhesion. Other models have been developed, for example, with the use of the harmonic mean instead of geometric mean [20], however, these are beyond the aim of this thesis.

2.5.2 Contact angle

The contact angle is a macroscopic measurement of the wettability of a surface by a liquid. The liquid is often water, so the result of this determination is a classification of a surface as hydrophilic, hydrophobic or superhydrophobic. When a drop of water is put on a smooth, homogeneous and rigid surface, its shape is the result of the equilibrium of three surface tensions. In Figure 2.3 the different conditions experience by the water molecules at the interfaces are represented.

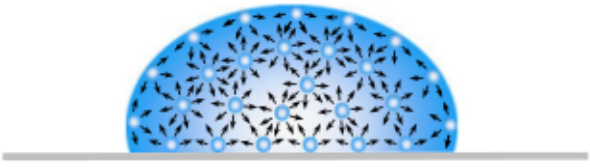

Figure 2.3: Surface tension in a drop of water due to the unbalanced forces acting at the interfaces. Image reprinted/adapted by permission from Springer Nature Customer Service Centre GmbH: Springer Surface Science Techniques by Yuan Y., Lee T.R. COPYRIGHT (2013).

The law that rules the shape of a drop in these conditions is the Young equation (as depicted in Figure 2.4):

$$\gamma_{sv} = \gamma_{sl} + \gamma_{lv}\cos\theta_Y \tag{2.25}$$

where γ_{sv} is the interfacial tension between the solid surface and the vapour, γ_{sl} is the interfacial tension between the solid surface and the liquid of the drop, γ_{lv} is the interfacial tension between the liquid and the vapour interface and θ_Y is the contact angle. The contact angle is defined "as the angle formed by the intersection of the liquid-solid interface and the liquid-vapor interface (geometrically acquired by applying a tangent line from the contact point along the liquid-vapor interface in the droplet profile)" [21].

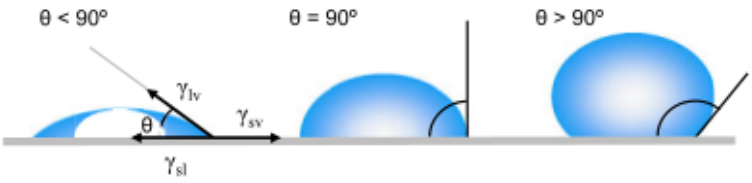

Figure 2.4: Illustration of the contact angle for three different values of the angle θ_Y (in this figure θ stands for θ_Y). The three vectors of the surface tensions are also depicted in the first image. Image reprinted/adapted by permission from Springer Nature Customer Service Centre GmbH: Springer Surface Science Techniques by Yuan Y., Lee T.R. COPYRIGHT (2013).

From the value of the contact angle θ_Y, a surface is classified into one of three aforementioned groups as follows:

- when $\theta_Y < 90°$ the surface is considered hydrophilic;
- when $\theta_Y > 90°$ the surface is considered hydrophobic;
- when $\theta_Y > 150°$ the surface is considered superhydrophobic.

The Young equation is only valid for smooth and homogeneous surfaces: it does not hold in presence of roughness or heterogeneities of the materials surfaces. Two other equations have been developed for these two cases, the Wenzel for rough surfaces and the Cassie-Baxter for heterogeneous surfaces. However, because the

Cassie-Baxter equation can be also applied to rough hydrophobic surfaces, it will be introduced in the section dedicated to the effect of roughness, together with the Wenzel equation.

2.6 Adhesion

'Adhesion' can be defined as the overall resultant of the interactions between two surfaces. In some contexts, it is still used to divide it into 'fundamental adhesion' and 'practical adhesion': the former refers to interactions that lead two surfaces to stick together, while the latter is addressed to interactions acting during the separation of two adhering surfaces. In this field of studies, the word adhesion is used with the meaning of practical adhesion and with this in mind, it will be used in the following discussion.

Thus, the 'force of adhesion' (also simply 'adhesion' in this thesis) is the sum of all the forces acting between two surfaces in contact. Types of forces and their magnitudes depend on the environmental conditions in which the adhesion is determined, the materials of the two surfaces involved and their dimensions and shapes. In fact, some forces can act only if the measurements are done in a specific environment, such as hydrodynamic forces, that act in a liquid environment or the capillary force, the presence and magnitude of which depends on the relative humidity. The presence of other forces is related to the characteristics of the materials of the two surfaces involved, as in the case of the magnetic force, which requires that the materials are magnetic. The nature of the materials involved is also connected to forces related to the chemical bonds or weaker chemical interactions that can be established, such as the chemical force (the force needed to break chemical bonds between two chemically bound surfaces) or the hydrogen bonding forces (forces necessary for breaking hydrogen bridges). Finally, shape and dimensions define the scale of the interactions, such as macroscale, microscale or nanoscale: according to the scale, different forces become predominant. For instance, van der Waals forces (vdW forces) are very weak but universal, and

become an important contribution at the nanoscale. Also the capillary force, if present, can become the main contribution at the micro- and nanoscale.

The measurements performed in this research were taken in air between organic and inorganic surfaces at the microscale: that scenario reduces the contributions to the adhesion to three forces, the capillary force, the vdW forces and the electrostatic force. Thus,

$$F_{\text{adh}} = F_{\text{cap}} + F_{\text{elec}} + F_{\text{vdW}} \tag{2.26}$$

A short introduction to these forces will be presented below: it will include some mathematical discussions, even if, for this research there will be only a qualitative interest in there.

2.6.1 Electrostatic force

The electrostatic force or Coulomb force is a force acting between two charged bodies, according to the Coulomb law:

$$F_{\text{elec}}(h) = \frac{Q_1 Q_2}{4\pi\varepsilon_0\varepsilon_r h^2} \tag{2.27}$$

where Q_1 and Q_2 are the values of the two point charges, ε_0 is the vacuum permittivity $\left(8.854 \times 10^{-12}\ \text{C}^2\text{J}^{-1}\text{m}^{-1}\right)$, ε_r is the relative permittivity of the medium and h is the distance between the two charges. If the interaction is in air, as is the case of this study, ε_r equals to unity. Thus, this force can be established only in presence of two charged bodies and depends on the distance (of a factor of h^{-2}); it could be positive or negative according to the charges' signs (i.e. attractive or repulsive) and it is additive (i.e. in a multi-charge system, the total force acting in the system is done by the vectors addition of all the pair interactions).

When this force is acting between two charged surfaces, it will depend on the geometry of the system. The geometry used in this research involves a sphere and a plane, so the force becomes [22]:

$$F_{\text{elec}} = -\pi\varepsilon_0\Delta V^2\frac{R}{h} \tag{2.28}$$

where ΔV is the voltage difference between the two bodies, R is the radius of the sphere and the negative sign stands for the attractive interaction. Equation 2.28 holds if $R \gg h$, that is the condition used in this thesis. Thus, differently from the two charged points model, the electrostatic contribution between a sphere and a plane is inversely dependent on the distance h.

2.6.2 Van der Waals forces

Van der Waals forces belong to the group of the electrical forces because they act among bodies that show at least a temporary partial charge. It is divided into three interactions:

- orientation or Keesom interaction. It is an electrostatic force that arises among permanent dipoles (a dipole is a separation of positive and negative charges: it can happen in a polar group in a molecule). In the simple system of two permanent dipoles that are free to rotate, the energy of the interaction (averaged over all the angles) is:

$$w(h) = -\frac{u_1^2 u_2^2}{3(4\pi\varepsilon_0\varepsilon_r)^2 \mathrm{k_B} T h^6} \tag{2.29}$$

  where u_1 and u_2 are the dipole moments of the dipole 1 and 2, respectively, $\mathrm{k_B}$ is Boltzmann constant and h is their distance.

- induction or Debye interaction. It is an electrostatic force that arises between a permanent dipole and an induced dipole. An induced dipole is a 'transient' dipole: it is a non-polar molecule where separation of charges arises from the presence of an external electrical field. The key parameter for this interaction is the polarizability (α) that determines the induced dipole moment in the presence of an electrical field E_{elec} for a specific species:

$$u_{\mathrm{ind}} = \alpha E_{\mathrm{elec}} \tag{2.30}$$

  A molecule can have a permanent dipole moment as well as a polarizability: in the most simple and general case of two molecules with permanent

dipoles u_1 and u_2 and with polarizabilities α_{01} and α_{02} the energy of this interaction is:

$$w(h) = -\frac{u_1^2\alpha_{02} + u_2^2\alpha_{01}}{(4\pi\varepsilon_0\varepsilon_r)^2 h^6} \tag{2.31}$$

- dispersion or London force. This force is quantum-mechanical in origin and it is always present even if there are not polar molecules or dipoles. This force arises when the fluctuation of the electrons origins an instantaneous dipole. This instantaneous dipole generates an electrical field that induces the polarization in a near molecule, and so on (in fact, the dispersion force arises between two induced dipoles). In the case of two dissimilar atoms or molecules, the energy of the London interaction is described by:

$$w(h) = -3\frac{\alpha_{02}\alpha_{01}}{(4\pi\varepsilon_0)^2 h^6}\frac{\pi\hbar\nu_1\nu_2}{\nu_1+\nu_2} = -\frac{3}{2}\frac{\alpha_{02}\alpha_{01}}{(4\pi\varepsilon_0)^2 h^6}\frac{I_1 I_2}{I_1+I_2} \tag{2.32}$$

where I_1 and I_2 are the first ionization potentials of the two atoms or (simple) molecules (usually in the UV region), and ν_1 and ν_2 are the orbiting frequencies of electrons of the two atoms or molecules. This force is not pairwise additive: in fact, the net effect of the electric field on a molecule 2 by a molecule 1 is influenced by the 'reflection' or interaction with this field and other molecules around. This force is also retarded because it requires that the field generated from molecule 1 reaches molecule 2 and, from this, returns to molecule 1: this process is not instantaneous and it takes time, according to the medium and the distance between the two molecules. If that time is comparable with the period of the fluctuation of the first inducted dipole, when the field reflected from molecule 2 returns to molecule 1, this has now another orientation, usually less favourable, and so the final interaction between the two molecules is lower. In a specific medium, this retardation effect arises with the increase of the distance between the two molecules: over a certain distance, retardation effect cannot be neglected and it causes a faster decay of the interaction energy with the distance, with a factor of h^{-7}, instead of h^{-6}.

Thus, the total van der Waals energy in air for two different molecules is the sum of these three contributions:

$$w_{\mathrm{vdW}}(r) = -\frac{1}{(4\pi\varepsilon_0)^2 h^6}\left[(u_1^2\alpha_{02}+u_2^2\alpha_{01}) + \frac{u_1^2 u_2^2}{3\mathrm{k_B}T} + \frac{3\alpha_{01}\alpha_{02}\pi\hbar\,\nu_1\nu_2}{\nu_1+\nu_2}\right] \quad (2.33)$$

Usually, the dispersion force overcomes the others, except in the case of small highly polar molecules (like water). It is important to note that all the three contributions vary inversely with the sixth power of the distance. It is derived that the vdW forces act over a smaller range than the electrostatic forces and become a relevant contribution to the adhesion force at very small scale. However, because of the predominance of the dispersion force and its retardation effect, the total vdW energy has a curious progression: it depends on h^{-6} at very short distance, then on h^{-7} at intermediate distance and finally again on h^{-6} at long distance. That happens because at short and intermediate distances, the dispersion force usually predominates, but at longer distance the Debye and Keesom forces become stronger because they do not suffer from retardation effects [23].

The above description of the van der Waals forces is related to small molecules in a medium however, it is now interesting to move from these to the interactions between macroscopic bodies. Two different approaches were developed to determine the van der Waals forces between macroscopic bodies: the microscopic or Hamaker approach and the macroscopic or Lifshitz one. The former is based on the pairwise summation of the forces acting between all the molecules in the bodies and so, it neglects the non-additivity effect. The latter considers bodies as continuous media and uses bulk properties, so, totally ignoring the atomic structure of the bodies. The final formulas for the description of the non-retardant van der Waals forces between two bodies are the same, but the form of the constant implied, called 'Hamaker constant', is different. These formulas now depend on the geometry of the two bodies: for the two more common geometries, i.e. the sphere–sphere and the sphere–plane interactions, the non-retardant van der Waals forces are:

$$F_{\mathrm{vdW}} = -\frac{A_{\mathrm{H}} R^*}{6 h^2} \tag{2.34}$$

where A_{H} is the Hamaker constant, h is the distance between the two bodies and R^* is the radius of the sphere in the sphere–plane geometry or the reduced radius for sphere–sphere interaction (reduced radius is defined in equation 2.43). As aforementioned, the Hamaker constant can have two different expressions, according to the chosen approach: this is beyond the aim of this work and can be found in specialized texts [23, 24]. In both cases, the Hamaker constant contains characteristics of the materials of the two interacting bodies. If the retardation effect is taken into account, the van der Waals forces have a behaviour similar to that seen in the case of the two molecules, with a dependence on the distance of a factor of $1/h^2$ for short distances, that becomes $1/h^3$ at intermediate distance and then comes back to $1/h^2$ for long distances. Typically, the intermediate range starts from distance from 2 to 5 nm. Of course the change of the power law among regimes is gradual however, a simple equation that can describe this behaviour completely does not exist.

The Hamaker constants are specific for each pair of bodies interacting in a medium; luckily some approximations have been developed in order to estimate them starting from the values of the Hamaker constants of each body in air or in vacuum. For example, for the bodies 1 and 2 interacting in air or in vacuum, the constant of Hamaker can be calculated as

$$A_{12} = \sqrt{A_{11} A_{22}} \tag{2.35}$$

where subscripts are related to the bodies.

Van der Waals forces can be both positive or negative: they are always positive for two bodies made of the same material or in air or in vacuum. Typical values of the Hamaker constant between macroscopic bodies in vacuum or in air are in the order of 10^{-19}–10^{-21} J.

2.6.3 Capillary force

The capillary force is a force that arises when a liquid (in this case water) meniscus is established between two surfaces (Figure 2.5). This meniscus can arise from capillary condensation or from the water adsorbed on the surfaces when two surfaces are brought into contact [24]. In the former case, the slit between the two surfaces acts as nucleus of condensation, where the water vapour will condense at the vapour pressure below the saturation vapour pressure P_{sat}, as studied by Lord Kelvin [25]. In the latter case, it is the joint between the two water adsorbed layers that creates the meniscus (Figure 2.9). Eventually, once established, this meniscus could grow because of the capillary condensation as well (situation C in Figure 2.9).

The capillary force is the attractive force acting through two mechanisms: a negative Laplace pressure and the surface tension of the liquid around the periphery of the meniscus [24, 26]. The former is usually the main contribution to the capillary force. It derives from the observation that, if there is a curved interface between two fluids and the system is in equilibrium, a difference of pressure should be present across them. The correlation between the curvature and the difference of pressure is described by the Young–Laplace equation:

$$\Delta P = \gamma_{lv}\left(\frac{1}{r_1} + \frac{1}{r_2}\right) \tag{2.36}$$

where ΔP is the difference of pressure (also called Laplace pressure), γ_{lv} is the surface tension of the liquid, r_1 is the azimuthal radius and r_2 is the meridional radius (an example of these radii is reported in Figure 2.5). The Laplace pressure can be positive or negative, it depends on the specific curvature: a radius is counted positive if concave with respect to the liquid, otherwise it is counted negative. For a meniscus arising between a plane and a sphere, the Laplace pressure is negative if $|r_2| < |r_1|$. The Young–Laplace equation describes a system in thermodynamic equilibrium and neglects the effect of gravitation (that is very small for small menisci). The equilibrium is reached when the Kelvin equation is satisfied: it relates the curvature of the liquid–vapour interface with the vapour pressure as follows,

$$\mathrm{R}\,T\ln\left(\frac{P}{P_{\mathrm{sat}}}\right) = -\,2\gamma_{\mathrm{lv}}V_{\mathrm{m}}\left(\frac{1}{r_1}+\frac{1}{r_2}\right) \tag{2.37}$$

where P is the actual vapour pressure, V_{m} is the molar volume of the liquid, R is the molar gas constant and T is the temperature. The contribution of the Laplace pressure on the capillary force, considering that it acts over a cross–sectional circular area of radius r_1, is:

$$F = -\,\pi r_1^2 \Delta P \tag{2.38}$$

The surface tension is often neglected in the calculation of the meniscus force.

The capillary force can be determined in two different experimental conditions: at the thermodynamic equilibrium (where the vapour is in thermodynamic equilibrium with its condensed phase) or at constant volume of the liquid that forms the meniscus. The first situation is the case of volatile liquids in equilibrium with their vapour phase during the entire measurement; while the second condition is the case of non-volatile liquids or out-of-equilibrium measurements. The difference between the two situations is due to the calculation of the radius of the meniscus at the liquid-vapour interface: in the first case the radius is constant during the entire measurement and is calculated by the Kelvin equation (equation 2.37), while in the second case the radius is not constant and depends on the volume of the liquid in the meniscus. In the latter case, equations are slightly more complicated but the dependence on experimental conditions does not change too much. Thus, in the following discussion, the thermodynamic equilibrium condition is usually assumed.

Many models have been developed to calculate the capillary force for different geometries and experimental conditions. However, because of the difficulty in accounting for all the effects, approximations are often introduced and that is why a fully comprehensive theory that can take into account all the experimental behaviours is still not available (and that is also why in this thesis, the theory about capillary force is not totally developed, leaving greater attention to experimental

results). For example, according to a quite comprehensive model, capillary force between a sphere and a plane is:

$$F = -\pi\gamma_{lv}R_1\sin\beta_1\left[2\sin(\theta_{Y1}+\beta_1)+R_1(\sin\beta_1)\left(\frac{1}{r_2}-\frac{1}{r_1}\right)\right]$$

where:

$$r_1 = R_1\sin\beta_1 - r_2\left[1-\sin(\theta_{Y1}+\beta_1)\right]$$
$$r_2 = \frac{R_1(1-\cos\beta_1)+h}{\cos(\theta_{Y1}+\beta_1)+\cos\theta_{Y2}} \qquad (2.39)$$

where all the geometrical parameters are given in Figure 2.5. In this model, the circular approximation is used to simplify the geometry of the meniscus using only two normal radii.

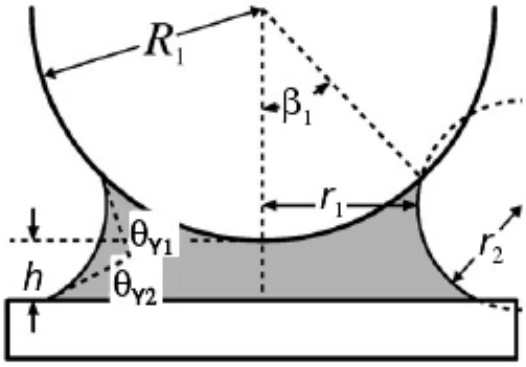

Figure 2.5: Liquid meniscus between a sphere and a plane. Symbols are indicated. Figure adapted and reprinted from [27], Copyright (2009), with permission from Elsevier.

Further approximations can be done if $R_1 \gg r_1 \gg r_2, h$: in this case the capillary force is

$$F = -2\pi\gamma_{lv}R_1\left(\cos\theta_{Y1}+\cos\theta_{Y2}-\frac{h}{r_2}\right) \qquad (2.40)$$

at the thermodynamic equilibrium, or

$$F = -2\pi\gamma_{lv}R_1\left(\cos\theta_{Y1}+\cos\theta_{Y2}\right)\left(1-\frac{h}{\sqrt{h^2+V/(\pi R_1)}}\right) \qquad (2.41)$$

at constant volume. Here, θ_{Y1} and θ_{Y2} are the contact angles of the sphere and the plane respectively, R_1 is the radius of the sphere, h is the distance between the two surfaces and V is the volume of the liquid in the meniscus. As can be noted, the capillary force described in equation 2.40 decreases linearly with the distance h as also shown in Figure 2.6 (in the case of constant volume, the capillary force is longer range than in the case of thermodynamic equilibrium and it does not decrease linearly with the distance). In both conditions, the contribution of the capillary force to the adhesion force for two contacting bodies is:

$$F_{cap} = -2\pi\gamma_{lv}R_1\left(\cos\theta_{Y1} + \cos\theta_{Y2}\right) \tag{2.42}$$

The capillary force does not depend on vapour pressure and r_2: this is due to the fact that, with the increase of the vapour pressure, r_1 increases while the Laplace pressure decreases because of increases of r_2. The two effects compensate each other and the capillary force is almost constant until at very high relative humidity (Figure 2.6).

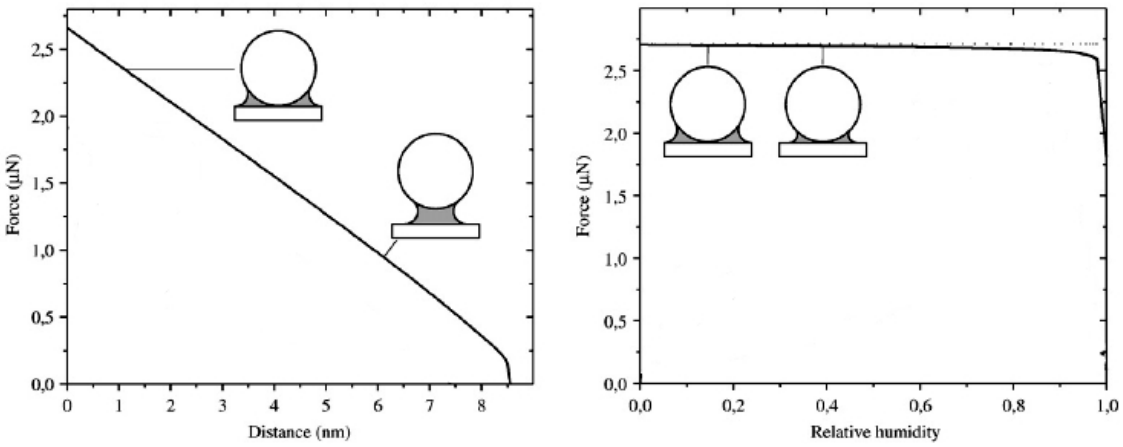

Figure 2.6: Distance (left) and relative humidity (right) dependence of capillary force for a plane-sphere geometry. Image adapted and reprinted from [27], Copyright (2009), with permission from Elsevier.

However, experimentally, different behaviours have been observed; focusing on data collected in the most similar conditions to those used in this work of thesis

(thus, between a surface and a nano-scale or micro-scale tip, as it will clearer in the following sections), the following behaviours are the most reported:

- if the two surfaces brought into contact are both hydrophilic, the capillary force is present and can be an important contribution. However, different behaviours of this force versus the relative humidity have been reported:
  - a monotonic increase of adhesion force with relative humidity (for example, in the case of glass colloidal probe on a naturally oxidized silicon wafer) [27], as reported in Figure 2.7;

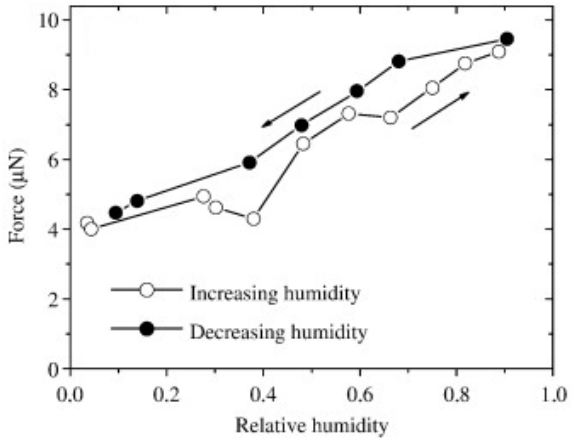

Figure 2.7: Example of monotonically increase of adhesion force versus relative humidity. These data are referred to a hydrophilic glass sphere of 20 μm radius interacting with a naturally oxidized silicon wafer. Figure adapted and reprinted from [27], Copyright (2009), with permission from Elsevier.

  - a non-monotonic increase of adhesion with relative humidity. In this case the plot of adhesion force versus relative humidity shows a maximum; after this, the capillary force contribution decreases. This behaviour was observed between a Si_3N_4 tip and SiO_2 surface [28], or between a Si_3N_4 tip and mica surface [29]. An example of this behaviour is illustrated in Figure 2.8.

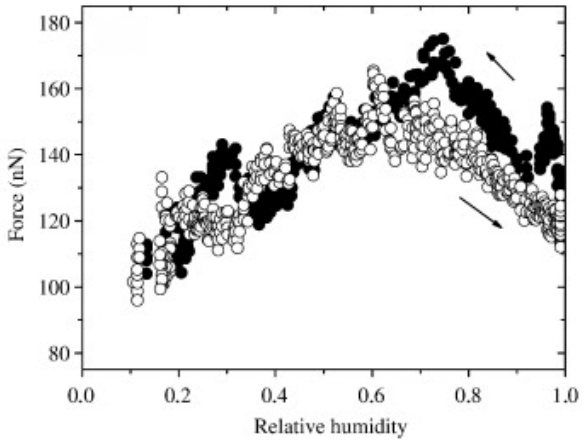

Figure 2.8: Example of non-monotonically increase of adhesion force versus relative humidity. These data are referred to adhesion between a silicon nitride AFM tip and a silicon wafer. Figure adapted and reprinted from [27], Copyright (2009), with permission from Elsevier.

There is not a unique explanation for these behaviours. Two main scenarios are usually accepted to explain the increase of the capillary force with relative humidity. In one case, the thickness of the adsorbed layers are considered: at low humidity, they should be not present or they have a very small thickness, so that the formation of the capillary neck between the two surfaces is impossible [28, 29]. Only when the adsorbed layers reach a certain thickness and probably a specific molecular organization, the formation of the capillary neck is possible and originates from the capillary force (as illustrated in Figure 2.9). The second hypothesis takes into account the surface roughness, which will be discussed in a dedicated section. The explanation of the decrease of the capillary force at high relative humidity is still not clear: a contribution of chemical interactions [29] is usually invoked. A more recent explanation implies the different hydrophilicity of one of the two surfaces [30]: if one surface is weakly hydrophilic, the capillary force will increase with relative humidity monotonically, while, if it is strongly hydrophilic, the capillary force will show a maximum at a certain value of the relative humidity (Figure 2.10).

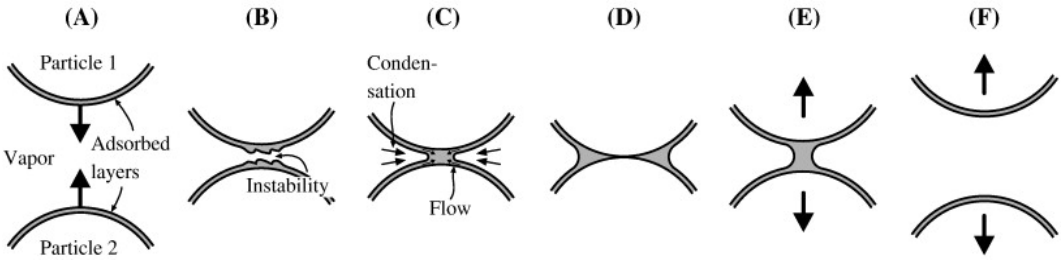

Figure 2.9: Diagram of formation and rupture of a liquid meniscus during an adhesion measurement. Figure reprinted from [27], Copyright (2009), with permission from Elsevier.

- if at least one of the surfaces brought into contact is hydrophobic, it is accepted that the capillary force contribution can be neglected unless the relative humidity approaches unity [31]. In fact, it is observed that there are no significant changes in the capillary force with the increase of the relative humidity. This is generally explained assuming that, for hydrophobic surface, there is no water adsorption unless the relative humidity approaches unity [28]. Examples of this behaviour are reported for adhesion between Si_3N_4 tip and hexadecanethiol (HDT) self-assembled monolayer [32], octadecyltrichlorosilane (OTS) coated tip and silicon surface, as well as for a Si_3N_4 tip adhesion on an octadecyltrimethoxysilane (OTE) self-assembled monolayer [28]. Figure 2.11 is a comparison of the different behaviours of adhesion force versus relative humidity for a hydrophobic and a hydrophilic surface.

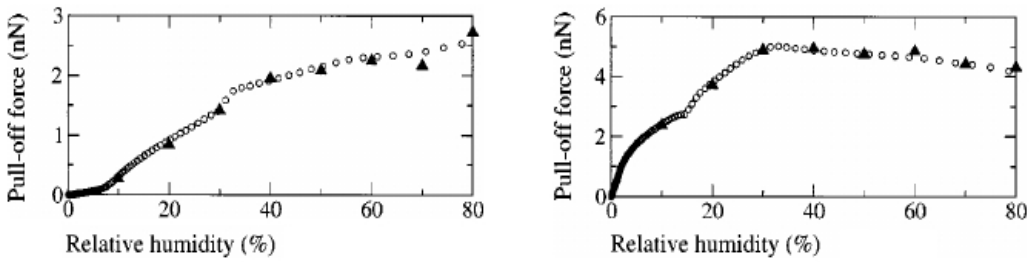

Figure 2.10: Calculated adhesion force for weakly hydrophilic tip (left) and strongly hydrophilic tip (right) on the same hydrophilic substrate. Figure adapted and reprinted from [30], with the permission of AIP Publishing.

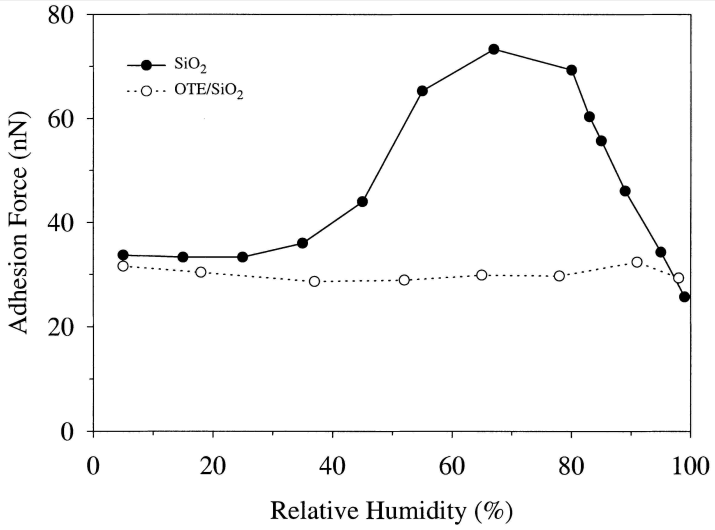

Figure 2.11: Comparison of the dependence of the adhesion force on the relative humidity for a hydrophilic surface (silica – solid line) and for a hydrophobic surface (OTE self-assembled monolayer – dashed line) with a Si_3N_4 tip. Image reprinted (adapted) with permission from [28]. Copyright (2000) American Chemical Society.

For completeness, it should be reported that a recent simulation of the capillary force acting between a tip used in the atomic force microscopy and a flat hydrophobic surface covered by an adsorbed liquid layer, shows a different result [30]. According to this calculation, the adhesion between the hydrophobic tip and the hydrophilic surface is dependent on the relative humidity: in fact the adhesion is zero up to 20% of relative humidity, but it increases with a steep jump between 20%-30% of relative humidity and finally it reaches a plateau over 30% of relative humidity. The calculated plot of the adhesion versus the relative humidity is shown in Figure 2.12.

However, the author of the article reported that, even if the calculation shows an increase of the adhesion also in the case of a hydrophobic tip, this increase is not generally observed experimentally.

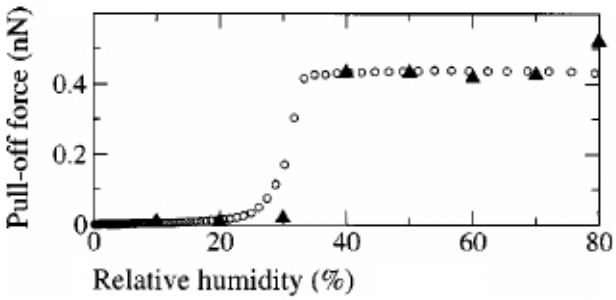

Figure 2.12: Calculated adhesion force (or pull-off force) for a hydrophobic tip in contact with a hydrophilic surface. Image adapted and reprinted from [30], with the permission of AIP Publishing.

There are also other two articles reporting an increase of the adhesion between hydrophobic and hydrophilic surfaces with the increase of the relative humidity [33, 34]. However, it can be noted that in one case, [34], adhesion was collected at only three different values of relative humidity: the so few measurements and the possibility of imperfections on those surfaces could explain the different result of this study. In the other case, [33], functionalized hydrophobic tips were used to test adhesion of fatty acids adsorbed on cellulose: it is a completely different system from the others presented above and also in this case it is possible to think that imperfections in the monolayers or in the preparation of the tips by means of adsorption could have a role in the explanation of this different behaviour in humid environment.

In conclusion, on the basis of the experimental data, the capillary force can be considered absent at low relative humidity (usually less that 20%) independently of the hydrophobic or hydrophilic nature of the surfaces in contact. In the case of two hydrophilic surfaces, two experimental behaviours have been found and, at the moment, it is not possible to know which one is specific for a determined surface, if not tested: in both cases there is an increase of the capillary force with the increase of the relative humidity. In the case of at least one hydrophobic surface, considering that there are more experimental evidences of the absence of capillary

force and that those systems are the most similar to conditions used in this research, this will be considered the case in the following.

2.7 Mechanics of adhesion

Until now, adhesion has been analysed in its contributions from different types of forces, however, it can be also related to specific characteristics of the system used to test it, such as dimensions of the adhering surfaces and their work of adhesion. Theories that relate the adhesion force with these characteristics belong to the field of the contact or fracture mechanics. They were initially a part of the contact mechanics, but later, approaches starting from fracture mechanics enlarged the insight into adhesion.

Different contact mechanics theories have been developed, according to different initial assumptions: the main ones will be presented in the sections below. The Hertz model will be also presented, even if it does not consider the existence of adhesion forces between the two surfaces in contact, however it is the base for other models.

About fracture mechanics, it will be not developed as in depth as for contact mechanics: relevant principles will be taken without further demonstration.

To obtain this type of information from the adhesion, a contextualization of some parameters about the geometry of the adhesion and some characteristics of the materials involved are needed. Most of these aspects will be analysed later, however, because the geometry of interest involves a flat surface and a sphere, only formulas related to that case will be presented.

2.7.1 Hertz model

In 1880, during the Christmas vacation, Hertz worked out the first satisfactory analysis of the contact between two deformable, elastic bodies without adhesion force acting between them [35]. If two deformable elastic spheres are brought into contact by an applied normal load along the z axis, they will be compressed as

depicted in Figure 2.13, where the numbers 1 and 2 are referred to the Sphere 1 and the Sphere 2, respectively, F is the applied force or load, T_1 and T_2 are two distant points along the *z* axis in each body, δ_1 and δ_2 are the displacements of distant points of each body, S_1 and S_2 are two points at the surface of the two bodies, u_{z1} and u_{z2} are the normal elastic displacements of the surfaces at S_1 and S_2, a is the contact radius and O is the contact point along the *z* axis. R_1 and R_2 are the radii of the two bodies: they are positive for convex surfaces (as in this case) or negative for concave surfaces.

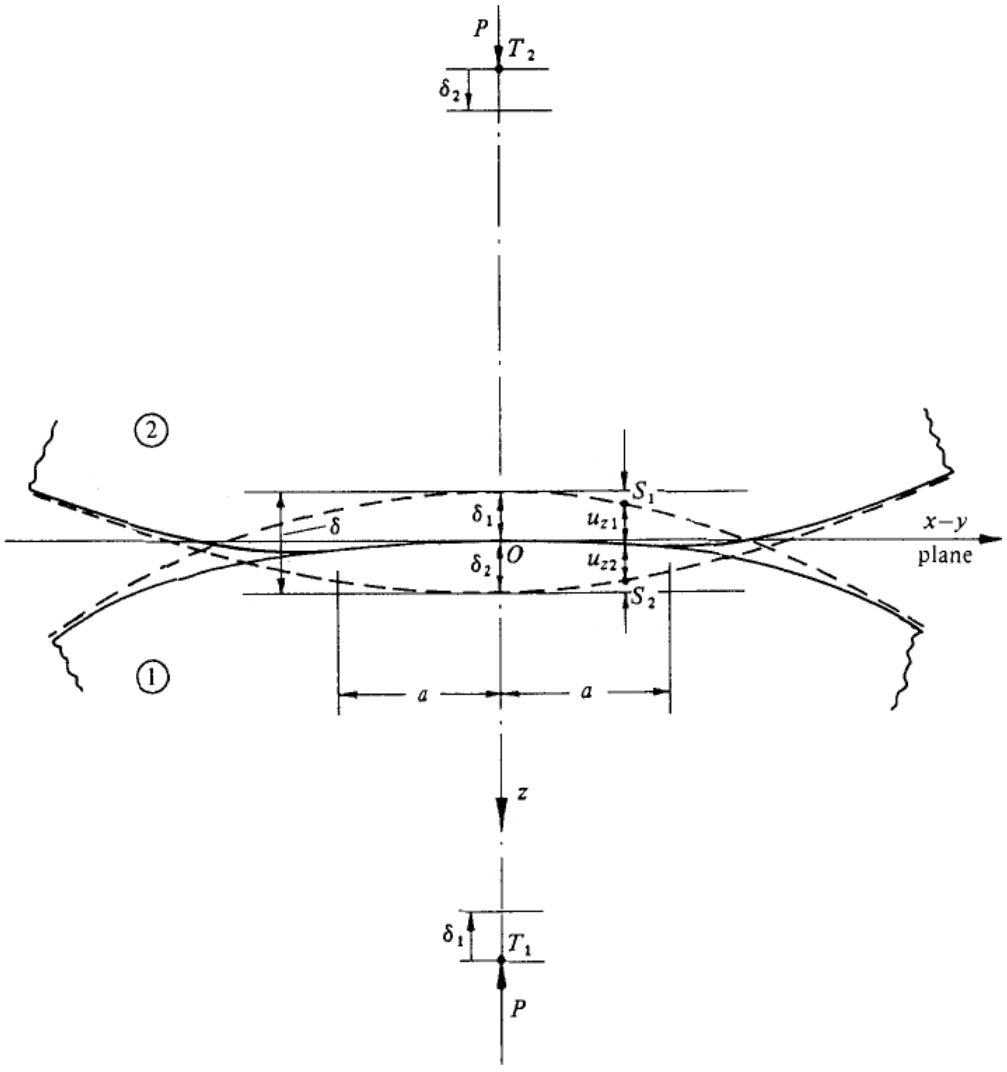

Figure 2.13: Sketch of the contact between two elastic spheres with no adhesion between them. Figure adapted from [35].

More often, the reduced radius R^* is considered, where

$$\frac{1}{R^*} = \frac{1}{R_1} + \frac{1}{R_2} \tag{2.43}$$

The geometry of two contact spheres can be easily converted in the case of the sphere and a plane putting $R_2 \rightarrow \infty$.

The profile of each surface close to O at points S_1 and S_2 can be approximated by

$$S_1 = a_{11}x^2 + a_{12}xy + a_{22}y^2 \tag{2.44}$$

and

$$S_2 = b_{11}x^2 + b_{12}xy + b_{22}y^2 \tag{2.45}$$

With a proper choice of the coordinates x and y, in order to let the xy term vanish, equations 2.44 and 2.45 can be written:

$$S_1 = \frac{x_1^2}{2R_1} + \frac{y_1^2}{2R_1} \tag{2.46}$$

and

$$S_2 = -\left(\frac{x_2^2}{2R_2} + \frac{y_2^2}{2R_2}\right) \tag{2.47}$$

where R_1 and R_2 are the radii of Sphere 1 and Sphere 2, respectively. Before the deformation, the separation h of points S_1 and S_2 is:

$$h = S_1 - S_2 = \frac{x^2}{2R^*} + \frac{y^2}{2R^*} \tag{2.48}$$

Once the bodies are compressed under the force F, the separation of points S_1 and S_2 becomes

$$h' = h - (\delta_1 + \delta_2) + u_{z1} + u_{z2} \tag{2.49}$$

Introducing

$$\delta = \delta_1 + \delta_2 \tag{2.50}$$

if points S_1 and S_2 are within the contact area, $h' = 0$ and the elastic displacement is:

$$u_{z1} + u_{z2} = (\delta_1 + \delta_2) - h = \delta - \frac{x^2}{2R^*} - \frac{y^2}{2R^*} \tag{2.51}$$

while if points S_1 and S_2 are outside the contact area, $h'>0$ and the elastic displacement is:

$$u_{z1} + u_{z2} > \delta - \frac{x^2}{2R^*} - \frac{y^2}{2R^*} \tag{2.52}$$

Equations 2.51 and 2.52 are the conditions that must be satisfied by the solution of the problem of contact mechanics. Thus, Hertz made the following assumptions:

- only the normal force is considered acting on the system; while tangential forces along x and y are zero;
- both the bodies are considered two elastic half-spaces: it means that $a \ll R_1$ and $a \ll R_2$;
- the strains are small in comparison with dimensions of the two bodies, thus, again $a \ll R_1$ and $a \ll R_2$;
- the two surfaces are continuous and non-conforming, thus, again $a \ll R_1$ and $a \ll R_2$.

Hertz found that, under the aforementioned assumptions and for the considered geometry, equations 2.51 and 2.52 are satisfied by the pressure distribution 2.53:

$$p = p_0 \sqrt{1 - \left(\frac{r}{a}\right)^2} \tag{2.53}$$

where p_o is the pressure acting on the origin O and r is the distance of the considered point from O, so $r^2 = x^2 + y^2$. The elastic displacement related to 2.53 is, for $r \leq a$:

$$u_z = \frac{1 - \nu^2}{E} \frac{\pi p_0}{4a} (2a^2 - r^2) \tag{2.54}$$

where E is the Young's modulus and ν is the Poisson's ratio. Introducing the reduced Young's modulus, E^*, as follows,

$$\frac{1}{E^*} = \frac{1 - \nu_1^2}{E_1} + \frac{1 - \nu_2^2}{E_2} \tag{2.55}$$

and substituting the expression for u_{z1} and u_{z2} into equation 2.51 and using the reduced radius (equation 2.43) it gives

$$\frac{\pi p_0}{4aE^*}\left(2a^2 - r^2\right) = \delta - \frac{x^2 + y^2}{2R^*} = \frac{1}{2R^*}\left(2R^*\delta - r^2\right) \tag{2.56}$$

from which, the contact radius a is given by

$$a = \frac{\pi p_0 R^*}{2E^*} \tag{2.57}$$

and the mutual approach of distant points, or indentation, is given by:

$$\delta = \frac{a^2}{R^*} = \frac{\pi a p_0}{2E^*} \tag{2.58}$$

The total load F is given by the integral of the pressure over the contact area S, so $F = \int_S p(r)\,dS$ and

$$\begin{aligned} F &= \int_S p_0 \sqrt{1 - \left(\frac{r}{a}\right)^2}\,dS = \int_0^a p_0 \sqrt{1 - \left(\frac{r}{a}\right)^2} 2\pi r\,dr \\ &= \frac{2}{3}\pi p_0 a^2 = \frac{2}{3}\pi p_0 R^* \delta \end{aligned} \tag{2.59}$$

where the last term is obtained by the substitutions of 2.57 and 2.58 for a and δ, respectively. Combining equation 2.59 with 2.57 and 2.58 and using 2.60, the equations for the contact radius, the indentation and the pressure along the z axis are obtained as function of the total force F, which is usually known:

$$a = \left(\frac{3F R^*}{4E^*}\right)^{1/3} \tag{2.60}$$

$$\delta = \frac{a^2}{R} = \left(\frac{9F^2}{16R^* E^{*2}}\right)^{1/3} \tag{2.61}$$

and

$$p_0 = \frac{3F}{2\pi a^2} = \left(\frac{6FE^{*2}}{\pi^3 R^{*2}}\right)^{1/3} \tag{2.62}$$

In fact, the Hertz model is a description of a pure elastic contact, because forces acting between the two bodies are neglected. If a zero load F is considered in equations 2.60, 2.61 and 2.62, the contact radius a, the indentation δ and the pressure p_0 are all zero. However, some experimental results showed that higher contact areas at lower force than those predicted by Hertz [36] were observed between compliant surfaces and sometimes also a quite high adhesion force [37]. All these 'discrepancies' stimulated the studies of new contact mechanics models to take into account the experimental results.

2.7.2 Bradley model

In 1932, Bradley calculated the adhesion force between two rigid spheres [38, 39]. Differently from Hertz, he introduced forces in the calculation, however he assumed there is no deformation when the two bodies come into contact. Using a Lennard-Jones potential, he performed a pairwise integration of the force between molecules and he found that the total force between the two spheres is:

$$F = \frac{8\pi\Delta\gamma R^*}{3}\left[\frac{1}{4}\left(\frac{h}{z_0}\right)^{-8} - \left(\frac{h}{z_0}\right)^{-2}\right] \tag{2.63}$$

where h is the distance between molecules, z_0 is the equilibrium distance [3] (usually assumed of few angstroms, as 4 Å) and $\Delta\gamma$ is the work of adhesion. It was found that the maximum adhesion force acting between the two spheres is

$$F_{\text{adh Bradley}} = 2\pi R^*\Delta\gamma \tag{2.64}$$

The contact radius and the elastic displacement at zero load are both zero because spheres are assumed to be completely rigid and non-deformable.

2.7.3 Johnson, Kendall and Roberts model

In 1971, Johnson, Kendall and Roberts published a new model of contact mechanics to take into account the adhesion force between two deformable contacting surfaces [36]. Their theory is still successfully used for the study of adhesion, and is often referred as 'JKR theory'. The geometry of the contact problem at the base of the JKR theory is the same as the Hertz model; also the assumptions used are the same as those of the Hertz model. What is new is that, in this case, adhesion forces are considered to be able to modify the contact profile, so a 'neck' is formed in the contact region. This implies that at least one of the two materials involved is deformable under the action of the interfacial forces. To take into account this neck formation a new pressure distribution should be used. This is composed by the addition of two terms: the Hertz pressure distribution and the rigid punch pressure distribution. In fact, the Hertz distribution describes the pressure between the two bodies due to the applied force; while the rigid punch distribution is considered a tensile contribution that describes adhesion forces acting between the bodies. The differences between the original Hertz distribution and the new one are in the centre of the contact region and mainly at the edge of contact, as depicted in Figure 2.14.

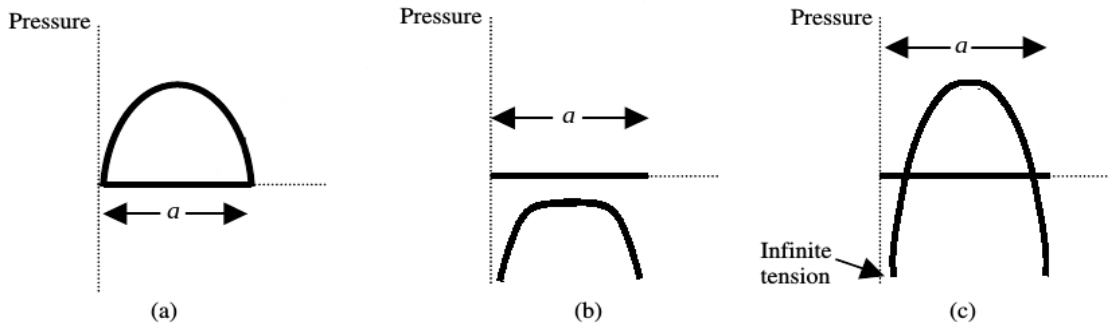

Figure 2.14: Contact pressure for (a) the Hertz model; (b) the rigid punch; (c) the resultant JKR addition of the previous pressure distributions. The contact radius a is indicated in the scheme. Figure adapted from [37].

Thus, the pressure distribution in the JKR model is [40]:

$$p = p_0 \sqrt{1 - \left(\frac{r}{a}\right)^2} + p_0' \frac{1}{\sqrt{1 - \left(\frac{r}{a}\right)^2}} \tag{2.65}$$

where $p_0 = (2aE^*)/(\pi R^*)$ from equation 2.57 and p_0' is negative because it refers to the tensile pressure due to the adhesion force.

At constant indentation δ, the total free energy of the system U_T is the sum of the stored elastic strain energy due to the compression in the contact region, U_E, and the surface energy due to the adhesion, U_S ([35]):

$$U_T = U_E + U_S \tag{2.66}$$

where the stored elastic strain energy is found to be [36]:

$$U_E = \int_S p u_z ds = E^* \left(\delta^2 a - \frac{2\delta a^3}{3R^*} + \frac{a^5}{5R^{*2}} \right) \tag{2.67}$$

and the surface energy is:

$$U_S = -\Delta\gamma \pi a^2 \tag{2.68}$$

where $\Delta\gamma$ is again the surface energy (or energy of adhesion or work of adhesion) per unit area.

At equilibrium, the derivative of the total energy vanishes

$$\left[\frac{\partial U_T}{\partial a}\right]_{\delta = cost} = 0 \tag{2.69}$$

so that

$$\left[\frac{\partial U_E}{\partial a}\right]_{\delta = cost} = -\left[\frac{\partial U_S}{\partial a}\right]_{\delta = cost} \tag{2.70}$$

As for the pressure distribution, that is the sum of two contributions, also the indentation can be calculated as the sum of the Hertz indentation and the rigid punch indentation

$$\delta = \frac{\pi a}{2E^*}\left(p_0 + 2p_0'\right) = \frac{a^2}{R^*} - \frac{\pi a}{E^*}p_0' \tag{2.71}$$

thus, the left hand of equation 2.70 becomes

$$\left[\frac{\partial U_E}{\partial a}\right]_{\delta=cost} = \frac{\pi^2 a^2}{E^*}\,p_0'^2 \tag{2.72}$$

Considering now the surface energy in equation 2.68, the right hand of equation 2.70 becomes

$$\left[\frac{\partial U_S}{\partial a}\right]_{\delta=cost} = -2\Delta\gamma\pi a \tag{2.73}$$

so that

$$\frac{\pi^2 a^2}{E^*}\,p_0'^2 = 2\Delta\gamma\pi a \tag{2.74}$$

from which

$$p_0' = -\left(\frac{2\Delta\gamma E^*}{\pi a}\right)^{1/2} \tag{2.75}$$

where the minus sign is chosen because at $r = a$ only the tensile pressure acts.

The total force is (using 2.65 for $p(r)$):

$$F = \int_0^a 2\pi r\,p(r)\,dr = \left(\frac{2}{3}p_0 + 2p_0'\right)\pi a^2 \tag{2.76}$$

and substituting p_0 from 2.57 and p_0' from 2.75 the relationship between a and F is:

$$\left(F - \frac{4E^* a^3}{3R^*}\right)^2 = 8\pi\Delta\gamma E^* a^3 \tag{2.77}$$

which can be rewritten as

$$a^3 = \frac{3R^*}{4E^*}F + \frac{3R^*}{4E^*}\left(3\pi\Delta\gamma R^* + \sqrt{6\pi\Delta\gamma R^* F + \left(3\pi\Delta\gamma R^*\right)^2}\right) \tag{2.78}$$

where the right hand side is written so as to clarify that the first term equals the Hertz contact radius and the second one can be seen as an 'adhesive correction' to it. In fact, if $\Delta\gamma = 0$ there is not adhesion between the two bodies, and it reverts to

the corresponding Hertz equation. At zero applied force F, the contact radius is not zero as in the Hertz model but, because of the adhesion force that brings into contact the two bodies, it becomes

$$a^3 = \frac{9\pi\Delta\gamma R^{*2}}{2E^*} \tag{2.79}$$

The indentation, as defined in equation 2.71 and substituting p_0 and p_0' from 2.57 and 2.75, respectively, becomes

$$\delta = \frac{a^2}{R} - \sqrt{\frac{2\pi a\Delta\gamma}{E^*}} \tag{2.80}$$

where again, the first term equals the Hertz indentation and the second one can be seen as an 'adhesive correction'. Equation 2.80 reverts to the corresponding Hertz equation if $\Delta\gamma = 0$, so when there is not adhesion between the two contacting bodies.

However, probably the most interesting result of the JKR theory concerns the adhesion force. Differently from the Hertz model, where at the zero applied force the two bodies separate, in the JKR theory it is necessary to apply a tensile (negative) pressure to get them separated. The force necessary for the separation, also called 'adhesion force', is

$$F_{\text{adh JKR}} = -\frac{3}{2}\pi R^*\Delta\gamma \tag{2.81}$$

from the condition of having a real solution from 2.78. It is noted that the adhesion depends only on the reduced radius (thus, from the curvatures of the surfaces of the two bodies) and the work of adhesion; there is no dependence on the applied load or the Young's modulus. And because there is adhesion force also at the separation point, it means that it happens because at the detachment the contact radius is not zero but is

$$a^3 = \frac{9\Delta\gamma\pi R^{*2}}{8E^*} \tag{2.82}$$

The same results can be obtained if also the mechanical energy is considered as in [36] or in the fracture mechanics approach [41].

2.7.4 Derjaguin, Muller and Toporov model

In 1975, Derjaguin, Muller and Toporov presented a different model to take into account the adhesion force between two deformable adhering surfaces [42]. In this model, also called 'DMT model', the authors considered that both the deformation of the bodies and the stress distribution are those calculated by Hertz. It means, that, differently from the JKR theory, the adhesion force is considered not to be able to change the surface profiles outside the contact area. However, the adhesion force is assumed to act in a ring-shaped region around the contact area, as an additional force.

Firstly, a relationship that describes the dependency of the distance h between points S_1 and S_2 belonging to Sphere 1 and the Plane 2 from the distance r (where r is the distance from O, the origin of the contact area, to S_2 or to the normal projection of S_1 on the Plane 2) is defined. It should be noted that, even if the DMT model was developed considering a geometry of a sphere of radius R_1 in contact with a plane, this analysis can be easily applied to the case of two spheres of radii R_1 and R_2 by replacing R_1 with the reduced radius R^*, as it will be done in the following equations. When $r \geqslant a$, that relationship was found to be (for the detailed calculation refer to [42]):

$$h = \frac{1}{\pi R^*}\left[a\left(r^2 - a^2\right)^{1/2} - \left(2a^2 - r^2\right)\arctan\left(\frac{r^2}{a^2} - 1\right)^{1/2}\right] + z_0 \qquad (2.83)$$

where z_0 is a constant added because also at the very contact point, the distance h cannot become shorter than the interatomic equilibrium distance [42]. Since from the Hertz model $\delta = a^2/R^*$ (first part of equation 2.61), equation 2.83 can be rewritten as:

$$h = \frac{1}{\pi R^*}\left[\left(\delta R^*\right)^{(1/2)}\left(r^2 - \delta R^*\right)^{1/2} - \left(2\delta R^* - r^2\right)\arctan\left(\frac{r^2}{\delta R^*} - 1\right)^{1/2}\right] + z_0 \qquad (2.84)$$

Then, a certain value of displacement δ is considered the resultant of the applied external force F, the stored elastic force and the surface force. Because the interest is mainly in the latter, the following discussion will be focused on that. Using the so called 'thermodynamic approach', Derjaguin, Muller and Toporov started from the corresponding energy contribution, so that the surface energy is:

$$U_S = \int F_S(\delta)\, d\delta \tag{2.85}$$

where F_S is the surface force. Under the Derjaguin approximation [43] it is possible to relate the surface force between a plane and a sphere (a special case of the two spheres geometry where $R_2 \rightarrow \infty$) to the surface energy between two planar surfaces:

$$U_S = \int_0^\infty \phi(h) 2\pi r\, dr \tag{2.86}$$

where $\phi(h)$ is the interaction energy for unit area of a flat surface (essentially a potential whose form can be decided later) and depends on the distance h between the two surfaces. It should be noted that the value of $\phi(h)$ rapidly decreases as h increases and that the region of interest is that where $h \ll R^*$, so that, the real upper limit of the integral 2.86 is unnecessary and may be assumed to be equal to infinity.

The integral of equation 2.86 can be analysed by applying it in the region of contact first, then in the region outside the contact area and finally summing these two contributions to obtain the total energy. The contact area region is described by the condition $0 \leqslant r \leqslant a$ where, $h = z_0$, so that, in this region, equation 2.86 becomes:

$$U_S^{'} = \int_0^a \phi(z_0) 2\pi r\, dr = \phi(z_0)\pi a^2 = \phi(z_0)\pi\delta R^* \tag{2.87}$$

where $U_S^{'}$ is the surface energy inside the contact area and the last term is obtained by the Hertz equation $\delta = a^2/R^*$ (first part of equation 2.61).

In the region outside the contact area equation 2.86 becomes:

$$U_S^{''} = \int_a^\infty \phi[h(r,\delta)] 2\pi r\, dr\,, \tag{2.88}$$

where $U_S^{''}$ is the surface energy outside the contact area and $h(r,\delta)$ is expressed by equation 2.84. Substituting $x^2 = r^2 - \delta R^*$ into equation 2.88 and differentiating in the new variable x, equations 2.88 and 2.84 become, respectively:

$$U_S^{''} = \int_0^\infty \phi[h(x,\delta)]2\pi x\,dx \tag{2.89}$$

$$h = \frac{1}{\pi R^*}\left[x(\delta R^*)^{(1/2)} - (\delta R^* - x^2)\arctan\left(\frac{x^2}{\delta R^*}\right)^{1/2}\right] + z_0 \tag{2.90}$$

According to 2.85, in order to obtain the surface force, the surface energy should be differentiated in the variable δ:

$$F_S = \frac{dU_S}{d\delta} = \frac{dU_S^{'}}{d\delta} + \frac{dU_S^{''}}{d\delta} \tag{2.91}$$

Again, it is possible to evaluate the contributions of the two regions (inside and outside the contact area) separately. In the contact area region, the contribution to the surface force is:

$$\frac{dU_S^{'}}{d\delta} = \phi(z_0)\pi R^* \tag{2.92}$$

while in the region outside the contact area, the contribution to the surface force is:

$$\frac{dU_S^{''}}{d\delta} = \frac{d}{d\delta}\int_0^\infty \phi[h(x,\delta)]2\pi x\,dx = 2\pi\int_0^\infty \phi_h^{'}[h(x,\delta)]\,\frac{d\,h(x,\delta)}{d\delta}x\,dx \tag{2.93}$$

where the derivative of $h(x,\delta)$ can be calculated:

$$\frac{d\,h(x,\delta)}{d\delta} = \frac{1}{\pi}\left(\frac{x\sqrt{\delta R^*}}{x^2 + \delta R^*} - \arctan\frac{x}{\sqrt{\delta R^*}}\right) \tag{2.94}$$

The adhesion force is found from equations 2.91-2.94 in the limit $\delta \to 0$ (the contact point condition). In this situation, equation 2.94 becomes:

$$\lim_{\delta\to 0}\frac{d\,h(x,\delta)}{d\delta} = -\frac{1}{2} \tag{2.95}$$

and h from 2.84, after the substitution $x^2 = r^2 - \delta R^*$, is

$$\lim_{\delta \to 0} h(x,\delta) = \frac{x^2}{2R^*} + z_0 \tag{2.96}$$

and from 2.96

$$x\,dx = R^*\,dh \tag{2.97}$$

Then, substituting equations 2.94-2.96 into 2.93, the contribution to the adhesion force of the region outside the contact area is:

$$\lim_{\delta \to 0} \frac{dU_S''}{d\delta} = -\pi \int_0^\infty \phi_h' R^*\,dh = -\pi R^* \phi_h\Big|_{z_0}^{\infty} = \pi R^* \phi(z_0) \tag{2.98}$$

because $\phi(\infty) \to 0$.

Finally, considering also the contribution of the region of contact area, the total adhesion force is:

$$\begin{aligned} F_{\text{adh DMT}} &= \lim_{\delta \to 0} F_S = \lim_{\delta \to 0} \frac{dU_S}{d\delta} = \pi R^* \phi(z_0) + \pi R^* \phi(z_0) \\ &= 2\pi R^* \phi(z_0) \end{aligned} \tag{2.99}$$

According to equation 2.99, the adhesion force has a dependence on the form of the potential ϕ, even if in the specific case it is a constant because in the contact area it assumes a numerical value (it derives from equation 2.83). From the pure DMT model it is not possible to develop this formula more if the potential $\phi(h)$ is not set (in the original work, the van der Waals potential is chosen, that is why, often, the DMT model is usually referred as an adhesion model for van der Waals solids). However, if the separation of the two contact bodies is seen in terms of surface tensions, for two flat surfaces the total energy of the system is:

$$\Delta\gamma = \gamma_1 + \gamma_2 - \gamma_{12} \tag{2.100}$$

Using the Derjaguin approximation [43] it is possible to relate the force acting between two separating spheres to the energy between two flat surfaces of the same material in the same medium, so that:

$$F = 2\pi R^* \Delta\gamma \tag{2.101}$$

The correspondence between equations 2.99 and 2.101 is clear because they refer to the same process of separation, so, it is possible to conclude that $\phi(z_0) = \Delta\gamma$ and thus equation 2.99 becomes:

$$F_{\text{adh DMT}} = 2\pi R^* \Delta\gamma \tag{2.102}$$

As can be noted, the adhesion force of the DMT model is the same that was found by Bradley (equation 2.64).

According to this 'thermodynamic approach', the authors found that the adhesion force decreases as the deformation δ increases. A few years later, the same authors, with a different method called 'force method', found the opposite results, with the adhesion force increases as the deformation increases [44]. It has been shown that these contradictory results derive from the use of non equilibrium profiles of the contacting bodies [45]. In any case, often the adhesion force in the DMT theory is considered a constant value as given by equation 2.102, following the approach of Maugis [24, 46], thus $F_{\text{adh DMT}}$ becomes independent of the deformation δ.

Until now, only the adhesion force between the two surfaces was considered, however, in the described system also the elastic force is present. Based on the initial assumption that the deformation is Hertzian, the elastic force is described by the same formula found by Hertz (equation 2.61). Thus, the total general force acting on the system is given by:

$$F = \left| \frac{4}{3} E^* R^{*1/2} \delta^{3/2} - 2\pi R^* \Delta\gamma \right| \tag{2.103}$$

from which it is possible to obtain the equations for the displacement

$$\delta = \sqrt[3]{\frac{9}{16} \frac{(F + 2\pi R^* \Delta\gamma)^2}{E^{*2} R^*}} \tag{2.104}$$

and the contact radius (recalling that $\delta = a^2/R^*$ from equation 2.61)

$$a = \sqrt[3]{\frac{3R^*}{4E^*}(F + 2\pi R^* \Delta\gamma)} \tag{2.105}$$

2.7.5 Maugis model

At this point, three models are been presented for the contact of elastic and deformable bodies and two of those include adhesion interactions between the two surfaces in contact or in the proximity of the contact area. However, in those two models (JKR and DMT), the formulas of the adhesion force are different and independent of bulk characteristics of materials of the two bodies, and this does not allow us to distinguish their specific fields of application. In particular, the reduced modulus E^* disappears from the formulas of the adhesion force (even if it is in the formulas of deformation and contact radius of the two theories), so they both seem to apply to any materials and seem to be contradictory. This was the cause of some debates in the scientific community in order to try to find which was the most correct model or to differentiate them according to fields of application. A closer consideration of the starting assumptions of the models shows that:

- in the JKR model, the attractive force between the two surfaces is able to deform the contact area and to create a neck when the two bodies start to be separated;
- in the DMT model, the geometry of the contact bodies is considered to remain Hertzian, so the attractive force is not able to deform the two surfaces.

Also, both models show limitations:

- in the JKR model, the attractive forces act only on the contact area, while outside those forces fall to zero (and this is not physically credible);
- in the DMT model, the attractive forces act only on a ring shaped region surrounding the contact area (it is assumed that the Hertz model already includes the forces acting in the contact area) and no deformation around the contact area is considered.

That could allow us to think that the JKR model is more suitable for softer materials that can be highly deformed by adhesion forces, or in the case of very strong

adhesion forces that could cause an important deformation of the contact region. The requirement of a non negligible deformation is important because only in this condition the limitation of considering the adhesion force acting only inside the contact area is possible. Whilst the DMT model is more suitable for harder materials or where adhesion forces are weaker because in both case surfaces will be not deformed and the DMT assumptions can hold. In this framework, both models are correct but they apply in different situations.

Tabor was the first that proposed a quantitative distinction between the fields of applications of these models [47]. He used the height of the neck around the contact area under zero load as parameter to know where the JKR model holds. The height of the neck is found from equation 2.80, using the contact radius calculated according to equation 2.78 when $F = F_{\text{adh JKR}}$. In fact, the assumption that the adhesion acts only in the contact area is acceptable if the height of the neck is much greater than the interatomic equilibrium distance z_0. If the two values are comparable, forces acting outside the contact area cannot be neglected. The parameter used for this comparison, later called the Tabor parameter μ_T, is the ratio of the height of the neck δ_{crit} to the interatomic equilibrium distance z_0, ignoring the numerical factor:

$$\mu_T = \frac{\delta_{crit}}{z_0} \approx \left(\frac{R^* \Delta \gamma^2}{E^{*2} z_0^3} \right)^{1/3} \tag{2.106}$$

For values of $\mu_T \ll 1$, the DMT model is valid, while for $\mu_T \gg 1$, the JKR model is applicable.

However, only few years later, Muller et al. [48] were able to demonstrate that the JKR and the DMT models represent the extreme situations of the same theory. They performed a self-consistent numerical calculation using the Lennard-Jones potential and found that there is a continuous transition from the DMT to the JKR model as a parameter proportional to μ_T increases.

Later, Maugis was able to find a set of analytical equations to describe this transition [46]. He looked at the adhesion problem introducing some aspects of the

fracture mechanics: in fact, the same situation of two contacting bodies that are being separated could be analysed considering changes in the adhesion region or considering this situation as a crack opening event, thus looking at the region outside the contact area (panels (a) and (b) in Fig. 2.15). Both forces acting in the contact area and in the surrounding region are taken into consideration, so overcoming the limitations of the previous models. The surrounding region is considered, as in fracture mechanics, the adhesive (or cohesive) region and it extends over a distance d from the contact area a. In this region, a Dugdale potential is assumed to be present: a constant attractive interaction σ_0 acts over the distance d and it becomes zero for distances greater than d (panel (c) in Fig. 2.15). At the distance d, the separation between the two bodies h_0 can be determined by correlating the Dugdale potential with the most used Lennard-Jones potential. In fact, the values of σ_0 and h_0 are chosen in order to have the work of adhesion $\Delta\gamma$ and σ_0 matching those obtained with Lennard-Jones potential, from which it appears that

$$h_0 = 0.97 z_0 \tag{2.107}$$

In the contact area, the JKR model is applied.

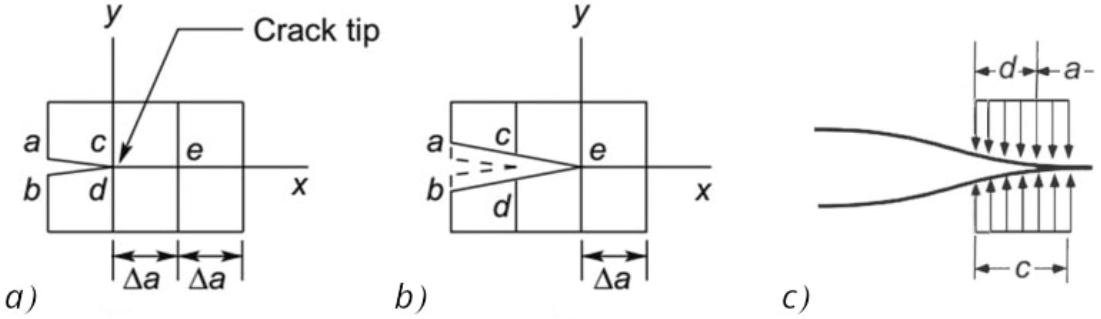

Figure 2.15: The adhesion problem considered from the point of view of fracture mechanics in panels (a) and (b) and the Maugis's description of contacting bodies (c). In fracture mechanics, the separation of two adhering bodies is seen as a movement of the crack tip which increases the crack length and reduces the contact radius. In panels (a) and (b), the contact radius is indicated as sum of Δa contributions. In panel (c), the Maugis's description of contacting bodies is depicted: in the cohesive region a Dugdale potential is present (indicated by the arrows and acts over the length d), while in the contact region adhesion interactions are considered to act like in the JKR model. Images in panel (a) and (b) are adapted and reprinted from Fracture Mechanics, Sun, C.T. and Jin, Z. -H., Copyright (2012); image in panel (c) is reprinted/adapted by permission from Springer Nature Customer Service Centre GmbH: Springer Recent Trends in Fracture and Damage Mechanics by Hütter, G., Zybell L. COPYRIGHT (2016).

Thus, using the contribution of the contact mechanics for the contact region and fracture mechanics equations for the adhesive zone where the interactions are simplified using the Dugdale potential, Maugis was able to find general equations that describe adhesion between elastic bodies. Introducing the ratio m between the total distance over which all the forces act, $c = a + d$, and the contact radius

$$m = \frac{c}{a} \tag{2.108}$$

and the dimensionless variables $\bar{a}$ for the contact radius, $\bar{F}$ for the force, $\bar{\delta}$ for the indentation and μ_M as transition parameter:

$$\bar{a} = a\left(\frac{4E^*}{3\pi\Delta\gamma R^{*2}}\right)^{1/3} \tag{2.109}$$

$$\bar{F} = \frac{F}{\pi\Delta\gamma R^*} \tag{2.110}$$

$$\bar{\delta} = \delta\left(\frac{16E^{*2}}{9\pi^2\Delta\gamma^2 R^*}\right)^{1/3} \tag{2.111}$$

and

$$\mu_M = 2\sigma_0\left(\frac{9R^*}{16\pi\Delta\gamma E^{*2}}\right)^{1/3} \tag{2.112}$$

the governing equations for the description of the system, that is, the dimensionless net contact force, the dimensionless indentation and the adhesive gap between bodies were found to be, respectively:

$$\bar{F} = \bar{a}^3 - \mu_M\bar{a}^2\left(\sqrt{m^2-1} + m^2\arctan\left(\sqrt{m^2-1}\right)\right) \tag{2.113}$$

$$\bar{\delta} = \bar{a}^2 - \frac{4}{3}\bar{a}\mu_M\sqrt{m^2-1} \tag{2.114}$$

and

$$\frac{\mu_M \bar{a}^2}{2}\left[\sqrt{m^2-1}+\left(m^2-2\right)\arctan\left(\sqrt{m^2-1}\right)\right] + \frac{4\mu_M^2 \bar{a}}{3}\left[\sqrt{m^2-1}\arctan\left(\sqrt{m^2-1}\right)-m+1\right]=1 \quad (2.115)$$

The parameter μ_M is proportional to μ_T because the parameters of the Dugdale potential were chosen to match those of the Lennard-Jones, thus [24]:

$$\mu_M = 1.1570\,\mu_T \quad (2.116)$$

As for the Tabor coefficient, when $\mu_M \rightarrow \infty$, the JKR model is a good approximation, while when $\mu_M \rightarrow 0$ the DMT model applies.

Using equations 2.113 and 2.115 Maugis plotted curves of the normalized contact radius versus the normalized force for different values of the parameter μ_M (Fig. 2.16). Even if these curves are approximated because of the use of Dugdale potential, the detailed calculation made by Greenwood showed that they are in good agreement with those obtained using the Lennard-Jones potential [49]. These curves are particularly interesting because the point where the tangent to the curves becomes vertical represents the adhesion force: it decreases from $F_{\text{adh DMT}}$ to $F_{\text{adh JKR}}$ as μ_M increases.

Considering that the Maugis model not only explained discrepancies between the DMT and JKR models, but also introduced equations that can describe any elastic system, it is easy to conclude that this should be the preferred model for the description of any system. Unluckily, it is necessary to know at least two parameters to use Maugis equations, specifically μ_M and a and they are both difficult to be determined experimentally. Once having these two values, with equation 2.115 is possible to know m and then, using equation 2.113, the contact force can be found. However, owing to the difficulties in obtaining experimentally accurate values for both μ_M and a, the main used approach is an estimation of μ_M and then the use of the JKR or DMT model, according to the estimated value of μ_M, hopefully, if it does not have one of the intermediate values between the two models. In the particular cases of an intermediate value of μ_M, it is not possible to use them: the Maugis model should be used.

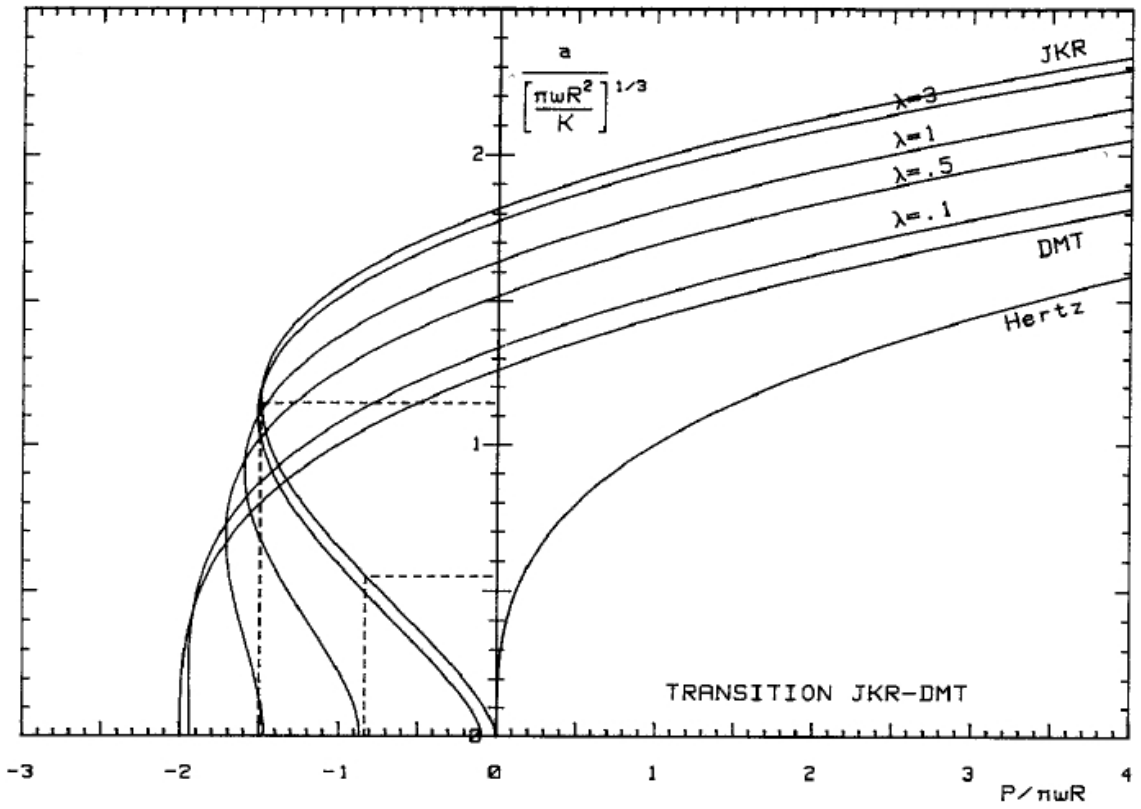

Figure 2.16: Normalized contact radius versus normalized force for different values of μ_M (in this picture λ is used instead of μ_M and P instead of F). Points where the tangent to the curve is vertical represent the contact radius at the moment where separation takes place and the force necessary for the separation to occur (adhesion force). For very small values of μ_M the DMT model is a good approximation, as is the JKR model for large values of μ_M. For intermediate values of μ_M, the adhesion force cannot be obtained from the DMT or JKR models and its value varies from the absolute value of 2 (DMT model) to the absolute value of 1.5 (JKR model). In the Hertz model, adhesion force is zero. The branches of these curves in the right-hand side of the plot beyond the adhesion force are to be considered physically meaningless because at this stage separation between the surfaces has been occurred (it is a nonsense to talk about normalized contact radius after separation). Image adapted and reprinted from [46], Copyright (1992), with permission from Elsevier.

Because of its relevance, a deeper remark about μ_T seems important. As defined in equation 2.106, it depends on the reduced radius R^* and the work of adhesion $\Delta\gamma$ directly and inversely on the reduced Young's modulus E^*. It means that in the case of large radii, large adhesion forces and compliant solids, μ_T tends to have a high value, and so the JKR model could be used. On the contrary, when small radii, small adhesion forces and rigid bodies are present, μ_T tends to zero and the DMT model could be used. This is usually the method used to decide which model is the

most suitable in the case of the lack of any other quantitative information. A more precise and quantitative information can be found in Greewood [49] and Feng [50]: in their articles, with a detailed calculation based on the Lennard-Jones potential, they found that the DMT model holds only for value of μ_T near to zero, while the JKR model can be considered a good approximation for values of μ_T greater than 3. However, with $\mu_T = 3$ there is a deviation from the JKR values for very small radii, while, with $\mu_T = 5$, the adhesion force is within the 2% of the JKR value [49]. That is why, even if for $\mu_T > 3$ the JKR model could be used, although it is generally more accepted to use it when $\mu_T > 5$.

An adhesion map was also developed in order to define better the field of application of the different models [39]. The two coordinates are the μ_M (that is correlated to μ_T) and the dimensionless load $\bar{F}$; the different regions are located according specific conditions (Fig. 2.17):

- at very high loads, even if adhesive forces can be present at any load, their contribution can be neglected and the Hertz model is a nice description for the system. To quantify a boundary condition for the use of that model, it is proposed that the ratio of adhesion force to the total force should be less than 0.05 (which means that the adhesion force is less than 5% of the applied load);
- when surface forces are large and the materials are compliant, so that the former are able to drive a large elastic deformation, the JKR model holds. The boundary conditions for the applicability of the JKR model are proposed to be, for high load, the same of the Hertz region, and for high deformations, the ratio of elastic displacement to the range of action of adhesion forces in the Maugis approximation that should be greater than 20;
- when surface forces are small and the material is rigid, so that surface forces are not able to deform surfaces, the DMT model can be used. The proposed boundary conditions for that model are, for high load, the same of the Hertz

region, and for small deformation, a ratio of elastic deformation to the range of action of adhesion forces in the Maugis approximation less than 0.05;

- when surface forces and the compliance of the material are intermediate between the two previous regions, the Maugis model is the most suitable;
- when the material is stiff and the applied load is light, and so that the latter is not able to drive an elastic deformation, the Bradley model holds. In this case the boundary condition is that the ratio of the Hertz elastic deformation to the range of action of adhesion forces in the Maugis approximation is less than 0.05.

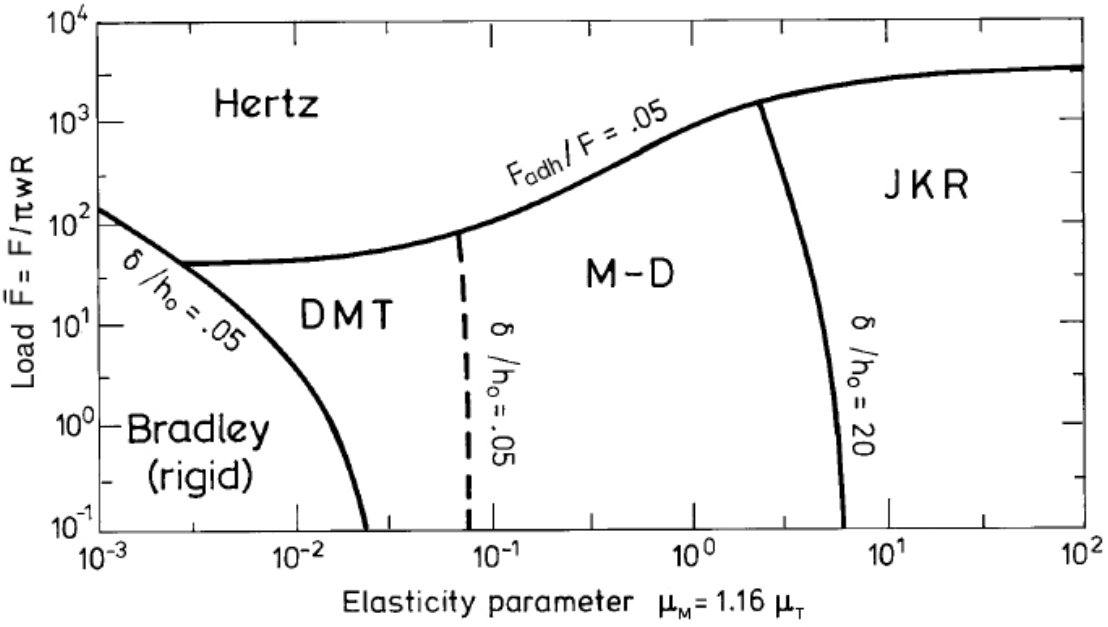

Figure 2.17: Calculated adhesion map according to ref. [39]. M-D stands for the Maugis (Dugdale) model. Image adapted and reprinted from [39], Copyright (1997), with permission from Elsevier.

In conclusion, for elastic spheres brought into contact, the Maugis model is the most general because it can be used over all the range of material compliance (i.e. from rigid and non-deformable materials to very soft and compliant ones). Moreover, even if an approximate potential was used in the model for accounting of the adhesive region, it has been shown by comparison with the rigorous

calculation that this approximation is quite good [49, 50]. However, even if all the previous models can be considered just as particular cases of the Maugis model, they are still used because they are the simplest to handle: they depend on macroscopic parameters (except for the contact radius a), like for example, the applied force F and the work of adhesion $\Delta\gamma$. Instead, the determination of μ_M or m is often complicated. That is why the Bradley, DMT and JKR models are still largely present even in recent literature and μ_M or μ_T are estimated from material characteristics and data from literature. The adhesion map in Fig. 2.17 represents a guideline for the most appropriate model, taking into account the characteristics of the material and the experimental conditions (the applied force). Also when the Maugis model is the only one that should be used, simpler models have been developed, like, for example, the Schwarz model (where a linear superposition of the JKR and DMT equations is used [24]).

2.7.6 Viscoelastic solids

All the previous models regard perfectly elastic solids; the dissipation of energy due to viscous or partially viscous processes is not taken into consideration. In the Hertz model, the displacement of the bodies is totally converted into deformation of the contact area according to equation 2.51, while in the JKR model, the total energy of the system is given by the sum of the elastic strain energy and the surface energy (equation 2.66). The other models use the Hertz approach (DMT) or the JKR approach (Maugis), so that they remain in the elastic approximation.

However, a perfect elastic solid is itself an approximation: few classes of materials and only in particular conditions can be considered to act as fully elastic bodies. That is why, the elastic behaviour is limited to 'very special' cases like for example, the application of small forces or small deformations. Particularly in the polymer field, a perfect elastic behaviour is limited to very soft conditions or to the initial part of some tests (like for the stress–strain test) and it is not a property of all the polymers but only of some of them. In the determination of the adhesion, viscoelasticity, if present, should not be neglected, because it can lead to different

results than those expected from the application of the elastic framework in a considered system. In the same article where the JKR model is introduced, a remark advices that the experimental adhesion force can be different from that expected from the theory because of viscous processes [36].

The introduction of the viscoelastic dissipation lets us move from the contact mechanics field to the fracture mechanics field: it may be noted that the boundary between the two fields should not be considered so strictly, considering that the JKR results can be found also using the fracture mechanics principles and that the Maugis model uses contributions from both. It is not the purpose of this work to go into the fracture mechanics, so only relevant points will be introduced in the remaining part of the section. As aforementioned, the adhesion of two bodies can be viewed also like a crack problem, where increasing the contact area means to close the crack, while decreasing the contact area means to extend the crack.

The introduction of viscoelasticity lets also the system be sensitive to experimental parameters that are not of interest in the elastic approximation, mainly the velocity of the loading or unloading process, temperature, applied load and dwell time.

There are mainly two approaches to take into account the viscoelasticity of polymeric materials: one is based on the elastic-viscoelastic correspondence principle while the other one uses the time-temperature superposition principle. The former is probably the most theoretically rigorous because it uses a function to describe the time dependence of the Young's modulus, however, it depends on the specific system and it requires a more complicated mathematical treatment. The latter has probably the least physical correspondence, because it assumes that the surface energy is time dependent, however it is more general and easier to handle than the former.

The elastic-viscoelastic correspondence principle enables the calculation of a property of a viscoelastic system starting for the solution of the correspondent elastic system. Usually, also the knowledge of the function that describes the

dependence of the (visco)elastic modulus on time, and for this, a good knowledge of the specific system is required. This approach is used for the description of experimental results [41] or for theoretical calculation [51]. In both cases, it is shown that in viscoelastic materials, the adhesion force increases as the velocity of the separation of the two contacting bodies increases, as reported in Fig. 2.18.

The same author, in a previous article about elastic contact, shows also that there could be an influence of the applied load on the adhesion force [52]. An increase in the applied load increases the adhesion force, but only for small loads; at greater loads, the adhesion force becomes independent of the load (saturation status).

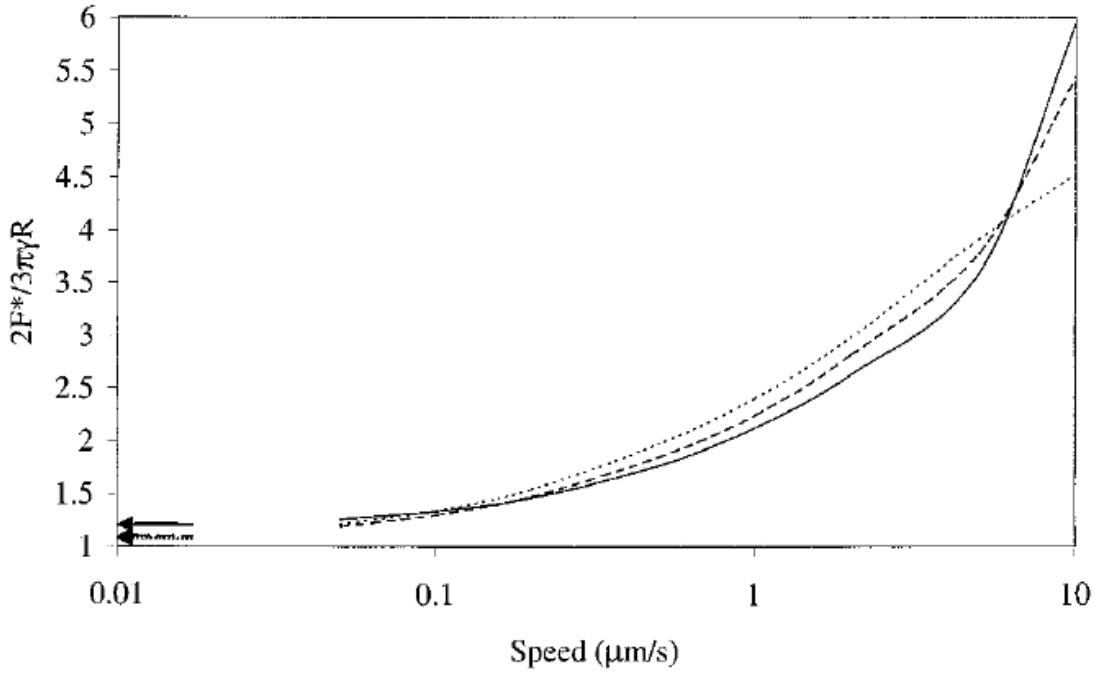

Figure 2.18: Calculated adhesion force dependence on velocity of unloading. The adhesion force normalized by the JKR adhesion increases as the speed increases for three bodies with different Hamaker constants. The speed is expressed in logarithmic scale. Image reprinted (adapted) with permission from [51]. Copyright (2001) American Chemical Society.

The time-temperature superposition principle establishes that the response of a viscoelastic material at high temperature equals the response of the same viscoelastic system at a lower temperature but in a longer time. According to this principle, it is possible to know the long time behaviour of a polymer just by

increasing the temperature. However, there is more than one shifting equations to correlate the behaviour of the polymer at two temperatures and they are all empirical expressions. Despite of this, the different shift factors are now used in well defined fields. In order to know how the time-temperature superposition and the shift factor come inside an adhesion model, the starting point is the same of the JKR model in its original version [36] where in a reversible and isothermal system, the total energy is the sum of the stored elastic energy, the surface energy and the potential energy (U_P) [53]:

$$U_T = U_E + U_S + U_P \tag{2.117}$$

A variation of the energy of system from the equilibrium will lead to a change in the contact area (that means that the crack will extend or recede in order to find the new equilibrium configuration). At equilibrium, the derivative of the total energy with respect to the area equals zero:

$$\frac{\partial U_T}{\partial A} = \frac{\partial U_E}{\partial A} + \frac{\partial U_S}{\partial A} + \frac{\partial U_P}{\partial A} = 0 \tag{2.118}$$

It is now possible to separate the term of the interfacial energy from the others:

$$-\frac{\partial U_S}{\partial A} = \frac{\partial U_E}{\partial A} + \frac{\partial U_P}{\partial A} \tag{2.119}$$

The surface energy can be expressed in terms of work of adhesion,

$$\partial U_S = -\Delta\gamma \partial A \tag{2.120}$$

while the right-hand term of equation 2.119 can be named H and represents the strain energy release rate in fracture mechanics:

$$H = \frac{\partial U_E}{\partial A} + \frac{\partial U_P}{\partial A} \tag{2.121}$$

Thus, it is now possible to rewrite the condition of equilibrium as:

$$\partial U_T = (H - \Delta\gamma)\partial A = 0 \tag{2.122}$$

which reduces to:

$$H - \Delta\gamma = 0 \tag{2.123}$$

also called the Griffith's criterion in fracture mechanics.

The meaning of equation 2.123 is that, if there is no dissipation, changes in the surface energy due to rupture or formation of interactions are 'immediately' balanced by the changes in the potential and elastic energy. If there is dissipation due to viscous processes, equation 2.123 does not equal zero but a term that represents the dissipated energy. It has been found that that term is proportional to the work of adhesion and it is a function of the velocity of the crack movements (that is now finite) and the temperature, thus:

$$H - \Delta\gamma = \Delta\gamma\,\Phi(a_T, v) \tag{2.124}$$

where a_T is the Williams-Landel-Ferry (WLF) shift factor for time-temperature equivalence. The most used expressions for this factor are:

$$\log(a_T) = -\frac{c_1^S(T - T_S)}{c_2^S + T - T_S} \quad \text{or} \quad \log(a_T) = -\frac{c_1^g(T - T_g)}{c_2^g + T - T_g} \tag{2.125}$$

where T_S is related to T_g, the glass transition temperature, by $T_S = T_g + 50$. The constants c_1^S, c_2^S, c_1^g and c_2^g were initially considered 'universal values' valid for the great majority of polymers, however it has been found that differences among polymers could be significant, so the use of the standard values should be not recommended unless as last resort. The universal values are 8.86, 101.6 K, 17.44 and 51.6 K, respectively.

A better look at equation 2.124 shows that viscoelastic properties (right-hand side) and surface properties $\Delta\gamma$ are separated from the elastic properties, geometry and applied load, that are all included in H. For example, if the JKR model is considered, starting from equation 2.77 and solving it for $\Delta\gamma$, leads to a H in the form:

$$H = \left(F - \frac{4E^* a^3}{3R^*}\right)^2 \frac{1}{8\pi a^3 E^*} \tag{2.126}$$

The fact that $\Phi(a_T, v)$ does not depend on the geometry of the system is an advantage. However, it is also an approximation that holds if the separation of the

bodies is mainly elastic and the viscoelastic loss is limited to small regions near the crack tip.

The relation between the form of $\Phi(a_T, v)$ and the viscoelastic properties of a material is still unsolved, however, the great part of experimental works have shown that for polymers it may be approximated by a constant, β, depending on the temperature multiplied by a power of the velocity of the crack:

$$\Phi(a_T, v) = \beta(T) v^n \tag{2.127}$$

Experimentally it has been found that the constant equals the WLF factor powered to n as v in the case of studies with variable temperature. However, the constant β is has been found also in studies where the temperature is constant and in this case is accepted that it equals the inverse of a characteristic speed v^* powered to n. Thus, two general equivalent formulas are accepted for $\Phi(a_T, v)$,

$$\Phi(a_T, v) = (a_T v)^n \quad \text{or} \quad \Phi(v^*, v) = (v/v^*)^n \tag{2.128}$$

with the exponent that typically lies between 0.1 and 0.8 [54]. In the case of the characteristic speed, there are not restrictions on the value of β.

An important point should be underlined: because equation 2.123 does not hold when there is dissipation, the general equations of the chosen contact mechanics model should be used. For example, for the JKR model these equations link the indentation to the applied load,

$$\delta = \frac{a^2}{3R} + \frac{F}{2aE^*} \tag{2.129}$$

and H to the indentation or to the load:

$$H = \frac{E^*}{2\pi a}\left(\delta - \frac{a^2}{R}\right)^2 = \left(F - \frac{4E^* a^3}{3R^*}\right)^2 \frac{1}{8\pi a^3 E^*} \tag{2.130}$$

As it is possible to note, when dissipative processes are introduced, $\Delta\gamma$ disappears from formulas and the system is described by a $\delta(F)$ relationship, together with a $H(\delta)$ or $H(F)$ equation. Equation 2.80, that describes the indentation in the non

dissipative JKR model, is immediately recovered from equation 2.129 when F is substituted by 2.130 in the case where $H = \Delta\gamma$.

An important clarification concerns the speed v: this is the crack speed, a parameter that is seldom available in adhesion tests. In fact, what can be set in adhesion tests is the speed of retraction or approaching of the probe to the sample or a control over the applied force or deformation, but usually the crack speed remains unknown. Moreover, during an adhesion test, there is not a unique value of the crack speed, but usually it changes along the entire measurements, especially when the two surfaces are next to be separated. In order to overcome these issues, different solutions have been proposed, however a unique method is still not available. For example, some authors assume that the crack speed is proportional to the velocity of the testing apparatus and use this as crack speed. In other articles, the crack speed is determined or estimated from optical images of the contact area [55]: in these cases the contact area is quite large, usually in the range of millimetres. In other cases, the evaluation of the crack speed is obtained starting from considerations about geometry of the tip of the probe and then connected with precise relationship to the speed of the equipment [56]. A group of author proposes of starting from the general equations of the chosen adhesion model and the general equation for $\Phi(a_T, v)$ to build the equations of v and $d\delta/dt$ from which the experimental $F(\delta)$ curve is calculated and values of the parameters n, β and $\Delta\gamma$ are found. Practically, starting from equation 2.124, inserting the expression for $\Phi(a_T, v)$ from 2.127 and equation 2.130 for H, v can be express as

$$v = \frac{da}{dt} = \left[\frac{a^3 E^*}{2\pi R^2 \beta \Delta\gamma}\left(1 - \frac{R\delta}{a^2}\right)^2 - \frac{1}{\beta}\right]^{1/n} \tag{2.131}$$

Then, in the most general case where the stiffness of the testing equipment cannot be considered infinite, the movement of the head of the testing apparatus, Δ, is the sum of the elastic displacements of the sample and of the probe according to

$$\Delta = \delta + \delta_m = \delta + \frac{F}{k_m} \tag{2.132}$$

where δ_m is the elastic displacement of the probe that can be considered as a spring of stiffness k_m. From equation 2.132, δ can be isolated, then substituting F by equation 2.129, finally derived as:

$$\frac{d\delta}{dt} = \frac{1}{1 + \frac{2aE^*}{k_m}}\left[\frac{d\Delta}{dt} - \frac{2E^*}{k_m}\left(\delta - \frac{a^2}{R}\right)\frac{da}{dt}\right] \tag{2.133}$$

Now, equations 2.131 and 2.133 can be solved with iterative numerical methods like the classical Runge-Kutta [57] or that proposed by Barquins [53, 58], providing n, β, E^* and $\Delta\gamma$ as guest parameters. To be precise, E^* and $\Delta\gamma$ are usually estimated from experimental data or from literature, respectively. The calculated $F(\delta)$ curve is compared with the experimental one and changes in the guest parameters are done until good agreement between the calculated and the experimental curves is achieved.

Authors that prefer the elastic-viscoelastic correspondence principle found a relationship similar to equation 2.124, usually in agreement with the experimental values of the exponent n reported by authors that uses the time-temperature superposition principle. This agreement is good in a great range of speeds, however at low speed, authors that prefer the elastic-viscoelastic correspondence principle found an exponent that is near or slightly greater than the unity [41, 59].

An example of the influence of the velocity of the crack speed, expressed as function of the velocity of the displacement of the two bodies, on the adhesion force based on a calculation is reported in Fig. 2.19 ([53]). It refers to a geometry similar to the one used in this work: it represents the resulting adhesion of a tack test between a glass ball on polyurethane, with three different constant cross-head velocities. The adhesion force greatly increases with the increase of the cross-head (or bodies displacement) velocity. In the original work is pointed out that also a slow speed of 1 µm/s results in a great increase of adhesion force in comparison with the purely elastic case (JKR limit).

The influence of the temperature is also calculated in same article, showing that increasing the temperature, the viscoelastic dissipation (and the adhesion force as consequence) decreases.

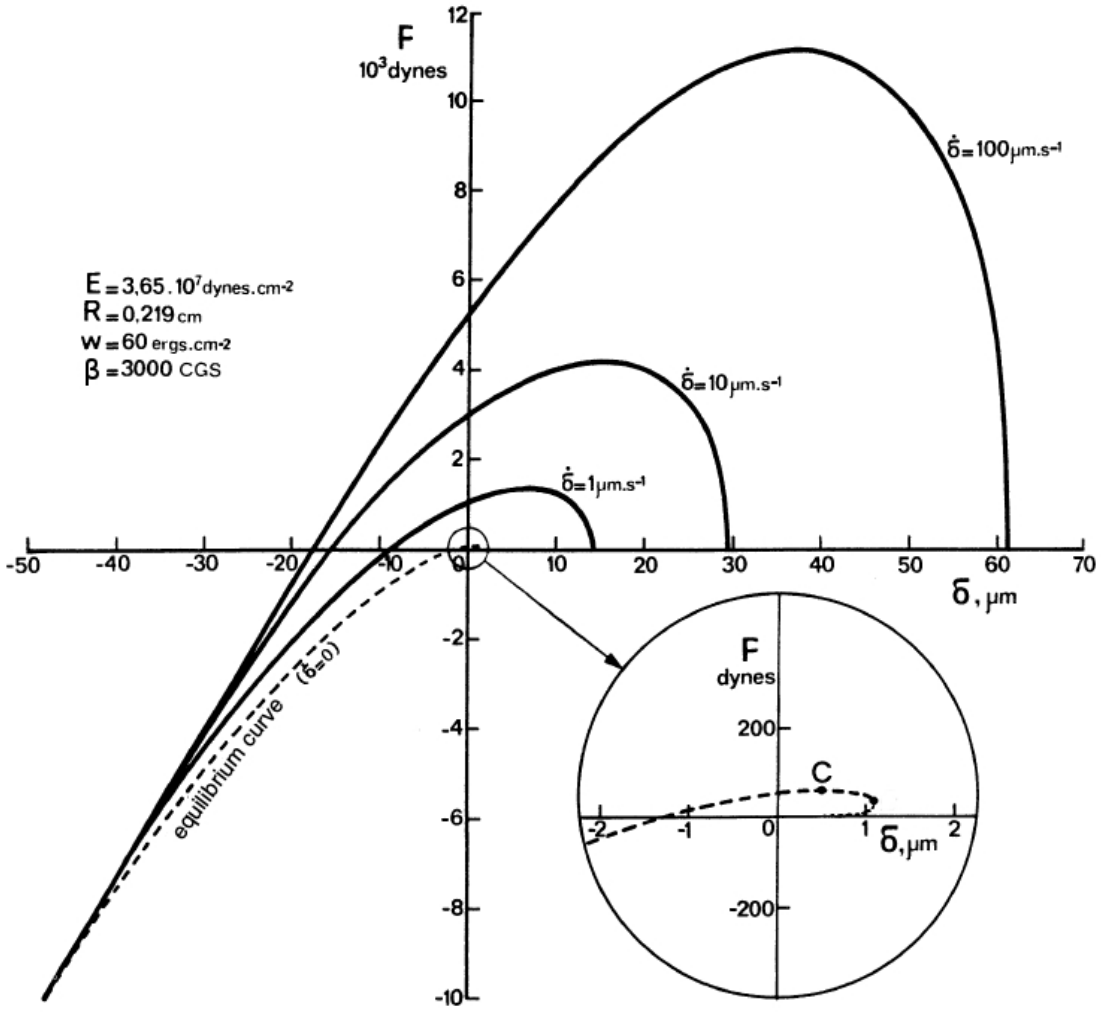

Figure 2.19: Calculated effect of cross-head velocity on adhesion force. The displacement velocity is $\dot{\delta}$, w corresponds to $\Delta\gamma$. In the inset, the adhesion force (point C) in the elastic approximation is shown for comparison. Image adapted from [53].

Both the elastic-viscoelastic correspondence principle and time-temperature superposition principle approaches hold only for linear viscoelastic material. In particular, the former does not hold when boundaries between regions with different time-dependent (displacement or surface interactions) behaviour change during the considered time. An extension of the principle to a complete loading and

unloading problem, where the contact area initially increases monotonically until a maximum is reached and then decreases monotonically to zero has been proposed, however, the knowledge of the contact history is required and this is not always determined in an easy way [60, 61]. On the other hand, the time-temperature superposition principle is only valid if the characteristic of interest translates with the temperature without further transformations. Both the approaches mainly consider the effect of velocity on adhesion; for example, it is known that adhesion in viscoelastic materials depends also on the loading force. This dependence is difficult to explain: for small loads, adhesion increases as the loading force increases, however, at very high loads, adhesion becomes zero or it reaches a constant value [36, 52]. In any case, even if the two approaches are so different, it has been found that they can be in good agreement [41] in a great range of crack speeds.

Theoretically, if there is no energy dissipation during the loading and the unloading part of an adhesion test, the two processes of crack opening and crack closing should be symmetrical, i.e. the traces of the loading and unloading processes should perfectly superimpose. However, it may happen that, even using a very low speed, this does not happen and more energy is required to separate the two surfaces than what has been required to get them into contact. This hysteresis cannot be ascribed to viscoelasticity but it may be due to many factors, such as the equipment used in the test (mechanical hysteresis because the testing machine does not have an infinite stiffness) or other characteristics of the materials such as deformability [62] (with the formation of the neck between the two contacting surfaces) or roughness [63]. In the special case of polymer, hysteresis can be also attributed to a mechanism of chain or loop extraction.

The conclusion of this section about mechanics of adhesion is that different models are been developed according to the type of the studied material. For perfectly elastic materials, a comprehensive model, the Maugis model, has been developed and it includes all the previous theories as particular cases. However,

these previous theories are still used in specific fields because they are sufficiently accurate and easier to handle. In these fields, adhesion is related to the work of adhesion and the reduced radius: for two systems where the work of adhesion and the contact radius are the same but the stiffness of the material is different, adhesion is maximum for rigid bodies and reaches a minimum for deformable bodies.

However, for materials that are not perfectly elastic, adhesion becomes dependent also on experimental parameters, especially on the velocity of the test. Because of the difficulty of dealing with a such complex phenomenon, a comprehensive theory does not exist, and the two developed approaches do not include all factors that can play a role in adhesion for viscoelastic materials. They usually consider the effect of the velocity as the main factor that can influence adhesion, showing that the experimental adhesion force increases as the speed of unloading increases. However, speed is not the only factor that could influence adhesion: thus, in the case of viscoelastic material adhesion, all the experimental parameter should be declared.

2.8 Crosslink density and adhesion

Apart from elasticity and viscoelasticity, whose effects on adhesion are discussed in the previous paragraph, in literature is sometimes reported that also changes in the crosslink density can modify adhesion. As first study about it, de Gennes is generally cited [64]: according to him, adhesion force depends on the square root of the number of monomers in the chain between two crosslinks. However, in the literature this behaviour is not always observed: for examples, some authors did not see any significant adhesion dependences on the crosslink density ([65]) or they could explain adhesion differences without relating them to crosslink densities but to a specific mechanism of detachment ([66]). Some others confirmed the dependency found by de Gennes (at least in some conditions where chain relaxations do not take place [67]), or more generally, an increase in adhesion with

the reduction of the crosslink density ([68]). In one case, a reduction in adhesion with a decrease of the crosslink density is also reported [69].

In conclusion, there is not a clear evidence or a comprehensive explanation that adhesion can depend on the crosslink density: contact mechanics theories do not consider this as a possible effect (that probably can be ascribed inside the more generic definition of viscoelasticity) however, some experimental observations lead to think that the they may be related.

2.9 Effect of roughness

Until now, the effect of the roughness of surfaces on interfacial adhesion and interactions has been neglected. The geometry used for all the models and theories previously presented (the sphere–plane geometry, which is a special case of the sphere–sphere geometry), simply considers that surfaces are perfectly smooth. However, because interfacial adhesion and interactions greatly depend on contact or neighbouring areas, it might be expected that roughness should have an influence on them, due to the fact that it changes those areas. Of course, if the change in the areas is minimal, maybe the effect of roughness can be neglected, otherwise it should be considered. In the next sections, how roughness influences the adhesion force, the capillary force, the contact angle and the hysteresis between the loading and unloading parts of the adhesion test is presented.

2.9.1 Roughness effects on contact angle

The Young equation was developed assuming that the surface where the drop lies on is flat, homogeneous and perfectly smooth. However, when these conditions are not respected, the value of the contact angle becomes different from this 'ideal' case. However, some equations that relate the contact angle of Young with experimental contact angles have been developed under specific conditions and will be present below.

If a surface is not flat, the same determination of the contact angle becomes difficult, and, in absence of a suitable software that takes into consideration surfaces depressions, largely inaccurate.

If a surface is not very rough, and water can completely penetrate into the valleys, the Wenzel model applies (panel (a) in Figure 2.20). According to this model, the contact angle equation becomes [70]:

$$\cos\theta_W = r_f \cos\theta_Y \tag{2.134}$$

where θ_Y is the contact angle for the corresponding smooth surface (that is determined by the Young equation), θ_W is the contact angle of the rough surface when the Wenzel model applies and r_f is the ratio between the actual and the nominal area of contact. For a rough surface $r_f > 1$, so that in the case of a hydrophilic surface, roughness increases the hydrophilicity, while in the case of a hydrophobic surface, roughness increases the hydrophobicity. The special case of $r_f=1$ corresponds to the Young condition. It has been pointed out that the dimension of the drop should be at least two or three orders of magnitude greater than the roughness scale to safely apply equation 2.134.

If a surface is flat but chemically non-homogeneous, the Cassie-Baxter equation should be used [71]:

$$\cos\theta_C = n_1 \cos\theta_{Y1} + (1 - n_1)\cos\theta_{Y2} \tag{2.135}$$

where θ_C is the contact angle of the heterogeneous surface, n_1 the fraction of the surface made of the chemical 1, $(1 - n_1)$ is the fraction of the surface made of the chemical 2 and θ_{Y1} and θ_{Y2} are the contact angles of Young for smooth surfaces made of chemicals 1 and 2, respectively. An important special application of the Cassie-Baxter equation is when air pockets are trapped between a hydrophobic rough surface and the drop of water. This situation can happen under particular rough patterns on hydrophobic surface: if the distance between two peaks is not too big, water cannot penetrate into depressions and air remains trapped underneath it (panel (b) in Figure 2.20). In this case, air could be considered as the

surface made of the chemical 2 with a contact angle air-water of 180°, so that equation 2.135 becomes:

$$\cos\theta_C = n_1 \cos\theta_{Y1} + n_1 - 1 \quad (2.136)$$

where, in this case, n_1 is the fraction of the surface that is wet by water. However, it is better to underline that this equation applies only if water does not penetrate into valleys and sits on the top of the peaks, so that the contact line among the three phases remains flat. To respect this condition, special ordered rough surfaces are produced, where the tops of the peaks are usually flat. Also in this case, equation 2.136 applies if the scale of chemical heterogeneity is much smaller than the size of the drop of water.

If the surface is rough and hydrophobic and, even if air pockets are present, water partially penetrates into valleys (actually an intermediate situation between the pure Wenzel and Cassie-Baxter conditions as depicted in panel (c) in Figure 2.20), the following equation applies [72-74]:

$$\cos\theta_{CW} = r_f n_1 \cos\theta_{Y1} + n_1 - 1 \quad (2.137)$$

where n_1 in this case is the fraction of the surface that is wet by water.

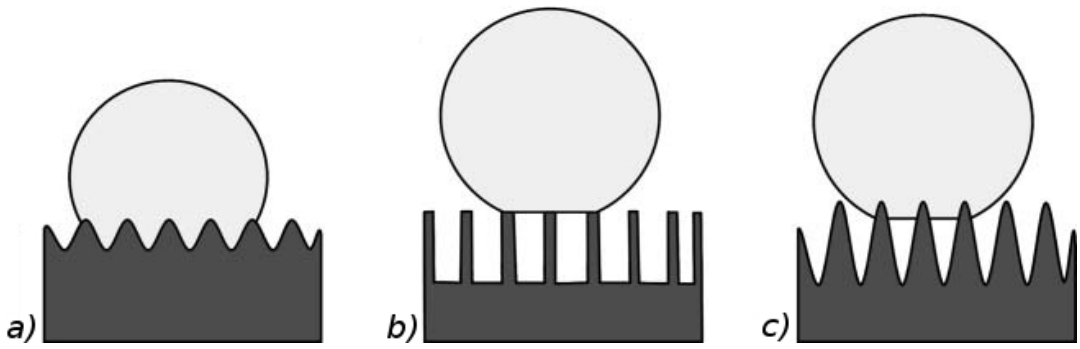

Figure 2.20: Scheme of different wetting regimes where different equations for contact angles apply. In panel (a) water completely wets a rough surface and contact angle is described by equation 2.134 (Wenzel's model); in panel (b) the water drop is sat on the top of the spikes and the contact line among phases is flat, so that the contact angle is described by equation 2.135 (Cassie-Baxter's model); in panel (c) an intermediate situation between (a) and (b) is depicted where water partially wets a rough surface also inside valleys but air pockets are still present underneath the drop. In this last case, the contact angle is described by equation 2.136 (mixed Wenzel and Cassie-Baxter's model). Image adapted from [75], reproduced with permission of ROYAL SOCIETY OF CHEMISTRY via Copyright Clearance Center.

Transitions between the wetting regimes described above are been observed on hydrophobic rough surfaces: the most studied is the Cassie-Baxter-to-Wenzel transition that may happen under drop evaporation, under application of electrical voltage, pressure or vibrations on the drop [76]. The Wenzel-to-Cassie-Baxter transition is usually assumed impossible, however, it was observed in a study ([77]), but more efforts are needed to clarify this point.

2.9.2 Roughness effect on capillary force

As introduced in a previous section, it has been proposed that roughness could explain the increase of the capillary force when the relative humidity increases when two hydrophilic surfaces are brought into contact [27]. According to this explanation, when relative humidity is low, capillary necks are formed only in correspondence of the top of the highest asperities, so the capillary force is much smaller than in the case of a smooth surface. With the increase of humidity, the number of capillary necks increases and so also the capillary force increases, until, when humidity is high, all the little necks merge in a unique capillary bridge, as in the case of a smooth surface. Thus, according this hypothesis, even if at low values of relative humidity on a rough surface the capillary force is lower than on the corresponding smooth surface, with the increase of relative humidity (and so of the number of the capillary necks) it becomes similar or close that on the corresponding smooth surface: however, this model cannot explain well one of the two different behaviours of the capillary force versus relative humidity previously described, and specifically, the monotonic one.

2.9.3 Roughness influence on adhesion force

How roughness influences the adhesion force is still a matter of discussion mainly because it depends on the type of materials involved, the scale and the type of the roughness.

Because the effect of roughness is to reduce the contact area, it is expected that this will also reduce the adhesion force between the two contacting surfaces. In fact, if at least one of the two bodies has a rough surface, the contact arises only on the tops of the highest asperities. However, according to the applied load and the material characteristics, these asperities may or may not be deformed. In the case where at least one of the two materials is very soft, the soft body can adapt to the other body, in order to get an intimate contact also in presence of roughness: in this case, roughness increases the contact surface with respect to the nominal area and adhesion increases. On the contrary, if both bodies are rigid, micro or nano roughness usually decreases adhesion because that roughness is sufficient to prevent intimate contact.

Another important factor is the scale of roughness. It is not easy to define it in a universal way, however in this case it usually refers to heights and radii of the asperities. If a surface is quite smooth, so that a small-scale roughness is present, in particular in the case of soft materials, its influence can be safety neglected (that is not always the case for rigid bodies). If the roughness scale becomes greater, a reduction or increase of adhesion may happen, according to the type of roughness and the involved materials. Also the geometry of the contact has been shown to have an effect on adhesion: in the case of the two contacting surfaces, if the contact area is not on in correspondence of the tops of the features of the two surfaces but it is 'lateral', adhesion can either increases or decreases [78, 79]. Similarly, this can also happen when one of the two surfaces is very rough and the other one remains blocked at a certain height of a narrow valley between two high asperities.

The type of roughness is more difficult to estimate: firstly because a universal way for its description has not been developed, yet and secondly because rough surfaces are often irregular, while models usually require a certain type of regularity. Roughness is often expressed as the root mean square (RMS) of the heights of asperities, however this is not a generally useful description of the real roughness (this subject will be dealt with in the next chapter). However, some models that relate the adhesion force to the roughness have been developed: all of

them show a reduction of adhesion due to the decrease of the contact area. A first simple model considers a single hemispherical asperity between a sphere and a plane and the adhesion force is found to be [80]:

$$F_{\text{adh}} = \frac{A_{\text{H}} R_1}{6 z_0}\left[\frac{r_1}{r_1 + R_1} + \frac{1}{\left(1 + r_1/z_0\right)^2}\right] \tag{2.138}$$

where R_1 is the radius of the sphere and r_1 is the radius of the asperity. The first term refers to the van der Waals forces between the sphere and the asperity, while the second to that between the sphere and the plane [81]. In fact, it is quite difficult to find a unique asperity, with a hemispherical shape and known radius. Thus, starting from this model, a more general one has been developed, where more than one asperity are considered and the RMS roughness is used instead of the asperity radius [82, 83]. In this case, the roughness of the second surface is modelled as a superimposition of two different scales of RMS roughness. The superimposition of the two roughnesses is obtained by considering two closed-packed spherical distributions of asperities with two different radii, r_1 and r_2 where $r_2 < r_1$ and two different peak to peak distances, λ_1 and λ_2 where $\lambda_2 < \lambda_1$. Because the distribution of asperities and valleys is regular it can be expressed also in terms of RMS roughness, namely, R_{rms1} and R_{rms2}. In this model, the general formula for the calculation of adhesion is found to be:

$$F_{\text{adh}} = \frac{A_{\text{H}} R_1}{6 z_0}\left[\frac{1}{1 + \left(58 R_1 R_{\text{rms2}}/\lambda_2^2\right)} + \frac{z_0}{\left(1 + 1.82\left(R_{\text{rms1}} + R_{\text{rms2}}\right)\right)^2} + \frac{1}{\left(1 + \left(58 R_1 R_{\text{rms1}}/\lambda_1^2\right)\right)\left(1 + 1.82 R_{\text{rms2}}/z_0\right)^2}\right] \tag{2.139}$$

Equation 2.139 is the most general formula: special cases and the presence of other forces or sample deformation are also considered. A further model considers regularly spaced displacement of very small rigid hemispherical asperities on the deformable sphere in contact with a smooth rigid plane [84]. The total adhesion force is calculated considering the contribution of asperities as additive to the contribution of plane-sphere interactions. According to this model the total van der Waals force is:

$$F_{\mathrm{adh}} = \left[1 + \sum_{i=1}^{i<a/x} \frac{360}{\arccos\left(1 - 1/2\,i^2\right)}\right]\left[\frac{A_{\mathrm{H}} r_1^4}{6\,z_0^2\left(z_0 + r_1\right)^3}\left(1 + \frac{2\,z_0}{r_1}\right)\right] + \frac{A_{\mathrm{H}} R_1}{6\left(r_1 + z_0\right)^2} \tag{2.140}$$

where a is the contact radius and x is the distance between asperities. Other models consider a Gaussian distribution of asperity heights [85] or a fractal model of surface roughness [86]. However, in the case of these two last models, it is necessary that the roughness of the surfaces really follows a Gaussian distribution or a fractal dimension otherwise they do not hold. Moreover, in the case of the former model, contact area should be much lower than nominal area and the contact should break uniformly, which is rarely the case.

In conclusion, even if it is clear that roughness influences the adhesion force, a comprehensive theory that can take into account all the possible effects it still not available. Considerations about the type of materials and roughness, together with an estimation of the scale of roughness should be evaluated in each case. Some models, which only considers the type of roughness, have been developed, however, they always assume that roughness follows a defined pattern.

2.9.4 Roughness influence on hysteresis in the adhesion test

As discussed above, in an adhesion test where viscoelasticity, instabilities, excessive deformability, capillary force and chains or loop extractions are absent, hysteresis between the loading trace and the unloading retrace may be still present. In a recent article different samples of the same polydimethylsiloxane material were moulded with different roughnesses, so that all the other properties were the same: the hysteresis between the loading and unloading parts of the adhesion test still exists and it was found that depends on the roughness of the surfaces [63]. According to the proposed explanation, hysteresis is due to the fact that, when roughness is present and it cannot be neglected, the crack closure and opening proceed by discrete steps in contrast to perfectly smooth (or quite smooth) surfaces. Sometimes steps are clearly visible in the loading and unloading curves;

this happens when the roughness of one surface is much greater than that of the other surface. Considering the case of a rough flat surface and a small spherical smooth surface brought into contact: they can be seen as pinning the small surface on depressions of the other one. If roughness is not as great but still present, steps become smaller and the loading and unloading curves appear to be continuum, however, the hysteresis loop between them remains.

2.10 Polydimethylsiloxane

Polydimethylsiloxane (or PDMS) is a polymer that belongs to the polysiloxane group: differently from other organic polymers, it contains silicon and oxygen atoms in the repeating unit. In the case of PDMS, each silicon atom is also connected to two other methyl groups (as short side chains). Siloxane polymers are used in many applications because of their good thermal, mechanical and optical properties. Some of them are also considered biocompatible and they are used in medicine, for example as medical devices. They can be used as fluids with different viscosities, or rubber with different elasticities. Viscosity and elasticity depend on the length of the polymer chains; the difference is due to the fact that fluids are composed by linear chains, while rubber is formed by crosslinked chains.

In this thesis, the laboratory synthesized rubber is a crosslinked PDMS with different chain lengths: this choice is partly related to the fact that this material is also used by Teknek and partly due to the fact that PDMS is reported to have ideal elastic behaviour [87-90] (and for this reason, it is often used in studies about adhesion on rubber).

Once having chosen the kind of polymer, two possibilities were considered for the crosslinking reaction: to use a two-packs commercial set, where, according to the ratio between the two components a different crosslink density is achieved, or to start from different linear polymer chains to be crosslinked in the laboratory. A very well known commercial set is readily available on the market and often used in many articles (Sylgard 184). However, because it is a commercial grade, it may

contain also additional additives to improve performance and these quantities are not declared. Moreover, the use of the same trademark does not guarantee that the product composition is constant. And finally, different crosslinking densities are achieved mixing different quantities of the curing agent on the base: that means that, except for using stoichiometric quantities of curing agent and base, all the other ratios between them will lead to incomplete crosslinking reaction and so, very likely, to material with high viscoelastic behaviour. Because of all these reasons, it was preferred to synthesized the PDMS rubber starting from linear polymeric chains of different lengths with a suitable curing system, in order to work always with stoichiometric ratios and avoiding additional sources of viscoelasticity. Next sections will deal with the different possible crosslinking reactions, the one that was chosen and why, together with an introduction of the mechanism of the chosen reaction.

2.10.1 Crosslinking reactions

There is not a unique crosslinking reaction for PDMS. A look in the literature has shown that there are at least three main groups of reactions:

- radical reaction or high temperature vulcanization [91-94]. It is carried on 'normal' PDMS or on PDMS with some vinyl side chains. With the former there is no control of the network (with the exception of the peroxide amount used), while with the latter, if a suitable vinyl specific peroxide is used, the control is done by the number of vinyl groups. Some improvements could be achieved using a less reactive radical like TEMPO [95].
- hydrosilylation [92-94, 96-102]. This is a reaction between a vinyl group and a Si-H bond in presence of platinum (Pt) as catalyst. It can be carried between:
  - vinyl-terminated PDMS and crosslinker of the desired functionality with Si-H groups;

- hydrogen-terminated PDMS and crosslinker of the desired functionality with vinyl groups;
- PDMS with some vinyl side chains and crosslinker of the desired functionality with Si-H groups;
- hydrogen-terminated PDMS and vinyl-terminated PDMS

- Condensation of OH-termined PDMS with a crosslinker of the desired functionality with tin (Sn) as catalyst [103-110].

To decide which of these reactions could be the most suitable for the project, the following evaluations have been done:

- radical reaction: radicals are very reactive species and so these reactions are difficult to control. With normal PDMS there is no way to control crosslinking sites along the chain: a better control could be achieved with the use of PDMS with vinyl groups at the end or somewhere along the polymer chain and with specific vinyl peroxide (it must be underlined that radical reaction is usually not used with vinyl-terminated PDMS, even if, at least in theory, it could work).
- hydrosilylation: it can be carried out selectively on PDMS with vinyl groups and it can be used to link directly two chains together (as in the radical reaction) or by means of a crosslinker of the desired functionality (and eventually of different length as in bimodal networks). Moreover, it is more difficult that side reactions can take place in comparison with the radical reaction.
- condensation: it is only used with OH-termined PDMS. So, even if it is generally considered a good reaction, it is not as versatile as hydrosilylation.

On the basis of these considerations, the hydrosilylation reaction was chosen as the preferred crosslinking reaction in this thesis.

2.10.2 Hydrosilylation reaction

Hydrosilylation is an addition of a Si-H bond across a carbon-carbon double bond with a platinum, or a platinum complex catalyst. Thus, a literature survey was performed to select a good combination of the possible reactants. From that, it appeared that a good choice of reactants could be:

- vinyl-terminated PDMS.
- tetrakis-(dimethylsiloxy)silane as crosslinker. A functionality of four is preferred because, even if the reaction is not complete, at least three functionalities will react, and so a crosslink is created; while with a functionality of three, if the reaction is not complete, only an elongation of the chain is obtained (and it is not interesting). A functionality of two is discarded because it is not able to create a crosslink but only an elongation of the polymer chain.
- Karstedt's catalyst as platinum complex.

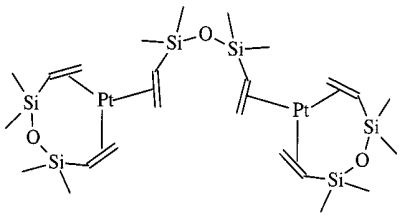

a)

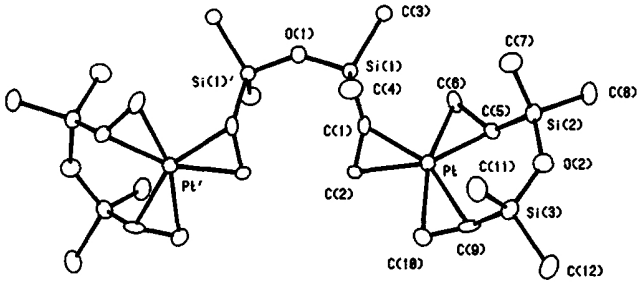

Fig. 1. Crystal structure of *rac*-**1**. Selected bond lengths [Å] and angles [°]: Pt-C(1) 2.19(2), Pt-C(2) 2.18(2), Pt-C(5) 2.19(2), Pt-C(6) 2.16(2), Pt-C(9) 2.21(2), Pt-C(10) 2.19(2), C(1)-C(2) 1.36(2), C(5)-C(6) 1.43(2), C(9)-C(10) 1.39(3), Si(1)-O(1) 1.645(7), Si(2)-O(2) 1.607(11), Si(3)-O(2) 1.631(13); C(1)-Pt-C(2) 36.4(6), C(5)-Pt-C(6) 38.3(6), C(9)-Pt-C(10) 37.0(7), Si(1)-O(1)-Si(1)' 146(1), Si(2)-O(2)-Si(3) 134.7(8).

b)

Figure 2.21: Karstedt's catalyst structure in panel (a) (image reprinted (adapted) with permission from [111]. Copyright (1999) American Chemical Society) and crystallographic structure of Karstedt's catalyst as determined by Lappert with the original caption in panel (b), (image reprinted from [112]).

Early syntheses had been carried out with chloroplatinic acid at high temperature, but new catalysts were developed to achieve a good control on

the reaction in milder conditions. The most used is Karstedt's catalyst that lets the reaction start also at room temperature. Other catalysts are: Speier's catalyst (chloroplatinic acid in isopropyl alcohol) and Lamoreaux [113].

Karstedt's catalyst is a complex of Pt^0 and 1,3-divinyl-1,1,3,3-tetramethyldisiloxane: its structure was determined by means of X-ray single crystal diffraction and it is a dimeric complex with a bridge ligand [112] (Figure 2.21).

- inhibitors (usually dimethyl maleate or dimethyl fumarate): these are used to stop the reaction for starting immediately. In fact, with inhibitors, the reaction will start at high temperature (or it is slowed down at room temperature). Inhibitors are mainly used in industry to let all reactants mix without problem and to carry out the network reaction only in the cast (or mould) that is kept at the highest temperature. In this work, inhibitors were used only if necessary.

A sketch of the reaction is depicted in Figure 2.22.

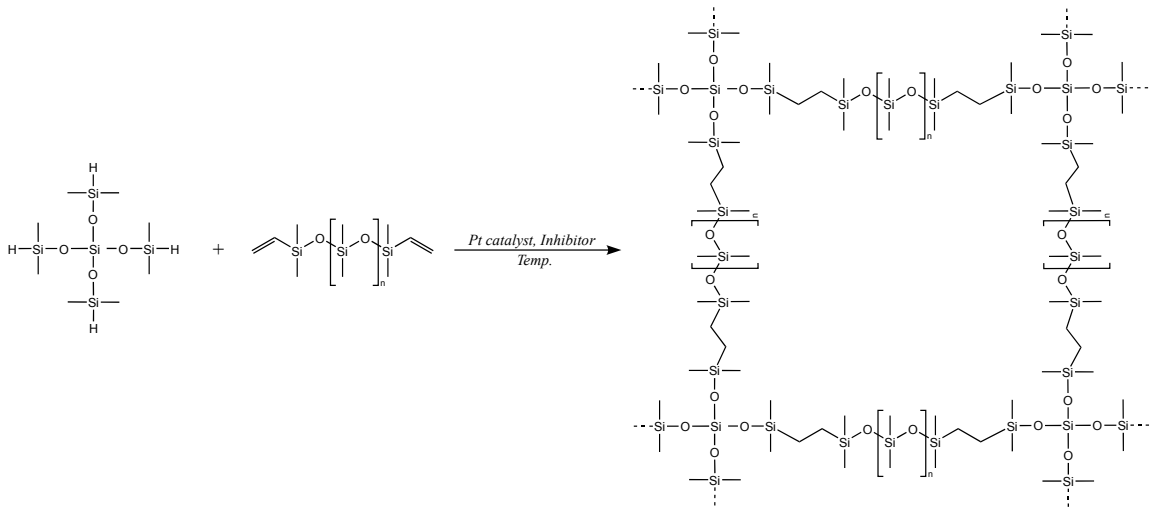

Figure 2.22: Sketch of the hydrosilylation reaction. In this picture, stoichiometry is not reported and the product should be considered an endless network constituted by the repetition of the depicted unit (in this regard, dashed bonds should be considered as single bonds with another unit).

The mechanism of this reaction is still under discussion: even if it not so relevant here, it plays a role in the understanding of reaction conditions. The first proposed mechanism is the Chalk-Harrod one [114, 115], which is a quite common mechanism in organometallic chemistry where there is an oxidative addition of the silane to the platinum centre, then there is the insertion of the olefin in the Pt-H bond followed by the reductive elimination of the product and catalyst regeneration (Figure 2.23).

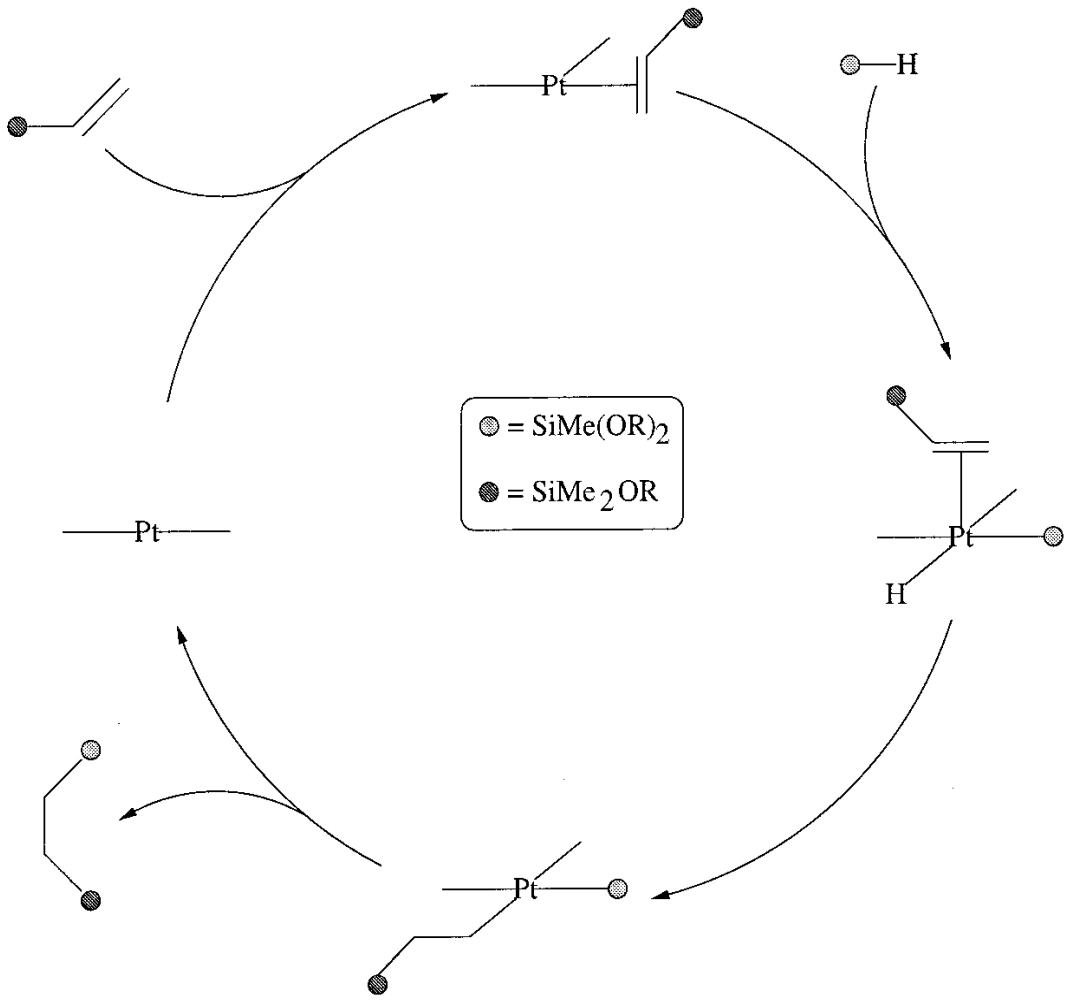

Figure 2.23: Chalk-Harrod mechanism, scheme reprinted (adapted) with permission from [115]. Copyright (2002) American Chemical Society.

This mechanism cannot explain some experimental observations such as the initial induction period, the role of oxygen and the formation of coloured bodies at the

end of the reaction. The suspect of a role of oxygen in this reaction was initially suggested by Harrod and Chalk [114]: “The oxygen effect is common knowledge among people who run hydrosilylation on a large scale, where deliberate aeration of the reaction may be required to sustain catalytic activity”. Subsequently, Lewis [116] proposed a mechanism based on platinum colloids as active catalytic species, explaining the formation of the colour bodies as 'agglomeration' of platinum colloids and assuming that a catalytic amount of oxygen could prevent this and enhance the platinum reactivity [117]. By the passing of time, Lewis revised his mechanism, which became quite similar to the initial Chalk-Harrod one: he found that the active catalytic species is always a monomeric platinum complex derived from the initial dimeric complex [111] (Figure 2.24). The new explanation for the role of the oxygen is then linked to the type of olefin used in the reaction: oxygen plays an important role in reactions with poorly coordinated olefins, allowing the reaction to proceed, even if it is not clear how it could do this (a proposed roles for the oxygen is its coordination to the platinum catalyst as weak ligand or a stronger interaction with platinum that could increase its electrophilicity) [111, 117, 118]. In any case, it is well established that oxygen is only a co-catalyst for the reaction: experiments with isotopic labelled oxygen show that there is not O-O consumption or breakage in the reaction [117]. What it is not so clear is the real necessary quantity of oxygen: it seems that only a catalytic quantity is able to improve the reaction, while an oxygen excess leads to side reactions [118] (but this study is based on another platinum catalyst).

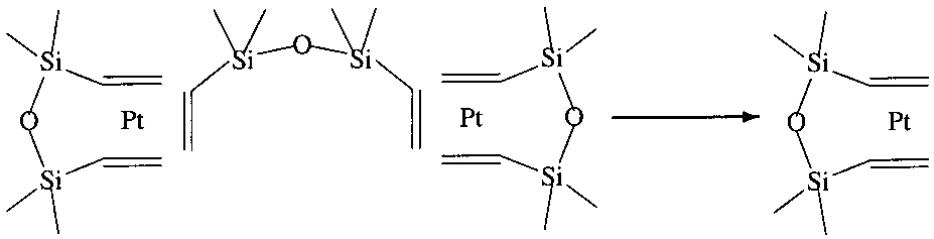

Figure 2.24: Monomeric active platinum complex formation. Picture reprinted (adapted) with permission from [115]. Copyright (2002) American Chemical Society.

What is well-established is that the type of silane and vinyl compounds influences the rate of the reaction: silane with electron-withdrawing groups are more reactive than silane with electron donating groups toward the same olefin, even if the sterical effect must be taken into account [117, 119]. For the vinyl compound it is exactly the opposite: vinyl compounds with electron-donating groups are more reactive than olefins with electron-withdrawing groups [111, 117]. It is known that the platinum of Karstedt's catalyst shows a stronger coordination toward the olefins with electron-withdrawing groups (i.e. the less reactive) and that, in presence of more than one olefins, the one that is preferentially hydrosilylated is that coordinates the Pt centre more strongly [111] (experiments were carried using equimolar quantities of different olefins).

An interesting issue regards the quantity of the crosslinker: it is known that a ratio Si-H/vinyl greater than 1 increases the rate of the reaction [89, 119] and the elastic modulus of the network [89] (and these are probably the reasons for which commercial crosslinkable PDMS formulations show stoichiometric imbalance). There are only a few hypotheses to try to explain these experimental observations [89] and it is generally assumed that the excess of crosslinker is consumed during the reaction without interfering (and that, at least, low temperature would ensure that there are not side or competitive reactions). The excess of crosslinker reacts with O_2 or H_2O from the environment and the moisture to form Si-OH groups that react with other Si-OH or Si-H groups, as reported in Figure 2.25 (hydrosilylation is often performed under atmospheric conditions [89, 120, 121]).

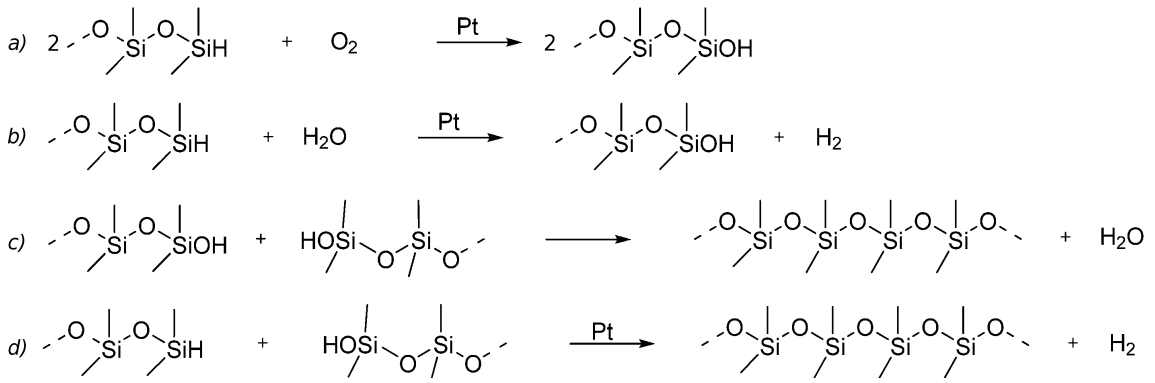

Figure 2.25: Side reactions due to the excess of crosslinker with oxygen in panel (a) and in presence of moisture in panel (b). The formed Si-OH species can then react with another Si-OH species, like in panel (c) or with the crosslinker, like in panel (d). Scheme reprinted (adapted) with permission from [89]. Copyright (2012) American Chemical Society, with reactions in panel (a) and (b) reprinted from [121], Copyright (2009), with permission from Elsevier.

Another point that is not completely clear is the role of the inhibitor: Karstedt's catalyst is so active that the hydrosilylation reaction usually requires only few minutes at room temperature to yield solid PDMS. Usually, a post-cure step at higher temperature is performed to ensure that the reaction will be complete (when the reactive mixture becomes solid or very viscous, the mobility of reactive species decreases and, as consequence, also the rate of the reaction decreases). Three types of inhibitors are the most used with Karstedt's catalyst: maleates, fumarates and β-alkynoles. A typical inhibitor is a species that coordinates preferentially the catalyst, i.e. the metal reactive centre, and prevents its reaction with the other reactants at room temperature. The raising of the temperature makes the inhibitor-catalyst interaction weaker, so the inhibitor is released and the catalyst is then in the active form. The inhibitors for the hydrosilylation reaction should not be considered 'typical inhibitors': they just slow down the rate of the reaction, but they are not able to prevent the reaction from starting even at room temperature [101]. Some studies try to investigate the mechanism of these inhibitors, but it is still not clear. Fumarates and maleates are molecules that contain a vinyl group linked to two electron withdrawing groups and they coordinate the platinum centre preferentially. For example, the addition of four

equivalents of these inhibitors with respect to the quantity of the platinum results in a complex where one of the ligand of Karstedt's catalyst is substituted by the inhibitor. The following addition of five equivalents of a silane results in a complex where platinum is bonded to the silane and the inhibitor [122]. A different explanation considers the hydrophobicity/hydrophilicity of inhibitors and reactants: it is found that vinyl-terminated PDMS and crosslinker are more hydrophobic than the inhibitors. This leads to think that the role of inhibitors is to solvate the catalyst, creating a phase separation between the catalyst and the other reactants. With the raising of the temperature inhibitors are volatilized and release the catalyst [115]. However, this theory is not able to explain why the reaction can occur also at room temperature when inhibitor is added. Also the quantities of the inhibitor are not clear: sometimes they are related to the reactant weight (usually 0.5% w/w) [113] and sometimes to the vinyl concentration [123].

Beyond the side reactions described above for the crosslinker, it is known that there could be also some other side reactions that could generally occur in the hydrosilylation reaction: a complete and extensive explanation of these side reactions, involving conditions and mechanism, is still far away from being obtained. It is not easy to study side reactions and to characterise their products, especially if they occur in small amounts as in the crosslinking reaction of PDMS. Moreover, they strongly depend on the conditions and reactants: for example, a slight difference in the catalytic species could lead to different results. One of the side reactions, or better, competitive reaction, that can occur is the dehydrogenative silylation: this reaction usually occurs with many catalysts that contains transition metals, but it does not seem to occur with platinum catalysts [123]. Platinum catalysts, and especially Karstedt's catalyst, are considered the most suitable catalysts for the hydrosilylation reactions because they show fewer side reactions than the others [97, 101, 123].

In this framework it is also difficult to find a unique description of reaction conditions: the reaction could be carried out in solution [99, 101], at room temperature until completeness [94] or at a higher temperature in the final step

[100], with inhibitor [101] or without inhibitor [94, 99, 100], under argon or nitrogen [101] or under atmosphere [100]. The quantity of Karstedt's catalyst can vary from 1 part of platinum per 10^4 parts of vinyl [94] to 10 ppm [100] or to 35 ppm [99], even if the most common quantity is 10 ppm or less. Same situation for the inhibitor quantity that can vary from 0.015% [101] to 0.5% [113] w/w. The ratio Si-H/vinyl group is 1 in all the syntheses to obtain a model network (in industrial formulations it is generally greater than 1 [89]). Considerations about the reactivity of the chosen silane and vinyl-terminated PDMS lead to say that both of them are not the most reactive, but neither the least reactive: the should have a 'middle-good' reactivity [111, 117, 119]. A probably important point is the sterical hindrance of the crosslinker that has four reactive groups quite near each other.

In conclusion, because there is no unique 'recipe' for this reaction, different attempts were done to find the best conditions that will be described in the next chapter.

3 Experimental

This chapter will deal with materials and techniques used in this work of research. Before this, two introductory sections will describe samples and the plan of the research. This choice is related to the fact that it may be difficult to fully understand the plan of the thesis, without having at least an idea of the types of samples: in fact, some analyses or choices were done because of the characteristics of some of the samples. After this, it will continue with a better insight into materials that formed the samples, in this case, presenting a short description of each, their uses and their relevant chemical-physical properties. The chemical-physical properties reported should be considered as qualitative: in fact, they refer to a generic class of materials and not to the specific sample. That is valid also when there is not a range of variation of a property; and in the case of the elastic modulus, the interest is mainly in the order of magnitude. For PDMS only, also the condition of the crosslink reaction are described. The last part of the chapter will introduce techniques and equipment used, together with a discussion between different methods, when there is more than one possibility to obtain a datum. In some cases, mathematical equations related to some procedures are also introduced. For each used technique, after the introduction, the experimental method chosen is also reported. Again, this arrangement of the subjects may appear fuzzy, however it seems suitable to let the reader follow the flow of information easily.

3.1 Introduction to samples

As introduced at the beginning of the previous chapter, the aim of this research is the study of the interfacial adhesion force between surfaces and particles. It is also correlated with an industrial application, the cleaning process developed by Teknek: this process is designed to be effective in removing particles from different types of surfaces. Teknek provided some of its cleaning rollers and some samples of surfaces that simulate some of the materials that need to be cleaned. In addition, some

laboratory made samples were synthesized in order to obtain a more complete view in the field of interfacial adhesion.

Teknek cleaning process is designed for the removal of particles that derived from previous steps of processing or from the interaction with the environment. This type of particles is usually of irregular shape and different dimensions as depicted also in Figure 2.2. A perfect simulation of Teknek process will require the use of these 'real' particles however, the use of irregular particles is too complex, because it requires the characterization of every single particle used, in particular of the part of the particle that will be brought into contact with a surface. In addition, a lot of adhesion analyses will be necessary, in order to have a sufficiently large amount of data for the correlation between adhesion and particle morphology (and size). In addition, if the surface used for the measurement of adhesion is not smooth (as is the case in this work), much more data will be necessary. However, because the main interest is in studying the differences in interfacial adhesion of different kinds of surfaces, probably a so complex situation is not necessary. What is important to focus on in this work are differences between the use of different materials, while the influence of irregularities in the shape, dimensions and roughness of the particles surface can be removed. That is why, in this work, real particles are simulated by colloidal spheres with a certified diameter of 10 μm of two different types of materials: borosilicate glass and polystyrene divinylbenzene (PS-DVB or more simply, PS). The choice of these two materials was due to the fact that former is hydrophilic and the latter is hydrophobic: they are used as the representatives of these two classes of materials (hydrophobic ones and hydrophilic ones). In this way it is possible to see if the studied surfaces show different adhesion for these two classes of materials, and so, if they are more suitable for specific applications or not.

Samples provided by Teknek are 6 cleaning rollers and five sheets, mostly made of plastic and one with the core made of metal.

Rollers were provided as they are usually sold to customer, i.e. as a complete product: they consist of an internal metallic cylinder with an external layer of an

elastomeric material (that is actually the cleaning material that will be analysed). The diameter of the entire roller is about 3 cm and its length can be variable from 15 to 30 cm. The thickness of the elastomeric layer is about 5 mm. The six samples are, as indicated by Teknek: FilmClean, UltraClean, PanelClean, UTFClean, NanoUClean and NanoClean. According to information provided by Teknek, these samples should be considered as three couples: FilmClean and Ultraclean, PanelClean and UTFClean and, finally, NanoUClean and NanoClean. In each couple, one of the two materials is ground in order to increase the surface roughness; the other is not. This treatment of surfaces is only a physical process and it does not involve changes in the chemistry of the treated sample. The first couple (FilmClean and UltraClean) is based on PDMS and the two samples differ in moduli, fillers and surface roughness. In this couple, UltraClean is the ground sample. The second couple (PanelClean and UTFClean) is also based on PDMS and the only difference between the two elastomers is the surface roughness. In this couple, UTFClean is the ground sample. The final couple (NanoUClean and NanoClean) is based on polyurethane, and the samples differ only in the surface roughness (actually, it is like the previous couple, with the difference to be made of a different polymer). In this couple, the ground sample is NanoClean.

The five sheets have two different sides, that should be characterized individually, so, actually, they are ten different surfaces. The differences between the two sides of the same sheet can lie in a different type of roughness or a different treatment of surface that in turn can lead to different surface properties. These sheets were provided in squares with sides of about 20 cm and they were identified by a number; because they have two different sides, the complete 'label' for every samples is composed of the sample number followed by the number of the side (that can be '1' or '2'). Both the numbers of the samples and the sides were identified directly by Teknek. A short description of the samples was also provided by Teknek, thus:

- 'Sample 9' is a polypropylene (PP) based sample;

- 'Sample 18' is a polyethylene terephthalate (PET) based sample;
- 'Sample 19' is a polycarbonate (PC) based sample;
- 'Sample 24' is a polyimide (PI) based sample;
- 'Sample 47' is a PI-copper laminate. In 'Sample 47' the two sides were not identified by Teknek: 'side 1' and 'side 2' were identified by me (choosing as 'side 1' the side where the number 47 is written, as in all the other samples).

To summarise the nature of all the Teknek's samples, Table 3.1 lists names of samples with the corresponding materials of which they are made.

Name of the sample	Material
FilmClean	Polydimethylsiloxane based
UltraClean	Polydimethylsiloxane based
PanelClean	Polydimethylsiloxane based
UTFClean	Polydimethylsiloxane based
NanoUClean	Polyurethane based
NanoClean	Polyurethane based
Sample 9	Polypropylene based
Sample 18	Polyethylene terephthalate based
Sample 19	Polycarbonate based
Sample 24	Polyimide based
Sample 47	Polyimide-copper laminate

Table 3.1: List of Teknek's samples analysed in this thesis (names and materials).

In addition to samples provided by Teknek, five laboratory made samples were also prepared. These samples are made of an identical material, PDMS, and with the same procedure: the differences among them are related to the elastic modulus, crosslink density and, probably, viscoelasticity. These differences were obtained changing the length of the polymeric chains between crosslinks, using the same crosslinking procedure for the five PDMS samples. The procedure was designed in order to obtain smooth samples and to avoid influence of roughness on adhesion. The choice of using PDMS for the preparation of these smooth

samples was related partly to the materials used by Teknek (four rollers are made of PDMS) and partly because it is considered an ideal elastomer in the literature.

3.2 Plan of the research

The objective of this work, that is the study of the interfacial adhesion between a particle and a surface, with a particular attention to the Teknek process, requires not only the study of the adhesion force, but also the characterization of the surfaces used and the consideration of the experimental conditions that could affect the results.

The adhesion analysis was performed on all the samples: this analysis is quite simple to perform with an atomic force microscope (AFM), however, adhesion depends on many factors (as seen in the previous chapter), like, surface material, roughness, environmental conditions and sample characteristics. Thus, in order to obtain data that can be correctly correlated to specific features, attention should be paid to all factors that can have an influence on adhesion.

Starting from environmental conditions, force analysis can be done in liquid or in air. The advantage of performing it in a liquid environment is the removal of the effect of the capillary force. However, the Teknek process works in air, mostly under normal atmospheric conditions, where the influence of the capillary force cannot be excluded. A way to know if and how much the capillary force contributes to the total adhesion force is the study of adhesion in closed cells with the control of the relative humidity. This would also require specific tools: basically a closed cell, a relative humidity sensor and a way for creating the desired humidity inside the cell. However, the absence of some of these tools, together with the consideration that the capillary force is involved only if both the contacting surfaces are both hydrophilic (that are just few cases in this work) leads to a compromised solution. Adhesion analysis was performed in air, without control of the relative humidity, but in any case, the relative humidity was recorded by a sensor; comparing the recorded values with the evidence provided in the literature it is possible to

hypothesize as to whether the adhesion force is affected by the capillary force or not. To determine if a sample is hydrophilic or hydrophobic, a contact angle measurement is performed on all samples.

Another important factor to take into consideration is the roughness of a surface. This aspect is not so easy to evaluate, not only because the same quantification of it is not unambiguous (as it will explain later) but also because of instrumental issues. Roughness can be evaluated by optical microscope or by AFM. With the former the resolution is the lowest, while with the latter better details can be achieved. However, imaging analysis with AFMs is designed for planar samples, as it will be clear later, when the software for the analysis of those images will be presented. In this work, there are curved samples (the roller) as well as planar samples with surface features greater than the size of the analysis (so that, at the end, these samples cannot be considered 'planar' at the microscale). The issue in these cases is how to obtain a reliable value for roughness. Should the curvature of the roller be included or removed before determining the roughness? And in the case of imaging only a part of a big feature, which part of that image can be considered the reference plane from which that feature arises? If the presence of the curvature of samples extracted by the roller can be seen by looking at the raw image, it is very hard to find the reference plane from a surface with unknown features. For these reasons, all of the samples were imaged with both the AFM and the optical microscope. Roughness analysis is performed on the AFM images using the photos obtained by the optical microscope as indication of the surface features in order to process the raw images collected with the AFM as well as possible. Of course, considering the types of samples, it is not always possible to delete ambiguities in the processing of the AFM images, however they can be reduced and become acceptable.

Surface materials can also influence adhesion between two contacting surfaces. The choice of the materials to use in this work is related to the colloidal spheres embodying the particles to be removed from the surfaces. This choice was already discussed in the introduction to the samples: here, it is important to underline that

the same kinds of colloidal sphere were used for all the samples, in order to have comparable results. Adhesion on samples provided by Teknek was studied using both the materials presented, while for the laboratory made PDMS samples only the borosilicate probe was used. This was partly due to the difficulty to get the same results of adhesion with the polystyrene particles and partly because, on those samples, attention was focused on the change of adhesion related to the change of the sample properties. These changes will affect the adhesion in the same way and are not depending on the probe material. That is why, also only one probe material is considered sufficient, and, between the two, for the adhesion between borosilicate and PDMS there also more data available in the literature than for PS and PDMS.

The adhesion data collected from all the Teknek's samples are firstly discussed individually for each sample (with considerations about adhesion, morphology and hydrophobicity or hydrophilicity) and then used to verify with roller is able to remove a specific particle from the supplied sheets, taking into account equation 2.1.

As introduced in the previous section, the rollers in each couple at least differ by surface roughness: one of the samples in each couple is ground, and the other one is not. However, the non-ground samples are not sufficiently smooth at the micro- and nanoscale to be used as reference samples and the ground ones are often too rough to be accurately imaged, so, differences in adhesion between them can be mainly ascribed to the change in the roughness (because this is the dominant characteristic) than to other characteristics, such as a difference in the modulus. Thus, in this work, Teknek's rollers are mainly used to study the changes of adhesion that depend on the surface roughness. In order to explore if and how adhesion can change, considering the same type of polymer (that is, chemistry) but changing some other properties, a set of smooth, planar samples made of the same material (PDMS), where the differences among them are in the length of the polymer chain between crosslinks, was prepared. What is expected to change among these samples is the elastic modulus, the crosslink density, the softness, the

completeness of the reaction and the type of network, that could be more or less near to an ideal network. These last two aspects of the network can be related to the more or less elastic or viscoelastic behaviour of a sample. Special attention was paid in having these samples as flat as possible in order to remove the effect of roughness from adhesion. As for Teknek's samples, also these five PDMS samples were imaged with the AFM to check the surface morphology. The contact angle was determined as for all the other samples, in this case just to check it with values reported in the literature. Differently from all the others, these samples required the determination of the completeness of the reaction and an evaluation of the type of network in terms of elasticity or viscoelasticity. The former was done by performing the determination of the extractable fraction of PDMS, the latter by swelling measurements and DMA analysis. The extractable fraction lets the determination of the non reacted chains, which are removed from the polymer bulk by the swelling solvent. DMA analysis lets the determination of the storage and loss moduli (together with the phase lag) which gives an indication of the elastic or viscoelastic behaviour of a polymer. Both swelling and DMA are also able to give information about the crosslink density: this is a further characterization of networks, because it provides an indication of how many elastic strands there are per unit volume and how long they are.

In conclusion, for sake of clarity, the plan of the analyses is summarized. The rollers provided by Teknek were used to see how adhesion is influenced by the roughness, while the other samples provided by Teknek (sheets) were used to know if they can be cleaned by the rollers, so actually to test the efficacy of the rollers. Laboratory made PDMS samples were used to study how adhesion is influenced by factors other than the chemistry, such as moduli, crosslink density, viscoelasticity....

Optical microscope images and contact angle determination were performed on all samples. These two experiments are important to have an idea of how to elaborate the raw AFM images in order to get the roughness and to know if the capillary force could influence the adhesion force, respectively. Swelling and DMA analysis were done only on the laboratory made PDMS samples for a better characterization of

these networks, that means an estimation of: the reaction completeness, the quality of the networks and their elastic or viscoelastic behaviour. Imaging and adhesion analysis with the AFM were done on all samples, even if with some differences between the samples provided by Teknek and the laboratory made PDMS samples. Specifically, Teknek's samples were imaged more times, and adhesion was determined with two different colloidal probes, while the other samples were imaged fewer times and adhesion was tested only with one colloidal probe, the borosilicate one. These differences were done because with Teknek's samples the aim was to investigate the differences of adhesion toward two different types of probes. In addition, because the important roughness of those samples could affect the precision of data, more repetitions were necessary. On the contrary, in the case of PDMS samples, the focus was on adhesion behaviour (and so a single probe is sufficient) and the samples smoother surfaces do not require many repetitions of the test to have a good precision.

3.3 Samples materials

In this section, general chemical and physical characteristics of the materials involved in this research are presented. Also the synthetic procedure for the laboratory made PDMS samples is presented in this section.

3.3.1 Polydimethylsiloxane (PDMS)

Polydimethylsiloxane or PDMS is a polymer belonging to the group of silicones. It is considered an organo-inorganic polymer because it has an inorganic backbone made of a succession of silicon and oxygen atoms and organic methyl pendant groups bonded to the silicon atoms [124] as sketched in Figure 3.1. PDMS can be an oil, when it is formed from only linear chains, or it becomes a rubber, when a crosslink reaction is performed. In both forms, PDMS is widely used for many applications and in many fields: for example, it is used in the cosmetics and pharmaceutical industry, mainly with the name of dimethicone, in the prosthesis industry (for example as retinal prosthesis), and in the electronic industry. Silicones

are appreciated in so many fields because of their peculiar properties like, for example, a low glass transition temperature, a high temperature and chemical resistance, low surface energy, hydrophobicity, good elastic properties, good biocompatibility, transparency and softness. Chemical and physical properties of PDMS that are relevant for this work are reported in Table 3.2.

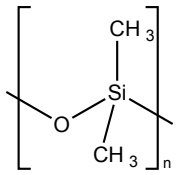

Figure 3.1: Sketch of the structure of linear PDMS. The part into brackets is the repeating unit.

In this thesis, the laboratory made PDMS samples were prepared starting from linear vinyl-terminated PDMS chains and performing the crosslinking using the hydrosilylation reaction with Karstedt's catalyst. Five different lengths of chain, expressed as molar mass, were used: 6000, 9500, 17000, 27500, 42500 g/mol (these masses are actually the average values of the mass ranges declared by the producer). PDMS samples were named according to their averaged molar mass and so PDMS-6K, PDMS-9.5K, PDMS-17K, PDMS-27.5K and PDMS-42.5K, respectively. Polymers were supplied by Fluorochem, a Gelest distributor, and used as received. The other reactants were: the four-functional crosslinker was tetrakis(dimethylsiloxy)silane (Sigma-Aldrich, used as received), the catalyst was Karstedt's catalyst (solution in xylene with 2% in platinum, supplied by Sigma-Aldrich and used as received) and dimethyl maleate as inhibitor (Sigma-Aldrich, used as received).

Property (units)	Symbol	Value	References
Contact angle (°)	θ_Y	95-113	[10]
Surface energy (mJ/m^2)	γ	22.8	[19]
Surface energy polar contribution (mJ/m^2)	γ^p	1.1	[10]
Surface energy dispersion contribution (mJ/m^2)	γ^d	21.7	[10]
Hamaker constant (J)	A_H	4.4 x 10^{-20} 6.4 x 10^{-20}	[125] [126]
Flory-Huggins polymer-solvent interaction parameter in toluene (constant single value)	χ	0.465	[127-129]
Flory-Huggins polymer-solvent interaction parameter in toluene (constants values – first order equation)	c_1 c_2	0.445 0.297	[130]
Flory-Huggins polymer-solvent interaction parameter in toluene (constants values – second order equation)	c_1 c_2 c_3	0.459 0.134 0.59	[131]
Poisson coefficient	ν	0.5	[128]
Glass transition temperature (°K)	T_g	150	[128]
Elastic modulus (MPa)	E	0.05-1	[124]
Viscoelastic dissipation function exponent values	n	0.36 0.38-0.4 0.5 0.68	[132] [57] [55] [56]

Table 3.2: Main physical and mechanical properties of PDMS reported in the literature. Many values of the viscoelastic dissipation function exponent are reported because there is not agreement in the literature about it.

Referring to the introduction at this reaction done in the previous chapter, it is clear that the conditions of this reaction should be optimised, due to the lack of a unique recipe in the literature and the specific needs of this work, which require a flat and smooth surface for the following analysis.

Because we are interested in the surface, the minimum number of reagents were used, in order to avoid their influence on the measured properties. Thus, the reaction was performed without solvent (except for the catalyst solution); attempts

were made to avoid the use of the inhibitor, however, because of the fast rate of the reaction at room and low temperature (it takes from seconds to few minutes after the addition of the catalyst to be quite complete, not allowing a good mixing of the reactants), the inhibitor should be used. The inhibitor chosen was dimethyl maleate and its quantity was evaluated by performing different tests with different quantities of it: it was found that the quantity of inhibitor is a critical factor. In fact, the more the used inhibitor is, the softer and stickier the elastomer results. Thus, the quantity of inhibitor should be as little as possible to ensure the production of a good sample and a reasonable shelf-life of the solution of reactants. On this basis, the stoichiometry used was:

- a ratio of 1:1 of vinyl group/Si-H group;
- 5 ppm of platinum over the weight of the previous reactants (the quantity of Karstedt's catalyst is calculated on the necessary amount of platinum);
- 0.017% w/w of dimethyl maleate as inhibitor.

Typical used quantities were: 30 g of the chosen linear vinyl-terminated PDMS, from 0.13 ml to 0.93 ml of tetrakis(dimethylsiloxy)silane (according to the PDMS chain length), 8.88 μl of the solution of the catalyst and 4.32 μl of dimethyl maleate. Reaction conditions and stoichiometry are reported in Figure 3.2.

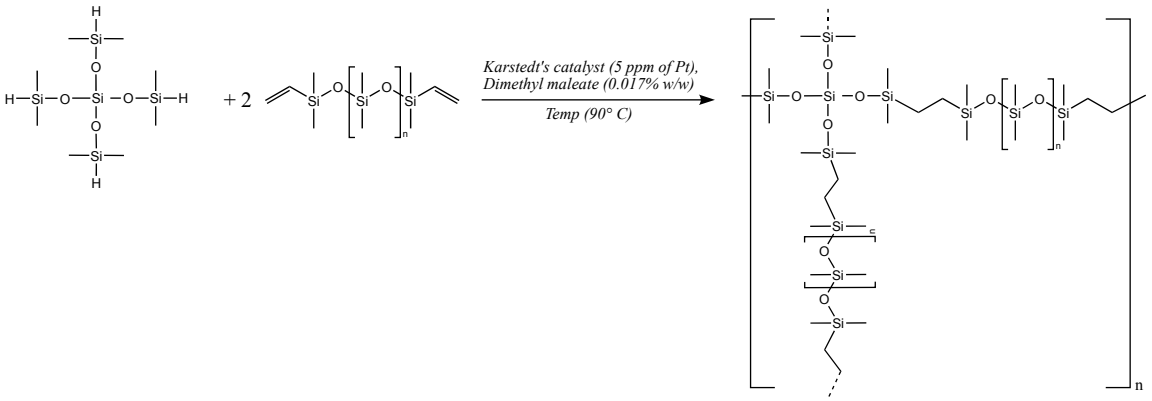

Figure 3.2: Reaction conditions and stoichiometry used for the hydrosilylation reaction in this thesis. Dashed bonds should be considered as single bonds with another repeating unit.

Apart from the stoichiometry of the reaction, also the other reaction conditions should be optimised, such as the role of oxygen, the order of adding reactants, time, temperature and container for the reaction. Moreover, an important point was to assure the repeatability of the samples with the same surface quality, which was a difficult target, considering that small changes in the inhibitor quantity can lead to samples with different surface characteristics and the very small amount of inhibitor used. In other words, due to the fact that the quantity of the inhibitor is very small, also a little imprecision in that is a significant difference in percentage.

Some tests were also performed to evaluate the influence of oxygen, and it was found that it increases the rate of the reaction, in comparison to samples prepared in the same way, but under nitrogen.

Considering the viscosity of the linear PDMSs, the limited miscibility of the inhibitor with the PDMS and the rate of the reaction in absence of the inhibitor (or when it is not well dissolved and mixed with the PDMS), the best order of addition of the reagents is: PDMS, inhibitor, catalyst and finally the crosslinker. At each addition of a reactant, the solution should be mixed in order to assure a good dissolution of it in the PDMS matrix. However, a solution prepared in this way is stable for not more than two weeks in a fridge, and this prevents the preparation of a large batch to use as needed, to reduce the possibility of imprecision in the addition of the inhibitor. To fix this, a solution similar to the one used for the commercial pack of crosslinkable PDMS was used: two different solutions of linear PDMS were prepared, where the first one contains also the catalyst, and the second one the inhibitor with the crosslinker; both of them were stirred overnight to assure a good dissolution of reactants in the PDMS matrix. The two solutions are stable till they are mixed together. So, they could be prepared also in a big amount, reducing the possibility of imprecisions. The quantities of reactants were calculated in the way to obtain the stoichiometry described above mixing the two solutions in the ratio of 1:1. Once the two solutions were added, they were stirred overnight, again for assuring a good dissolution of reactants in the PDMS matrix.

Tests with different temperatures and times were performed, which revealed that two hours at 90°C assured that the reaction reached completion.

Finally, the crosslinked PDMS is required have a smooth, planar and non-contaminated surface: this means that it should be cast in a suitable mould, without the aid of a releasing agent. To fix this issue, Teflon or acetal copolymer (POM) moulds were found to be effective in allowing samples to be removed easily. In addition, PDMS has a high thermal expansion coefficient that causes it to shrink and, at the same time, to be thicker along the edges when brought back at room temperature after the reaction. To overcome this problem, the moulds used have larger dimensions than necessary, allowing the removal of the edge without reducing the size of the sample too much. Three different types of moulds were used: two laboratory made Teflon ones and a commercial SamplKups (Buehler) made of POM. The Teflon moulds have two shapes: disks with a diameter of 13 mm and a rectangular shape of 2 x 4 cm^2. Disks were used for samples of which studying the adhesion, while the rectangular sheet was used for the determination of the contact angle. SamplKups moulds are circular with a diameter of 50 mm: they were used for casting the samples to analyse with the dynamic mechanical analysis (DMA). In all cases, the thickness of samples is 2 mm and the edges were removed before each analysis. Some of those edges were used for the swelling and extractable fraction measurements.

In conclusion, the optimised conditions were:

- the preparation of two solutions of linear PDMS, the first one containing the catalyst and the second one containing the crosslinker at the required concentrations together with the inhibitor;
- these two solutions were stirred overnight to assure a good dissolution of the reactants in the PDMS matrix;
- once the two solutions were added in a ratio 1:1, the resulting solution was stirred overnight, again for assuring a good dissolution of the reactants in the PDMS matrix;

- this solution was then put into the mould and then heated for two hours at 90°C under atmospheric condition;
- when the reaction was complete, samples were carefully removed from the mould, placed on glass slides and carefully served in a closed box for the following analyses.

3.3.2 Polyurethane (PU)

Polyurethane or PU is a large class of polymers, whose repeating unit is characterized by the presence of the urethane group, as sketched in Figure 3.3.

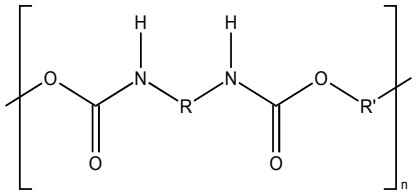

Figure 3.3: Sketch of the structure of repeating unit of polyurethane polymers. R and R' may be different organic fragments.

Polyurethanes are largely used as foams (flexible or rigid) and as elastomers: as foams, their main application is protective packaging and thermal insulation, while as elastomers, polyurethane are used as adhesives, water-line tubings and in the textile industry [128]. Some chemical and physical properties of polyurethane elastomers are reported in Table 3.3.

Property (units)	Symbol	Value	References
Contact angle (°)	θ_Y	89	[128]
Surface energy (mJ/m^2)	γ	21	[128]
Glass transition temperature (°K)	T_g	200 - 250	[128]
Elastic modulus (MPa)	E	3 - 600	[133]

Table 3.3: Main physical and mechanical properties of polyurethane elastomer reported in the literature. Elastic modulus range is so large because it includes most of the types of polyurethane polymers.

3.3.3 Polypropylene (PP)

Polypropylene is a widely used thermoplastic polymer. It derives from propylene, from which it takes the name, even if in its repeating units does not have any double bonds, as the ending of its name may suggest (Figure 3.4). Because in the repeating unit of this polymer there is a stereocenter, there are different types of polypropylene polymers: they do not usually differ for chemistry but for the relative stereochemistry of the side chain methyl groups. Briefly, polypropylene can be atactic (if the stereochemistry of the methyl groups along the chain is random), syndiotactic (if the methyl groups are on both sides of the polymer chain in an alternate fashion) or isotactic (if the methyl groups are all placed on the same side of the polymer chain). To these different arrangements correspond different physical and mechanical properties, related to how the polymer chains can arrange themselves in the solid state (types and numbers of inter- and intra-molecular interactions).

Polypropylene is mainly used for fibres, films, automotive interior trim, appliance housings and components [128].

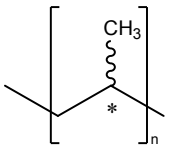

Figure 3.4: Sketch of the structure of repeating unit of polypropylene. Different types of PP have the side chain methyl group with different stereochemistry.

Some of the physical and mechanical properties of isotactic polypropylene (the most widespread) are listed in Table 3.4. The only exception is for the elastic modulus, that refers to syndiotactic polypropylene: however, in this work, the interest is mainly in the magnitude rather than in the real value of the elastic modulus.

Property (units)	Symbol	Value	References
Contact angle (°)	θ_Y	116	[128]
Surface energy (mJ/m^2)	γ	29.0	[128]
Glass transition temperature (°K)	T_g	275 - 284	[128]
Elastic modulus (MPa)	E	483	[128]

Table 3.4: Main physical and mechanical properties of polypropylene reported in the literature.

3.3.4 Polyethylene terephthalate (PET)

Polyethylene terephthalate is the most common and used polymer belonging to the class of polyesters. It is characterized by the presence of a specific repeating unit (Figure 3.5).

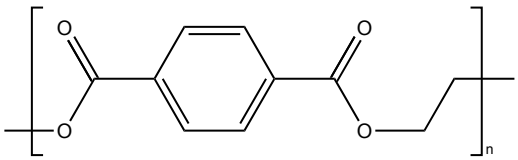

Figure 3.5: Sketch of the structure of repeating unit of polyethylene terephthalate.

This polymer is extensively used in form of films and fibres [134]. It is transparent, with good mechanical and barrier properties and for that it is largely used in food industry as packaging material [128]. Because of the large amount of this resin produced every year and the possibility to obtain items with good quality from recycled PET, many efforts have been devoted to study its reuse and recycling in recent years [135, 136]. Some of its physical and mechanical properties are reported in Table 3.5.

Property (units)	Symbol	Value	References
Contact angle (°)	θ_Y	76 - 82	[19] - [137]
Surface energy (mJ/m^2)	γ	41 - 42	[20]
Glass transition temperature (°K)	T_g	342 - 388	[128]
Elastic modulus (GPa)	E	1.7	[128]

Table 3.5: Main physical and mechanical properties of polyethylene terephthalate reported in the literature.

3.3.5 Polycarbonate (PC)

Polycarbonate is a group of polymers that belongs to the class of polyesters: its repeating unit is characterized by the presence of the carbonate group (Figure 3.6).

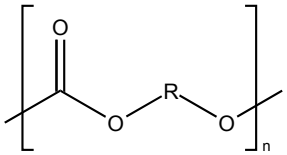

Figure 3.6: Sketch of the structure of repeating unit of polycarbonate (R stands for an organic fragment).

Polycarbonate polymers are highly transparent and they have an excellent impact resistance together with a good thermal stability. They are usually used for lens or for break resistance windows (or protective equipments that require high transparency). Some of their physical and mechanical properties are reported in Table 3.6.

Property (units)	Symbol	Value	References
Contact angle (°)	θ_Y	78 – 81.7	[138] - [139]
Surface energy (mJ/m^2)	γ	42.9	[128]
Glass transition temperature (°K)	T_g	423	[128]
Elastic modulus (GPa)	E	2.38	[128]

Table 3.6: Main physical and mechanical properties of polycarbonate reported in the literature.

3.3.6 Polyimide (PI)

Polyimides are a high-tech and high-performance class of plastic with high thermal radiation, moisture and chemical resistance [140]. In addition, polyimides also have high mechanical strength and optical transparency [141]. The repeating unit is reported in Figure 3.7.

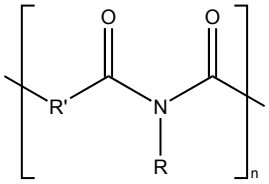

Figure 3.7: Sketch of the structure of repeating unit of polyimide polymers. R and R' may be different organic fragments.

Because of their properties, polyimides are used in many fields where high resistance is required, for example, in medical devices, composites, fuel cells and nanomaterials [140, 141]. Some of their physical and mechanical properties are reported in Table 3.7.

Property (units)	Symbol	Value	References
Contact angle (°)	θ_Y	70	[142]
Surface energy (mJ/m^2)	γ	41.0	[143]
Glass transition temperature (°K)	T_g	425 – 602	[144]
Elastic modulus (GPa)	E	1.5 – 3.0	[140]

Table 3.7: Main physical and mechanical properties of polyimides reported in the literature.

3.3.7 Copper (Cu)

Copper is just quickly introduced because one of the sample is a polyimide copper laminate: its core is made of copper, covered by a thin transparent film of polyimide. Copper is a ductile, high reflective metal with high thermal and electrical conductivity. Because of this structure, that sample shows the same appearance of a copper foil (if colour and mechanical behaviour are considered) however, it is expected its surface properties should be the same of polyimide (that are reported Table 3.7).

3.3.8 Polystyrene divinylbenzene (PS-DVB)

Polystyrene divinylbenzene is actually a crosslinked polystyrene: it derives from styrene, but this molecule cannot create crosslinks because its functionality is two. For that reason, a certain quantity of divinylbenzene is added as co-monomer and crosslinker. The repeating unit of PS-DVB is depicted in Figure 3.8.

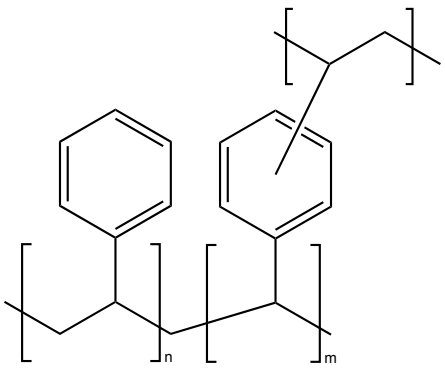

Figure 3.8: Sketch of the structure of repeating unit of polystyrene divinylbenzene.

It is used as material for resins or porous particles. Crosslinks improve the mechanical properties and the chemical resistance of polystyrene (PS). Some of the physical and mechanical properties of this polymer are listed in Table 3.8. For the contact angle and surface energy, the same values found for linear polystyrene are reported because the crosslinks are considered not to be able to vary the surface properties (mainly for two reasons: the small quantity of the copolymer and its chemistry which is quite similar to that of styrene).

Property (units)	Symbol	Value	References
Contact angle (°)	θ_Y	84 - 91	[145] - [20]
Surface energy (mJ/m^2)	γ	39.3 – 40.7	[128]
Glass transition temperature (°K)	T_g	376 - 401	[146]
Elastic modulus (GPa)	E	1.5	[147]

Table 3.8: Main physical and mechanical properties of polystyrene divinylbenzene reported in the literature (contact angle and surface energy are referred to non crosslinked polystyrene).

3.3.9 Borosilicate (glass)

Borosilicate is a particular type of glass, that contains boron, that has low coefficient of thermal expansion and a good resistance to chemicals. This is the only material studied in this work that is not organic (except for copper). Some of physical and mechanical properties of borosilicate glass are reported in Table 3.9.

Property (units)	Symbol	Value	References
Contact angle (°)	θ_Y	26.8	[148]
Surface energy (mJ/m^2)	γ	67.5	[148]
Surface energy polar contribution (mJ/m^2)	γ^p	33.6	[148]
Surface energy dispersion contribution (mJ/m^2)	γ^d	33.9	[148]
Hamaker constant (J)	A_H	6.5 x 10^{-20}	[149]
Elastic modulus (GPa)	E	64	[150]

Table 3.9: Main physical and mechanical properties of borosilicate glass reported in the literature.

3.4 Techniques and equipment

3.4.1 Cleaning procedures

All the samples provided by Teknek were cleaned before each analysis, according to the cleaning procedure provided by the company. Firstly, particles were removed using an adhesive paper provided by Teknek, then, other contaminants like grease, were removed washing the surfaces with isopropyl alcohol.

Laboratory made PDMS samples did not undergo to any cleaning procedure, but they were analysed a short time after their preparation and always stored in sealed boxes.

All samples were checked with the optical microscope before each analysis.

3.4.2 Optical microscopy

Optical microscopy is used to have a first glance to the surfaces that will be later analysed with the AFM. In this case, it is used in a qualitative way, just to have an idea of the roughness or curvature of a surface.

An optical microscope, sometimes called a light microscope, is a microscope that uses light and lens to magnify small details of a sample. There are different types of

optical microscopes, optimized for different uses in different fields of science (from biology to geology, for instance). Roughly, they can be distinguished according to the type of illumination of the sample and the available magnifications. For example, for transparent samples, the transmission mode is usually used, while for non-transparent samples, the reflection mode is required. In the first case, light passes through the sample and then is collected by lens, while in the second case, light is reflected by the sample surface. The magnification is the ratio between the apparent size and the real size of the sample: it is a positive dimensionless number when the apparent size is bigger than the real size. The magnification of an optical microscope is obtained by the power of the ocular (or eyepiece) times the power of the objective lens. Ocular and objective lens can be changed according to the type of the experiment: typical values for the ocular lens are from 1X to 10X, while objective lens can vary from 10X to 100X. However, resolution should be also taken into account: it is the smallest distance between two resolved points of the surface of the sample. There is not a unique formula for the resolution in optical microscopy: in any case, resolution is proportional to the wavelength of the radiation used and it is inversely proportional to numerical aperture (that depends on the diffraction index of the medium and the half-angle of the cone of light that comes inside the lens). Usually, in air, resolution cannot go beyond 200 nm. That is why optical microscope should be calibrated with a reticle, that is a transparent ruler that is superimposed on the image of the sample and that should be calibrated for each magnification.

The optical microscope used in this thesis is a Nikon Eclipse ME600, equipped with a PixeLINK camera to take pictures of the magnified images. PixeLink software version 1.4.6.12 was used for images evaluation. A scheme of a similar optical microscope is reported in Figure 3.9.

The nominal objective lens magnifications used are 20X, 50X and 100X (in some specific cases, also 5X and 10X were used, too). All samples were imaged in reflection mode using non-monochromatic visible light. A qualitative calibration

was done using three images of certified particles with 10 μm of diameter for each magnification and using the same scale for the images of samples.

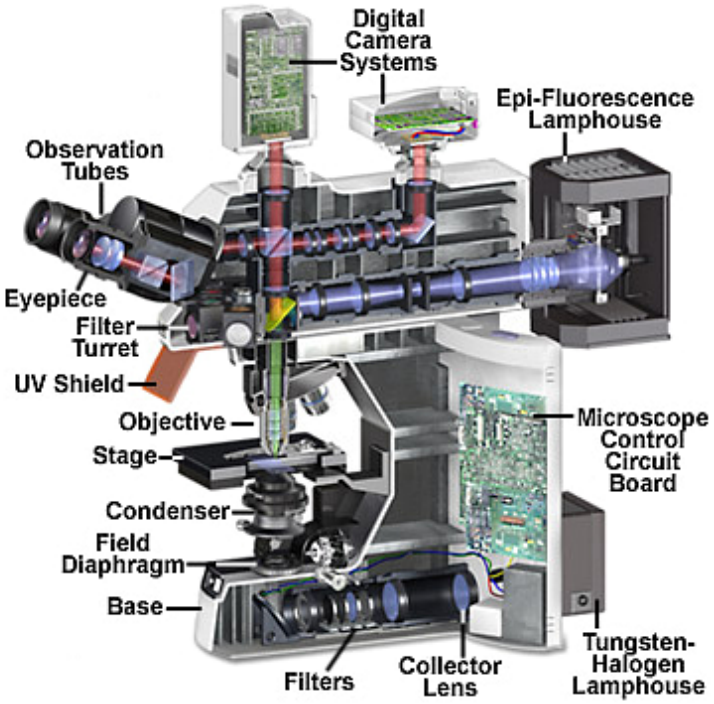

Figure 3.9: Scheme of a Nikon Eclipse series microscope. Image adapted from [151].

Images were taken of the same samples used for the adhesion force or contact angle determination: all samples were cleaned according to the previously described procedure before being imaged. Some difficulties arose from curved samples at high magnification: in this situation, due to the surface curvature, only the central region of the image could be focused well. A similar situation happened also with very rough surfaces: at the highest magnifications, only upper or lower details could be focused separately, but not together in the same image. On the other hand, images of very flat, smooth and transparent samples were discarded because they were not considered significant.

3.4.3 Contact angle determination

In this thesis, the contact angle is mainly a qualitative determination, firstly because some sample surfaces have curvature, and the effort to get them planar was not totally fulfilled. Secondly, some surfaces were not smooth enough to provide satisfactory results and the corresponding smooth samples made of the same materials were not available. Thirdly, the interest in the contact angle determination is just to know if a surface is hydrophobic or hydrophilic, to know if the capillary force could have a role in the found adhesion force.

For the determination of the contact angle, optical contact angle meters, or tensiometers or goniometers are used. They are composed by a flat stage where the sample is placed, a micrometer syringe for the drop formation and deposition and an optical system to capture the profile of the drop on the flat surface of the sample. In modern instruments, the determination of the contact angle is made by the software after the collection of a series of magnified photos of the profile of the same drop.

The tensiometer used in this thesis is an Attension Theta Lite (by Biolin Scientific), equipped with a Hamilton micrometer syringe (1000 µl). Instrument accuracy is reported to be 0.1° for contact angle. The software OneAttension version 4.1.0 was used to collect photos and to perform the determination of the contact angle. Before each run of measurements, the stage was checked to be horizontal with a level and calibration of the magnification of the camera was performed using a 4 mm metal calibration ball (Biolin Scientific calibration kit) placed in the place of the drop. A scheme of the Attension Theta Lite instrument is depicted in Figure 3.10.

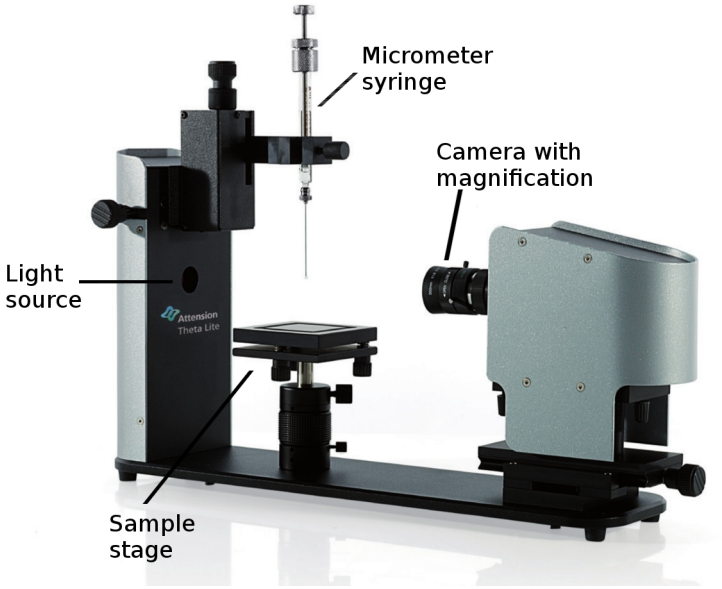

Figure 3.10: Schematic diagram of an Attension Theta Lite optical tensiometer. Image reprinted and adapted from the website of the manufacturer (https://www.biolinscientific.com/attension/optical-tensiometers/theta) in 2014, Copyright, with permission from Biolin Scientific Group.

For the contact angle measurements, samples provided by Teknek were cut into strips (with a width of at least 1 cm and a length of at least 4 cm), while laboratory made PDMS samples were directly cast as strips of 2 x 4 cm^2. All the samples provided by Teknek were cleaned according to the aforementioned cleaning procedure before the measurement: to avoid influences on the measurements, at least ten minutes were waited before starting the analyses, with repetitive measurements at different times. The laboratory made PDMS samples, for which a cleaning procedure does not exist, were analysed in less than 24 h from the synthesis, in order to avoid surface contamination. Only static contact angle was determined, thus, the sessile drop method was used. According to this method, a drop of Milli-Q water was set down on the sample, using the micrometer syringe and then, after a short time to ensure that the system is static, usually 200 pictures of the drop were taken. After that, on the first picture, the position and the tilt of the baseline were checked and then the calculation of the contact angle was performed. The method used for the contact angle determination is based on the Axisymmetric Drop Shape Analysis (ADSA) [21], which is a group of methods based

on different equations for the recognition and fitting of the profile of the drop. From the picture of the drop, its profile is extracted and a specific equation is then used to fit it in the best way, using one or more adjustable parameters. In this thesis, the Young-Laplace fitting method is used for all samples: in this case the extracted profile is fitted using the Young-Laplace equation with the surface tension as an adjustable parameter (equation 2.36). The best fit is then used for the calculation of the contact angle. The software determines the right, the left and the average contact angle: in this work, the average angle is used. To work well, the Young-Laplace method assumes that the drop has a Young-Laplace profile and it is axysimmetric: that is why, in the case of not flat surfaces, the contact angle becomes qualitative.

3.4.4 Young's modulus, storage and loss moduli, crosslink density and extractable fraction determinations

All these measurements are dealt together because they can be obtained by the same analysis. For example, the Young's modulus can be used for the determination of the crosslink density (and viceversa) and thus, techniques useful for the determination of the modulus can be used to get also the crosslink density. However, these different techniques can also allow the determination of specific parameters other than the Young's modulus: for example the storage and loss moduli or the extractable fraction. In this thesis, two techniques were used for the determination of the crosslink density (or the Young's modulus) and one of these also lets the determination of the extractable fraction, while the other lets the determination of the storage and loss moduli. All these properties are interesting for a complete characterization of the laboratory made PDMS samples: extractable fraction is useful to know how much the crosslink reaction is complete, crosslink density and the Young's modulus are important bulk properties for network characterization, storage and loss moduli can inform of elastic/viscoelastic behaviour.

There are two ways that are often used for the determination of the crosslink density: using the Young's modulus or the determination of the swelling in a good solvent. At the beginning, attempts were made to find the Young's modulus determining it with the tensile test, however this determination is not straightforward. This type of test is commonly used in companies for the determination of the Young's modulus and it is described in details in many ISO and ASTM standards (like for examples, ISO 527-1, ISO 527-2, ASTM D 638 for plastics, ISO 37 for rubber and elastomers and others, restricted to specific types of materials, like polymer composites). It requires the use of the tension machine and, in particular, a sample with a specific shape and dimension. That is due to this test being very sensitive to small variations both in the sample dimension (and shape) and in parameters used for the measurement (such as the speed of application of the stress). There is also an influence in the way the sample is prepared, especially for polymeric materials, so that the standards specify also the method of preparation and the range of temperature and time to be used in each step of the preparation. The requirements for the sample shape and dimensions are the same for different polymeric materials. For this kind of material a shape of a dogbone with specified dimensions and thickness is the most used. Attempts were made in the laboratory to cure PDMS samples in a dogbone shape: the worst issue to face with was to ensure that samples can have the same height in each position. Attempts were made to cure the PDMS in a dogbone Teflon mould using different procedures (for example, using different heat sources, with and without lubricants to improve the removal of the sample from the mould without breaking it, with and without a lid to counteract thermal expansion), but it was impossible to ensure that the sample has the same thickness in each position, due to the thermal expansion and shrinkage during and after the cure, respectively.

Because of all these issues, it was thought to determine the shear modulus with the DMA and then to convert it into the Young's modulus using equation 2.3. However, four different laboratories were involved in this analysis and only one could provide results for these samples. It was found that, because they are so soft

and deformable, only the laboratory that have a rheometer suitable not only for solids, but also for viscous fluid could grip well these samples without deforming or breaking them during the measurements. The advantages of DMA are that a smaller strain than in tensile test is required (and so test conditions are more similar to those of the adhesion analysis) and also the loss modulus and the phase lag are found in same experiment.

The instrument used was a ReoStress RS100 by Haake Fisons with the parallel plate geometry, using circular serrated plate with a diameter of 20 mm. The gap between the plates was in the range of 1.75-1.90 mm and the contact between the plates and the sample was verified every time before the measurement. To determine which was the most suitable load for the analysis, a stress sweep test on two samples, PDMS-9.5K and PDMS-42.5K (the former synthesized with short linear chains and latter with the longest linear PDMS) was performed, starting from 10 Pa to 100 Pa and incrementing the load of 4.74 Pa at each step. DMA analysis was finally done on all samples in frequency sweep mode with 24 steps in the frequency range from 10^{-2} rad/s to 10^{2} rad/s and an applied load of 50 Pa. In order to have a sample with constant thickness in the region between the two plates, avoiding the problems of thermal expansion and shrinkage during and after the cure, disks of a greater diameter (50 mm) than that was necessary for the DMA were prepared. In this way, the DMA analysis could be performed in the central part of the disks, where the height was constant and nominally of 2 mm.

Because it was not so straightforward to measure the Young's modulus of PDMS, and, in fact, it was the last analysis to be successfully performed because of all the described difficulties, also the determination of the swelling of PDMS samples in a good solvent was used. This was easier to perform and it was done after the first failed attempts of getting the Young's modulus with the tensile test. Swelling can be based on the determination of the change of volume or weight of the sample in two steps: after the swelling (so when the sample is swollen by the solvent) and at the end, when the swelling solvent is removed. In this thesis, the determination based on weight was used. In fact, the volume fraction of the

polymer in the swollen state φ_2 used in equation 2.12 and 2.13 is the reciprocal of the degree of swelling Q

$$\varphi_2 = Q^{-1} \tag{3.1}$$

and can be calculated from experimental quantities, according to

$$Q = \frac{V_{sw}}{V_f} = 1 + \frac{V_{sw} - V_f}{V_f} = 1 + \frac{m_{sw} - m_f}{m_f} \frac{\rho_p}{\rho_s}, \tag{3.2}$$

where V_{sw} is the volume of the sample in the swollen state, V_f is the final volume of the sample, m_{sw} is the mass of the sample in the swollen state, m_f is the final mass of the sample, ρ_p is the density of the polymer and ρ_s is the density of the solvent. Then, using equations 2.12 or 2.13-2.14 and 2.11, the molecular weight between crosslinks can be determined. To use equation 3.2, m_{sw}, m_f, ρ_p were determined experimentally, while ρ_s was taken from solvent properties provided by the manufacturer. For the determination of the density of the polymer a Brand BlauBrand liquid pycnometer was used, with a certified volume of 5.0079 cm^3 and an uncertainty of ± 0.0100 cm^3 (data provided by the manufacturer). A Sartorius Research R160P analytical balance was used for the weights determination.

The procedure used for the determination of the crosslink density is the following: a piece of the polymer was soaked in toluene for 48 h in order to reach swelling equilibrium, then it was extracted and the excess of solvent removed before being weighed (this is the m_{sw} determination). After that, it was dried under vacuum at room temperature for 24 h and finally weighed again (this is the m_f determination). A critical point of procedures for the crosslink density determination is the weighing in the swollen state: to have a correct measurement, the swollen sample should be weighed with the equilibrium solvent that swells it. However, this is quite difficult because solvent can be in excess (because the sample is wet also on the surface), or at fault because solvent has started to evaporate on the surface. In this work, the pieces removed from the solvent were gently dried with a nitrogen flow and, when the excess of solvent was removed from all their surfaces, they were immediately weighted. In any case, it was noted

that, even if toluene is not a volatile solvent, when the weighing of the same piece was repeated twice, the second time its weight was always less than the first time, meaning than solvent evaporation was quite fast.

The procedure for the determination of the density of the polymer was the following: first, the pycnometer full of water was weighed, then the sample was added on the scale stage and the weight of the pycnometer full of water plus the sample was recorded. After that, the sample was inserted inside the pycnometer letting the same volume of water going out of it: the pycnometer with water and the sample inside was weighted. From these three weights it is possible to get the weight of the sample and the weight of the volume of the removed water. In fact, from the difference between the third and the second weights the weight of the removed water is obtained, while from the difference between the second and the first weights the weight of the sample is known. Knowing the temperature, it is possible to relate the weight of the removed water with its volume and so, to know the volume of the sample. From the volume and the weight of the sample it is straightforward to find the density of it.

The extractable fraction is the fraction of chains that are removed when a sample is immersed in a good solvent: the extracted polymer chains are those that did not react during the crosslink reaction. The greater the extractable fraction is, the less complete was the crosslink reaction and so the network shows more imperfections.

The procedure for the determination of the extractable fraction of polymers is quite straightforward: it requires weighing the sample before swelling and after the complete removal of the swelling solvent. In this thesis, the extractable fraction was determined on the same samples used for crosslink density determination: they were weighed also before the immersion in the toluene (initial weight m_{i}). The extractable fraction W_{ext} is calculated according to

$$W_{\mathrm{ext}}(\%) = \frac{m_{\mathrm{i}} - m_{\mathrm{f}}}{m_{\mathrm{i}}} \times 100 \tag{3.3}$$

The advantage of the extractable fraction is that the method is robust because samples are in stable states during the two measurements. On the other hand, the crosslink density is an interesting parameter because it is related to the chain length between two crosslinks, but it is more difficult to have a reliable measurement of it and it should be considered as qualitative. Moreover, because the swelling of a polymer in the solvent is also ruled by imperfections and heterogeneities which avoid the complete stretching of chains, like loops and physical entanglements, the experimental crosslink density is influenced also by these imperfections, so it gives the averaged 'real' chain length in the network.

3.4.5 Surface and force analyses: introduction to the AFM

Surface and force analyses are the core of this thesis and they are both performed by AFM. The advantage of the AFM over optical microscopy for surface analysis is related to the better resolution of small details: with an AFM nanoscale and also sub-nano scale details are well determined, while an optical microscope usually provides information in the microscale region. And, for the force analysis, the advantage of using an AFM over other techniques (like Surface Force Apparatus, also SFA, or the JKR apparatus) is related to a better versatility in the force range, types of sample (both for material and shape) and to the possibility to linking together the image of a surface with the adhesion force at any point.

The operating principle of an AFM is quite straightforward: a microlever (cantilever) with a sharp or shaped tip at the end is used to scan or to test a surface. When the tip is next to the surface, or in contact with it, it is able to detect surface forces or to track the outline of a surface. Both the surface forces and the height profile of a surface cause a deflection of the cantilever: in the case of attractive force or pores on the surface, the cantilever bends downwards, while in the case of repulsive force or high feature on the surface, it bends upwards. The position of the cantilever is determined with an optical system: a laser beam is focused on the back of the cantilever and, from there, it is reflected on a photo-detector. This is usually a split photo-diode: it is split in four quadrants (usually called A, B, C and D) to let

both the vertical and horizontal movements of the cantilever be known. Relative movements of the cantilever and the sample are driven by the piezo-actuator or scanner according to the settings of the experiment, the position of the reflected beam from the cantilever on the photo-diode and a feedback loop. To fully understand this, some other details about the structure of an AFM are needed. A schematic diagram of an AFM is reported in Figure 3.11.

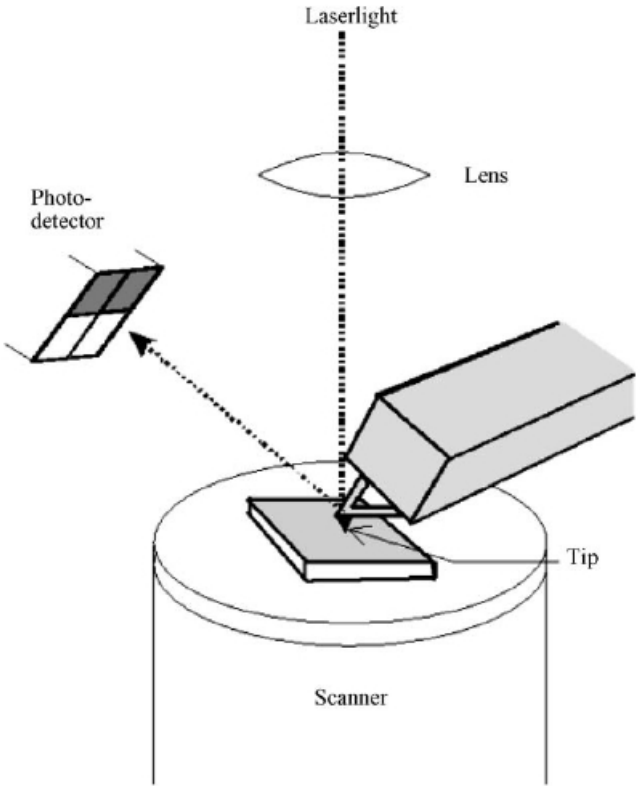

Figure 3.11: Schematic diagram of an AFM structure. Image reprinted from [81], Copyright (2005), with permission from Elsevier.

The tip is probably one of the most important parts in an AFM experiment: it is that part that interacts with the sample and its response is collected as experimental signal. Common tip geometries commercially available are the pyramidal, conical and tetrahedral [152]; however, with a proper choice of a colloidal particle to be glued on the cantilever, it is also possible to have spherical tips of different radii. Commercial tips are also made of different materials, like

silicon and silicon nitride [153], and are sometimes also available with different coating materials, like gold. However, also in this field, the possibility to choose a proper colloidal tip to attach to the cantilever, increases the availability of different and more materials. In any case, the shape of the tip is usually of primary importance in both imaging and force analysis, as will be clear in the following part of this section; however, to know perfectly that shape is quite difficult, because defects in the tip that can influence measurements are in the nanoscale range and, in addition, the shape of the tip can change during the measurements because it can wear out or become contaminated or can drag small particles.

Different types of cantilevers have been developed to perform different types of measurements or to adapt to different kinds of sample. A cantilever can also be tipless, in order to allow for customization because the researcher can choose to glue a specific tip on it or an object, such as a colloidal probe, a bacterium or any other relevant small object. Commercial cantilevers have usually two shapes and are made of silicon or silicon nitride. The most common shapes are rectangular and v-shaped: it partly depends on the cantilever characteristics (the rectangular shape is usually preferred for stiffer cantilevers) and use (because the v-shaped cantilevers are more stable with respect to torsional forces) [152]. In any case, a cantilever can be thought as a spring that supports the tip and it is mainly characterized by its spring constant and resonance frequency: the former is used as qualitative information for the choice of a cantilever according to the type of the experiment to perform or as a quantitative information in force analysis, while the latter is mainly used as qualitative information for the cantilever selection and it is used in some kinds of experiments where an oscillation at (or near to) the resonance frequency is required.

The piezo-actuator (or 'Scanner' in Figure 3.11) is usually under the sample or the surface to be analysed. Thus, it is the sample that is lifted up or lowered by the feedback loop. This position of the piezo-actuator limits the kinds of samples that can be analysed, in particular the limitation is due to the dimensions of the piezo-actuator. A sample cannot be bigger than the piezo-actuator stage and, usually,

only one sample for each measurement can be loaded on the piezo-actuator: to load a following sample it is often necessary to remove the cantilever holder (as in the Multimode AFM). Due to the type of samples involved in this project, this instrumental design is not the most suitable: thus, the AFMs used in this project do not have the piezo-actuator on the bottom but on the top, linked to the cantilever holder. Thus, it is the upper part of the instrument (and so the cantilever) that is lifted up or lowered by the feedback loop. This design has the advantage of providing larger stage for samples and an easier way to analyse numerous samples (rising the upper part of the instrument to shift from one sample to another is straightforward) without removing the cantilever holder. Piezo-actuators are made of piezoelectric materials, usually synthetic ceramics: these materials convert a change in the applied electrical potential to a change in their position. A typical expansion coefficient for these materials is in the order of 0.1 nm per volt [153] and this explains why they are used for the control of small movements during AFM scanning. Unfortunately, piezo-actuators do not have a linear response on the full range of potentials used in a AFM experiment, showing two main non-linear behaviours: hysteresis and creep. Hysteresis is related to the piezo-actuator tendency to maintain its shape when a linear voltage ramp is applied, while creep is related to the piezo-actuator tendency to continue to move in a direction even when the voltage impulse in that direction is stopped. These non-ideal behaviours should be taken into consideration, otherwise distortions can appear in the measurements. There are mainly two methods to do this: a calibration of piezo-actuator distortions, used for the following correction of the collected data or the use of displacement sensors integrated into the piezo-actuator that can provide its position independently from the voltage applied to the piezo-actuator (closed loop configuration).

The collected signal that originates the AFM output can be the voltage generated in the photo-diode detector by the laser beam deflected by the cantilever or the voltage used in the feedback loop. In previous equipments for imaging, such as in the stylus profiler (a predecessor of the AFM with relatively poor topographic

resolution), the movements of the cantilever were monitored and collected as output signal (by means of the reflected laser beam); nowadays the movements of the cantilever are usually used to drive the feedback loop that drives the piezo-actuator. Usually, in the AFM measurements, a set-point value is defined at the beginning of the experiment, according to the type of the experiment: this value represents the 'rest' position of the cantilever or the threshold value of bending to be reached. When the experiment starts the position of the cantilever on the photo-detector changes according to the features and the characteristics of the analysed surface. If the feedback loop is active, the position of the cantilever detected from the deflection of the laser beam is compared with the initial set-point: the difference between these two values is considered as an error signal and is used from the feedback loop to 'correct' the piezo-actuator position. Actually, the aim is to set parameters in order to maintain the cantilever always in the same position. The feedback loop is a proportional-integrative-derivative controller (PID) that works according to [153]:

$$Z_{\mathrm{v}} = \mathrm{P} \times Z_{\mathrm{err}} + \mathrm{I} \times \int Z_{\mathrm{err}}\,dt + \mathrm{D} \times \frac{dZ_{\mathrm{err}}}{dt} \tag{3.4}$$

where Z_{v} is the voltage sent to the piezo-actuator for the correction of the vertical (or z) position, P is the proportional parameter, Z_{err} is the difference between the set-point position and the actual cantilever position given as voltage, I is the integrative parameter and D is the derivative parameter. At the beginning of the measurement, the operator sets the P, I and D parameters in order to minimize Z_{err} (this is usually achieved by some trial tests before starting). The I parameter controls the movement of the tip over large surface features, while the P and D parameters facilitate its movement over the smallest and high-frequency features. Usually the D parameter is not used because it can easily create artefacts: its aim is to forecast surface features using the data collected from previous sweeps, however, it works well for surfaces with regular features, while in the other cases tends not to let the tip follow surface features quickly and so may create artefacts. Ideally, if these parameters are set properly, the piezo-actuator moves up and

down at the right frequency and amplitude to maintain the cantilever deflection constant. In practice, this condition is very difficult to achieve and the parameters were adjusted in order to minimize the cantilever deflections.

3.4.6 Imaging with the AFM

A surface can be imaged using different modes: they can be divided into two groups, contact modes and oscillating modes. In the former, the main mode used is the so called 'contact mode' where data are collected at constant force. There is also a contact mode collected at constant height that is less frequently used nowadays. All contact modes imply that the tip is brought into contact with the surface and the topography is collected scanning the surface over a square or rectangular area. The tip is dragged back and forth along a line (usually identified as x direction or fast scan axis) and then is moved on the next line (y direction or slow scan axis). In the constant force mode, the feedback loop is active and maintains the cantilever at a defined deflection, as decided by the operator at the beginning of the measurement. In the constant height mode, the feedback loop is off and the collected signal derives directly from the cantilever movement rather than from the voltage applied to the piezo-actuator. The advantage of contact modes over the oscillating modes is their extremely high resolution [153]; however, because the tip is dragged on the surface, damages to both the tip and the surface can happen if an excessive force is used or a very soft sample is analysed. Moreover, in this mode, there is a high lateral force too, and this force can damage some soft samples. For all these reasons, the constant force contact mode is suggested for hard samples and soft and v-shaped cantilevers are usually used. In the oscillating modes, the cantilever oscillates at the resonance frequency (or near it) and, when it experiences the force field of the sample or it taps the sample, the amplitude of the oscillation decreases. As for the case of the contact modes, also for the oscillating modes a setpoint is defined before starting the experiment: in this case it is an amplitude setpoint, thus it is amplitude that is used as target by the feedback loop. In fact, if the measured amplitude is lower than the setpoint, the

cantilever is lifted up, if it is greater than the setpoint, the cantilever is lowered (in reality the control of the feedback loop is performed using the three parameters of the PID controller explained above). There are two main oscillating modes: the non-contact or close-contact mode and the tapping mode. In the non-contact or close-contact mode, the cantilever does not touch the surface, but it is close enough to it to experience surface forces and it bends according to the strength of forces. In the tapping mode, the oscillating cantilever touches the surface and then is retracted. In this case, the change in the amplitude of the oscillation is due to the direct contact between the cantilever and the surface. The interaction between the tip and the surface not only modifies the amplitude of the oscillation but also its phase. Differently from the amplitude, changes in the phase do not depend only on the topographic features of the surface, but also on its composition (it is sensitive to changes in viscoelasticity or stiffness for example). However, in the case of rough surfaces it is not trivial to separate the topographic contributions from the others, so that phase changes are really interesting and unambiguous for samples which are known to be flat [153]. In general, oscillating modes are more delicate than contact modes because the applied force is less and the lateral force is reduced, and for these reasons they are suggested for soft samples analysis (however, also a 'hard' oscillating mode can damage a very soft surface, as is shown in Figure 3.12). Between the two oscillating modes, the tapping mode is the most widely used especially in air because it has a better resolution and it ensures that there is a contact with the surface. The non-contact mode is surely the less damaging for the sample but has worse resolution; moreover, in air measurements, a sample can be covered by a contamination layer, and, in this case it is this layer that is imaged. In tapping mode, instead, contact between the tip and the surface is assured, so the tip passes through the contamination layer and the real surface is imaged. For oscillating modes, stiff cantilevers are usually used, because they can experience the attractive forces of the surface without jumping to contact. In non-contact mode, a small oscillation amplitude is used, in order to avoid the contact with the sample, while, in tapping mode, a bigger amplitude is used.

In general, for the imaging modes, the tip apex should be as sharp and thin as possible, in order to detect all the details of a surface. In fact, the final image is a convolution of the sample surface profile and the line shape of the tip and this is why the use of a rounded apex could not be able to detect the finest details of the surface. Some very sharp tips have been developed, for example using nanotubes [154] or even single molecules [155], however the problem is that they can be easily damaged during the engagement or during the scanning of the surface. Thus, when a tip is chosen, a good compromise should be found between the need of a good resolution and the preservation of the tip apex.

The selection of the type of cantilever is usually less difficult: it depends on the imaging mode chosen and sample characteristics, however there is a good availability of cantilevers on the market and often, on the same chip, more cantilevers with different stiffness, resonance frequencies and tip apexes are present and they can be selected according to the specific needs.

The collection of the image is done by defining the area that should be imaged (it can be square or rectangular and its dimensions are set in nm or μm directly) and the PID parameters in order to minimize Z_{err} as previously discussed (this is done with a trial an error procedure). The error is also shown as an image (an error image), that in the ideal case should be completely flat (zero). This image presents high amplitude signals in correspondence of suddenly changes of the surface height, and, for irregular and rough surfaces, these changes cannot be completely compensated by the PID feedback loop.

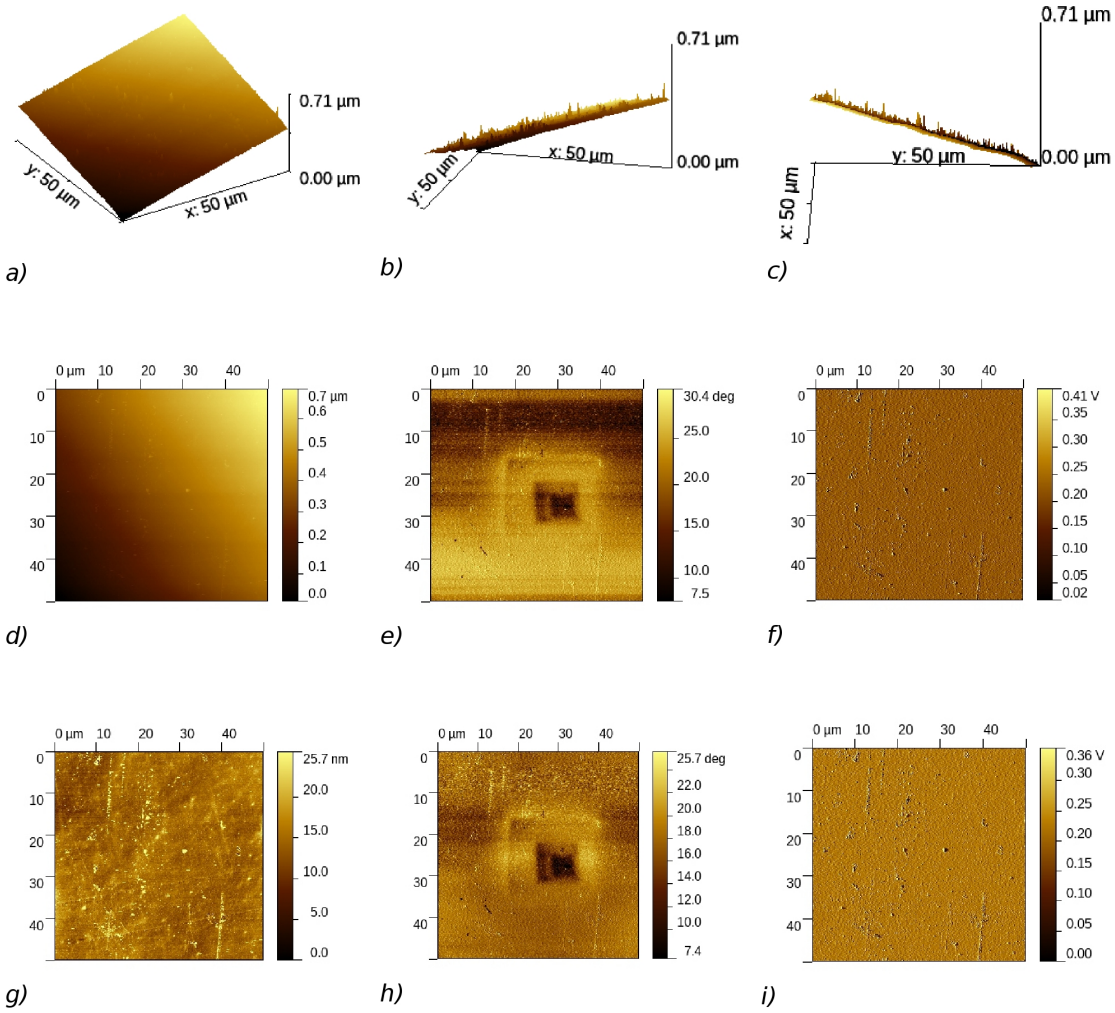

Figure 3.12: Example of raw and levelled data collected with the AFM in tapping mode. In panels (a), (b) and (c), the three-dimensional rendering of the raw image of height is illustrated from front side, the x side and the y side, respectively. It can be noted how the effect of the tilt is significant and prevalent on the effective roughness of the surface (the R_{rms}, a measurement of the roughness, of this raw image is 143.7 nm). In panels (d), (e) and (f) the raw images of height, phase and error of the same surface are depicted, respectively. In panels (g), (h) and (i), the corresponding processed height, phase and error images are shown. In this case, the processing consisted of a plane fitting, then a first order polynomial fit in the horizontal direction to remove the 'jumps' of the piezo-actuator in the height and finally a second order polynomial fit in the horizontal direction to remove the bow effect. The final R_{rms} of the height image is now 3.5 nm. The phase and the error images were processed in the same way, even if this is not usually done, to show that for them there is not a so great difference between the raw and the processed images. In this specific case, the phase image shows a damage of the surface due to a too hard tapping in the previous scans at smaller scan sizes (the squares) that is not so visible in the height image, even after the flattening. This shows how the phase image is sensitive to topographic changes.

Once an image is collected, it can be processed. In reality, almost all the images collected with an AFM are processed, and often, there is also an in-line processing during the acquisition. To understand these types of processing it should be remembered that the AFM is thought for the imaging of planar samples, so the first type of processing, almost always applied, is the levelling or flattening. Levelling includes different types of algorithms that ensure that the background of an image becomes flat, so that topographic features and different points on a sample retrieve the correct elevation. This is an important step, in particular if the image should be used subsequently for quantitative analysis, such as the determination of roughness. In fact, even a small tilt or a small background distortion influences the following analysis and can mask the finest details of the surface features (as it is shown in Figure 3.12). Tilt can arise from the surface of the sample and the AFM not being perfectly orthogonal [153], or the sample not being flat; other background distortions can be due to piezo-actuator non-linearity (this causes the image to have a form of bow or to be curved in the fast scan axis), or the vertical drift during the scanning of the surface (this causes suddenly changes in height along the slow scan axis). Thus, different types of levelling options are usually available for the processing of raw images. One of the simplest options is the polynomial fit: each line is fitted with a polynomial of the chosen order and then the polynomial fit is subtracted from the original line. Polynomial order usually ranges from 0 (that just set a height offset that is subtracted to each line) to 3, and the most used are 1 (where a straight line is fit for each scan line) and 2 (in this case a second order polynomial is subtracted): the first order polynomial is used for removing the tilt, while the second order is used for the removal of the bow shape or the curvature in the fast scan axis. Similar to the polynomial fit is the plane fitting (or planefit): in this case the entire image is processed as a whole and not line by line. In fact, the image is fitted by a flat plane that is then subtracted to the raw image. Similar to this approach is the three points fitting: three points are chosen that should belong to a plane that is then fitted and subtracted to the raw image. The polynomial fit is probably the most used, however it can create artefacts, in particular when the

beginning and the end of a line are not at the same level or when there are high features with respect to the background. In the former case, another algorithm should be used, while in the latter, the region with the highest features should be excluded from being fitted. Planefit and three points fitting do not introduce the errors seen for the polynomial fitting, if the surface of sample is really a plane or the three chosen points are really on the same plane. An example of levelling is illustrated in Figure 3.12.

Another type of processing is the removal of unwanted noise that has a defined frequency, such as acoustic or floor vibrations or PID parameters (if set to high). This can be achieved by the use of filters or fast Fourier transform (FFT). Filters are matrices that average adjacent points and, according to the type of matrices, they can be low-pass or high-pass (the former allows the low frequency components of the image to pass, the latter acts in the opposite way) [153]. The main disadvantage in using filters is that they can smooth or blur data. The FFT is a powerful tool for the removal of frequency dependent noise: in this case, the raw image, from the spatial domain, is converted into the frequency domain by the use of the FFT. In the frequency domain it is easy to remove the unwanted low or high frequencies and then to return to the spatial domain again. However, if not well used, the FFT will also introduce patterns that did not exist in the original image. In conclusion, the choice of the processing algorithms is crucial for a robust analysis and should be evaluated case by case.

Raw or processed images can also show artefacts. Some of them can be seen also during the scanning of the sample surface and so can be easily solved. For example, sample drift is quite easily noticed because all of the features of the surface are deformed in the same direction. Another way to check if this kind of artefact is present is to change the scan angle: if the image remains the same, there is no drift, otherwise the sample should be fixed in a better way. Another kind of artefact that is easily found is related to the tip apex: when there is a double, blunt, contaminated or damaged tip apex. In these cases all the features of the image will show the same types of details: they are all blurred, doubled or with a repetitive

pattern. In these cases it is sufficient to change the cantilever. Artefacts due to the non-linearity or creep of the piezo-actuator can be (partially) removed with a calibration on a calibrated grid; the bow artefact or the curvature on the fast scan axis is removed during flattening, as mentioned above. Also a poor choice of the PID parameters can create artefacts, because the tip apex does not follow the sample surface properly, but this is easily seen from the error image, which will show a large error signal. Sometimes the tip apex looses the contact with the surface for a small stroke or for an entire line: in the former case scars appear on the image and in the latter case an entire line may not have any information about the sample surface. In this case it is possible to apply a scar correction or a line skip: the missing points are reconstructed by averaging the next points belonging to the next lines. However, this correction should be use with caution, because it actually artificially creates parts of an image. Finally, also the processing can also create artefacts, especially if not well applied as mentioned above.

The analyses that can be done on AFM images usually aim to reveal evidence of topographic features of a surface. In addition, some other information regarding also the changes in composition (for example, using phase images as discussed above) or particular surface properties can be extracted (for example in the case of specific experiments which are designed to test electrical or magnetic properties of a surface). In this thesis, the main interest is in the analysis of the topography of surfaces, together, where possible, with changes in the composition visible in the phase image. The advantage of using an AFM for the characterization of the surface features with respect to an optical microscope is also related to the collection of a three-dimensional dataset. In fact, an AFM image is the rendering of a set of data where each point is described by three spatial coordinates, two for the position on the plane and the third is the height from the plane. Images taken with the optical microscope do not contain reliable information about the third dimension (height). There are different types of topographic analyses that can be done on an AFM image: line profiles, grain or particle analysis, Fourier transform analysis, autocorrelation analysis and roughness analysis. Line profile analysis is based on

the extraction of a line from the image and the view of its height profile from which, for example, information like height of peaks, or distance between them can be easily obtained. For these reasons, this type of analysis is quite useful in the study of samples with regular patterns. Grain or particle analysis uses specific algorithms for the evaluation of grain or particle edges in a process known as image segmentation [153]. In this way, particle or grain characteristics (like height, width, radius, area and volume) are determined and usually exported for statistical analysis. Particle analysis can be also performed on images taken with an optical microscope, however, as aforementioned, an AFM image usually shows a better resolution. Fourier transform analysis is used to reveal a repeating pattern and it is the same type of analysis that can be done for the removal of periodic noise as discussed before. Autocorrelation analysis is useful to know if a certain pattern is repeated in an image; it is similar to the Fourier analysis, but it does not involve the conversion from the spatial domain to the frequency domain. Both the autocorrelation and the Fourier analyses are usually performed on samples that show repetitive patterns such as atomic lattices. Roughness analysis is a group of techniques for the evaluation of the roughness: this is also the analysis tool that is the most used in this thesis, so it will be described in more detail in the following. Actually, the description of the roughness of a surface is not straightforward: different parameters can be used and are usually accepted for that, however, they are usually based on the assumption that the distributions of heights in a sample is normal. This is not always the case, and it may happen that surfaces with different topographic features show the same value of a roughness parameter (such as, for example, depicted in figure 3.13).

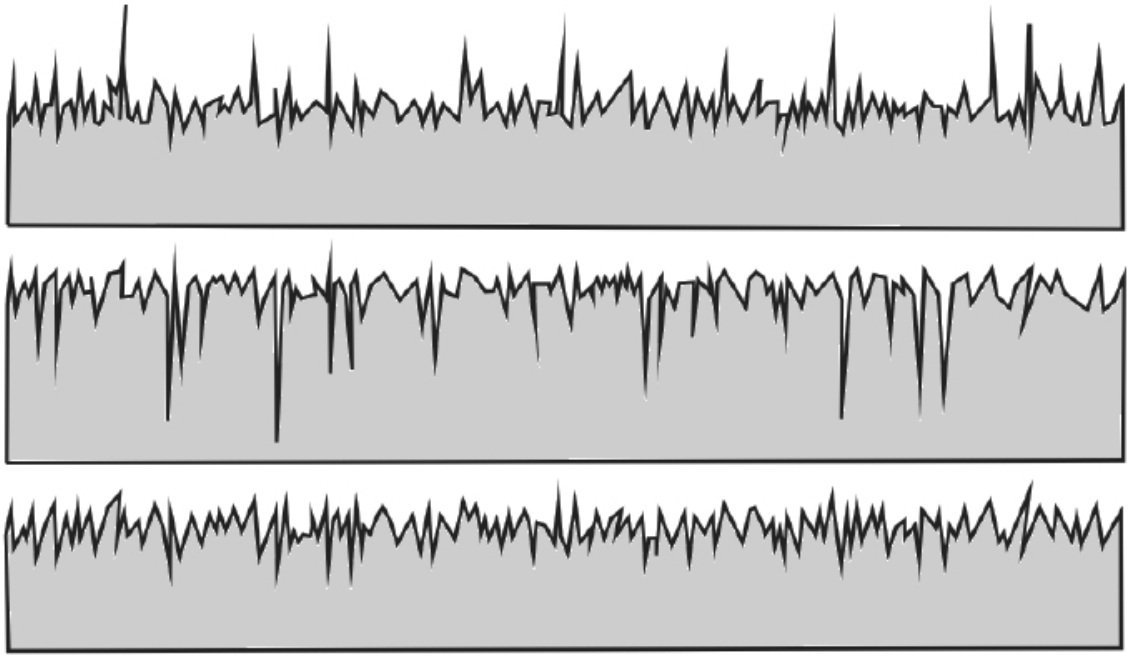

Figure 3.13: Example of surfaces with different profiles but with the same R_a. Figure taken from [156].

However, the advantage in using these parameters is that they are also used for roughness evaluation in other techniques and this makes them useful for correlations. The most commonly used roughness parameters are the arithmetic roughness R_a and the root-mean-squared roughness R_{rms} (or R_q), which are calculated as the average and the standard deviation of the heights of each point from the mean height, respectively. Bot these parameters are positive and greater values indicate greater variation in the surface height; it should be noted that R_q is usually greater than R_a and more sensitive to peaks and valleys (outlier points) then R_a, as shown in Figure 3.14.

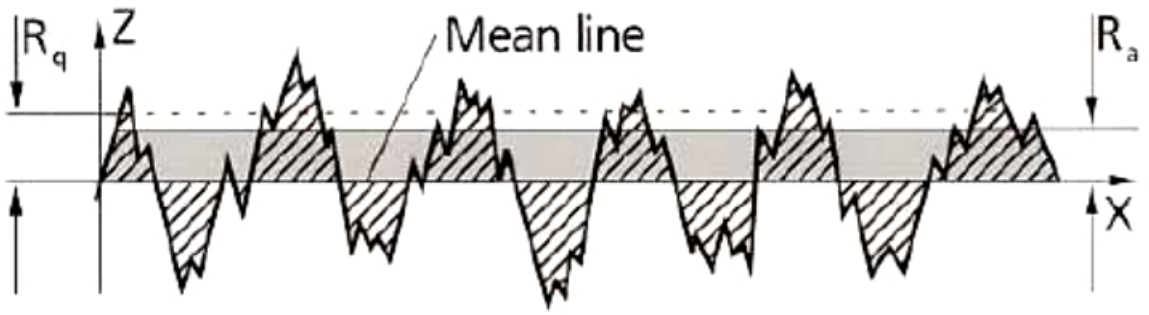

Figure 3.14: Difference between R_{rms} (R_{q} in the image) and R_{a} (X indicates the mean height. Figure taken from [156].

Others, less used, roughness parameters are the maximum profile valley depth R_{v}, the maximum profile peak height R_{p}, the maximum height of the profile R_{t}, skewness R_{sk} and kurtosis R_{ku}. Formulas of all these parameters are listed in Table 3.10; shortly, R_{v} is the depth of the deepest valley from the mean height, R_{p} is the height of the highest peak from the measured mean height, R_{t} is the sum of the previous two parameters, R_{sk} is a statistical measure of the asymmetry of the height distribution from a normal distribution and R_{ku} is a statistical measure of the peakedness of the distribution in comparison to a normal distribution.

It is easy to note from the formulas and definitions of these roughness parameters how much a levelling algorithm can influence them (or also the tilt of a sample, when levelling is not performed). Different levelling algorithms can result in completely different roughness parameters, because of the introduction or removal of differences in heights of the features of the sample surface. Thus, the importance of the correct choice of the levelling algorithm is critical in the roughness analysis. Moreover, some surfaces can show a texture that consists of waviness plus roughness. The difference between waviness and roughness lies in the wavelength of the fluctuation of the height along the surface profile: long wavelength fluctuations are related to waviness, while short wavelength fluctuations are ascribed to roughness (and sometimes, very short wavelength fluctuations are referred to as noise). How to separate these two components is described in the international standards ISO 4287 and ISO 4288; in any case,

wavelengths smaller than 13 μm and amplitudes of less than 25 nm (that are typical in the case of AFM measurements) are not covered by these standards [157]. However, considering the influence of waviness on roughness, in some cases it can be useful to distinguish between the two also at the AFM scale. This distinction can be done using polynomial levelling or the FFT analysis. An example of a profile formed by waviness plus roughness is depicted in Figure 3.15.

Another parameter that can be useful and is related to roughness is the projected area, i. e. the ratio between the calculated area of the surface over the area of the flat mean plane.

Parameter name	Abbreviation	Formula
Arithmetic roughness	R_a	$R_a = \frac{1}{N}\sum_{i=1}^{N} z_i$
Root-mean-squared roughness	R_{rms} (or R_q)	$R_{rms} = \sqrt{\frac{1}{N}\sum_{i=1}^{N} z_i^2}$
Maximum profile valley depth	R_v	$R_v = \left\lvert \min_{1 \le i \le N} z_i \right\rvert$
Maximum profile peak height	R_p	$R_p = \left\lvert \max_{1 \le i \le N} z_i \right\rvert$
Maximum height profile	R_t	$R_t = \left\lvert \min_{1 \le i \le N} z_i \right\rvert + \left\lvert \max_{1 \le i \le N} z_i \right\rvert$
Skewness	R_{sk}	$R_{sk} = \frac{1}{NR_{rms}^3}\sum_{i=1}^{N} z_i^3$
Kurtosis	R_{ku}	$R_{ku} = \frac{1}{NR_{rms}^4}\sum_{i=1}^{N} z_i^4$

Table 3.10: Roughness parameter names, abbreviations and formulas. The z_i values are the distances of the profile height or depth from the mean height, and N is the number of points that constitute an image of a surface [156].

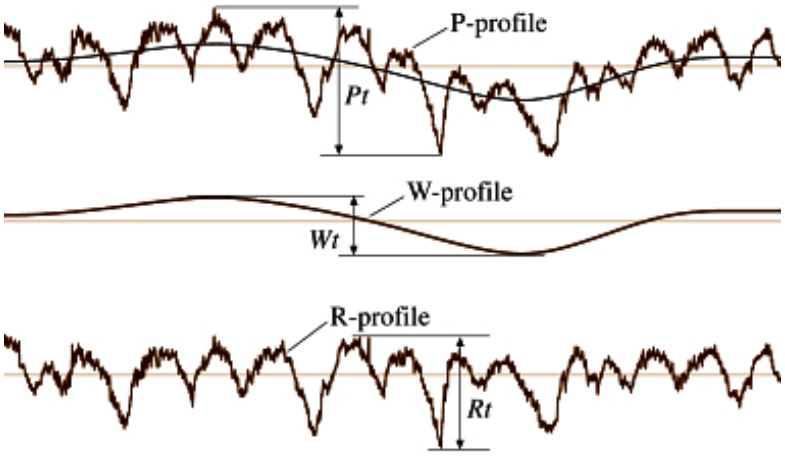

Figure 3.15: Primary profile of the surface (top), separated into waviness (center) and roughness (bottom). Figure reprinted/adapted by permission from Springer Nature Customer Service Centre GmbH: Springer Handbook of Materials Measurement Methods by Seah M., Chiffre L. COPYRIGHT (2006).

Presentation of surface topography usually consists of two dimensional data visualization using colours to show the heights of the features of the surface obtained after processing. A legend is also shown to correlate colours with the respective heights. The colour palette is usually monochromatic, but it is possible to use also multi-chromatic ones, that have the advantage to increase the resolution of details, if the heights extension and distribution is very large (a human eye can distinguish less than 100 brightness levels of a particular colour [153]). Colour can be applied linearly: however, if the distributions of heights is divided into different groups in quite different regions of the palette, the image can be very dark with some light peaks or viceversa. In order to obtain a more 'observable' image of the surface, software usually has different types of options like the choice of the range in which the linear palette is applied, or non-linear colour palette (in this last case, the legend shows only the minimum and maximum value of the height range). Sometimes, also a three-dimensional rendering of the height image can be useful to show interesting details: this three-dimensional image can be rotated, tilted, scaled and lighted up in order to put in evidence the most important details (examples of the final presentation of images both in two dimensional visualization

with a monochromatic linear palette and in three dimensional rendering orientations are in Figure 3.12).

The processing, analysis and presentation of height images as previously presented can be applied also to the phase and the error images, however for these images often a basic presentation with a linear colour palette is sufficient. In fact, the phase image is relevant in particular if a surface is flat, just to show regions with different mechanical properties, and the error image (in theory) should be as flat as possible.

In this thesis, the AFM used for imaging the surfaces of the great majority of the samples is a Nanoscope IV Dimension 3100 atomic force microscope (Digital Instruments, Cambridge, UK). All of the samples provided by Teknek were imaged with this instrument, while the laboratory made PDMS samples were imaged with the same AFM used for the determination of the adhesion force (that will be described in the following section). This difference is related to the smoothness, softness and adhesiveness of the latter samples: because of these characteristics, the PDMS surfaces are quite adhesive and, with the Dimension 3100, good imaging was very difficult and time consuming. A peculiar feature of the Dimension 3100 is the big stage that allows the analysis of samples with different sizes and shapes (Figure 3.16). In this AFM, the piezo-actuator is a piezo tube placed in the scanner above the stage, with a travel of 6 μm along the vertical axis and a declared bow effect along the x-axis of 2 nm for a scan size of 10 μm.

Images were acquired in tapping mode, using a silicon tapping mode cantilever (TESPA, Bruker), with a nominal tip radius of 8 nm. Topographic data were collected from images of three different locations for each sample and in three different scan sizes, moving from the smallest to the greatest (1 μm, 5 μm and 10 μm). In this way it is possible to check if the previous scans altered the surface. Each image has 256 x 256 data points: this is a medium resolution, however it was a good compromise between details resolution and acquisition time. For each scan, the height image, the phase image and the error image were collected. The acquired height images

were processed and analysed with the Gwyddion software (version 2.37); phase and error images were not processed.

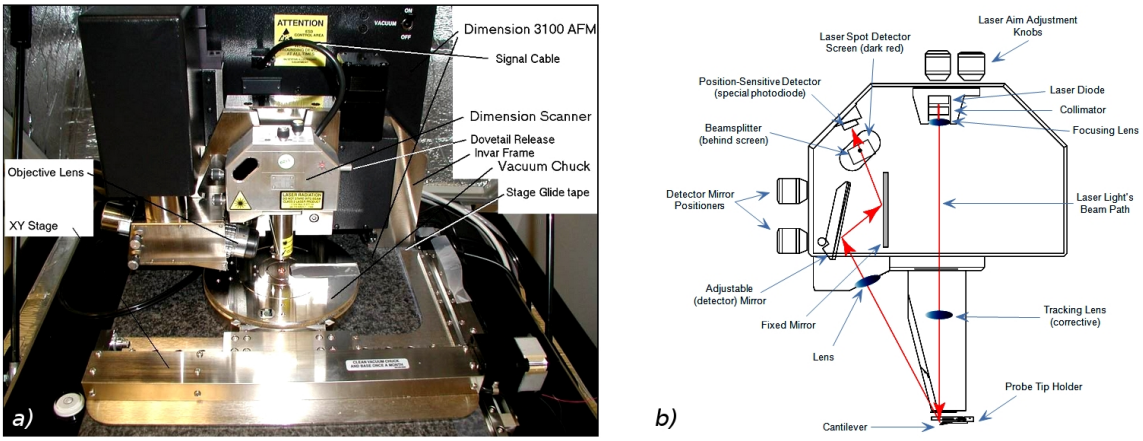

Figure 3.16: Scheme of a Nanoscope IV Dimension 3100 in panel (a), photo courtesy of Advanced Surface Microscopy, Inc. www.asmicro.com. Details of the head in panel (b); image courtesy of Prof. David Haviland and Prof. Vladislav Korenivski, KTH Royal Institute of Technology, section for Nanostructure Physics (Stockholm, Sweden) – http://www.nanophys.kth.se/nanophys/facilities/nfl/afm/icon/bruker-help/Content/System%20Overview/SPM%20Head.htm.

For samples provided by Teknek, preparation consisted of cutting squares of about 1 x 1 cm^2 from the provided samples and sticking them on a glass slide with double-sided tape (for flat samples) or gluing them on a glass slide with Araldite Rapid (for non-flat samples). Before each analysis, samples were cleaned according to the provided cleaning procedure.

Data processing usually consisted in the levelling of the collected raw images: however, due to the large differences among the samples, it was impossible to apply the same levelling algorithm to all of them. Thus, the processing of the images depended on the specific sample and will be discussed in the next chapters for each case. In any case, the choice of the flattening algorithm was done in order to minimize the levelling introduced artefacts. Optical images were also used to help in the choice of the levelling procedure.

Image analysis focused on the determination of roughness, usually expressed as RMS roughness. Because the great majority of the samples do not show regularities

in the surface features neither at the greatest scan size, it was usually chosen to present all the data collected for each repetition of the analysis rather than the corresponding averaged value.

Image presentation is done with a monochromatic palette: the linear palette was used as preferred, however, in some cases, where the observation of details was difficult, a reduced range linear or a non-linear palette was chosen.

3.4.7 Studying adhesion with the AFM

As described in the introduction, a cantilever can be seen as a spring ending with the tip or the probe apex: thus, it can be characterized by a certain elastic force. If the spring constant is known, it is possible to correlate the deflection of the cantilever with the applied force or the experienced adhesion (force) according to equation 3.5 (where k_c is the spring constant of the cantilever and δ_c is the deflection or the indentation of the cantilever).

$$F = - k_c \delta_c \tag{3.5}$$

A typical 'adhesion' experiment implies the approach of the tip apex toward the surface of the sample, the contact between them and finally the retraction of the tip apex from the surface. In moving back and forth toward the sample, the cantilever may firstly experience a force when it is next to the surface, and later, after the contact, when it is withdrawn, it may experience the adhesion force. The way in which a tip apex experiences forces is monitored by recording the cantilever deflection: when the tip apex is attracted toward a surface or when there is adhesion force between it and the surface, the cantilever bends downward, while when the tip apex experiences a repulsive force, the cantilever bends upward. Thus, the deflection of the cantilever (that can be expressed as a force acting on the cantilever if the spring constant is known) can be recorded as function of the sample (or tip) displacement (actually the piezo-actuator displacement). This deflection- or force-displacement curve is the output of the force spectroscopy with an AFM (an example of a deflection-displacement curve is depicted in Figure 3.17).

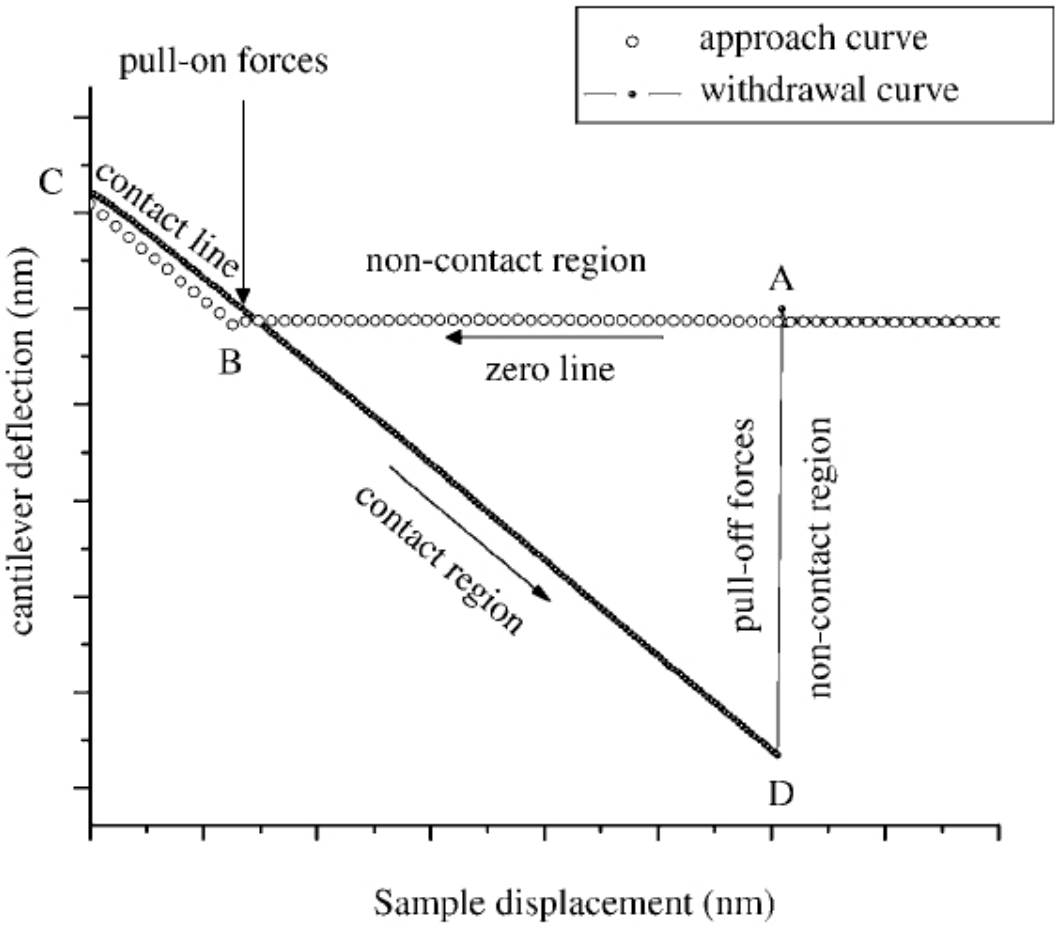

Figure 3.17: An example of a deflection-displacement curve. Contact and non-contact regions indicate when the tip apex is touching the surface or not, respectively. Pull-on forces and pull-off forces indicate the jump-to-contact and the jump-off-contact, respectively. Image reprinted from [29].

Often, this curve shows two points of instability (usually they are discontinuities), the first one during the approach, when the force experienced by the tip apex is greater than the elastic force of the cantilever, so that the cantilever jumps into contact with the surface; the second during the retraction, when the elastic force of the cantilever becomes greater than the force experienced between the tip apex and the surface, so that the cantilever can return in the horizontal or rest position. These discontinuities are called the jump-to-contact and the jump-off-contact, respectively (names can be slightly different according to authors). In the case of repulsive force between the surface and the approaching cantilever, there is no jump-to-contact, but the cantilever bends in the opposite direction until it is forced

to touch the surface. Another different case is when there is no adhesion force between the tip apex and the surface (Hertz model): in this case the retraction and the approach curves do not show any discontinuities. Some examples of deflection-displacement curves are presented in Figure 3.18.

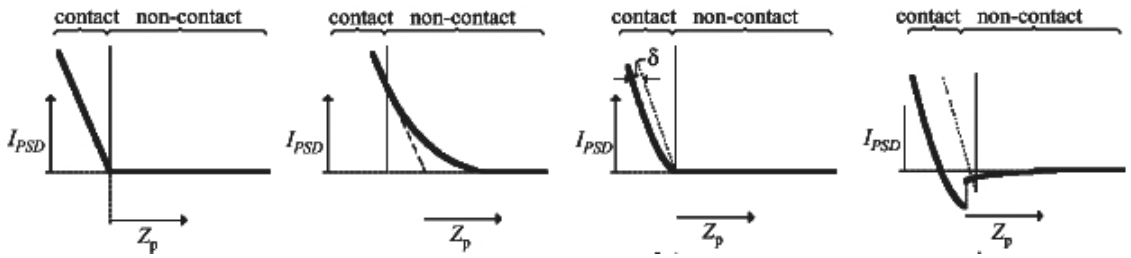

Figure 3.18: Examples of deflection-displacement curves of different materials. From left to right: a hard surface without contact forces; a hard surface with long-range repulsive forces; an inelastic deformable material without surface forces and an inelastic deformable material with adhesion forces. Examples of deformable elastic materials are not showed here: in these cases the slope of the contact region is less steep than in the case of hard materials, and the approach and retraction curves superimpose. Image reprinted from [81], Copyright (2005), with permission from Elsevier.

From a force-displacement curve, interesting information about the sample surface can be obtained:

- during the approach, in the proximity of the first instability point, the appearance of the curve provides information about force field of the surface, that can be attractive (with the jump-to-contact), absent or repulsive (with an upward bending of the cantilever);
- the following contact region in the approach curve, when the tip apex is 'pressed' on the surface, provides information about the stiffness of the surface. If the surface is hard and non-deformable, the bending of the cantilever reflects the upward movement of the piezo-actuator. If the surface is not so hard and it deforms because of the force applied by the cantilever, then the slope of this part of the curve is less steep than in the case of a hard surface. Actually, the slope can be considered an indication of material hardness: the less hard the material is, the less steep the slope is.

- the first part of the retraction curve, until the jump-off-contact, provides information about the elasticity, viscoelasticity or plasticity of the sample. If this part is perfectly superimposed to the approach trace, the surface is elastic; in fact, reducing the applied force, the surface returns at same height seen during the approach and it means that it stores all the energy acquired during the approach as elastic energy. If the slope of this part is different from the slope of the approach curve, the surface is viscoelastic: it remains partially deformed (on reducing the applied force the surface does not return to the same height seen during the approach). Finally, if the slope of the retraction part is the same of the approach curve, but is shifted toward the left, the surface exhibits plastic behaviour. Thus, in this case, the energy acquired during the approach curve is completely dissipated by the deformation of the sample.
- the region in the proximity of the jump-off-contact in the retraction curve is used for the evaluation of interactions between the surface and the tip apex. If there is jump-off-contact it means that there is adhesion force acting between the two surfaces. The adhesion force is extracted from the plot as the difference between the minimum of the retraction trace and the rest position of the cantilever.

There are also some other 'mixed' cases: for example, if the surface shows initially an elastic behaviour and then a plastic one, the contact part in the approach curve shows two straight regions with different slopes. Or, in the case of 'multi-adhesion' behaviours, in the retraction curve, more than a minimum appears in the contact region. 'Multi-adhesion' behaviour can be due to chain extraction or roughness of the surface, as previously discussed.

When there is adhesion, two interesting points of the force-displacement curves to go into are the instabilities and the hysteresis between the approach and the retraction curves. The instabilities are the jump-to-contact and the jump-off-contact, however these are usually discontinuities. In fact, only if the cantilever is much stiffer than the force acting between the surface and the tip apex both during the

approach and the retraction traces, the instabilities can be reduced to points and virtually, eliminated [158]. However, the use of a stiff cantilever can have negative effects on resolution, reducing it. Thus, a compromise between the stiffness of the cantilever and the complete tracking of the force curve should be reached. According to the strength of surface-tip forces involved, a too soft cantilever should be avoided, because in this case the regions of the discontinuities become too large.

The hysteresis between the approach and retraction curves cannot be avoided because the jump-off-contact force and distance are always greater than the jump-to-contact force and distance, respectively [158]. This effect can be related to different factors like, for example, the formation of chemical or physical bonds, or the enlargement of the contact area during the contact between the tip apex and the surface. Thus, in the AFM field, this hysteresis should be considered of mechanical source, intrinsically related to this technique. It should be noted that, with special feedback loops, that infinitely increased the stiffness of the cantilever, also this hysteresis can be removed [158] however, these systems are not commonly used.

As aforementioned, the raw data collected during force experiments are the cantilever deflection and the piezo-actuator position. The cantilever deflection is in volts, when the optical detection system is used. The collected voltage does not depend only on the position of the cantilever but also on the shape, dimension and position of the laser on the cantilever: it strongly depends on the specific experimental conditions. A way to transform this output from volt to nm, is to perform a force experiment on a hard and non-deformable surface: in this case, the bending of the cantilever in the contact region corresponds to the movement of the piezo-actuator. In this condition, it should be possible to divide a variation of the voltage by the corresponding movement of the piezo-actuator and to correlate the voltage with the deflection in nm, directly (this process is known as optical sensitivity determination).

Once the cantilever deflection is expressed in nm, if the spring constant is known, it is possible to calculate the force applied or experienced using equation 3.5. However, the determination of this constant is not so trivial. Even if manufacturers provide a nominal spring constant, this could be not very accurate because each cantilever has its proper spring constant, even if they come from the same wafer. There are different methods for the determination of the spring constant and the most commonly used are:

- to use the cantilever dimensions and mechanical properties. In fact the spring constant of rectangular cantilevers is related to the shape and the Young's modulus of the cantilever, according to ([158, 159])

$$k_c = \frac{E t_c^3 w}{4 L^3} \tag{3.6}$$

where E is the Young's modulus of the cantilever, t_c is its thickness, w is its width and L is its length. However, the determination of the shape of the cantilever requires precision and, in addition, its Young's modulus is not easy to determine.

- by means of the change of the resonance frequency when a known mass is added to the cantilever [160]. The resonance frequency of a cantilever is related to its mass according to

$$\omega_{0c} = \sqrt{\frac{k_c}{m_c^*}} \tag{3.7}$$

where ω_{0c} is the resonance frequency, m_c^* is the effective mass that is determined by the mass of the tip m_t and the mass of the cantilever m_c according to

$$m_c^* = m_c + 0.24 m_t \tag{3.8}$$

When a known mass M is added to the cantilever, the resonance frequency ω_{1c} changes according to equation

$$\omega_{1c} = \sqrt{\frac{k_c}{m_c^* + M}} \tag{3.9}$$

Knowing ω_{0c} and ω_{1c}, which can be determined experimentally and the mass M, the spring constant is determined by

$$k_c = \frac{M}{1/\omega_{1c}^2 - 1/\omega_{0c}^2} \tag{3.10}$$

The known mass is usually a sphere of a material with well-known density and dimensions, that adhere to the cantilever by means of adhesive forces, without glue [158].

- to use a calibrated cantilever as reference for the determination of the spring constant of the others [161]. In this case, the calibrated cantilever is the sample, so that it is moved by the piezo-actuator: when the other cantilever touches it, both of them bend. If δ_c is the deflection of the cantilever and δ_p is the piezo-actuator displacement, the spring constant of the cantilever is determined by

$$k_c = k_{ref}\frac{1 - \delta_c/\delta_p}{\delta_c/\delta_p} \tag{3.11}$$

where k_{ref} is the spring constant of the reference cantilever and δ_c/δ_p is the slope of the contact region of the approach curve.

- to use the intensity of the thermal noise [162]. If the cantilever is considered a perfect harmonic oscillator, it will show a fluctuation due to the thermal noise. According to the equipartition theorem, the mean square deflection $\langle\delta_c^2\rangle$ due to the thermal noise is related to the spring constant by means of Boltzmann's constant k_B and the temperature T,

$$\frac{1}{2}k_c\langle\delta_c^2\rangle = \frac{1}{2}k_B T \tag{3.12}$$

From equation 3.12 is possible to extract the spring constant of the cantilever using

$$k_c = \frac{k_B T}{\langle \delta_c^2 \rangle} \tag{3.13}$$

However, the use of the correction factor g and the effective deflection δ^* provides a better estimation

$$k_c = g \frac{k_B T}{\langle \delta_c^{*2} \rangle} . \tag{3.14}$$

This method is often implemented in the AFMs: in practise a noise spectrum is acquired, and the peak of the resonance frequency (that corresponds to the first mode of oscillation) is fitted with a Lorentzian curve. The mean square deflection is obtained by integration of this peak.

- to use the quality factor and the resonance frequency of the cantilever together with its dimensions (length and width) [163]. According to this method, the spring constant is determined from

$$k_c = 0.1906 \rho_f w^2 L q \Gamma_i(Re) \omega_{0c}^2 , \tag{3.15}$$

where ρ_f is the density of the fluid surrounding the cantilever, q is the quality factor and $\Gamma_i(Re)$ is the imaginary part of the hydrodynamic function [81]. The quality factor is a characteristic of the cantilever and it is a measurement of the cantilever damping in a specific fluid (proportional to the ratio between the stored and the loss energies) [164]. The determination of the quality factor is also implemented in the AFM software because it can be found from the width of the resonance frequency peak or from the decay of the free oscillation amplitude of the cantilever [165]. The hydrodynamic function depends on the Reynolds number that in turn depends on the viscosity of the fluid and the resonance angular frequency [81]. This method is suitable when the measurements are performed in air [163].

There is not 'the best method', because all of these methods have sources of errors. The choice of one of these methods is related to the available possibilities. For instance, two methods require the determination of the dimensions of the

cantilever and one requires the knowledge of the attached mass: this information is achievable if a calibrated and precise instrument for dimension determination is available (for example a good optical microscope or better, an electron microscope [163]). On the other hand, the method based on the calibrated cantilever requires the use of one of the other methods for the determination of the spring constant of the reference cantilever. Finally, the method based on thermal noise has a dependency on the position and dimension of the laser spot (and on the temperature).

If the transformation of the deflection from V to nm is straightforward and the determination of spring constant can be routinely done, the determination of the tip-sample real distance of a soft sample with attractive forces is not always easy. What is recorded during a force experiment is the piezo-actuator displacement, which is a combination of the cantilever deflection, the sample deformation δ and the distance between the tip apex and the sample surface D according to equation 3.16 and as depicted in Figure 3.19.

$$\delta_p = D + \delta + \delta_c \tag{3.16}$$

The most interesting distance is D that cannot be known without knowledge of the deflection of the cantilever and the deformation of the sample. The deflection of the cantilever can be found as described previously, using a hard reference surface, while the deformation of the sample can be estimated using data from literature and from the suitable contact mechanics model. At least, this information can be used as initial value to be refined subsequently. In the AFM software, often the transformation from displacement to distance is done indicating the zero distance point (also called contact point), and this is not an easy task when a deformable surface with acting forces is studied: a common convention is to choose the first point after the jump-to-contact [166]. However, some other authors that used PDMS samples prefer to choose as contact point the point immediately before the jump-to-contact region [56, 167]: that means that there is not a unique procedure for the choice of this point and that, according to the specific system studied, the contact point should be evaluated every time.

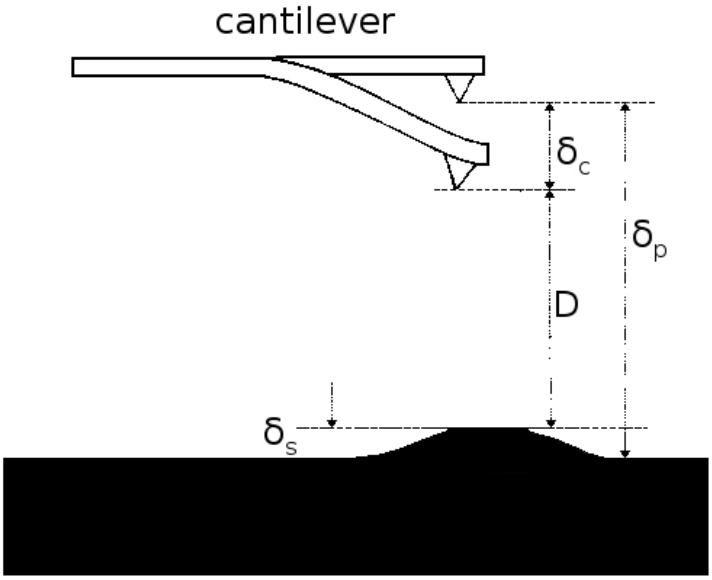

Figure 3.19: Tip-sample distances (image adapted and reprinted from [158], Copyright (1999), with permission from Elsevier).

Sources of artefacts are the same as for the imaging: for example, the creep and hysteresis of the piezo-actuator, which can lead to the 'reverse path effect' (the contact region of the retraction curve is over the contact curve as in Figure 3.17), or external vibrations can add noise to the curve. To reduce the effect of the non-linear behaviour of the piezo-actuator, apart from its calibration, the close loop system is recommended, while to avoid effects due to external vibrations, the instrument is usually protected by an acoustic enclosure. Other sources of errors can be related to imperfections in the tip shape and error in the spring constant evaluation. Tip damage and surface roughness also can lead to wrong determination of forces.

Cantilever and tip choice should be carefully considered, taking into account the type of surface, the strength of the forces involved and the aim of the study. The choice of a cantilever is usually related to the spring constant, which should be chosen according to the force strength as previously mentioned. The spring constant of cantilevers for force analysis is usually less than that of tapping mode cantilevers. The tip shape, or better, the shape of the tip apex, is fundamental if one

of the contact mechanics models needs to be applied. Moreover, it is the tip apex that experiences or applies forces, and force or pressure profile is shape dependent. Sharp tips provide a better resolution of force analysis, however, considering the same force applied on the cantilever, the pressure applied to the sample is greater than the pressure applied by a less sharp tip. The application of a great load on a sharp tip can damage it, or the surface can be damaged easier than in the case of using a less sharp tip (if the damage is placed on the tip or on the surface is matter of how hard is the analysed surface and how much load is applied on the cantilever). There are some commercially available cantilevers for force analysis, with a defined tip shape (usually, spherical, conical or pyramidal) and materials (for example, silicon, silicon nitride or diamond), or, in some cases, also cantilevers for contact imaging can be used. The range of available materials can be increased by evaporation, adsorption or chemically bonding of a new material on a tip or using tipless cantilever where a 'probe' of the desired material is attached. In the latter case, usually colloidal particles of different materials are used, often spheres of defined diameter: they can be stuck at the end of the cantilever with glue. An optical microscope with a micromanipulator or an AFM can be used: the technique is based on putting down a drop of glue on a clean substrate, then touching it with the end of the cantilever and then, pressing the end of the cantilever on the colloidal particle to glue. Also this 'colloidal probe' can be covered by another material by evaporation, adsorption or chemical processes. Also single molecule probes can be created in this way.

A force analysis can be done in a specific point of a surface, or it can be used to map the adhesion over a specific area. In the latter case, the area is selected as a square or a rectangular with a defined number of points for adhesion collection in each dimension. If, during the force analysis, also the height of the surface is collected, it is common to call it 'force mapping' or force 'volume data'. However, the height resolution is really lower than the one obtained with the imaging modes, because the number of points is much lower than in imaging modes. In addition, force analysis usually requires more time than imaging. However, a force map can

be interesting for non-homogeneous or very rough surfaces, because it is possible to correlate the force analysis to a specific part or feature of a surface. The force and the height maps are usually presented as false colour, pixelated images, where each pixel corresponds to a single force analysis.

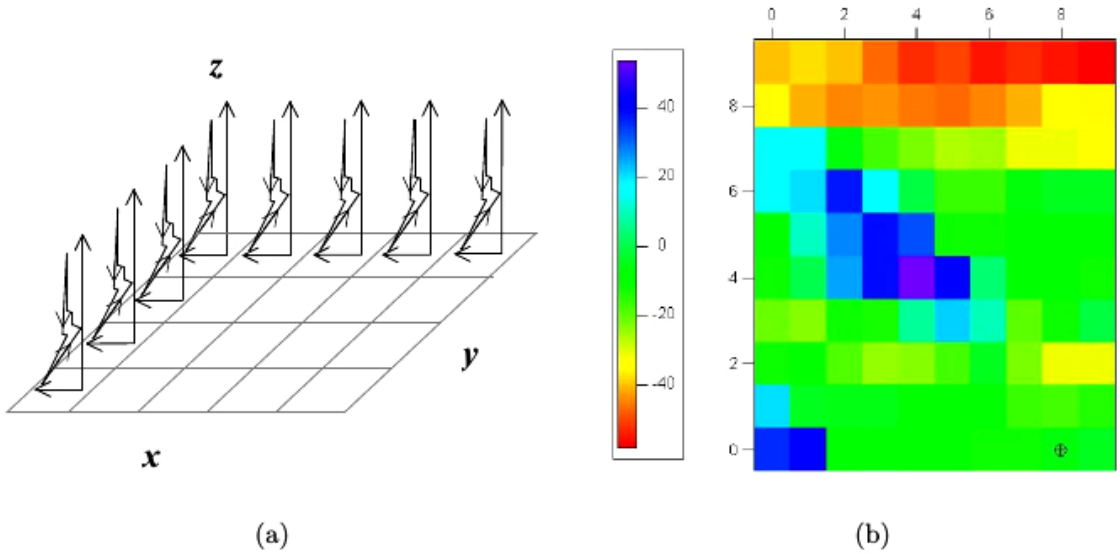

Figure 3.20: Scheme of a force map acquiring process in panel (a) and a height map (or force map, because unit of measure is not indicated) in false colour in panel (b). Image adapted and reprinted from [168], © 2008 IEEE.

There are many parameters that can be set at the beginning of the analysis and that can influence the results, as for example the final applied load (called 'trigger point') and the speed of the approach and retraction of the cantilever, (their contributions to the force analysis were discussed in the previous chapter).

The output of a force analysis is a quantity extracted from the force-displacement curve, usually the adhesion force. When a force map is performed, the output is a set of values, for example, adhesion force values. These results are usually elaborated with a suitable statistical analysis. If the measured quantity shows only a random error, the normal distribution (and statistics) can be used; however, often the distribution of the data are not normal, and other types of distributions should be considered (for example, the log-normal distribution is

often used in biological field, or bimodal distributions are used when two regions with different adhesion are present).

In this thesis, the AFM used for the force analysis was a MFP-3D BIO atomic force microscope (Asylum Research). This instrument is specifically designed for biological samples, however it is more precise and versatile than the Nanoscope IV Dimension 3100 for force analysis and includes a specific software. Like the Nanoscope IV Dimension 3100, also the MFP-3D BIO has a stage that allows large samples to be studied. The piezo-actuator is placed over the stage and it can travel of 15 μm along the vertical axis. The MFP-3D BIO was also used for the imaging of the laboratory made PDMS samples.

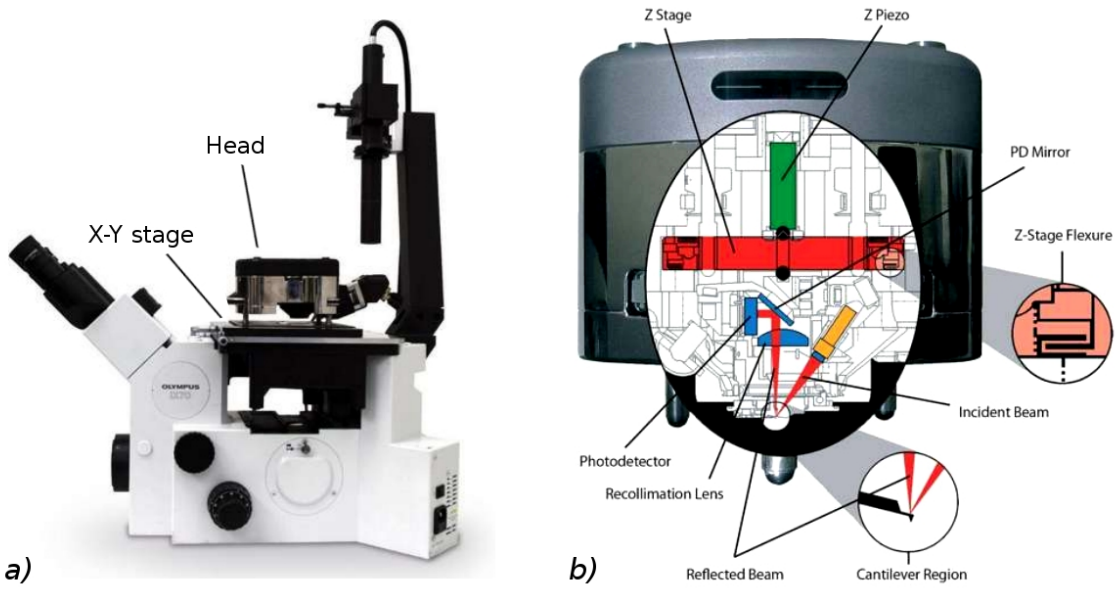

Figure 3.21: Scheme of a MFP-3D BIO AFM microscope in panel (a); details of the scanner in panel (b); images reprinted and adapted from the website of the manufacturer (http://www.asylumresearch.com) in 2014, Copyright, with permission from Asylum Research.

Adhesion measurements were acquired using tipless aluminium coating silicon cantilevers with a nominal spring constant of 7.4 N/m (All-In-One, Budget Sensors). Different types of particles (a polystyrene divinylbenzene particle by Duke Scientific Co., CA, USA with certified mean diameter of 10 μm, and a borosilicate particle, by

Duke Scientific Co., CA, USA with certified mean diameter of 10 μm) were attached with Araldite Rapid glue at the end of tipless cantilevers using the Nanoscope IV Dimension 3100. After at least 12 hours, cantilevers were used for the measurements. All the colloidal probes cantilevers were controlled with the optical microscope before the use. The optical sensitivity and the spring constant were determined before and after use, to verify if the cantilever was still in the same condition. For the sensitivity determination, the used hard surface was mica, which has an atomically flat surface and a layered structure (these features avoid effects of roughness and contaminants, because a fresh layer is used for the determination of the sensitivity). Mica sheets were provided by Agar Scientific and used as received. For the spring constant determination, the thermal method was used because it does not require the knowledge of the dimensions of the cantilever and it requires the least manipulation of the cantilever, reducing the possibilities of damaging it. In addition to the check of the sensitivity and the spring constant, also the resonance frequency was controlled at the beginning and at the end of each run of measurements: in fact, the resonance frequency is sensitive to changes in the cantilever weight (so if the colloidal probe is damaged, lost or dirty). Thus, only if, after the last measurement, the optical sensitivity, the spring constant and resonance frequency were reasonably similar to those collected at the beginning, the measurement were considered acceptable (variation smaller than 10% for the optical sensitivity and spring constant and 1% for the resonance frequency were considered acceptable).

All the samples were analysed with force maps, thus collecting height and force data at the same time on areas of 10 x 10 μm^2 in at least two different locations, using the closed loop system. However, different settings were used for the mapping of the samples related to the Teknek project and the laboratory made PDMS samples.

Teknek's samples were cut into squares with sides of about 1 cm and cleaned with the procedure provided by the company before the measurements. The 10 x 10 μm^2 area was sampled in 32 lines with 32 points each (for a total of 1024 points with a

step of 322.6 nm). Both types of colloidal probes were used to see if they show a different adhesion toward hydrophilic and hydrophobic surfaces. Force maps were collected in air, using a trigger point of 1 μN. A humidity sensor HIH-4000-003 by Honeywell was also used for collecting the relative humidity during the measurements, just to have an idea of the possibility of the presence of the capillary neck in the case of hydrophilic surfaces. The choice of this specific type of sensor was related to the fact the MFP-3D BIO manufacturer implements it in some applications. The sensor was placed as near as possible to the sample. The output of the sensor was read with a digital voltmeter Duratool and then transformed into relative humidity according to the calibration plot provided by the manufacturer. The statistical analysis of the adhesion force collected from the samples related to the Teknek project were not done by means of statistical distributions, but only by means of average and standard deviations. And, as in the case of the roughness analysis, it was usually preferred to show the results of each repetition of an adhesion analysis separately, without averaging them. This is because samples have quite different features and an average could mask import results. In addition, some samples show regions with different adhesion, often correlated with specific surface features. In some cases, also the appearance of data distributions is used for qualitative comparisons.

The laboratory made PDMS samples were analysed a day after they were produced, because there is not a cleaning procedure for them that can assure that their surfaces will be not modified. Before each measurements their surfaces were checked with the optical microscope to verify the absence of contaminants. However, extreme care was taken during the crosslinking reaction and the storage of these samples, in order to avoid contamination. Samples were obtained by the 13 mm disks, removing the non flat edges: because PDMS naturally adheres on glass, no glue was necessary to immobilise them on the glass slide. The 10 x 10 μm^2 area was sampled with 20 points: their surfaces were more homogeneous than all the other samples, and an increase in the number of force curves did not provide further information. Only the borosilicate colloidal probe was used, because it

provided more precise data than the PS-DVB probe. Force maps were collected in air, using trigger points ranging from 125 nN to 1.5 μN (precisely, 125 nN, 250 nN, 500 nN, 1000 nN and 1500 nN) at a fixed speed of 3.5 μm/s and a speed ranging from 0.5 μm/s to 14.0 μm/s (precisely, 0.5 μm/s, 1.75 μm/s, 3.5 μm/s, 7.5 μm/s and 14.0 μm/s) with a fixed trigger point of 500 nN. Curves collected at different speeds were used to verify the effect of viscoelasticity on adhesion force. For this analysis the crack speed should be calculated as introduced in the previous chapter. The used procedure was:

- firstly, the contact point is chosen, so that the raw deflection-displacement curve can be converted into the usual force-indentation curve;
- then, the non contact region before the contact point is fitted by a line that is then subtracted to the curve: this part of the curve should be flat because there is not contact between the probe and the sample, but sometime there is a tilt due to the instrument. However, even if the tilt is about few micrometres, this can reduce the precision of the measurement of the adhesion force;
- the reduced elastic modulus E^* is calculated from the first part of the retraction curve. This part is usually linear because a separation without crack movements is assumed. The fitting line is calculated using the points in the range 1%-5%: first points are usually discarded because of the creep of the piezo-actuator;
- the coordinates δ and F of the minimum of the retraction curve (adhesion force point) and the points before and after it are found from the curve;
- from the general equations of the JKR model 2.129 and 2.130, the contact radius a and H corresponding to these three points are calculated. The calculation of a from 2.129 is done using the formula for the solution of cubic equation with positive discriminant: in this case there is only one real solution.

- with the finite difference formula, the crack speed at the adhesion point is calculated (the instrument collects a point each 0.5 ms)
- analysis of how H varies with the crack speed is done.

The humidity sensor was not used in these measurements because the PDMS surface is hydrophobic, so capillary forces are considered not to act in this case. Also in this case, statistical analysis is based on the average of data. These samples were also imaged with the MFP-3D BIO, in tapping mode, using the same silicon tapping mode cantilever (TESPA, Bruker) seen for Nanoscope IV Dimension 3100. A difference between the two AFMs in imaging mode is that the MFP-3D BIO rarely needs adjustments of the proportional gain because the frequency of the scanner is below the range of the frequency range used by the proportional gain.

4 PDMS samples

In this chapter, results and discussion of the analyses on PDMS samples will be presented. Characterization of PDMS samples includes: determination of the extent of the crosslinking reaction calculated by the extractable fraction, discussion about the crosslink density and the Young's modulus by the swelling and DMA analyses, morphological study by means of AFM, investigation of the hydrophilic/hydrophobic behaviour of the surfaces, investigation of the elastic/viscoelastic behaviour and adhesion study. Results of the different analyses are correlated and influences or changes in the adhesion are also considered.

4.1 Yield of the crosslink reaction

In the case of the crosslink reaction of PDMS used in this work, the extractable fraction represents the percentage of the unreacted (or partially reacted) reagents. In fact, if the reaction is complete, all reactants will take part of the three-dimensional network and will not be removed by the swelling solvent. If something is extracted by the solvent, it means that it was not linked to the network: in the case of this reaction, it is assumed that the extracted part is formed only by PDMS chains (this assumption is justified by the consideration that the crosslinker has a negligible mass with respect to the PDMS chains in all the samples).

Even if the extractable fraction is already an indication of the completeness of the reaction, from the determination of the same weights (m_{i} and m_{f}), it is possible to calculate the yield. Yield is the most common way to express the completeness of a reaction in chemistry: in this case, the initial and the final weights are considered the theoretical weight of the complete reaction and the real weight of the reaction, respectively. This is justified by the fact that in this reaction there is no solvent and that the main reactants will take part of the final network (inhibitor and catalyst are in negligible quantities). This calculation leads to a yield that is the complementary value of the extractable fraction to 100.

Extractable fractions and yields of all the PDMS samples are listed in Table 4.1: as it is possible to see, the best reaction has a yield around 80% while the worst is around 60%. The yield of the hydrosilylation reaction mostly decreases with the increase of the molecular weight of the PDMS chains: this can be equally ascribed to the increasing density of the linear PDMS with the weight and the consequently less efficient mixing of the reactants or to the reducing concentration of the reacting groups with the weight and so a lower probability that a reactive event can occur.

Only PDMS-9.5K has a yield that is similar but a little bit lower of that of PDMS-17K: this may be due to randomness of chemical reactions. However, the yield of those two samples may be considered similar.

PDMS sample	Extractable fraction (%)	Yield (%)
PDMS-6K	18	82
PDMS-9.5K	27	73
PDMS-17K	22	78
PDMS-27.5K	33	67
PDMS-42.5K	40	60

Table 4.1: Extractable fraction and yield of the five PDMS samples. Values are the average of four measurements for each sample.

The different yields of the hydrosilylation reaction show that samples could have different elastic (or viscoelastic) properties. In fact, elasticity is a characteristic of a perfect network: defective or imperfect networks usually have near-elastic or a more or less pronounced viscoelastic behaviour, according to the degree of defects or imperfections.

4.2 Surface morphology

Surface morphology of PDMS samples acquired by AFM does not show significant roughness on a 10 x 10 μm^2 scale: RMS roughness is around 1 nm for all samples. Sometimes, on all samples, there are little isolated peaks with similar

characteristics: they are not higher than 10 nm with a circular base with a radius of about 0.5 μm or less. A selection of surface images is reported in Figure 4.1 and RMS roughness values are listed in Table 4.2.

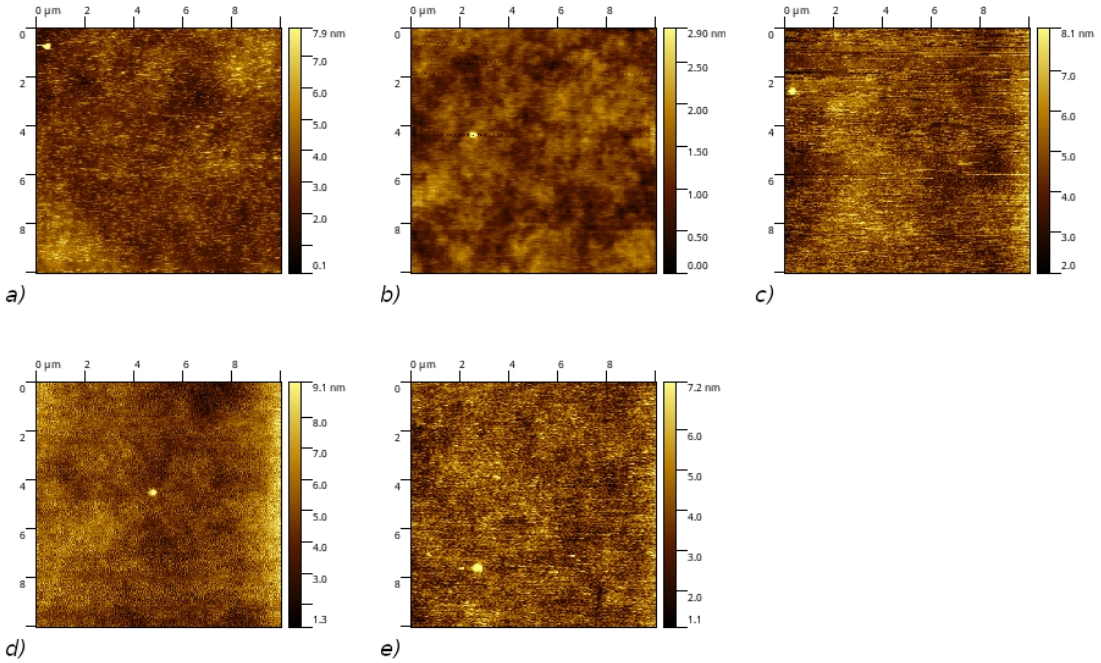

Figure 4.1: AFM images of PDMS-6K in panel (a), PDMS-9.5K in panel (b), PDMS-17K in panel (c), PDMS-27.5K in panel (d) and PDMS-42.5K in panel (e). Images were flattened and 1D FFT filtered for noise removal. A selection of images showing peaks was done in order to show that peaks have similar characteristics and that they can be present on all samples. It is important to note that peaks are very rare and they are not usually present in most of the 10 X 10 μm^2 AFM images.

PDMS sample	Averaged RMS roughness (nm)	RMS roughness min – max range (nm)
PDMS-6K	0.88	0.57 – 1.1
PDMS-9.5K	0.66	0.32 – 0.88
PDMS-17K	1.1	0.97 – 1.4
PDMS-27.5K	1.1	1.1 – 1.3
PDMS-42.5K	0.97	0.83 – 1.1

Table 4.2: RMS roughness values are the average of three measurements. The min – max range is shown because it can give an idea of the variability of surfaces.

Roughness values in the range of few nanometres (around 2 – 6 nm) are typical of PDMS as reported in literature [57, 69].

A RMS roughness in this range does not influence adhesion of these samples because they are very soft and deformable, so little asperities are flattened when the probe is pushed against the surface. Moreover, the probe is a colloidal one, with a radius of 5 μm, so the adhesion that it experiences is not affected by this low roughness.

4.3 Surface hydrophilic/hydrophobic behaviour

Contact angle measurements show that the surfaces of all samples are hydrophobic with similar values. Experimental values agree with those reported in literature and summarised in Table 3.2. The hydrophobicity of PDMS samples excludes that adhesion is humidity sensitive even if probed with a hydrophilic surface. Experimental values of the contact angles are reported in Table 4.3.

PDMS sample	Contact angle ± standard deviation (degree)
PDMS-6K	111 ± 1
PDMS-9.5K	110 ± 3
PDMS-17K	108 ± 3
PDMS-27.5K	109 ± 3
PDMS-42.5K	107 ± 2

Table 4.3: Contact angles of PDMS samples. Values are the average of six runs of 200 measurements each.

4.4 Crosslink density and Young's modulus

Crosslink density and Young's modulus are presented together because they are determined by the same experiments: in fact, even if swelling provides a direct measurements of the crosslink density, while DMA is used to find the shear modulus (and consequently the Young's modulus), these two properties are linked

together by equations 2.16 and 2.17 according to the chosen model. In the specific case of these PDMS samples, the two measurements do not match: the Young's modulus determined from the shear storage modulus of the lowest four angular frequencies of the DMA leads to crosslink densities that are lower than those calculated from the swelling as reported in Table 4.4 (in the calculation of the crosslink density by the swelling measurement, equations 2.12 and 2.14 were used with the value of χ of 0.465 as reported in Table 3.2).

PDMS sample	Crosslink density from swelling (phantom model) ± standard deviation (10^{-5} mol/cm^3)	Crosslink density from swelling (affine model) ± standard deviation (10^{-5} mol/cm^3)	Crosslink density from DMA ± standard deviation (10^{-5} mol/cm^3)
PDMS-6K	18 ± 2	11 ± 1	1.993 ± 0.003
PDMS-9.5K	2.5 ± 0.4	1.4 ± 0.3	1.256 ± 0.004
PDMS-17K	4.6 ± 0.4	2.6 ± 0.2	0.680 ± 0.002
PDMS-27.5K	1.31 ± 0.06	0.72 ± 0.03	0.415 ± 0.002
PDMS-42.5K	0.56 ± 0.6	0.30 ± 0.03	0.170 ± 0.007

Table 4.4: Crosslink densities calculated from swelling (phantom and affine models) and from the shear modulus of the four lowest frequencies used in the DMA analysis. DMA analysis was done using samples that were not swollen, i.e. on PDMS as it was synthesised.

The difference is significant, from one half to ten times less than the crosslink density calculated from the swelling measurements, according to the sample, for both the affine and phantom models. Between the two measurements, probably the most critical is the swelling: it is based on specific boundary conditions and also in literature there is discussion about the validity of equations 2.12 and 2.13-2.14 and often they are 'corrected' in different ways to get an agreement with experimental values. For example, sometimes an additional term is added to take into consideration also the contribution of entanglements to the elasticity of the network ([130, 169]), or some variations are proposed for lightly crosslinked network ([170]) or hydrogels [171]: none of those 'corrections' worked well in the present work and also some other 'adjustments' based on the real yields of the

reactions were not able to match the values found from the DMA. The main reason for that is probably due to the poor yield of these reactions and the quite large amount of free chains in the samples, that cannot be taken into account by 'delicate' models for crosslink density: a comparison with networks described in some of those articles shows that their worst network could correspond to the best one in this work, the PDMS-6K, and it is known that these formulas can fail when the networks are away from being perfect. On the other hand, the grips used in the DMA are ideal for poorly crosslinked polymers or viscous materials, thus very likely values provided by DMA are more realistic than those obtained from swelling.

If the framework of equations 2.12 and 2.13-2.14 should be retained the only 'correction' that can be done is about the Flory-Huggins polymer-solvent interaction parameter, that may have a dependence on the volume fraction. In [130], an interesting test to verify the Flory-Huggins polymer-solvent interaction parameter is suggested: the Flory-Huggins polymer-solvent interaction parameter versus the volume fraction of the polymer in the swollen state is graphed and the dependence of χ from ϕ_2 is found by the best fitting curve. The Flory-Huggins polymer-solvent interaction parameter is calculated, for both the affine and phantom models, using the crosslink density obtained by the DMA (from the corresponding equations 2.16 and 2.17 for the shear modulus) and the volume fraction of the polymer obtained by the swelling. As seen previously, there is not a unique value or function of the parameter χ: this can be a constant or a function of first or second order of φ_2. Of course, a test like this one assumes that all the deviations from ideal conditions of the swelling models are contained in the parameter χ. Results of the test are almost similar: in Figures 4.2 and 4.3 data and fittings are shown, for both the affine and the generalised phantom model, respectively. Linear fitting is used because it shows the best correspondence with experimental values with an R^2 of 0.98 for both models. The values of the coefficients of the fitting lines for the affine model are 0.461 ± 0.006 and 0.45 ± 0.05 for the intercept and the slope, respectively. For the phantom model the fitting coefficients are 0.463 ± 0.006 and 0.46 ± 0.05 for the intercept and the slope, respectively.

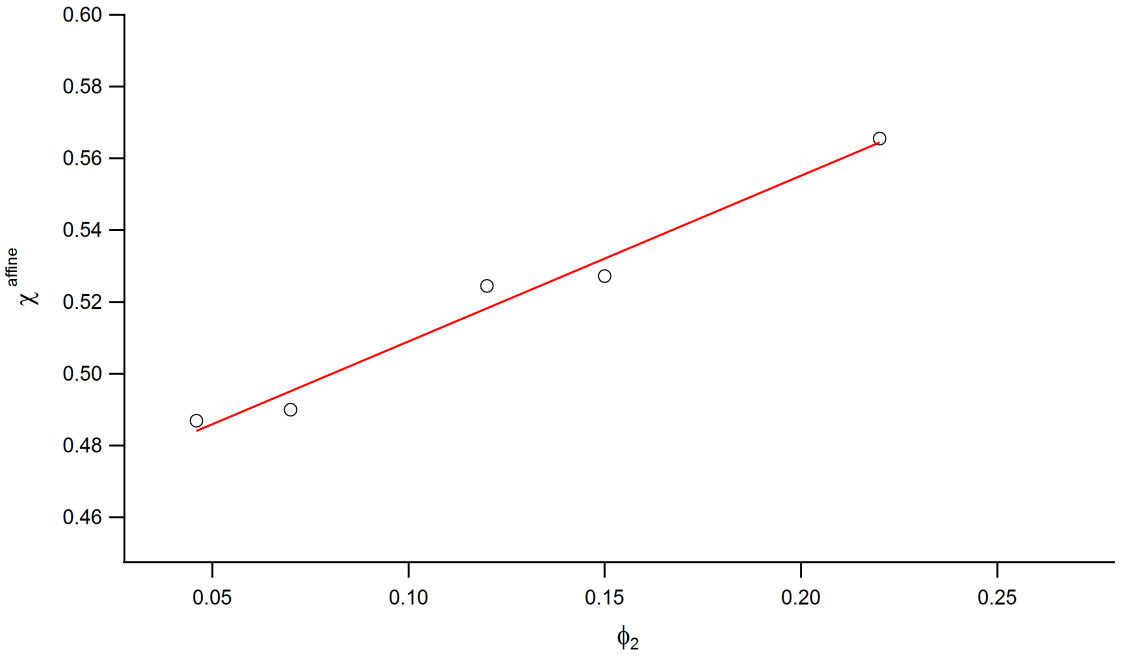

Figure 4.2: Calculated χ values from the four storage moduli of the DMA at the lowest frequencies versus the polymer volume fraction obtained from the swelling measurements (affine model).

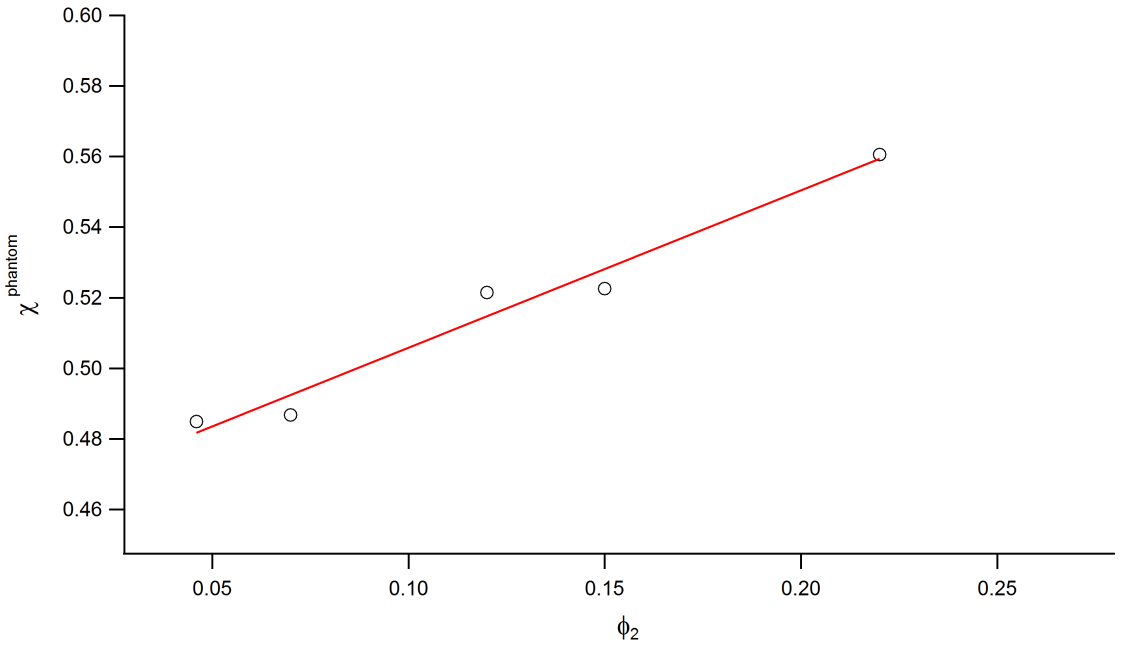

Figure 4.3: Calculated χ values from the four storage moduli of the DMA at the lowest frequencies versus the polymer volume fraction obtained from the swelling measurements (generalised phantom model).

Thus, the relationship is linear in both cases and with similar values. The interesting point is that the intercept of the line is really near to the values reported in literature for the linear correction of the Flory-Huggins polymer-solvent interaction parameter, while the slope is about the double of the usually accepted value. However, this can be seen also as a further indication that values from swelling are not 'wrong' but that a comprehensive formula for swelling has not been found yet and for that usually in literature swelling is not used in the case of networks with high percentage of extractable chains.

The fact that both the affine and phantom models show a similar behaviour is not surprising because equations 2.12 - 2.13 (or 2.14) are quite similar except for a small term in φ_2 in the denominator that becomes significant at high values of φ_2, which is not the case of this work ([130]). However, because the amount of swelling, and so of network deformation, is quite large, probably the phantom model can be selected as the reference model.

Thus, with a quite important correction of the Flory-Huggins interaction parameters, swelling data confirm the DMA values for the crosslinking density. Crosslink density values confirm that these reactions were not complete and that the elastic active strands between two crosslinks are quite long.

Considering the two techniques and what has been discussed above about them, only the DMA was used for the calculation of the Young's modulus from the shear storage modulus using equation 2.3 with a Poisson coefficient of 0.5. Values are the average of the four values at the lowest angular frequencies and are reported in Table 4.5. They show that the elastic modulus decreases as the crosslink density decreases: this is not surprising because the shorter the elastic active strands are, the greater the elastic modulus is.

PDMS sample	Young's modulus ± standard deviation (10^5 Pascal)
PDMS-6K	1.480 ± 0.002
PDMS-9.5K	0.932 ± 0.003
PDMS-17K	0.505 ± 0.001
PDMS-27.5K	0.308 ± 0.002
PDMS-42.5K	0.126 ± 0.005

Table 4.5: Young's moduli of five PDMS samples (calculated from the average of the storage shear moduli at the four lowest angular frequencies).

4.5 Elasticity/viscoelasticity behaviour

Viscoelasticity is evaluated from the values of the storage and loss shear moduli of the DMA analysis. These values show that samples are mostly elastic: the only two of them that show from a low and to a mild viscoelasticity at medium-high angular frequencies are PDMS-27.5K and PDMS-42.5K, respectively. All the other samples show an elastic behaviour at quite all the angular frequencies except for those really high. Storage and loss shear moduli of all the samples at each frequency are reported in Figure 4.4.

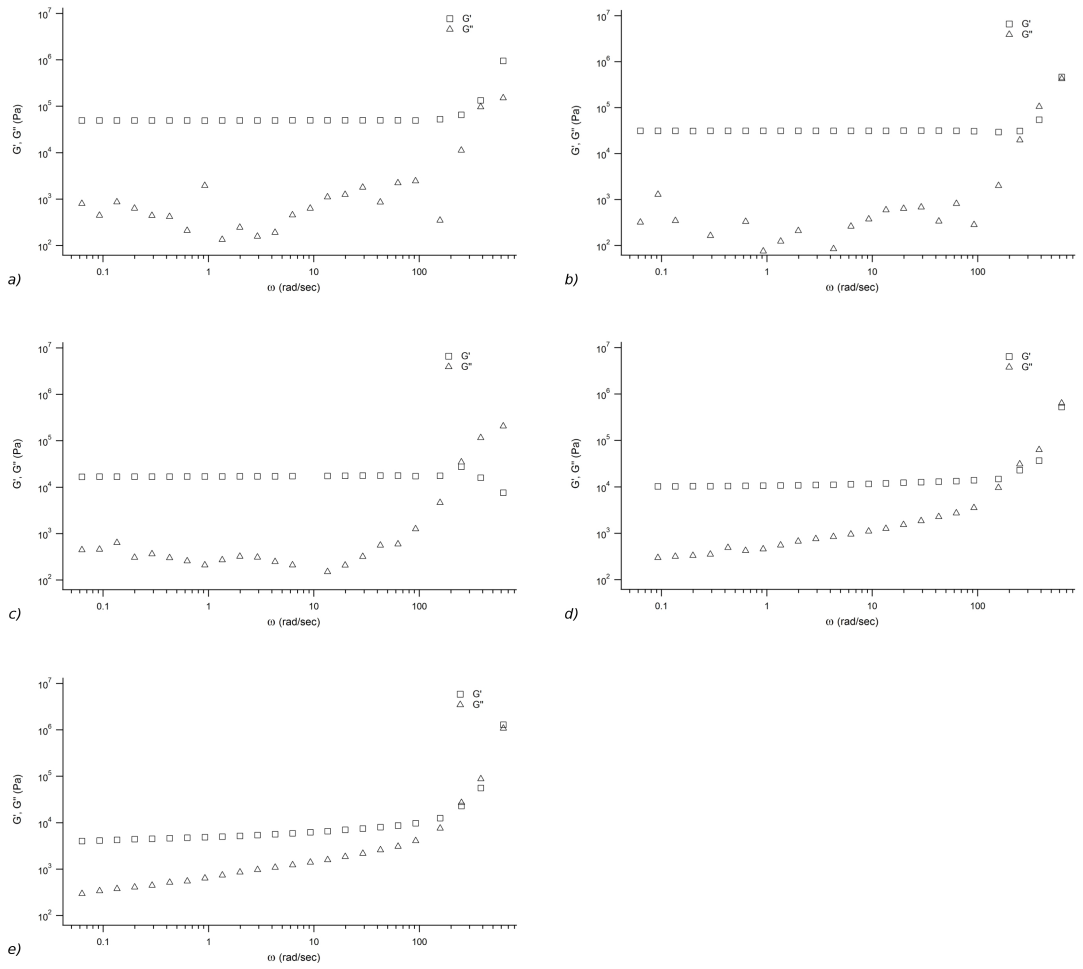

Figure 4.4: Storage and loss shear moduli of PDMS-6K in panel (a), PDMS-9.5K in panel (b), PDMS-17K in panel (c), PDMS-27.5K in panel (d) and PDMS-42.5K in panel (e).

4.6 Adhesion behaviour

Before studying the adhesion behaviour of these samples, in order to define which can be the best maximum load to use in the following experiments a preliminary test was done at the reference AFM head speed of 3.5 μm/s changing the maximum applied load from 125 nN to 1500 nN: the test was repeated twice for each sample collecting twenty points every time and the adhesion force is then averaged on the two runs. Results are shown in Table 4.6: adhesion force is almost similar at every load. However, it was chosen not to use too low and or too high

loads in order to avoid low precision or too much deformation, respectively. Actually, a maximum load of 500 nN seems a good compromise.

PDMS sample	Adhesion force ± standard deviation (10^{-7} N)				
	125 nN	250 nN	500 nN	1000 nN	1500 nN
PDMS-6K	9.7 ± 0.1	9.6 ± 0.1	9.6 ± 0.1	9.8 ± 0.1	8.8 ± 0.2
PDMS-9.5K	9.94 ± 0.05	9.82 ± 0.07	9.9 ± 0.1	10.2 ± 0.1	10.5 ± 0.2
PDMS-17K	9.74 ± 0.08	9.67 ± 0.04	9.72 ± 0.03	9.77 ± 0.04	9.83 ± 0.04
PDMS-27.5K	10.05 ± 0.06	9.93 ± 0.02	9.972 ± 0.002	10.07 ± 0.02	10.14 ± 0.03
PDMS-42.5K	10.4 ± 0.1	10.5 ± 0.1	10.6 ± 0.1	10.57 ± 0.05	10.70 ± 0.09

Table 4.6: Adhesion force of the five laboratory made PDMS samples at five different maximum loads.

Then, determination of the adhesion force at the reference condition of a maximum applied load of 500 nN and the AFM head speed of 3.5 μm/s is done for all the samples in six different locations acquiring 20 points in an area of 10 x 10 μm^2 every time. An example of a typical force curve of these samples is reported in Figure 4.5.

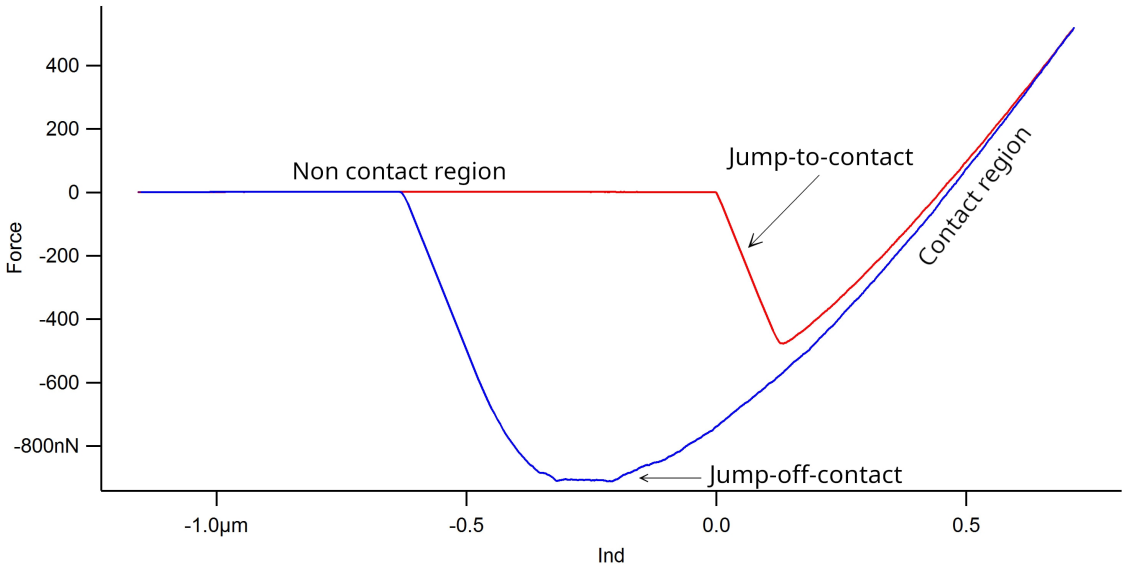

Figure 4.5: Typical force curve of laboratory made PDMS samples (in this case PDMS-6K). The red trace is the approach curve, while the blue one is the retraction curve; different regions are also indicated.

Results reported in Table 4.7 show that there is no significant difference in the adhesion force with the reduction of the crosslink density (and so the increase of the length of the chain strands) or with the decrease of the reaction yield. Examples of force curves for each sample are reported in Figure 4.6.

PDMS sample	Adhesion force ± standard deviation (10^{-7} N)
PDMS-6K	9.9 ± 0.2
PDMS-9.5K	9.8 ± 0.2
PDMS-17K	10.1 ± 0.3
PDMS-27.5K	10.5 ± 0.2
PDMS-42.5K	11.3 ± 0.4

Table 4.7: Adhesion force on five laboratory made PDMS samples with an AFM head speed of 3.5 μm/s and a maximum load of 500 nN.

Then, to check if viscoelasticity can have a role in determining the adhesion force and if this can be described in the usual framework, measurements of the adhesion force at the maximum applied load of 500 nN and at variable AFM head speeds were collected. Five different head speeds were chosen: 0.5 μm/s, 1.75 μm/s, 3.5 μm/s, 7.5 μm/s and 14.0 μm/s. Going beyond the lowest or the greatest speeds is not helpful because of instrumental limits: at lower speed, the instrumental and thermal noise would be able to reduce the precision of measurements too much, while greater speeds are not always possible with the used equipment.

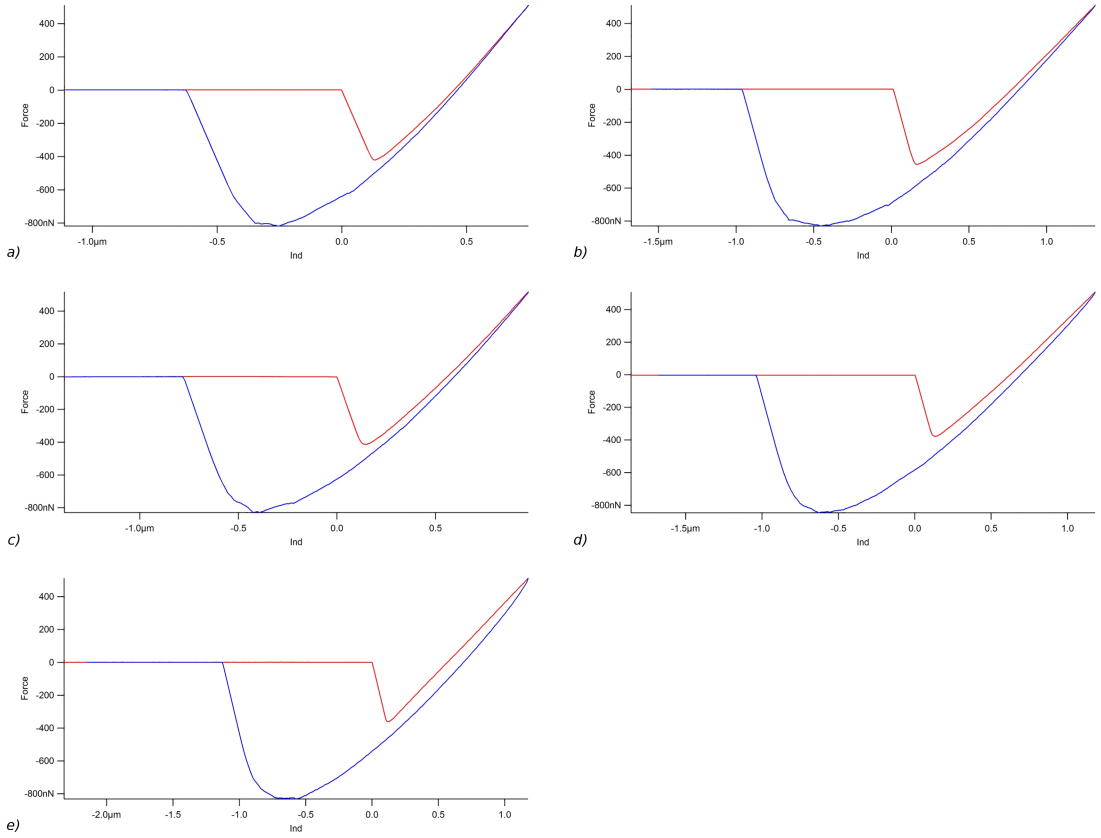

Figure 4.6: Examples of force curve of PDMS-6K in panel (a), PDMS-9.5K in panel (b), PDMS-17K in panel (c), PDMS-27.5K in panel (d) and PDMS-42.5K in panel (e) collected at the AFM head speed of 3.5 μm/s and a maximum applied load of 500 nN.

To study the effect of viscoelasticity on adhesion, the knowledge of the crack speed is necessary. As previously mentioned, this parameter is not easily accessible, especially in an AFM test. This is why the contact area in AFM tests is usually very small and cannot be imaged with optical system, so its direct measurement is almost impossible. Other methods must be found to extract it from force curves or from the AFM head speed. However, in all these methods, it is necessary to establish where the contact point is along the raw deflection-displacement data in order to transform them in a reliable force-indentation curve. For the y-axis the main problem is not the bare transformation from deflection to force that is straightforward with equation 3.5, but the choice of the origin of this axis. For the x-axis, the determination of the contact point is crucial to make a correct transformation of it into indentation according to equation 3.16 and to get reliable

data. Determination of the contact point on soft surfaces is not trivial: they can deform immediately when touched (and so a true zero-indentation point does not exist) or they can be deformed by attractive forces, before the contact with an extension of the surface toward the probe. That is why some authors justified their different choices of the contact point according to the characteristics of the material they were studying. In the case of PDMS, the main and often the unique contribution to the adhesion force is due to the van der Waals forces: this is due to the fact that the electrostatic force is not usually present and, in any case, it is also well visible in the force curve, while the capillary force cannot be established because PDMS is hydrophobic, so only the van der Waals forces, that are ubiquitous, remain. An estimation of the F_{vdW} using equation 2.35 with the values of the Hamaker constant reported in Tables 3.2 and 3.9 shows that it can overcome the cantilever force for distances from the sample that are in the order of nanometres, while, if the distance is just an order greater, the van der Waals forces are not able to bend the cantilever. By inspecting the deflection-displacement curves it is possible to see that only sometimes the first point of the incoming jump-to-contact region is in the range of nanometres from the previous points, while in the great part of curves, the first point of the jump-to-contact region is in the range of 10^{-8}m (in panel (b) of Figure 4.7 an enlargement of the first part of the jump-to-contact region is shown: the first point just next to the zero force line is in the nanometres range from the previous ones). Thus, to be precise, the real contact point should be the first point of the jump-to-contact region: however, because the polymer is very soft, when the probe and the PDMS are in contact, suddenly the probe indents the surface driven by adhesion forces. Actually, the process is so fast that the AFM often cannot capture the two different steps (the initial contact and then the adhesion induced indentation) even if it collects points every 0.5 ms. Attempts to use the first point of the jump-to-contact region were made, however, because these points can have quite different distances from the zero force line, this resulted in a less precise determination of adhesion force. On the other hand, it was evaluated that the error due to the neglecting of the real contact point in the

nanometres range is lower or of the same order of the experimental error found on the adhesion force. That is why, in the end, the last point of the zero force line, just before the beginning of the jump-to-contact region, is chosen as contact point (some authors that worked with PDMS made the same choice).

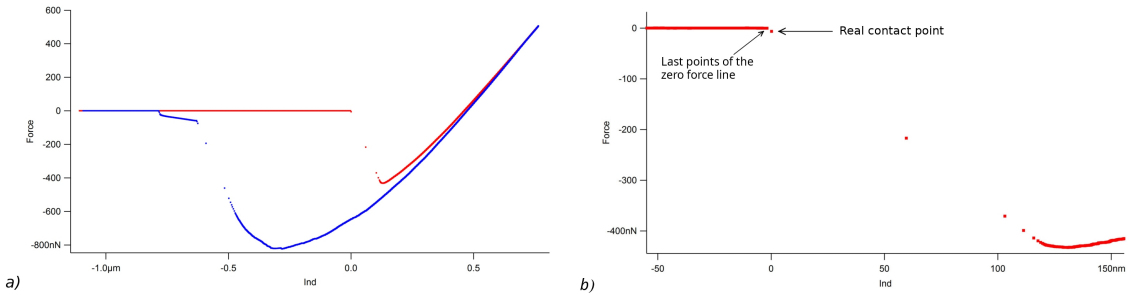

Figure 4.7: An example of force-indentation curve collected on PDMS-6K sample in panel (a) and an enlargement of the beginning of the jump-to-contact region in panel (b).

It was written that van der Waals forces often are the unique contribution to adhesion force for the studied system. However, in just one case, also an attractive electrostatic force was observed (it is thought that is an electrostatic force because it acts over a long range): it happened with the second run of adhesion measurements on PDMS-6K and an example of one of the force curve collected is shown in Figure 4.8. In this case, even if the choice of the contact point was done carefully, further corrections of the force values were needed to get them in the same order of all the others collected. Specifically, it was evaluated that, when this force is present, adhesion is usually greater of 0.2 μN with respect to the usual values: so experimental force data were reduced by this amount.

Once the force-indentation curve is obtained, a strategy to find out the contact radius should be chosen. However, before going into the details of the calculation, the choice of the suitable adhesion model should be done. An easy way to decide is the calculation of the Tabor parameter μ_T defined in equation 2.106. With an estimated values of $\Delta\gamma$ PDMS-borosilicate glass of 66 mJ/m^2 (from equation 2.23 with values from Tables 3.2 and 3.9) and E^* of 1 MPa (choosing the higher limit of the values reported in Table 3.2) the Tabor parameter μ_T is much greater than 1

and so the JKR model can be used (z_0 was chosen in the range of 0.3-0.5 nm [41, 59]).

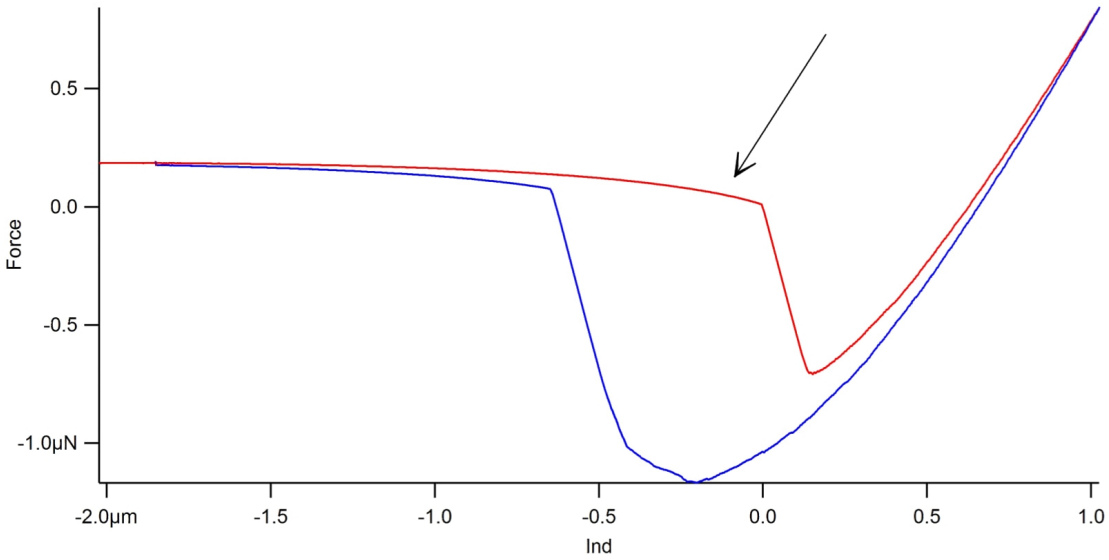

Figure 4.8: Example of force curve collected on PDMS-6K: the arrow shows that an extra long-range force is present.

Models that can link the AFM head speed to the contact radius based on the geometry of the contact are not developed for a spherical probe. An additional problem of this type of models when applied to very soft samples is also that they are not able to distinguish between the receding of the crack or the extension of the polymer during the retraction curve. This is because, when the probe is removed from a soft surface, the unloading process can be both with or without crack opening: if the contact area is reduced, then there is a crack opening event, but if the polymer deforms and elongates itself toward the probe the contact area (and so the crack) remains constant. Often both behaviours can be present, with one of the two dominating. That is why these models are applied with simpler geometry than the sphere and usually in experimental conditions where the maximum applied force is very low, that is not the case of this work.

Attempts to use the approach of inserting the general formula of the dependence of H from v into the general formula of the JKR model and then rebuilding the

force-indentation curve failed both if the Runge-Kutta or the Barquins methods were used. In this case, a suitable set of guest parameters to replicate the entire force-indentation curve could not be found: very often the calculated curve showed a minimum much lower than the experimental one. Consideration of the conditions used in articles where these methods are applied for PDMS, like in [57], reveals that the experimental conditions used are different from those used in this thesis: in that article, the maximum applied load is ten time greater and also adhesion force and the area between the force axis and the negative part of the retraction curve are greater. Thus, in that case, adhesion tests are performed in more extreme conditions than those used in this work.

Because all the methods found in literature and tried were not applicable or not suitable for the used test conditions, a different strategy was developed. There are two general equations of the JKR model but with three unknown parameters, a, E^* and H: in order to solve them it is necessary to know at least one of these parameters in a different way. In the case of this work, there could be the possibility of estimating E^* from the DMA or the swelling measurements. However, because of the difficulties found in the way to obtain and let those values be congruent, and, more importantly is the fact that both the two methods are bulk techniques, it seemed better to look for another strategy to obtain E^*. The same authors that used the numerical methods like the Runge-Kutta or that suggested by Barquins were able to get the value of E^* from the first part of the retraction curve. In fact, this part of the curve is usually linear and that means that there is not change in the contact radius: equation 2.129 expressed in the form $F(\delta)$, if a is considered a parameter, is linear and so, fitting the first part of the curve with a line to get the intercept and the slope lets the determination of both E^* and the maximum a. This approach was preferred because one can obtain a value of the modulus in same conditions as those used for the adhesion test. Once E^* is known, general formulas of the adhesion model can be solved for a and then H can be calculated. The values of a and H were calculated for the minimum of the retraction curve (adhesion force) and one point before and one point after it: a is obtained solving the cubic

equation 2.129 for a, knowing the couple of values F–δ from the curve, and because the discriminant was always positive, there was only one real solution. The crack speed is then calculated with the forward finite difference formula using the contact radius of the adhesion point and the following one, knowing that the AFM collected points each 0.5 ms. Finally H is calculated from equation 2.130. The advantage of this strategy is that v and H, which assume different values especially near the minimum of the curve are calculated exactly in the adhesion point without using averaged values. Moreover, inspection of the curve in the region of the minimum may also provide information about the detachment mechanism. Disadvantages are probably linked to the fact that this strategy is very local and so imperfections due to the type of measurements or connected to the fact that the minimum is where detachment is taking place (and this is not a quasi-static process) can lead to less precise measurements.

Starting with data analysis, values of E of the five samples obtained from the linear fitting of the first part of the force curves are reported in Table 4.8 (force curves at the lowest AFM head speed are used, to avoid or to reduce the effect of viscoelasticity on the modulus).

PDMS sample	Young's modulus ± standard deviation (10^5 Pascal)
PDMS-6K	2.67 ± 0.07
PDMS-9.5K	1.13 ± 0.01
PDMS-17K	1.62 ± 0.02
PDMS-27.5K	0.86 ± 0.05
PDMS-42.5K	0.68 ± 0.06

Table 4.8: Values of the Young's modulus of the five laboratory made PDMS samples. Values were calculated from the linear fit of the first part of the retraction curve at the lowest AFM head speed and they are the average of three sets of twenty measurements each.

A comparison with values reported in Table 4.5 shows that the Young's moduli calculated from force curves are much greater than those calculated with the DMA analysis for all the samples. Surely, the main difference between the two used

techniques, the DMA and the AFM, is that the former is used to determine bulk properties, while the latter is designed for the study of surface characteristics. In the present work, the experimental conditions used in the AFM analysis are far away from those used, for example, in nanoindentation test that usually provides values of moduli similar to those of the bulk. Specifically, the use of a spherical indent with a relatively large diameter very likely results in a test that probes surface properties without touching the bulk.

Discrepancies between bulk and surface measurements of the modulus have been already reported in literature, especially for polymers: the surface modulus can be either greater or lower than the bulk one and this is often related to the higher mobility of chains near the surface [172-174]. For that reason, values of E obtained from the AFM test are used in the following calculations for the determination of the crack speed and H: all of them are determined using light conditions for surface properties determination and it does not seem correct to use the bulk moduli in a study of surface parameters.

Then, surface Young's moduli are calculated from force curves at every AFM head speed and their values are reported in Table 4.9. As it is possible to note, only samples PDMS-27.5K and PDMS-42.5K show relevant increases in the modulus at the highest speeds, while in the other cases differences are not so significant (for example, there are not changes in the modulus according to the speed for PDMS-6K). Actually, this situation confirms what previously seen with DMA analysis.

Continuing the data analysis, values of the energy release rates and the crack speeds are reported in Tables 4.10 and 4.11, respectively, referring to the AFM head speeds. As it is possible to see, the energy release rate is mostly constant at all speeds for samples PDMS-6K, PDMS-9.5K and PDMS-17K, while increases significantly at the greatest speeds for samples PDMS-27.5K and PDMS-42.5K, in a similar fashion as seen for the bulk and surface Young's moduli.

AFM head speed (μm/s)	Young's modulus ± standard deviation (10^5 Pascal)				
	PDMS-6K	PDMS-9.5K	PDMS-17K	PDMS-27.5K	PDMS-42.5K
0.5	2.67 ± 0.07	1.13 ± 0.01	1.62 ± 0.02	0.86 ± 0.05	0.68 ± 0.06
1.75	2.72 ± 0.08	1.15 ± 0.01	1.66 ± 0.02	0.92 ± 0.05	0.77 ± 0.06
3.5	2.72 ± 0.07	1.160 ± 0.009	1.69 ± 0.02	0.97 ± 0.05	0.85 ± 0.06
7.5	2.72 ± 0.07	1.177 ± 0.009	1.75 ± 0.02	1.04 ± 0.05	0.95 ± 0.06
14.0	2.70 ± 0.06	1.20 ± 0.01	1.79 ± 0.02	1.11 ± 0.05	1.05 ± 0.06

Table 4.9: Young's moduli of the five laboratory made PDMS samples at five different AFM head speeds.

AFM head speed (μm/s)	Energy release rate ± standard deviation (mJ/m^2)				
	PDMS-6K	PDMS-9.5K	PDMS-17K	PDMS-27.5K	PDMS-42.5K
0.5	38.5 ± 0.9	41 ± 1	40 ± 2	41 ± 1	42 ± 1
1.75	39 ± 1	41 ± 1	41 ± 2	41 ± 1	43 ± 2
3.5	39 ± 1	41 ± 1	42 ± 2	42 ± 1	47 ± 2
7.5	40 ± 1	42 ± 1	43 ± 2	45 ± 1	52 ± 3
14.0	39.8 ± 0.7	43 ± 1	45 ± 2	47 ± 1	55 ± 3

Table 4.10: Energy release rate of the five laboratory made PDMS samples at the adhesion point.

Crack speed has a different behaviour because it always increases with the increase of the AFM head speed. However, interestingly, at the same AFM head speed there is usually a decrease in the crack speed along with the increase of the polymer chain length, with the exception of PDMS-17K that shows values similar but slightly higher than PDMS-9.5K.

AFM head speed (μm/s)	Crack speed ± standard deviation (μm/s)				
	PDMS-6K	PDMS-9.5K	PDMS-17K	PDMS-27.5K	PDMS-42.5K
0.5	2.15 ± 0.05	1.39 ± 0.05	1.7 ± 0.1	1.32 ± 0.01	1.7 ± 0.1
1.75	5.9 ± 0.3	3.6 ± 0.1	4.9 ± 0.3	3.5 ± 0.2	3.25 ± 0.9
3.5	8.8 ± 0.2	7.3 ± 0.1	9.7 ± 0.6	6.5 ± 0.3	5.4 ± 0.2
7.5	19.3 ± 0.9	14.2 ± 0.4	15 ± 1	12.8 ± 0.3	11.9 ± 0.6
14.0	32 ± 1	24.9 ± 0.6	25.9 ± 0.5	21.7 ± 0.8	18 ± 1

Table 4.11: Crack speed of five laboratory made PDMS samples at the adhesion point.

A useful way to verify the relationship between the energy release rate and the crack speed is to express equation 2.124 with the dissipative function in the form of 2.127 as Log-Log relation:

$$\log\left(\frac{H-\Delta\gamma}{\Delta\gamma}\right) = n\log(v) + \log(\beta) \tag{4.1}$$

where the left-hand side is also called normalised energy release rate. In this way, the relationship becomes linear and the slope provides the value of the exponent n. The value of $\Delta\gamma$ should be the adhesion work referred to the perfect elastic contact. In the case of the couple PDMS-borosilicate glass this value can be estimated from the contributions of the surface energies reported in Tables 3.2 and 3.9 or from the value of H at the lowest speeds. Calculation of $\Delta\gamma$ from surface energies leads to a value of 66 mJ/m^2, that is greater than any experimental values of H found in this work. Because $\Delta\gamma = H$ when there is no energy dissipation (elastic materials), inspection of values of H at the lowest speeds, suggests a value of $\Delta\gamma$ of 38 mJ/m^2, that is similar but lower than that of PDMS self-adhesion. A value of the adhesion work for the couple glass-PDMS that is similar to that of the self-adhesion of PDMS has been already noted in literature: some authors explain that with the tendency of PDMS to leave some loose chains on the glass surface after the first contacts [175]. They justified this explanation with the observation that in the first contacts adhesion is usually greater than in the following contacts: however, in this work, this behaviour has not been observed. Moreover, it was not easy to find the surface

energy of glass in literature: for glass, surface energy is often determined in the melt state and not at room temperature. In addition, glass can be of different types, so an accurate value of its surface energy is really difficult to find, and the one reported in Table 3.9 should be considered just an indication. In fact, other authors found values of $\Delta\gamma$ referring to glass and PDMS adhesion also lower, like 26 or 30 mJ/m^2 [176, 177], without problems due to contamination of the glass surface because of PDMS loose chains. However, because the energy release rate of PDMS-6K is almost the same at all the AFM head speeds, and this is the expected behaviour when there are no dissipative processes during the detachment, 38 mJ/m^2 is taken as the value of $\Delta\gamma$: the choice of a value that is slightly lower than the experimental ones is due to the fact of avoiding a null argument in the logarithm of equation 4.1. Figure 4.9 shows the Log-Log relation between the normalised energy release rate and the crack speed (equation 4.1). As seen before, only the last three points of PDMS-27.5K and the last four points of PDMS-42.5K are significantly different and so the linear fitting is done only for these two samples and among the specified points. In both cases the fitting is rather good, with an R^2 of 0.97 and 0.98 and the slopes of the fitting lines, i.e. the values of n, of 0.54 ± 0.09 and 0.65 ± 0.06 for PDMS-27.5K and PDMS-42.5K, respectively. As reported in Table 3.2, many values of n were found in literature: in the case of this work, values are around 0.6, the most common one.

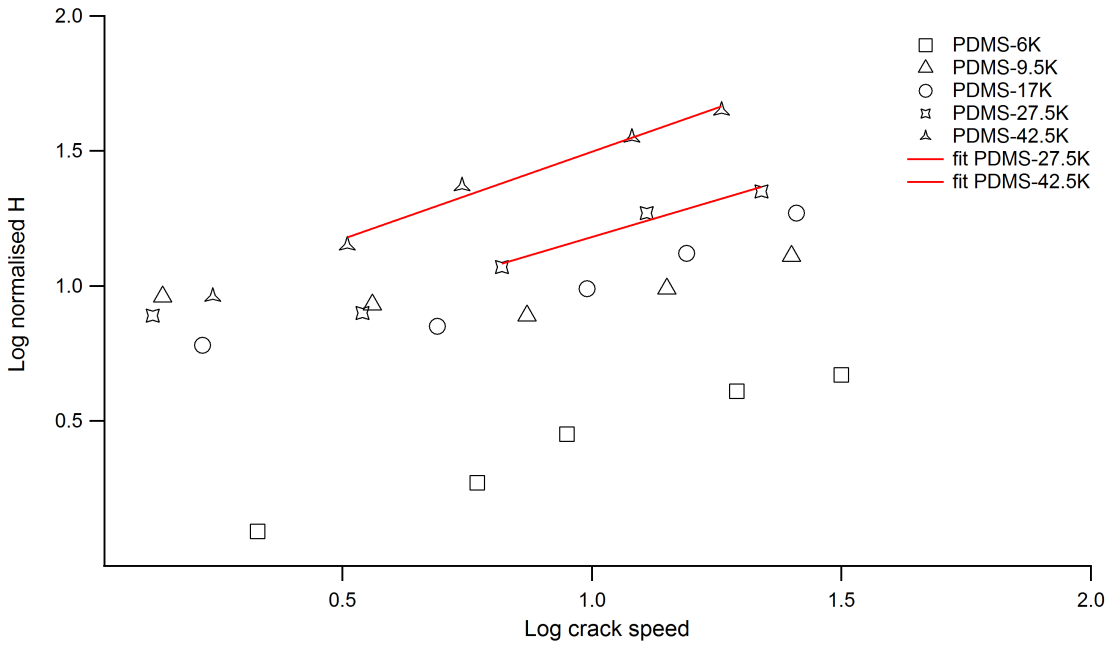

Figure 4.9: Log-Log plot of the normalised energy release rate versus crack speed. Fitting lines of the last three speeds and the last four speeds are shown for PDMS-27.5K and PDMS-42.5K, respectively.

An interesting insight into the detachment mechanism of PDMS is provided by the inspection of the retraction force curve near the adhesion point. Even if the following discussion is limited to the point immediately before and after the minimum, the same conclusion can be assumed for the near points, as is possible to note in Figure 4.10. For all the samples and at all speeds, the absolute value of the difference of the radii of the adhesion point and the point before is always lower than the difference of the radii of the adhesion point and the point immediately after it. The greatest discrepancy of the two differences happens at the lowest speed, however, also at the highest speed this discrepancy is significant, ranging from 20% to 40%. That means that the crack speed suddenly changes at the adhesion point, increasing after it; before it, just looking at Figure 4.10, it is almost similar without abrupt changes, even if the detachment is occurring. A behaviour like this can be explained from macroscopic observations of the detachment dynamics of soft PDMS samples: optical images of debonding PDMS from a cylindrical polished stainless steel flat-ended probe with a diameter of few mm show that the contact area remains more or less constant until the pull-off,

while, after it, air fingers become prevalent and spread until the two surfaces are no longer in contact (Fig. 4.11) [55].

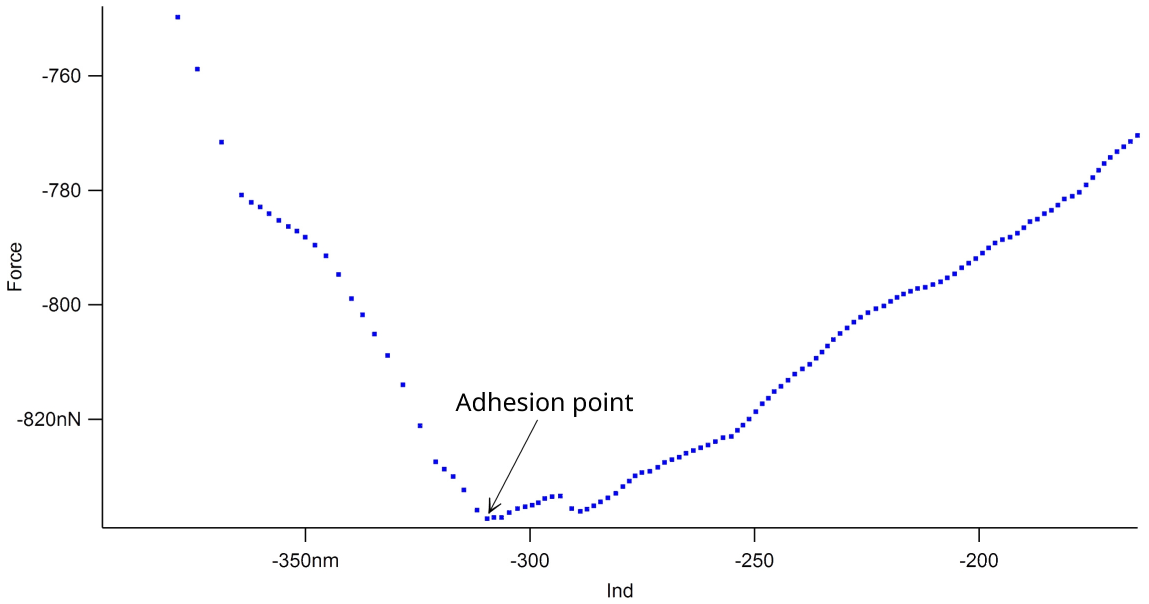

Figure 4.10: Enlargement of the jump-off-contact region with the adhesion point and the near points.

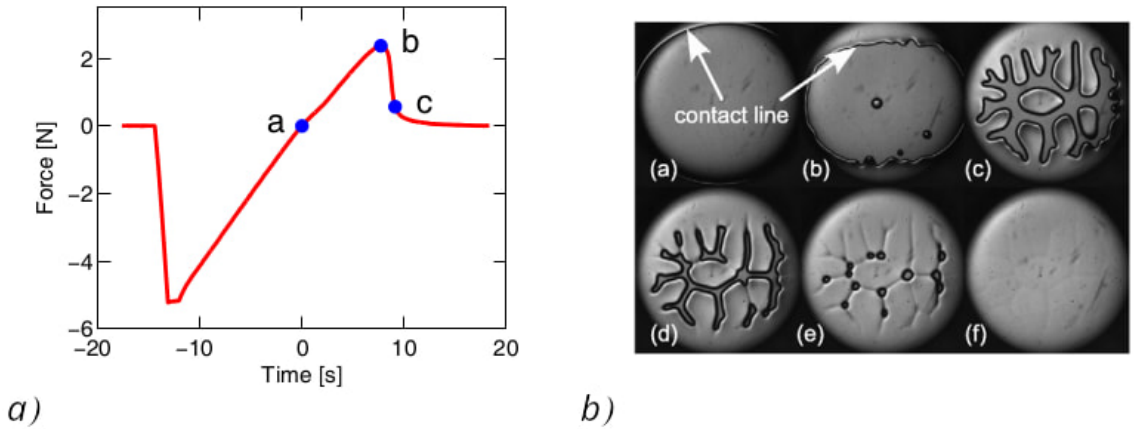

Figure 4.11: Macroscopic debonding mechanism of PDMS using a 6 mm circular polished steel punch. A typical force versus time curve is shown in panel (a): the point a is the zero force point after the jump-to-contact region; the point b corresponds to the pull-off point while c is the point at which the force drops to 25% of the maximum force. The corresponding optical images of the detachment process are shown in panel (b): the letters a, b and c correspond to the a, b and c points of the curve shown in panel (a). As it is possible to see, the contact line (and so the contact area) hardly moves before the pull-off point; after it, the detachment process continues with air fingers formation. Images reprinted by permission from Springer Nature Customer Service Centre GmbH: Springer The European Physical Journal E, Debonding Energy of PDMS, Nase, J., Ramos, O., Creton, C., Anke, L. COPYRIGHT (2013).

This suggests that soft PDMS is greatly deformed (elongated) before the beginning of the reduction of the contact area, and that, later, with the fingering process, deformation is extreme. Despite this high deformation, it is reported that there are no residues remaining on the probe and that, after the debonding, the PDMS surface remains intact. Very likely, a similar behaviour can happen also at microscale: from the inspection of force curves, it is difficult to believe that just before the adhesion point the contact radius is still close to the maximum contact radius. However, the fact that after the adhesion point the debonding continues with greater changes in the contact radius suggests that a different debonding behaviour begins at that point until the detachment is complete. Looking at the withdraw curve as a whole, as previously noted, the initial part is usually linear or with slight changes in the tangent slope and that is recognised as a detachment without crack opening, i.e. at constant contact radius. Only in the part next to the minimum the slope of the tangent changes quickly and that means that also the contact radius is changing and finally, after the minimum, changes in the contact radius are greater and less regular until complete debonding is achieved. This framework, together with the observations made at the macroscale, suggests that the detachment process starts in a similar manner as seen at the macroscale, with polymer deformation rather than debonding, continues with a stage in which the contact radius changes almost regularly (for example with a change in the whole contact radius) and goes to the end after the adhesion point with sudden reductions of the contact radius that can find a reasonable explanation in the fingering detachment process. The reasons why in this case, differently from the macroscale, the stage in which the contact radius changes regularly can be observed, probably lies in the different contact geometry used. At the macroscale, a flat end probe is used: there is no lateral adhesion and, when the probe is withdrawn, the distance between it and the surface is the same for all the points of the surface and so the polymer deforms as a whole in a similar way on the entire surface; only when this deformation reaches the maximum, the polymer quickly detaches from the probe with the fingering process. At the microscale, in this work,

a spherical probe is used: contact is not only on the bottom of the sphere, that could be assumed to be almost flat, but all around it and when the withdraw begins, polymer surface that is laterally in contact with the probe experiences a stronger deformation and begins to detach before the central part. When only the central part remains in contact and when it reaches the maximum deformation, probably a detachment process such as fingering starts or becomes the main one. It is reasonable to think that the lateral debonding could happen with a more regular 'movement' of the contact radius as a whole, or, at least, with a minor fingering process. This hypothesis can be supported by the fact that, also at the macroscale, sometimes the movement of the contact perimeter as a whole is observed before the adhesion point. Very likely, the change in the geometry of the contact with a probe that allows the polymer to adhere also laterally, can enhance this stage of the detachment process that is not always observable with a probe where 'lateral' contact is not allowed. For sure, at the adhesion point there is a change in the crack speed that can be reasonably explained with the (prevalence of) fingering processes as seen at the macroscale.

A short consideration about why this change in the detachment regime is less evident at the highest AFM head speeds should be done. Very likely, this can be due to the fact that at the lowest speeds the debonding is a relatively quasi-static process and in this situation, can be thought to proceed through two stages that can be well distinguished. In fact, it is reasonable to think that in this condition, after the initial deformation, debonding starts as a whole process, where the contact line moves as a whole with possibly initial or limited fingering processes, and then, when the contact region is extremely deformed, the faster fingering detachment takes place. When the AFM head speed is increased, also the detachment rate increases and there is not a quasi-static regime: in this case, the rate of the process does not allow the polymer chains to (partially) comply with the new situation and it is likely that the difference between the two stages is reduced, probably because fingering will start in advance or the contact line will not move as a whole but with fingers along its perimeters. In this work, a speed that could

eliminate the passage between the two stages was not reached. It can be that it exists and it is greater than those used in here, or it is also possible that the two stages cannot be completely merged into a unique detachment mechanism with the ratio between the difference of the two radii changes reaching a plateau value. Further studies are needed to clarify this point.

Considering this situation, where the adhesion point is a sort of 'turning point' in a change of the detachment regime, a reconsideration about how to calculate or estimate the crack speed is appropriate. In this work the contact radius is calculated in three points and only two of them are used for the determination of the crack speed: is that a right procedure? Attempts to use another couple of points were made: for example with the use of the backward finite difference formulas between the adhesion point and the point before it. It appears that values of the crack speeds are lower, and apart from that, also the accuracy of these measurements is lower because often at the two lowest AFM head speeds the thermal and/or instrumental noise of the probe overcomes the calculated radii differences leading to results with no physical meaning. The use of only the last three highest speeds was carefully considered, but then discarded after the consideration that only three data points for each polymers are too few to draw useful conclusions. For the same reasons linked to the thermal/instrument noise, also the use of the central finite difference formula with the radii of the point before and the point after the minimum, was discarded. Of course, noise in the measurements is present also for the contact radius after the adhesion point: however, because in this case the change in the contact radius is always significant, noise could influence the precision of the measurements at the lowest speeds but could not be in the same order or greater of the measurements themselves. That is why, in the end, the choice of the forward finite difference formulas is basically forced.

4.7 Conclusions

Five PDMS samples were synthesised with end-linking reaction starting from different lengths of the initial linear chains and care was taken to have surfaces as

smooth as possible. Even if the yields of these reactions range from 80% to 60% and the crosslink density is extremely different from sample to sample, they do not show relevant differences in adhesion behaviour when force curves are acquired at low speeds. Only PDMS-27.5K and PDMS-42.5K which are those with the lowest crosslink densities and yields show a mild increase in adhesion with the increase of the AFM head speed, confirming the viscoelastic behaviour shown during the DMA analysis. It is quite surprising that networks like those, that are quite far away from being ideal, have mostly an elastic behaviour.

Because models and procedures reported in literature to analyse how the adhesion or the energy release rate change with the crack speed were not applicable or not working properly with these samples, crack speed was directly calculated from the force-indentation curve at the adhesion point and at the following point. In according to the DMA analysis results, only PDMS-27.5K and PDMS-42.5K show a change in the energy release rate with respect to the crack speed: this change follows the most used power relationship with an exponent in the expected range of 0.6. A close look also at the point before the adhesion point suggests that probably, also at the microscale, the debonding of PDMS is similar to that observed at the macroscale, with the contact line moving continuously until the adhesion point where it is likely that fingering processes take place.

An interesting remark should be done on the choice of the Young's modulus that should be used in equations to obtain the contact radius: it was chosen to calculate it from the initial linear part of the force-indentation curve, where it is known that the detachment proceeds without crack opening. The modulus calculated in this way is different from that obtained from bulk techniques, like DMA, showing that attention should be paid in choosing 'coherent' sets of parameters.

From the results summarised in this chapter and the data reported in the literature mostly about similar systems and analyses in the two introduction chapters it is clear that results and conclusions are sometimes different and strongly dependent on the specific conditions used. Apart from the synthesis of PDMS, that can be different because of stoichiometry and/or the yield, careful

attention should be paid to the experimental conditions (parameters) used for the determination of bulk and surface properties. Especially for the latter and in particular for adhesion, considerations about the applied load and the geometry of the tip can be crucial in determining if bulk or surface properties are actually tested. This may explain why PDMS samples that are proved to be elastic with macroscopic analysis can show adhesion depending on chains lengths (and so on crosslink density) like in [67, 68]: conditions used in these articles are different from the ones used in this work and in particular, greater loads are generally used and probably this results in testing bulk properties, rather than surface ones.

However, even if there is not agreement on adhesion-crosslink density dependency, viscoelasticity influence on adhesion is well studied and results show that the more viscoelastic the PDMS is, the greater the adhesion is. There are still differences mostly on the values of the exponent that correlates the crack speed to energy release rate. This can be due to the fact that this relationship is empirical and still not very clear in the physical meaning, together with the difficulties in determining the crack speed.

It may be also possible that the effects ascribed to the differences in the crosslink density may be due to viscoelasticity: maybe when adhesion is probed with high loads, the elastic framework does not hold and also samples that are elastic at the macroscale can show viscoelastic behaviour at microscale. Results shown in this chapter may suggest that this could be a nice explanation of the discrepancies seen in the literature: in fact, with the laboratory made PDMS samples, the viscoelastic behaviour appears only in particular conditions. The same sample could be elastic at low (angular or crack) speeds but shows viscoelastic effects when conditions become less mild like in the case of higher speeds or, (why not?) greater loads.

Again, studying so difficult properties, like viscoelasticity, at the microscale can be tricky and a lot of care should be used in choosing the best conditions to avoid unusual conclusions.

5 Teknek's samples

In this chapter a complete analysis of Teknek's samples will be presented. Samples provided by Teknek can be divided in two main groups (rollers or elastomers and plastic sheets): because they are quite different, results of analyses will be described into different subsections. Rollers will be also divided into the couples specified by Teknek (FilmClean/UltraClean, PanelClean/UTFClean and NanoUClean/NanoClean). Names and corresponding materials of Teknek's samples are listed in Table 3.1.

Sample characterization is done by means of: optical microscopy and AFM imaging for the study of morphology, contact angle measurements for the determination of hydrophobic/hydrophilic character of the surfaces, and again AFM for adhesion analysis with colloidal probes.

This chapter is organised in this way: firstly, results of the measurements are reported and commented in the same order they are listed in the previous paragraph; then, discussion and comparison about all the data collected are done in order to find a correlation between adhesion and morphology and to determine which surface can be cleaned by which roller and finally, conclusions are drawn together with suggestions for improving roller performances.

5.1 Surface morphology

5.1.1 Rollers

These six samples are provided as end products and so with a significant curvature: even if care was taken in cutting them trying to have a flat base and selecting the regions to analyse, curvature and tilt of the surfaces, at least in one direction, could not be always avoided. As a consequence, optical images will show some parts not completely focused (usually the perimeter). In the AFM images, processing is mainly done preserving curvature: this choice is due to the fact that programs for AFM image analysis are not able to remove the so significant curvature and tilt of these

surfaces without heavily affecting surface features (in fact, roller curvature is out of the range of the waviness filters of program for the AFM images processing). However, curvature and tilt can affect values of RMS roughness in a significant way: the choice to preserve surface features and consequently have qualitative RMS roughness values is justified by the better qualitative description of surfaces without artefacts which are difficult to quantify. Moreover, RMS roughness depends also on the tip of the probe used for the imaging: because in this work, roughness is important in its correlation with adhesion, roughness values acquired with colloidal probes during the adhesion measurements are sometimes more indicative than an 'absolute' roughness.

With these rollers, often RMS roughness values are so different according to the location of the analysis that to provide an average of the collected values does not accurately represent the specific differences in features. Thus, RMS roughness will be presented as collected for each scan sizes and repetition of the analyses.

5.1.1.1 FilmClean/UltraClean

FilmClean and UltraClean rollers appear to be quite different also at first glance: the former is blue with a quite smooth surface, while the latter is red with a rough surface. Optical images of these two samples, together with three AFM images of 10 x 10 μm^2 are shown in Figures 5.1 and 5.2.

Optical microscopy of FilmClean confirms that the surface is quite smooth with presence of straight lines often at regular distance, probably due to the production process. There are also holes of irregular and different sizes, usually in the micrometre scale and smaller peaks. Some holes resemble the shape of craters because they have some peaks inside them. These features are confirmed by the AFM images, where the dimensions of holes and peaks is more accurate. Both in the first and third AFM images of Figure 5.1 is evident the presence of small peaks inside the beginning depressions.

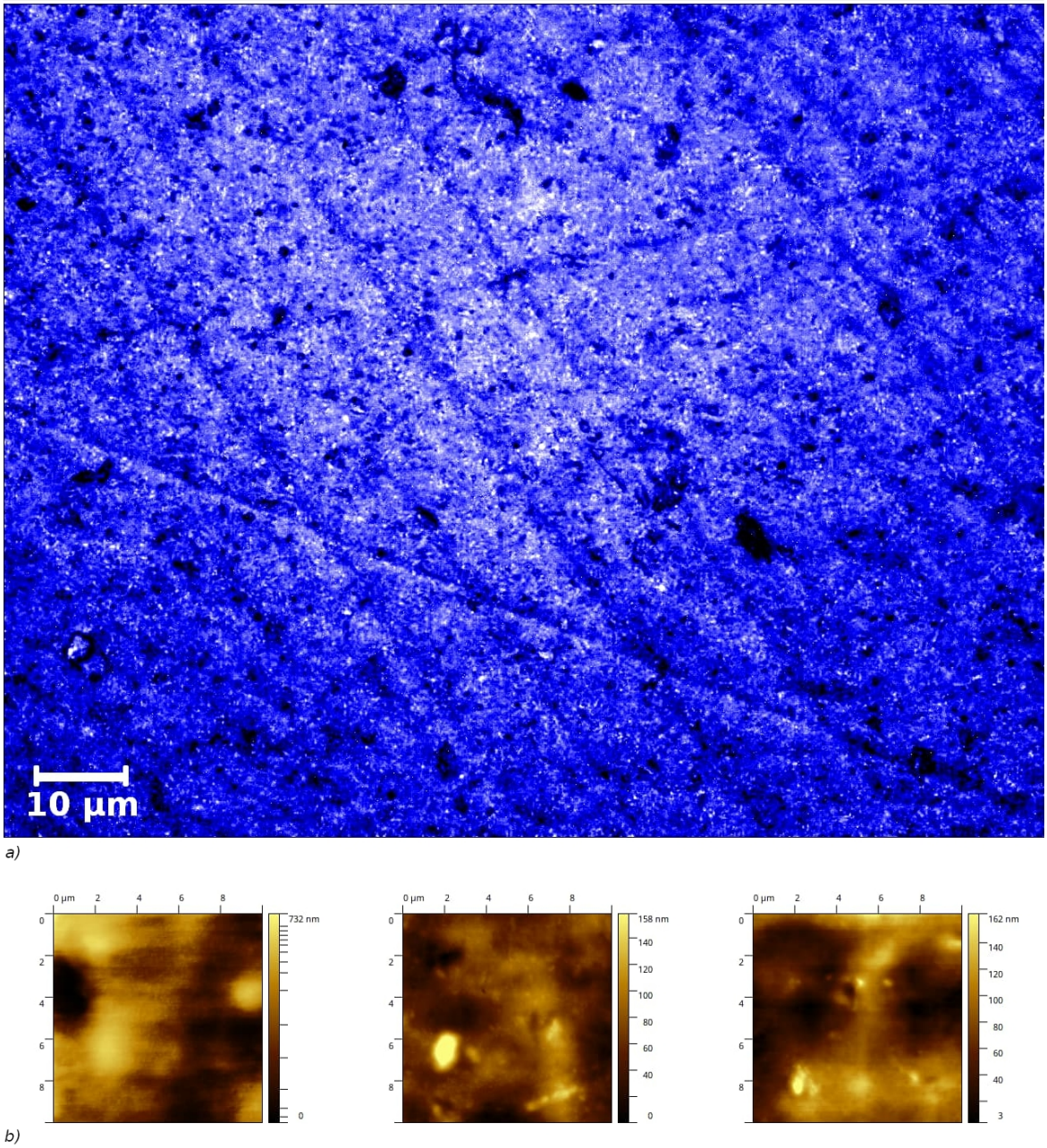

Figure 5.1: FilmClean morphology by optical microscopy at 50X magnification in panel (a) and by AFM in three different locations of 10 x 10 μm^2 in panel (b).

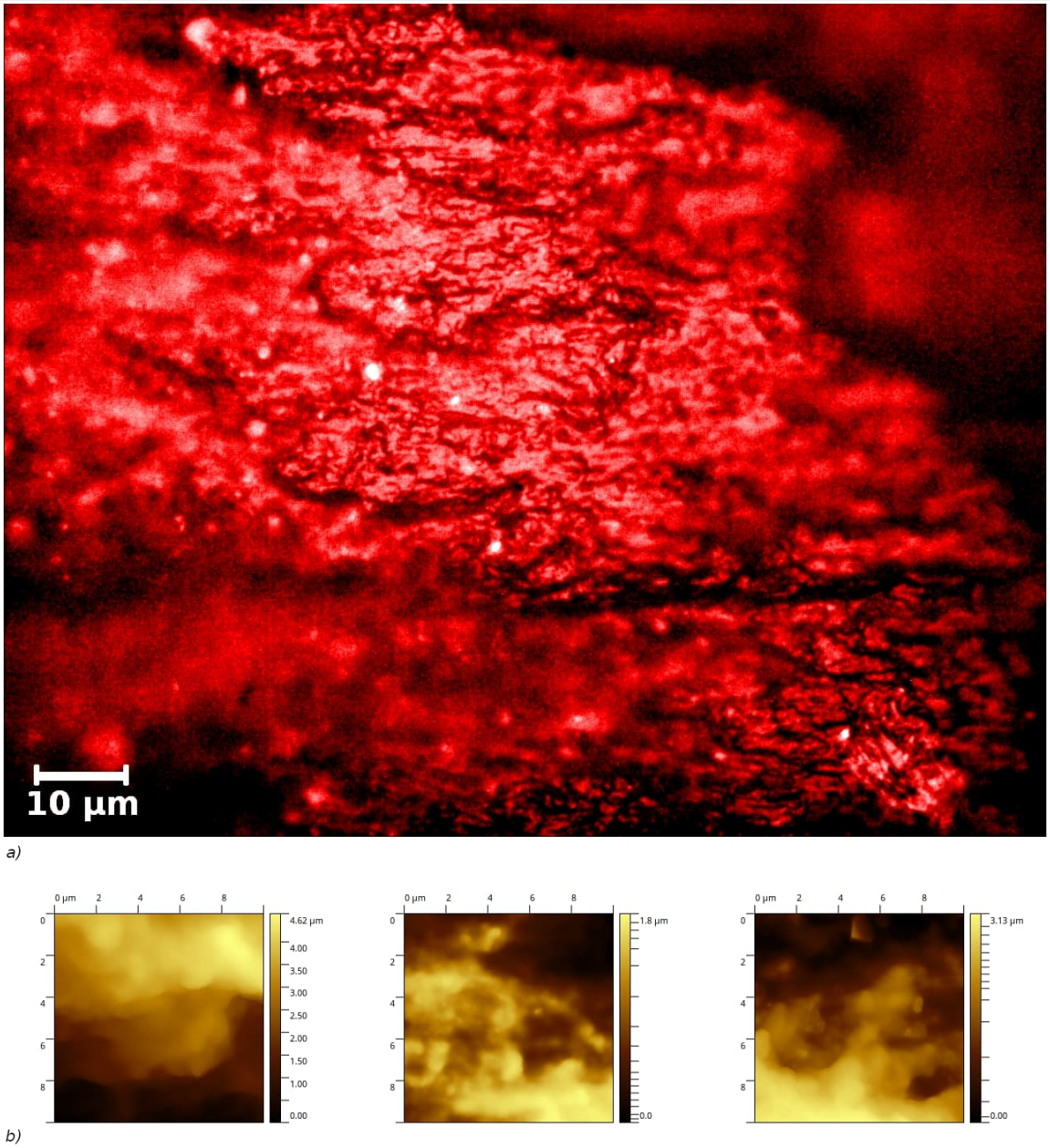

Figure 5.2: UltraClean morphology by optical microscopy at 50X magnification in panel (a) and by AFM in three different locations of 10 x 10 μm^2 in panel (b). Optical image is not completely focused because of the presence of planes with different heights, that could not be focused together at this magnification.

Optical analysis of UltraClean confirms that this is the ground sample of this couple of rollers: it shows 'terracing' at different heights with steep slope regions connecting them. Terracing appears to be quite large (more than 10 μm) with rough and irregular surfaces. AFM images show this surface in greater detail

confirming that it is quite rough with differences in height also around 5 μm and rounded blunt edges.

To quantify roughness, RMS roughness collected in three different locations and at three different scan sizes is reported in Table 5.1 and in Table 5.2 for FilmClean and UltraClean, respectively. In both cases, RMS roughness increases with the scan sizes: it is not possible to achieve a unique value of roughness for each scan size because roughness is very dependent on the specific features that are present. In any case, the highest RMS values are related to locations with the greatest differences in height.

FilmClean	RMS roughness first run (nm)	RMS roughness second run (nm)	RMS roughness third run (nm)
Scan size 1 μm	18.0	11.7	27.6
Scan size 5 μm	90.7	19.8	28.2
Scan size 10 μm	91.1	26.4	34.3

Table 5.1: RMS roughness of FilmClean in three different locations and scan sizes.

UltraClean	RMS roughness first run (nm)	RMS roughness second run (nm)	RMS roughness third run (nm)
Scan size 1 μm	252	79.1	99.3
Scan size 5 μm	656	188	291
Scan size 10 μm	1250	316	715

Table 5.2: RMS roughness of UltraClean in three different locations and scan sizes.

5.1.1.2 PanelClean/UTFClean

PanelClean and UTFClean rollers seem more similar to each other than the previous couple: they have the same colour and the material does not appear to be very different. The only main difference that is evident at first glance is that UTFClean has a very rough surface, while PanelClean seems as smooth as FilmClean. Images

from optical microscopy and AFM of these two samples are shown in Figure 5.3 (PanelClean) and Figure 5.4 (UTFClean).

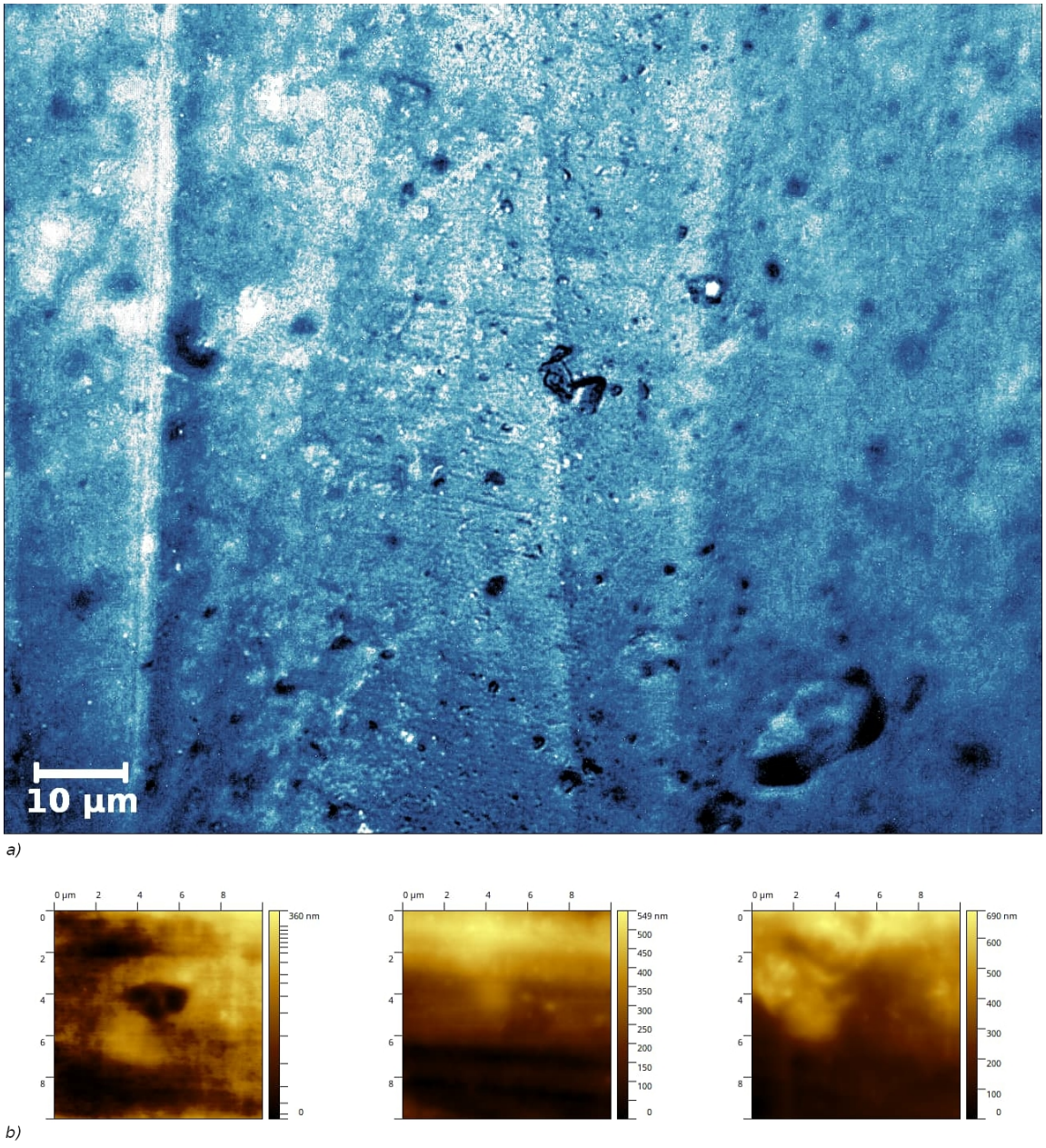

Figure 5.3: PanelClean morphology by optical microscopy at 50X magnification in panel (a) and by AFM in three different locations of 10 x 10 μm^2 in panel (b).

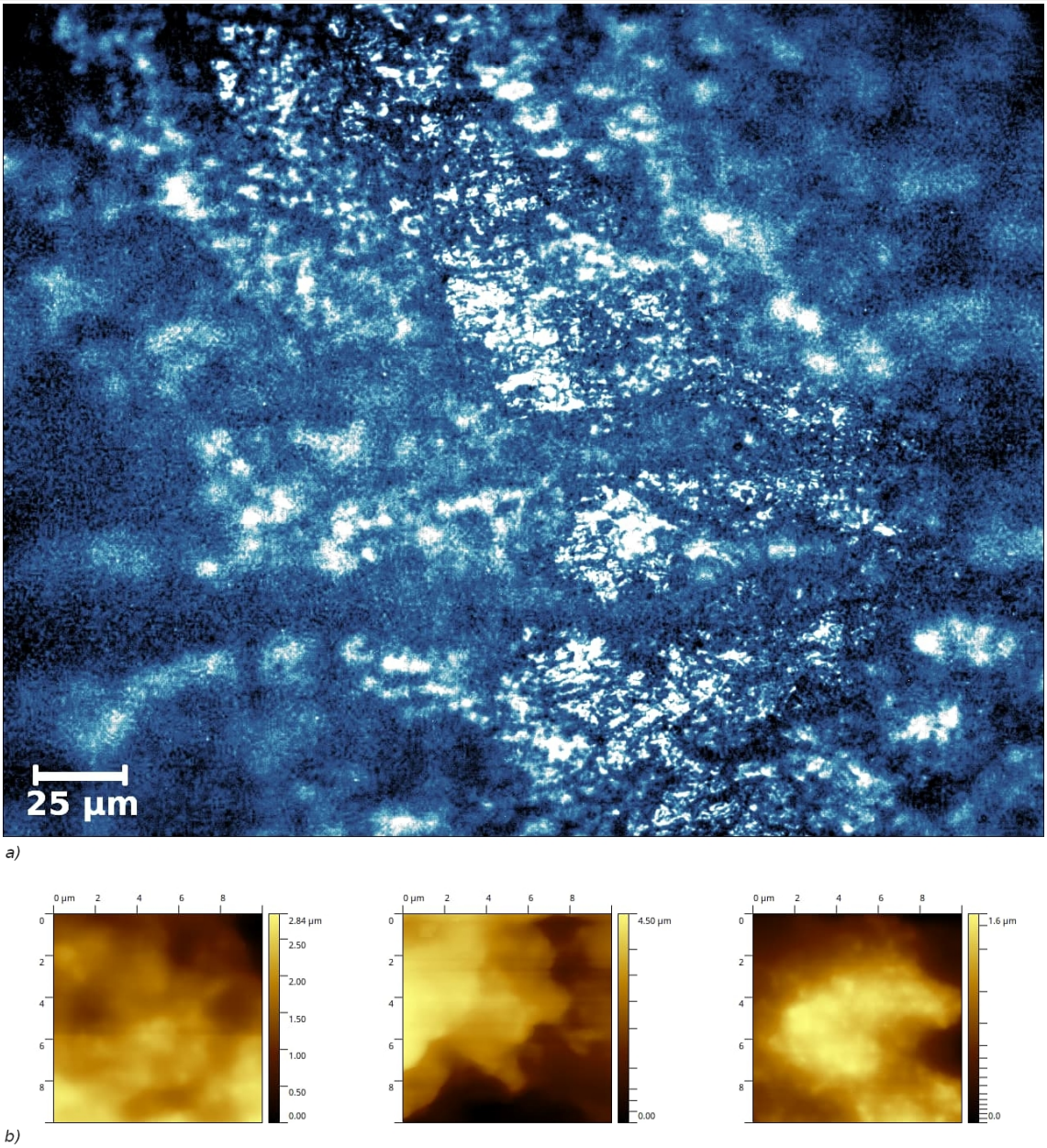

Figure 5.4: UTFClean morphology by optical microscopy at 20X magnification in panel (a) and by AFM in three different locations of 10 x 10 μm^2 in panel (b). Even if the magnification of the optical image is only 20X, the surface is not completely focused because of the significant differences in height among the central highest region and the lowest lateral regions.

Optical image of PanelClean confirms that this sample has a quite smooth surface, which remembers the one of FilmClean. In fact, also on the PanelClean surface there are straight lines and holes. Straight lines are larger that those of FilmClean and they are in relief contrary to FilmClean where they are hollowed,

however they are probably due to the production process as in FilmClean. Holes appear to be fewer and bigger than those in FilmClean, and again, some of them resemble craters because there are some peaks inside them. Peaks are fewer and smaller than those seen in the optical image of FilmClean: that is probably why PanelClean seems to have a smoother surface than FilmClean, at least looking at the optical microscopy images. AFM images confirm that the PanelClean surface shows fewer irregularities than FilmClean, in fact, aside from the holes, the remaining parts of the images are quite smooth. In the first AFM image it is also possible to see that inside the hole there are some thin walls that divide it into three parts. UTFClean is the ground sample of this couple of roller as is very evident in the optical image. Its surface is quite irregular and resembles the surface of UltraClean. However, in the case of UTFClean regions do not have the same extensions and they are not at constant heights like the 'terracing' of UltraClean. In addition, optical microscopy images suggest that the slope of the descending parts of the surface is less steep than in UltraClean surface. For all these characteristics, the UTFClean surface appears to be more irregular than Ultraclean and probably it is not completely correct to deals with higher and lower regions, because it is not easy to define boundaries among them: it probably better to describe the UTFClean surface as a very irregular surface, having some higher locations that quickly descend. The difference in heights are also evident in Figure 5.4 where, even if with a lower magnification, it is not possible to focus the entire surface. AFM images of UTFClean show that, at a scan size of 10 μm, the details of the surface are similar to those seen for Ultraclean: there are descending regions with rounded blunt edges.

RMS roughness collected in three different locations and at three different scan sizes is reported in Table 5.3 and in Table 5.4 for PanelClean and UTFClean, respectively. Also for the couple PanelClean and UTFClean roughness increases with scan size, in a greater way for UTFClean. Also in this case roughness values are strongly dependent on the specific features presented in each location: only for PanelClean at the scan size of 1 μm it is possible to say that roughness has similar values around 20 nm. Roughness values of UTFClean show that roughness

behaviour is similar to that of UltraClean, even if with a different range of values for each scan size.

PanelClean	RMS roughness first run (nm)	RMS roughness second run (nm)	RMS roughness third run (nm)
Scan size 1 μm	19.2	22.0	15.3
Scan size 5 μm	48.9	34.5	90.0
Scan size 10 μm	56.0	161	185

Table 5.3: RMS roughness of PanelClean in three different locations and scan sizes.

UTFClean	RMS roughness first run (nm)	RMS roughness second run (nm)	RMS roughness third run (nm)
Scan size 1 μm	72.9	60.3	11.3
Scan size 5 μm	253	507	64.5
Scan size 10 μm	534	951.6	243

Table 5.4: RMS roughness of UTFClean in three different locations and scan sizes.

5.1.1.3 NanoUClean/NanoClean

NanoUClean and NanoClean rollers seem quite similar each other: they have the same colour and the material does not appear to be very different. The only main difference that is evident at first glance is that NanoClean has a rougher surface than NanoUClean. Images from optical microscopy and AFM of these two samples are shown in Figure 5.5 (NanoUClean) and Figure 5.6 (NanoClean).

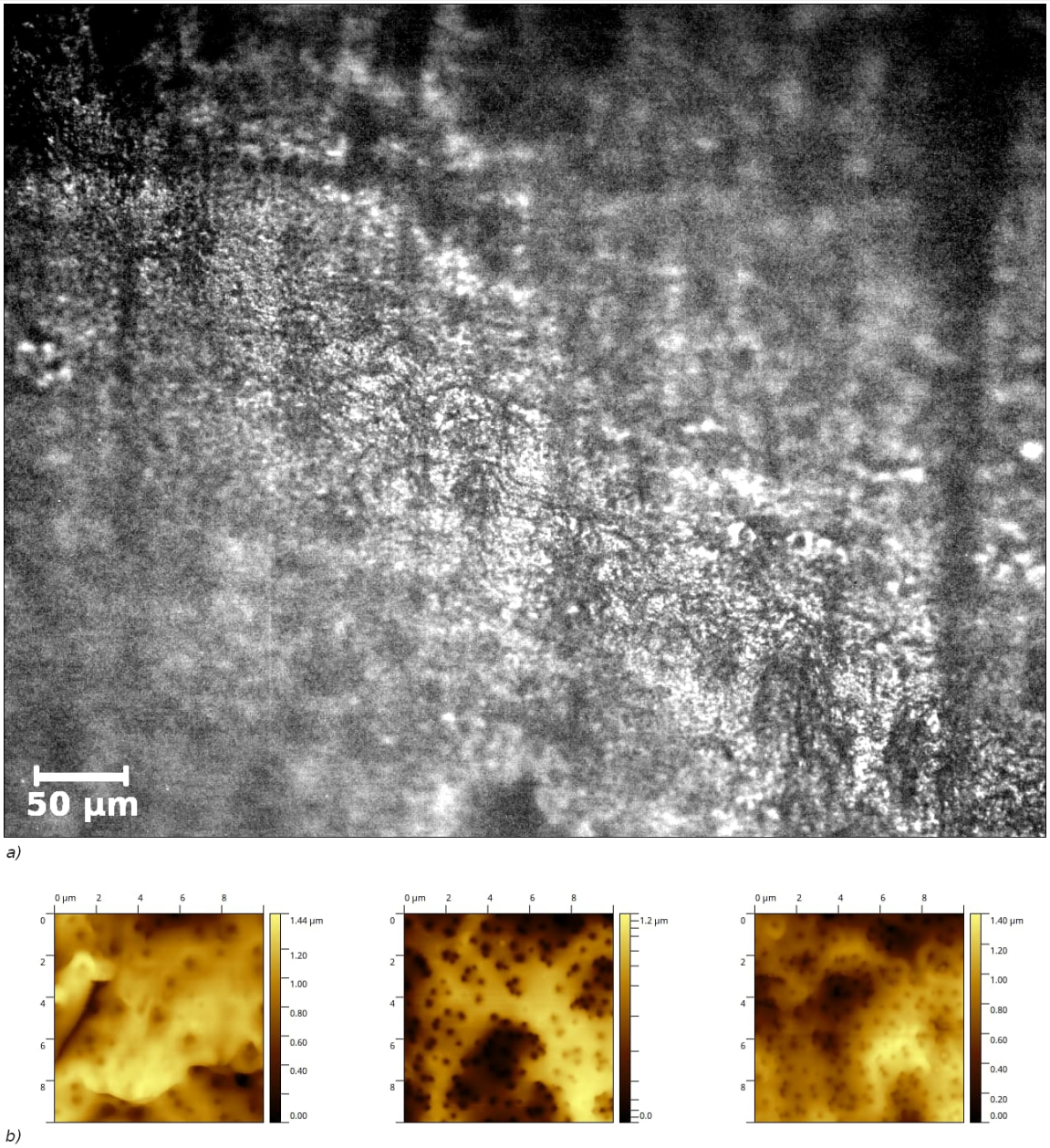

Figure 5.5: NanoUClean morphology by optical microscopy at 10X magnification in panel (a) and by AFM in three different locations of 10 x 10 μm^2 in panel (b). Even if the magnification of the optical image is only 10X, the surface is not completely focused because of the significant differences in height among the central highest region and the lowest regions.

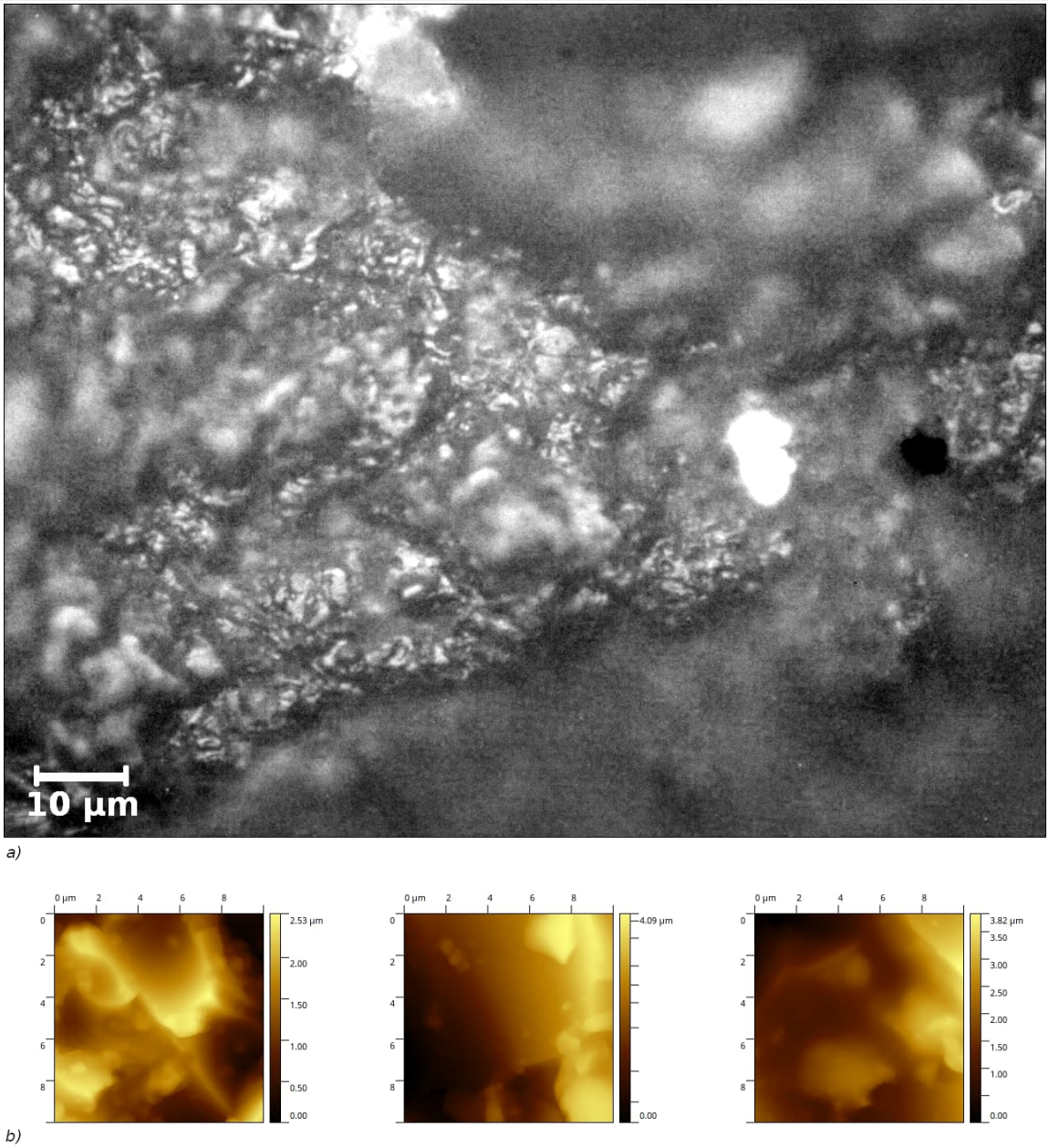

Figure 5.6: NanoClean morphology by optical microscopy at 50X magnification in panel (a) and by AFM in three different locations of 10 x 10 μm^2 in panel (b). Optical image shows some regions that are not focused because of the significant difference in height with the central part of the image.

Optical microscopy shows that neither NanoUClean nor NanoClean have smooth surfaces. NanoClean, the ground roller of the couple, shows a quite irregular surface with regions at different heights connected to each other with very steep slope regions. It resembles the 'terracing' described for UltraClean; in fact, the main difference with UltraClean is that the differences in height of the 'terracing' are

greater than in UltraClean and the slope of the small region connecting 'terracing' is greater than in UltraClean. NanoUclean shows a roughness that ranges in a smaller scale than NanoClean: it has an irregular surface but without showing sharp edges between boundary regions.

AFM images show that NanoUClean has an irregular surface with high and low regions continuously connected without harsh edges. A specific characteristic of the NanoUClean surface is the presence of small round holes quite regularly distributed on it. These holes have a diameter of 0.4-0.6 μm with regular shape. On the contrary, NanoClean shows large horizontal regions, eventually with some asperities, and very sharp descending edges. A specific characteristic of the NanoClean surface is that edges are angular: no one of the other rollers shows this characteristic. Differently from NanoUClean, there are not small round holes on NanoClean surface.

RMS roughness values of NanoUClean and NanoClean are listed in Table 5.5 and in Table 5.6, respectively. Like in the case of the other two couples of rollers, also NanoUClean and NanoClean show an increase of roughness with the increase of the scan size. In the case of NanoUClean, it appears that the values of roughness at the highest scan size are similar and, probably, a value around 250 nm can be a good indication of roughness at the scan size of 10 μm. Comparing NanoUClean roughness with the values of the other two non-ground samples, it appears to be the roughest, however it is not rougher than the ground samples: it is possible to say that it has a roughness that is intermediate between ground and non-ground samples. NanoClean roughness depends on the specific features presented on the surface like in the case of the other two ground samples. Despite this, it could be noted that in the scan size of 1 μm and 5 μm roughness is more homogeneous than in UltraClean and UTFClean.

NanoUClean	RMS roughness first run (nm)	RMS roughness second run (nm)	RMS roughness third run (nm)
Scan size 1 μm	50.6	98.0	81.3
Scan size 5 μm	173	181	288
Scan size 10 μm	256	203	282

Table 5.5: RMS roughness of NanoUClean in three different locations and scan sizes.

NanoClean	RMS roughness first run (nm)	RMS roughness second run (nm)	RMS roughness third run (nm)
Scan size 1 μm	102	49.4	106
Scan size 5 μm	344	302	551
Scan size 10 μm	532	750	1790

Table 5.6: RMS roughness of NanoClean in three different locations and scan sizes.

5.1.2 Plastic sheets

These samples are quite different from rollers seen before: firstly, they are provided as flat sheets and so in more suitable shape for a morphological analysis and secondly, they differ from roller materials because they are not made of elastomeric material. Considering the material which they are made of, they are also very different each other, like if they have to represent the behaviours of different classes of plastics. 'Sample 47' is copper-plastic laminate: with this in mind, on the whole speaking this sample will be referred to as plastic sample.

In order to maintain a homogeneous way to show results, also for these samples roughness values will be listed as they are collected, and not in the form of average and error. As for the rollers, this way of reporting results highlights the variability of some of these samples.

Each sample will be presented in a different subsection where morphology of its two sides will be discussed.

5.1.2.1 Sample 9

Optical and AFM images of 'Sample 9' are reported in Figure 5.7 and Figure 5.8 for side 1 and side 2, respectively. Images collected using the optical microscope do not reveal big differences in the features of the two sides. They look quite smooth with some round holes or protuberances and straight lines. In this case, some of these lines resemble scratches rather than something connected to the production process. Also the AFM images of the two sides are not very different, showing similar features like little holes, some peaks, waviness and straight lines (or scratches).

RMS roughness values of 'Sample 9' are listed in Table 5.7 and Table 5.8 for side 1 and side 2, respectively. As already seen, RMS roughness increases with the scan size for both sides. As a comparison between the two sides, it is possible to say that they show quite similar values of RMS roughness.

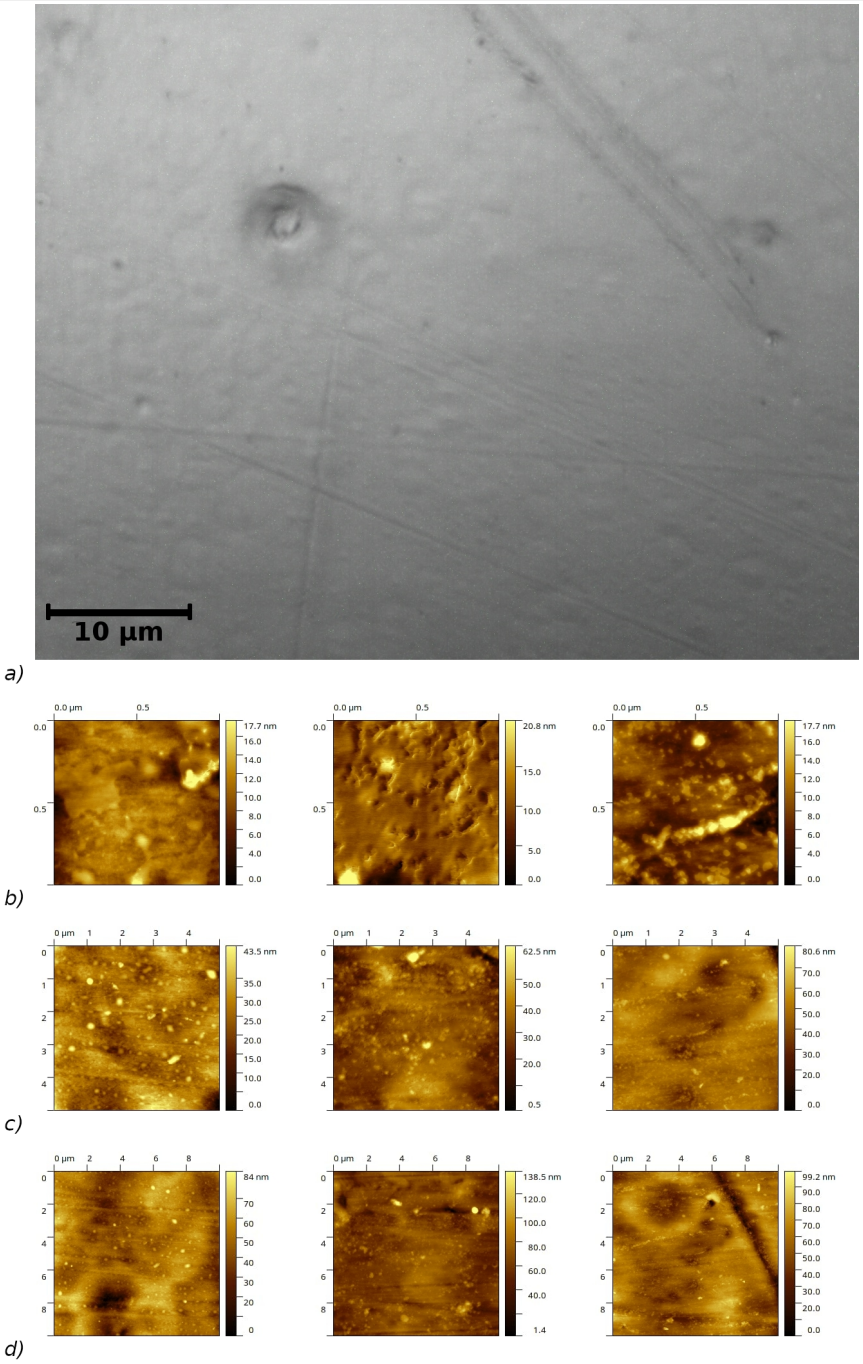

Figure 5.7: 'Sample 9 – side 1' morphology by optical microscopy at 100X magnification in panel (a) and by AFM at three different scan sizes of three different locations: 1 x 1 μm^2 in panel (b), 5 x 5 μm^2 in panel (c) and 10 x 10 μm^2 in panel (d).

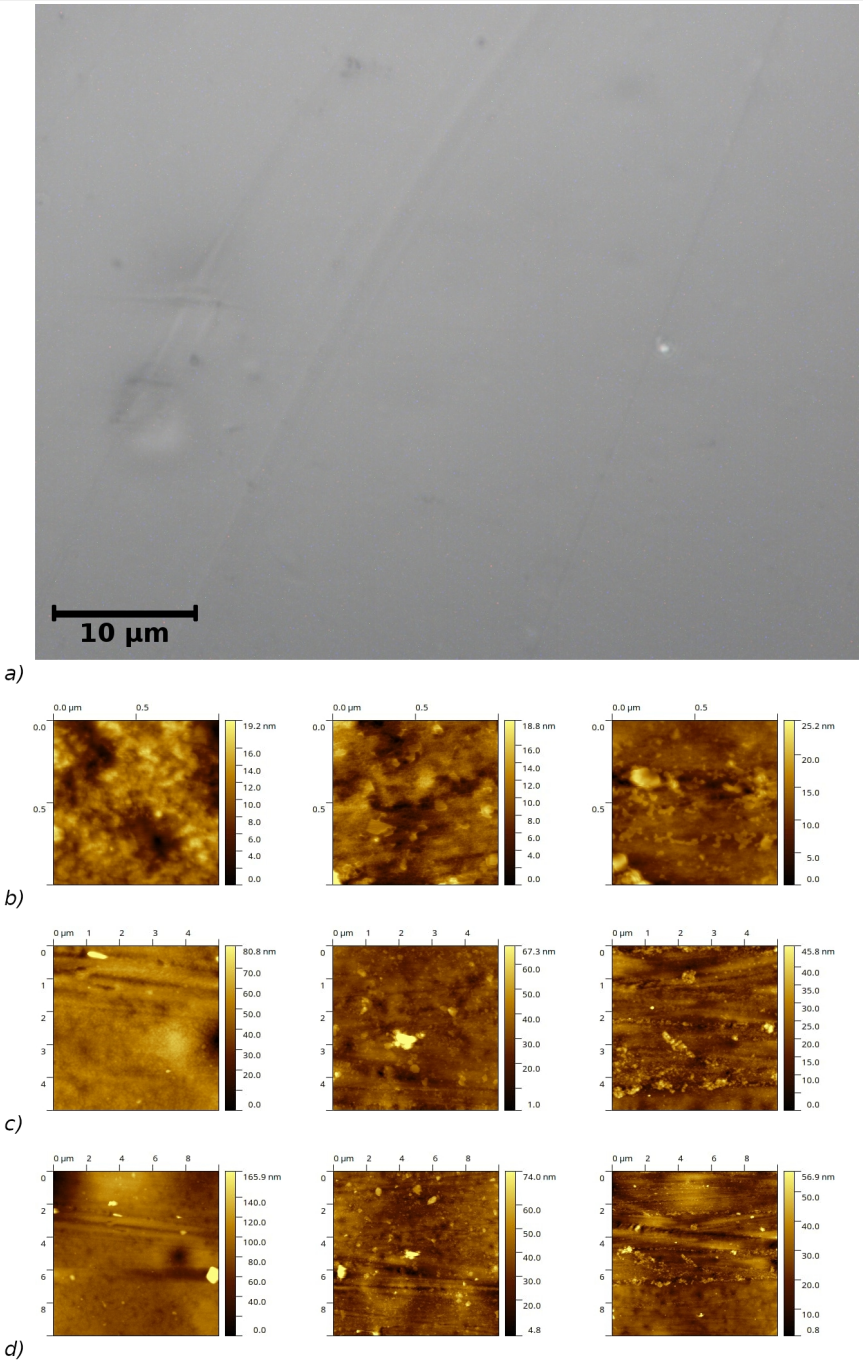

Figure 5.8: 'Sample 9 – side 2' morphology by optical microscopy at 100X magnification in panel (a) and by AFM at three different scan sizes of three different locations: 1 x 1 μm^2 in panel (b), 5 x 5 μm^2 in panel (c) and 10 x 10 μm^2 in panel (d).

Sample 9 – side 1	RMS roughness first run (nm)	RMS roughness second run (nm)	RMS roughness third run (nm)
Scan size 1 μm	2.25	2.81	2.78
Scan size 5 μm	4.92	7.29	7.17
Scan size 10 μm	10.7	11.6	13.1

Table 5.7: RMS roughness of 'Sample 9 – side 1' in three different locations and scan sizes.

Sample 9 – side 2	RMS roughness first run (nm)	RMS roughness second run (nm)	RMS roughness third run (nm)
Scan size 1 μm	2.92	2.62	2.66
Scan size 5 μm	7.23	9.27	4.91
Scan size 10 μm	19.7	8.59	6.55

Table 5.8: RMS roughness of 'Sample 9 – side 2' in three different locations and scan sizes.

5.1.2.2 Sample 18

Optical and AFM images of 'Sample 18' are reported in Figure 5.9 and Figure 5.10 for side 1 and side 2, respectively. Optical microscopy shows that the two sides of this sample are quite different: side 1 is quite smooth with some infrequent spots on it, while the side 2 is actually covered by hemispherical spots with different heights and diameters. The difference in height is quite significant: at the greatest magnification it is impossible to focus both the tops and the bases of these spots at the same time. Especially for side 1, AFM images reveal some features of the surface: in fact, on side 1, it is possible to see that there are small non-sharp peaks. These peaks show specific characteristics that do not seem to be random, so it is possible to group them into four sets. A first set comprises the smallest peaks observed in the scan size of 1 μm: they are mostly high 10 nm with a diameter of about 50-60 nm. In the same images, sometimes there are peaks that can be higher (between 10-20 nm) and larger (with a diameter of about 0.5 μm): these peaks belong to the second set and they are also visible in the images at the scan size of 5 μm as the lowest ones (in fact, in the images of 5 μm the details about the first set

of peaks are mostly lost). The third and the fourth sets are visible in the images at 5 and 10 μm, respectively. Peaks belonging to the third set are usually 40-50 nm high with a diameter of about 0.5 μm, while those of the fourth set have similar diameters but their height is about 70 nm. On side 2, AFM images show some parts of the big spots seen in the optical image: those that are present in these images have a diameter of about 0.5 μm and a height between 2 and 3 μm. It does not seem to see other significant feature in this side, such as the peak hierarchy seen on side 1. However, it is not possible to totally exclude that there are not further features: maybe there are too small to be well defined on those curve surfaces. This is also suggested by the first image of panel (b) of Figure 5.10 where it is possible to note some little spots on the curve surface, but it is not easy to go into greater details with an AFM on a surface that is so dense of big spots.

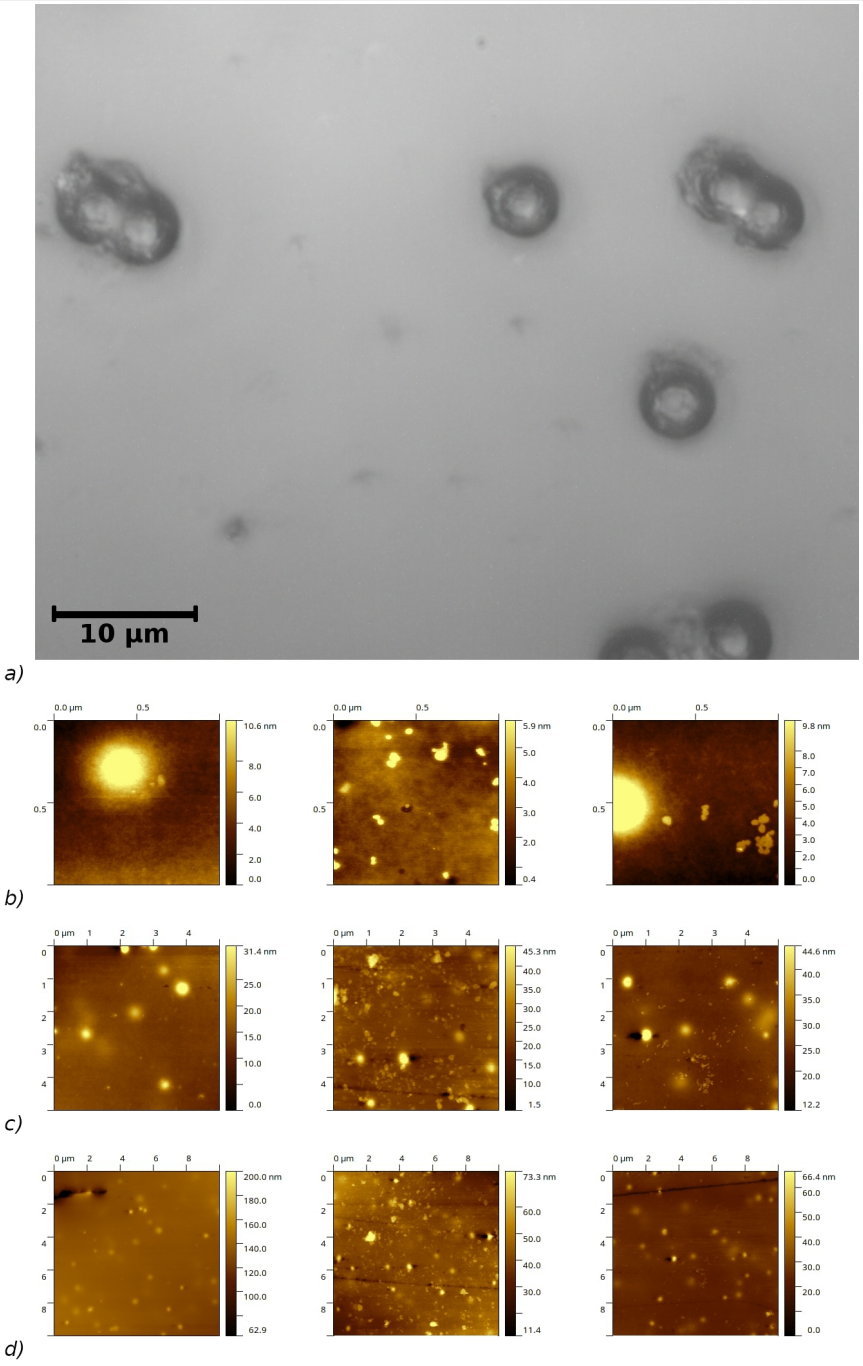

Figure 5.9: 'Sample 18 – side 1' morphology by optical microscopy at 100X magnification in panel (a) and by AFM at three different scan sizes of three different locations: 1 x 1 μm^2 in panel (b), 5 x 5 μm^2 in panel (c) and 10 x 10 μm^2 in panel (d).

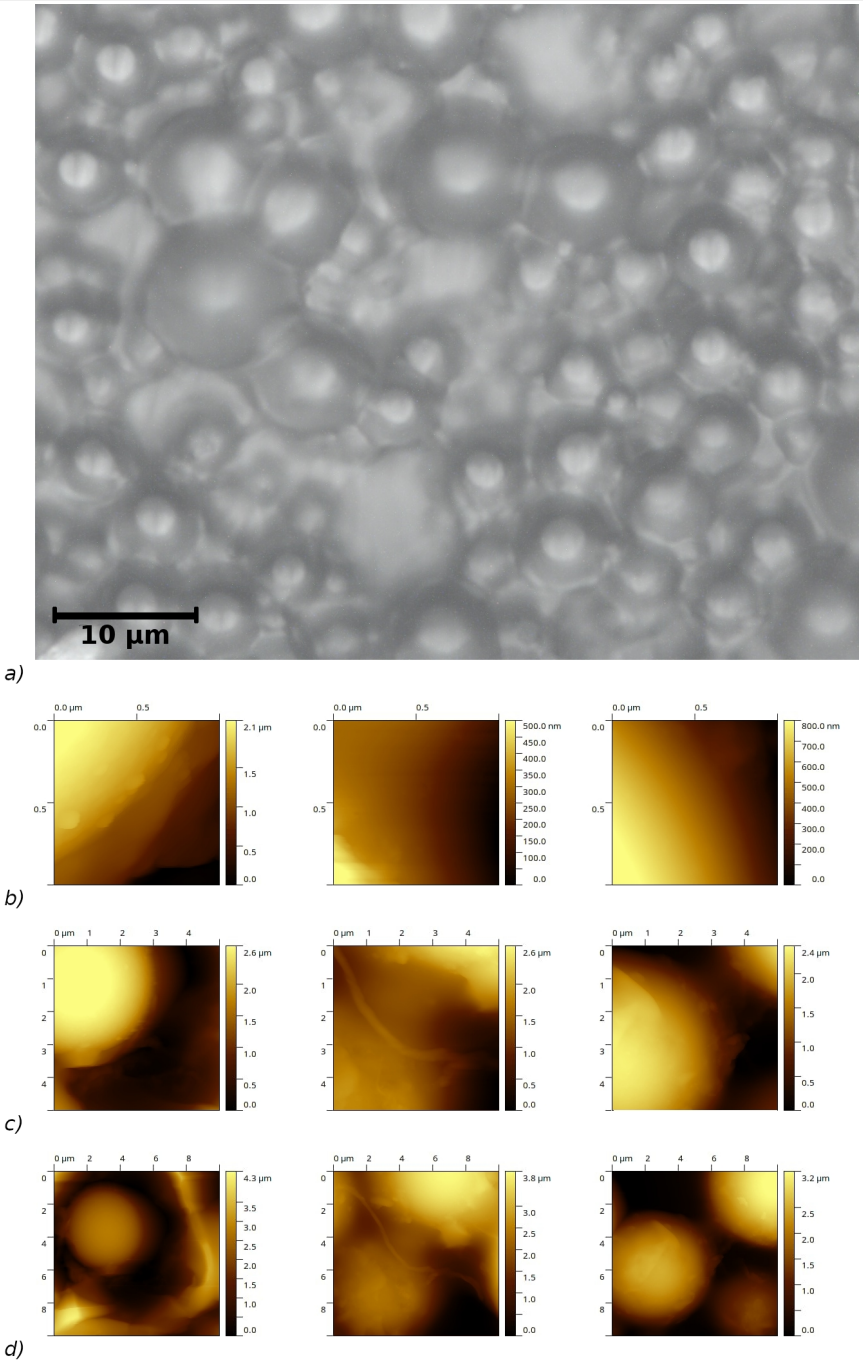

Figure 5.10: 'Sample 18 – side 2' morphology by optical microscopy at 100X magnification in panel (a) and by AFM at three different scan sizes of three different locations: 1 x 1 μm^2 in panel (b), 5 x 5 μm^2 in panel (c) and 10 x 10 μm^2 in panel (d). AFM images of this side are shown as they were collected without post-processing elaboration, such as flattening, because on this surface it will introduce heavy artefacts and distortions.

RMS roughness values of side 1 and side 2 are listed in Table 5.9 and Table 5.10, respectively: they reflect the big difference between the two sides. It is important to say that, due to the topological features of side 2, these images were not flattened. The flatten or planefit algorithm creates distortions and artefacts, so it was considered that the best solution consists in using the data as they were collected. Moreover, these surfaces are quite flat, and similar considerations and tests done on other samples with similar problems, just showed that the maximum positive bias in the RMS roughness values could be about 40 nm. Considering the RMS roughness values for the side 2, a similar bias (if there is this bias) does not change so much their description. The RMS roughness values of side 1 are quite the same for each scan size: most of them can vary from 2 nm to 4 nm. The greatest value found in the first run at the scan size of 10 μm is mainly due to the scar that can be seen in the image. Without that scar, the RMS roughness is around 4.70 nm. In conclusion, it is possible that there is an increase of roughness at the scan size of 10 μm, however, it is not as significant as in other samples. RMS roughness values of side 2 are quite different from the values of side 1. Side 2 shows also very different values of RMS roughness among the three runs for the same scan size. The presence of the big spots on this surface makes difficult to define clear values of RMS roughness: the only scan size that seems more reliable than the others is the 10 μm scan, with RMS roughness values around 900 nm.

Sample 18 – side 1	RMS roughness first run (nm)	RMS roughness second run (nm)	RMS roughness third run (nm)
Scan size 1 μm	2.24	0.73	2.83
Scan size 5 μm	2.94	4.00	2.93
Scan size 10 μm	7.87	6.15	2.90

Table 5.9: RMS roughness of 'Sample 18 – side 1' in three different locations and scan sizes.

Sample 18 – side 2	RMS roughness first run (nm)	RMS roughness second run (nm)	RMS roughness third run (nm)
Scan size 1 μm	572	95.5	225
Scan size 5 μm	951	500	726
Scan size 10 μm	915	903	882

Table 5.10: RMS roughness of 'Sample 18 – side 2' in three different locations and scan sizes.

5.1.2.3 Sample 19

Optical microscopy and AFM images of side 1 and side 2 of 'Sample19' are reported in Figure 5.11 and Figure 5.12, respectively. Optical images show that the two sides have different surface features on it: side 1 is characterized by the presence of irregular bumps, while side 2 is characterised by the presence of big round peaks not evenly distributed on the surface. AFM images confirm that the two sides of this sample have different features and provide new insight: side 1, that in the optical microscopy image appears as the most irregular is quite smooth at micrometre scale; on the contrary, side 2 that, from optical microscopy seems less rough, at micrometre scale presents several straight lines and some peaks of irregular shape.

RMS roughness values or the two sides of 'Sample 19' are listed in Table 5.11 (side 1) and Table 5.12 (side 2). In the case of the side 1, data collected were not flattened. In fact, considering the surface features of this side from the optical microscopy, where features on the surface smoothly descend and ascend continuously in the 10 μm scale, the application of a flattening algorithm can create artefacts and distortions rather than improvements. Again, the absence of the application of a flattening algorithms could lead to a maximum positive bias around 40 nm for the biggest scan size, as evaluated from other images. The situation of side 2 is more complicated, because, again, collected raw images show a tilt. Also for this side it is quite difficult to decide: from the optical image, it seems quite flat with some large peaks. However, these peaks are not sharp, and they have a scale that can be more than 10 μm. It means that the tilt seen in the raw data can be

ascribed both to the tilt of the sample or to surface features. In this case, even if it is quite clear that the flatten can create distortions in the images, it was chosen to flatten them to put in evidence the fine surface features that are confirmed in all the three runs, and that is not so evident in the raw data. RMS roughness values of side 1 increase with the increase of the scan size, with values below 100 nm in the scan size of 1 μm, until values greater than 300 nm in the scan size of 10 μm. However, according to the specific position on the surface, the scan sizes of 5 μm and 10 μm show similar values. This shows that also at the biggest scan size the surface is not uniform. RMS roughness values of the side 2 should be cautiously taken. Based on the discussion above, these results are probably an underestimation of the real values. In this case it is difficult to have an idea of the maximum negative bias. Some distortions due to the flattening algorithms are clearly seen in the images at the scan size of 10 μm, resulting in a false curvature of the surface. However, only applying the flattening algorithms it is possible to see well the fine structure of this surface, otherwise not visible in the raw images. In fact, all of these images show the presence of horizontal lines and irregular peaks, that are confirmed in all the runs and also in the same run itself. In fact, these lines are seen in the scan size of 5 μm and they are confirmed in the scan size of 10 μm in the same run: this excludes that they are an artefact of the AFM scanner. A quick look at the RMS roughness values show an increase of the roughness with the increase of the scan size, but not in the same way of the side 1.

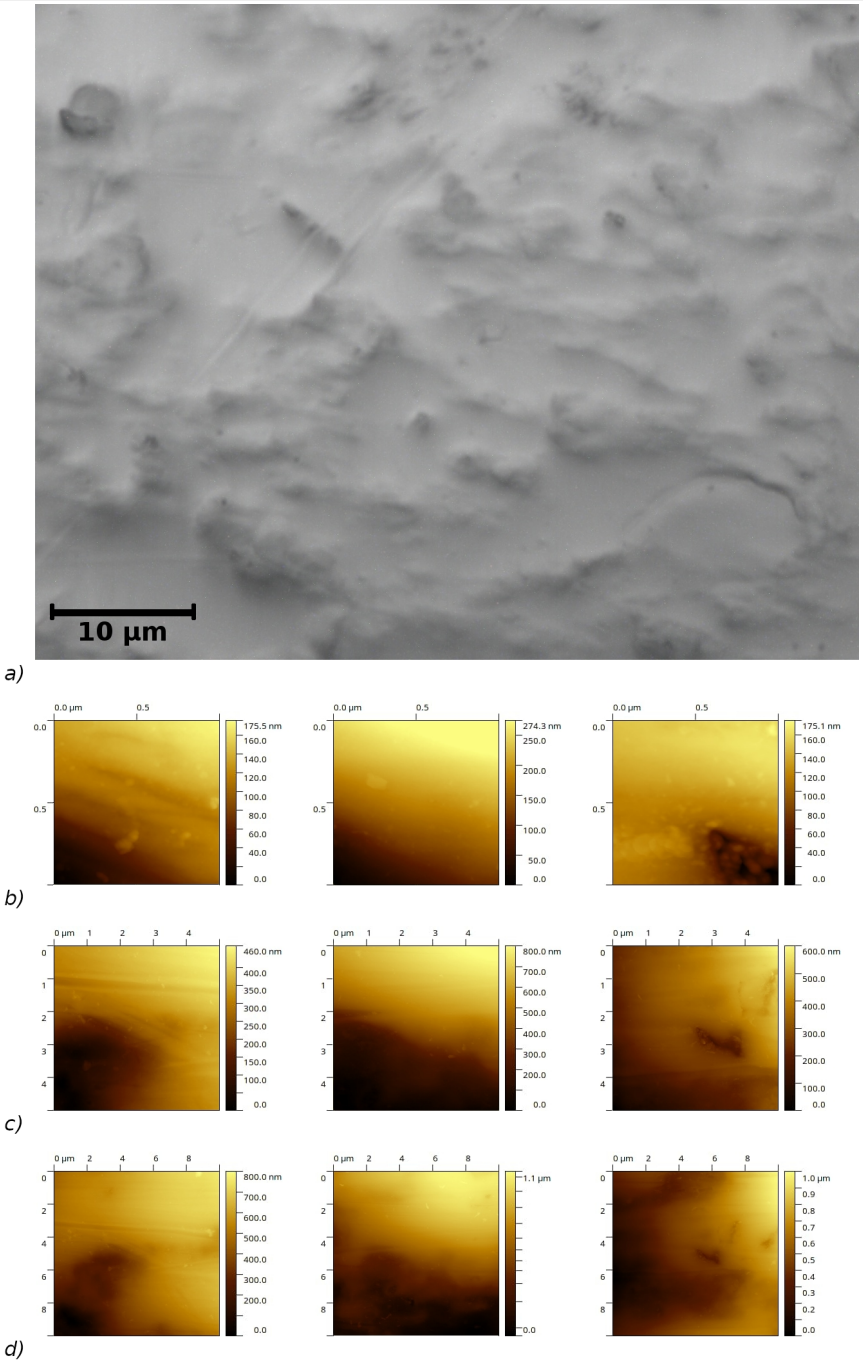

Figure 5.11: 'Sample 19 – side 1' morphology by optical microscopy at 100X magnification in panel (a) and by AFM at three different scan sizes of three different locations: 1 x 1 μm^2 in panel (b), 5 x 5 μm^2 in panel (c) and 10 x 10 μm^2 in panel (d). AFM images of this side are shown as they are collected without post-processing elaboration, such as flattening because on this surface it will probably introduce heavy artefacts and distortions.

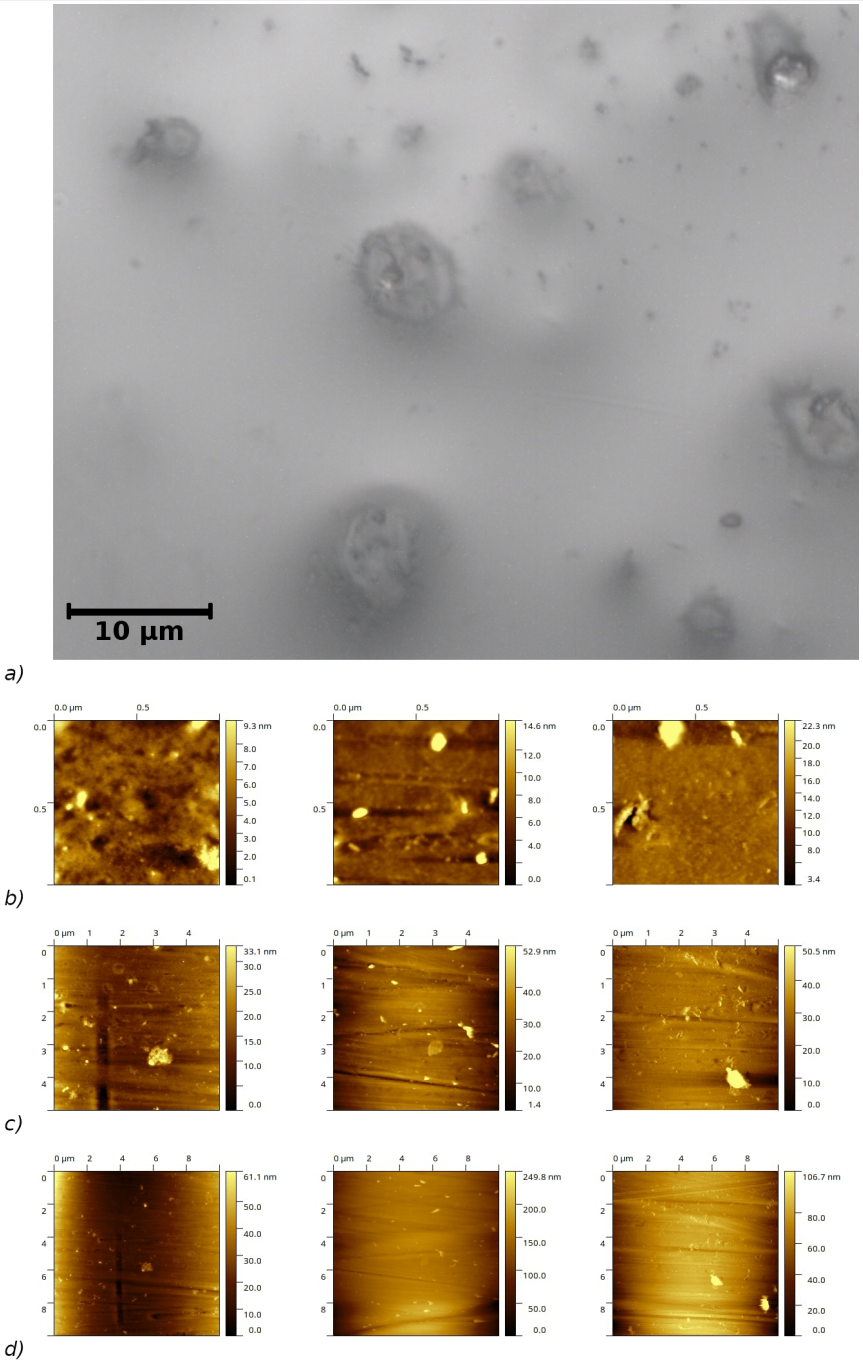

Figure 5.12: 'Sample 19 – side 2' morphology by optical microscopy at 100X magnification in panel (a) and by AFM at three different scan sizes of three different locations: 1 x 1 μm^2 in panel (b), 5 x 5 μm^2 in panel (c) and 10 x 10 μm^2 in panel (d). AFM images of this side are flattened even if this causes visible distortions (curvature sees in panel (c) and (d*)* is clearly an artefact). However, only flattening them, other details like lines and peaks can be appreciated.

Sample 19 – side 1	RMS roughness first run (nm)	RMS roughness second run (nm)	RMS roughness third run (nm)
Scan size 1 μm	39.2	73.2	34.5
Scan size 5 μm	117	240	110
Scan size 10 μm	161	327	214

Table 5.11: RMS roughness of 'Sample 19 – side 1' in three different locations and scan sizes.

Sample 19 – side 2	RMS roughness first run (nm)	RMS roughness second run (nm)	RMS roughness third run (nm)
Scan size 1 μm	1.45	1.99	2.47
Scan size 5 μm	4.50	7.22	7.00
Scan size 10 μm	13.1	32.1	18.0

Table 5.12: RMS roughness of 'Sample 19 – side 2' in three different locations and scan sizes.

5.1.2.4 Sample 24

Just only looking at 'Sample 24' some differences between the two sides can be noted: side 1 is yellow and shiny, while side 2 is a non-reflecting paler yellow surface. Optical images shown in Figure 5.13 e Figure 5.14 for side 1 and 2 respectively give a better insight into their different features. 'Sample 24 – side 1' appears to be completely flat and smooth with the presence of horizontal fine straight lines (very difficult to focus well at high magnification with the optical microscope because of the reflectiveness of this side, that is why for this surface the 20X magnification is reported in the Figure 5.13). 'Sample 24 – side 2' at the highest magnification show a pock-marked surface; at lower magnifications it reveals a structure where pock-marked regions are confined into zones of similar areas delimited by higher edges and piled up into columns (in some ways, this recalls the structure of a cellular tissue, with columns of cells). AFM images confirm the differences of two sides of 'Sample 24' giving a better insight into lines of side 1 and morphology of side 2. Lines have different widths ranging from 0.1-0.2 μm to 0.4-0.5 μm. Characteristic of these lines is that they have prominent edges, differently

from 'Sample 19 – side 2' where lines seem curvings into the surface. Images of the side 2 are shown as collected, so without flattening them for the same reasons reported above for 'Sample 19 – side 1' and 'Sample 18 – side 2'; they show an irregular pattern also at the scan size of 10 μm.

RMS roughness values of side 1 and 2 of 'Sample 24' are listed in Table 5.13 and Table 5.14, respectively. RMS roughness values of the side 1 are quite small and similar at all the scan sizes, ranging mainly between 2.5 and 3.5 nm. Side 2 has completely different and greater values. They show an important increase from the scan size of 1 μm to the scan size of 5 μm, while values of the scan size of 10 μm are similar or lower than those of the 5 μm scans (also considering that the absence of flattening may have a positive bias of 40 nm for the first run, 20 nm for the second and 30 nm for the third).

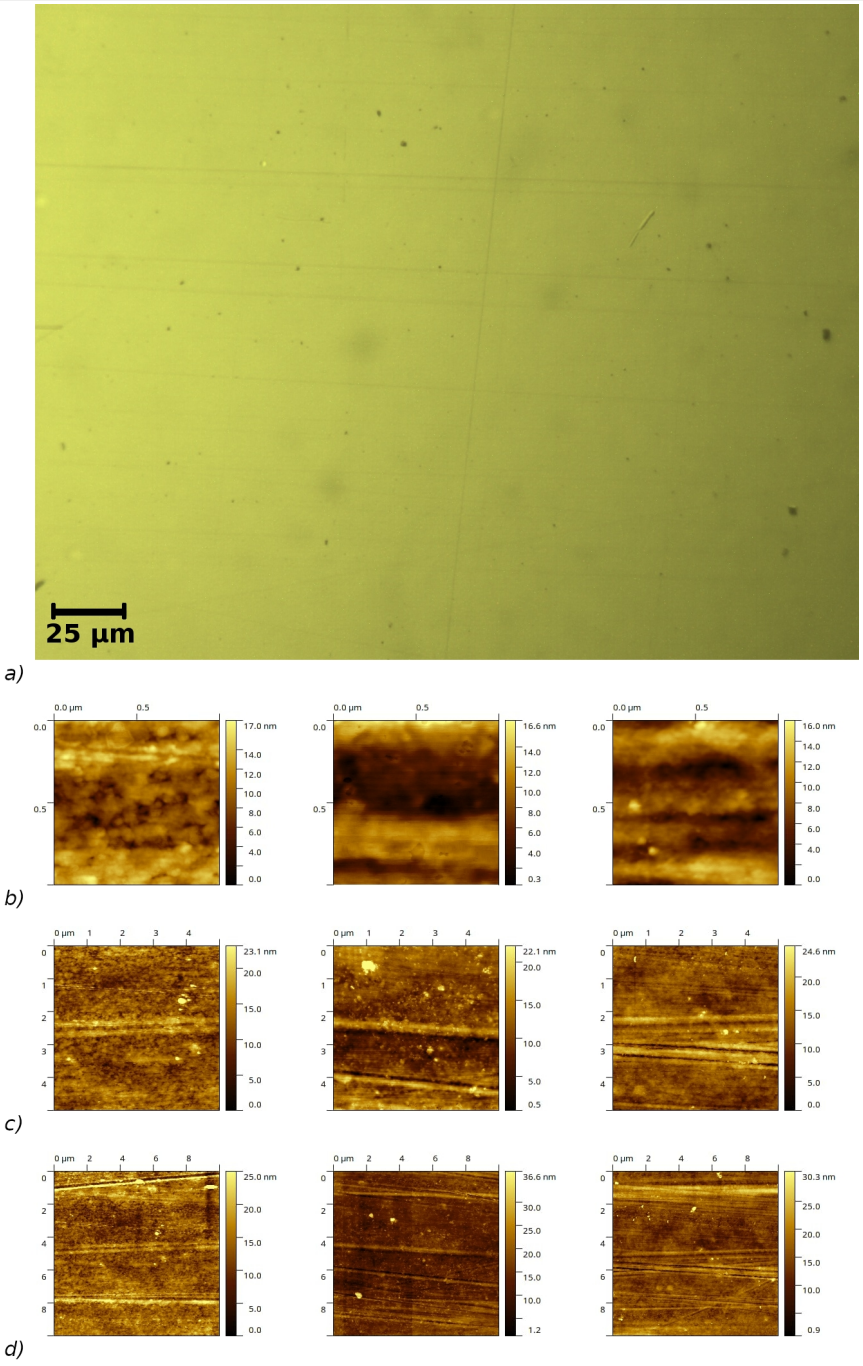

Figure 5.13: 'Sample 24 – side 1' morphology by optical microscopy at 20X magnification in panel (a) and by AFM at three different scan sizes of three different locations: 1 x 1 μm^2 in panel (b), 5 x 5 μm^2 in panel (c) and 10 x 10 μm^2 in panel (d).

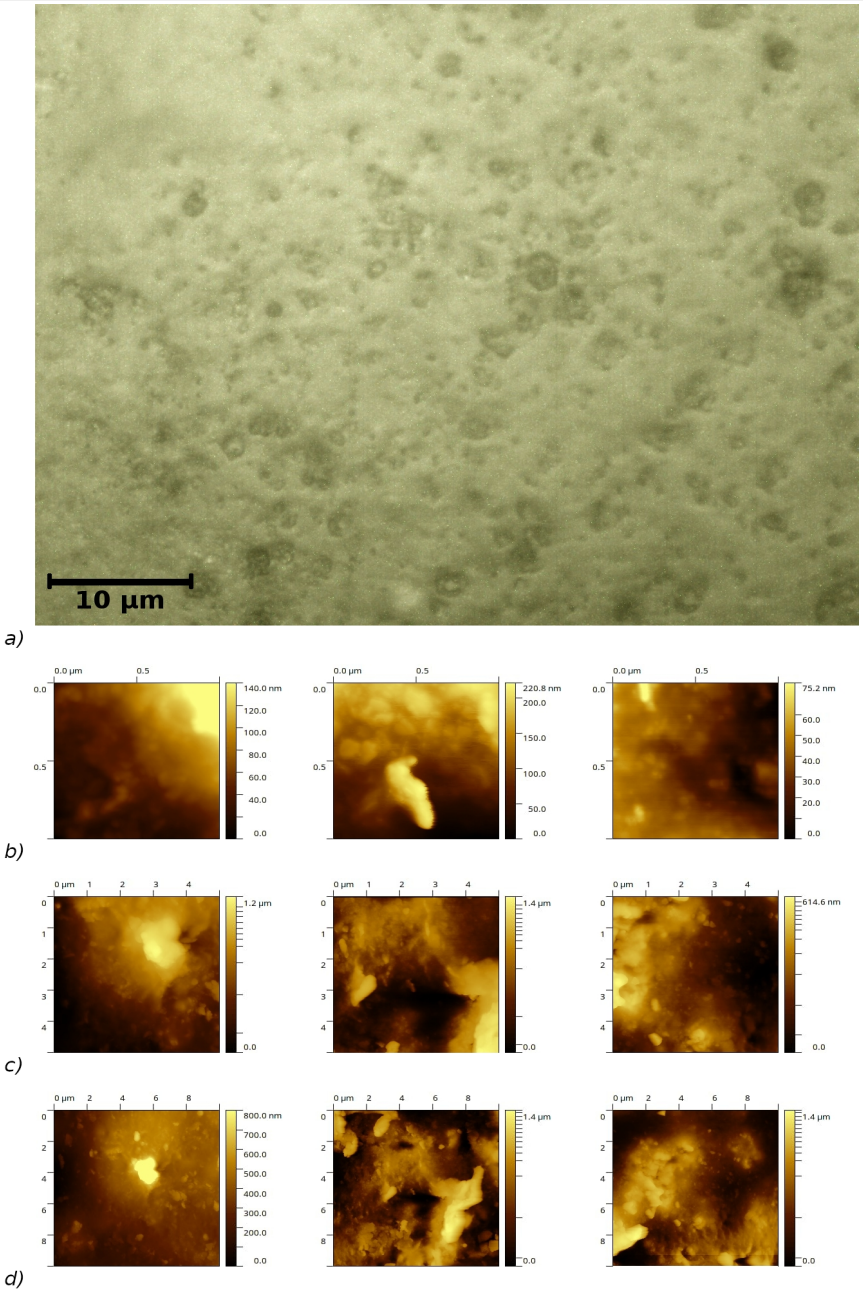

Figure 5.14: 'Sample 24 – side 2' morphology by optical microscopy at 100X magnification in panel (a) and by AFM at three different scan sizes of three different locations: 1 x 1 μm^2 in panel (b), 5 x 5 μm^2 in panel (c) and 10 x 10 μm^2 in panel (d). AFM images of this side are shown as collected without post-processing.

Sample 24 – side 1	RMS roughness first run (nm)	RMS roughness second run (nm)	RMS roughness third run (nm)
Scan size 1 μm	2.47	3.24	2.74
Scan size 5 μm	2.76	3.42	2.92
Scan size 10 μm	4.54	3.61	3.43

Table 5.13: RMS roughness of 'Sample 24 – side 1' in three different locations and scan sizes.

Sample 24 – side 2	RMS roughness first run (nm)	RMS roughness second run (nm)	RMS roughness third run (nm)
Scan size 1 μm	37.3	41.9	14.5
Scan size 5 μm	179	179	85.4
Scan size 10 μm	158	178	142

Table 5.14: RMS roughness of 'Sample 24 – side 2' in three different locations and scan sizes.

5.1.2.5 Sample 47

At first glance, 'Sample 47' appears to be made of copper: it has the same colour and reflectivity of that metal. Optical and AFM images are shown in Figure 5.15 and Figure 5.16 for side 1 and side 2, respectively. Looking at the images, the two sides appear to be quite similar with several parallel straight lines, probably due to the copper production process. However, this sample has organic PI layers on its surfaces but, at the same time, because of its thinness, the PI layers retain the roughness features of the underlying copper core. AFM images also reveal that both sides show globular features, more evident in the smallest scans size because in the others they are masked by the straight lines. RMS roughness values for both sides are reported in Table 5.15 and Table 5.16 for side 1 and side 2, respectively. Because the scan size of 1 μm of all runs and the size of 5 μm of both the first runs of the two sides are not flattened, these values may have a small positive bias. However, application of a flattening algorithm to images like these where the superior and the inferior parts are not on the same plane will create evident distortions and artefacts. Both sides show that there is a small increase of

roughness from the scan size of 1 μm to the scan size of 5 μm (a little bit more evident in side 2) and that values of the scan size of 5 μm and 10 μm can be considered quite similar.

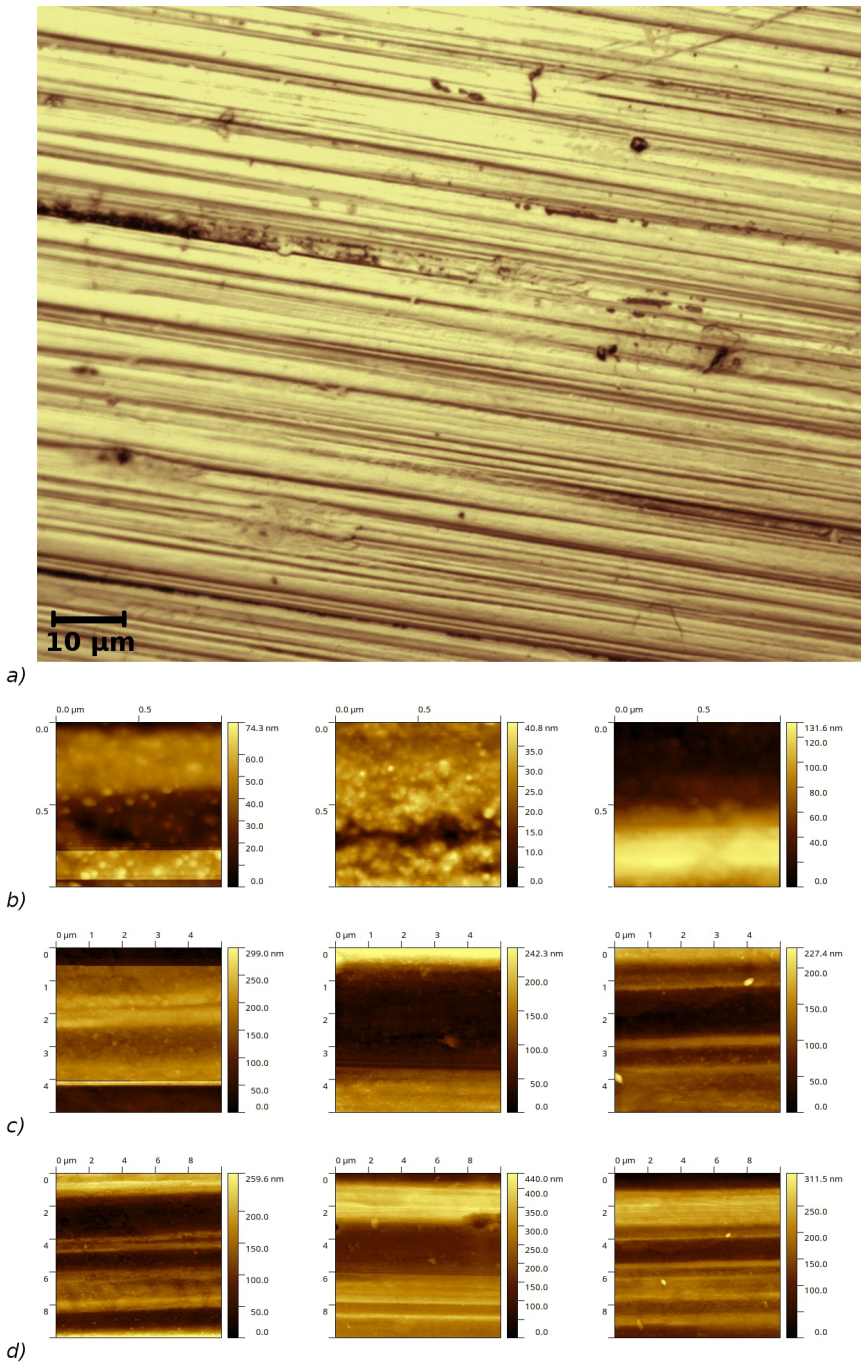

Figure 5.15: 'Sample 47 – side 1' morphology by optical microscopy at 50X magnification in panel (a) and by AFM at three different scan sizes of three different locations: 1 x 1 μm^2 in panel (b), 5 x 5 μm^2 in panel (c) and 10 x 10 μm^2 in panel (d). AFM images of panel (b) and the first one of panel (c) are shown as collected without post-processing.

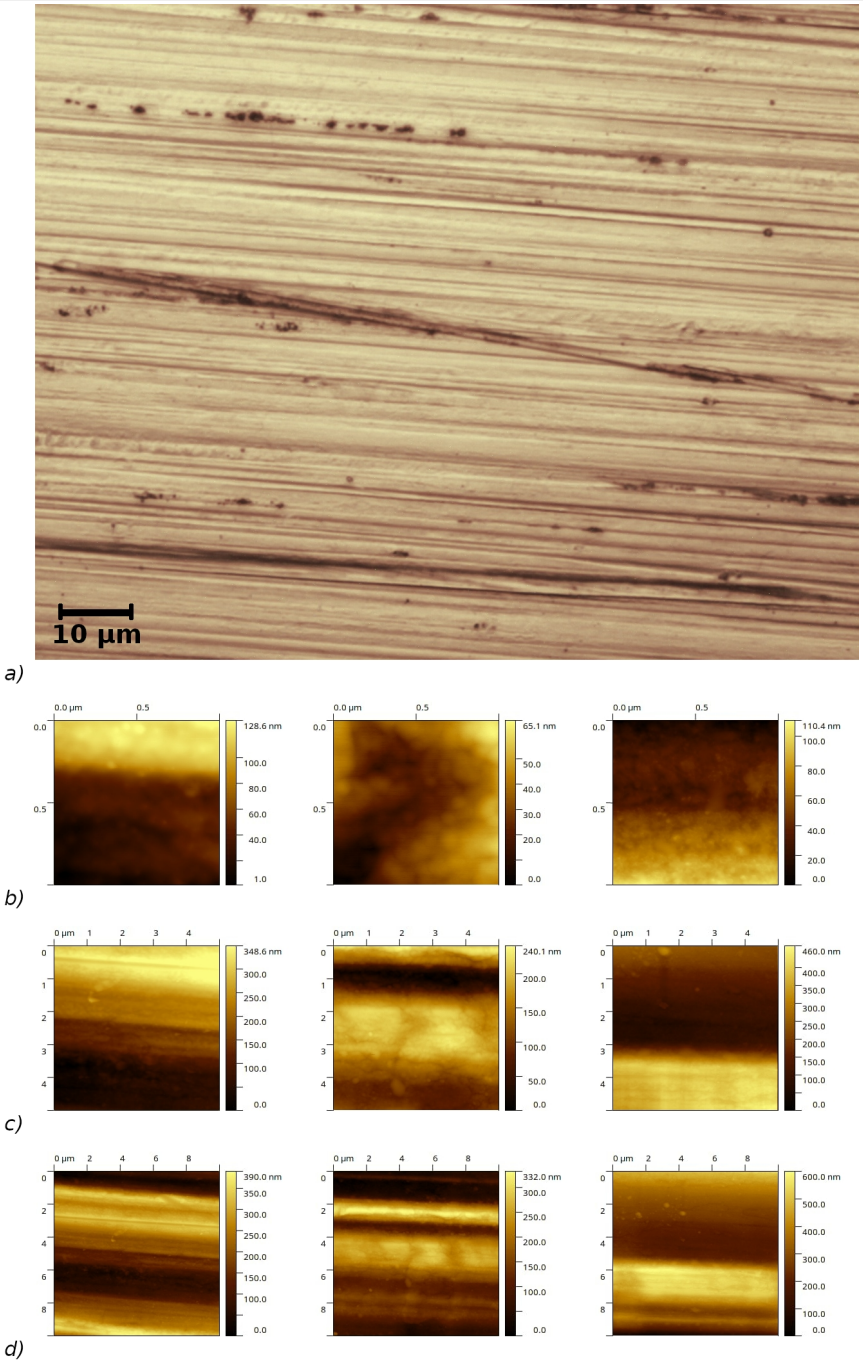

Figure 5.16: 'Sample 47 – side 2' morphology by optical microscopy at 50X magnification in panel (a) and by AFM at three different scan sizes of three different locations: 1 x 1 μm^2 in panel (b), 5 x 5 μm^2 in panel (c) and 10 x 10 μm^2 in panel (d). AFM images of panel (b) and the first one of panel (c) are shown as collected without post-processing.

Sample 47 – side 1	RMS roughness first run (nm)	RMS roughness second run (nm)	RMS roughness third run (nm)
Scan size 1 μm	15.3	6.13	43.8
Scan size 5 μm	63.7	67.5	40.4
Scan size 10 μm	59.3	86.3	56.2

Table 5.15: RMS roughness of 'Sample 47 – side 1' in three different locations and scan sizes.

Sample 47 – side 2	RMS roughness first run (nm)	RMS roughness second run (nm)	RMS roughness third run (nm)
Scan size 1 μm	38.1	12.2	23.8
Scan size 5 μm	107	58.2	125
Scan size 10 μm	93.0	77.1	116

Table 5.16: RMS roughness of 'Sample 47 – side 2' in three different locations and scan sizes.

5.1.3 Morphology and roughness comparison among samples

Rollers morphology is quite different from sample to sample. The non-ground samples FilmClean and PanelClean have almost similar features with smooth surfaces with lines and holes and similar roughness. NanoUClean, instead, has characteristics in the middle of ground and non-ground rollers in both morphology and roughness values. In fact, its surface it is not as smooth as PanelClean and FilmClean, but it does not show regions with difference in height as significant as in the ground samples: looking at the optical image it resembles a fine-grained material. From AFM images its morphology is unique among the studied samples: it is not possible to recognise or describe it like a (flat or smooth) surface with features because its surface is continuously wavy without steps. Instead, steps of different heights can be seen in all the ground samples. Ground samples can be in fact described as formed by 'terracing' or regions at different heights connected among them with more or less sharp slope and edge parts. NanoClean is the ground sample with the largest regions, the greatest differences in height among them and sharpest edges at the boundaries of regions. UTFClean, instead, is the

ground sample with the smallest regions, the least steep slope and the most smooth edges among regions. UltraClean offers intermediate characteristics with less extended 'terracing', smooth edges among these regions and the slopes of the parts that connect the different regions that is in the middle of that of NanoClean and UTFClean. RMS roughness values of ground samples are very dependent on the specific features on the surface at least at the studied scan sizes: so they can also show similar values among them.

Plastic samples show that they are quite different from each other and often, the two sides of the same sample can differ each other. Only 'Sample 9' and 'Sample 47' show similar features on both their two sides; while 'Sample 18', 'Sample 19' and 'Sample 24' have two completely different sides. Also the nature of the surface features strongly changes from one sample to another. The range of variation of the surface features goes from the quite smooth 'Sample 24 – side 1' (with a RMS roughness of about 3 nm) and 'Sample 18 – side 1', passing through presence of some protuberances in 'Sample 19 – side 2' or holes in 'Sample 9 – side 1' and 'Sample 9 – side 2' (with a RMS roughness that is not higher than 35 nm at the scan size of 10 μm), to the irregular protuberances of 'Sample 19 – side 1' until the straight horizontal lines of 'Sample 47', the spots of 'Sample 18 – side 2' and the 'cellular tissue like' of 'Sample 24 – side 2'. Of the latter listed samples an intermediate to greater roughness is shown by 'Sample 47', 'Sample 19 – side 1' and 'Sample 24 – side 2' that are quite rough, however, 'Sample 18 – side 2' is the roughest.

Comparing the roughness of the plastic sheets with rollers, it appears that the former have a roughness that is less or similar to those of PanelClean and FilmClean, with the exception of 'Sample 19 – side 1' that is in the range of NanoUClean and 'Sample 18 – side 2' that is maybe also rougher than the ground rollers.

5.2 Surface hydrophilic/hydrophobic behaviour

Contact angle measurements of all Teknek's samples are reported in Table 5.17 (names of the samples and their corresponding materials are provided in Table 3.1).

Contact angles of elastomers may be affected by errors due to the fact that these samples are not flat, even if care was taken in choosing the best parts of the prepared strips: in fact, some of the elastomers are not very soft and compliant, such as NanoUClean and NanoClean. FilmClean, UltraClean, PanelClean and UFTClean show contact angle values that are in the expected range indicated in Table 3.2. UFTClean shows a greater value as expected as effect of its roughness; this is not the case of UltraClean that has a value similar to that of FilmClean, but maybe this can be an effect of the not completely flat surface like also the greater error suggests. NanoUClean and NanoClean, that should be expected to be hydrophilic according to the value reported in Table 3.3, show values greater than 100°. In this case, measurements were repeated twice with the same results. An explanation of that may be that the definition of 'polyurethane' is rather generic: even if usually PU is reported to be hydrophilic or with a contact angle near to 90°, some kinds of PU can be hydrophobic, like Lycra [178]. More precise information on these samples are not available but it can be concluded that they are made of hydrophobic PU: NanoUClean contact angle is in the range of the value reported for Lycra (105°) and the greater value of NanoClean may be ascribed by its roughness.

Contact angles of plastic sheets should not show bias due to the curvature of surfaces because they are all flat, however some effects due to roughness may be expected. 'Sample 19', 'Sample 24' and 'Sample 47' show values similar to those expected or near to them, as reported in Table 3.6 and 3.7, respectively. 'Sample 24 – side 2' shows a lower value than the other side (that is, an increase of hydrophilicity), maybe due to roughness. However, other samples have contact angle values that are unexpected. For example, 'Sample 9' that should be hydrophobic is hydrophilic on both its sides: also in this case, measurements were

repeated twice with the same results. Again, an explanation may be that the surfaces of this specific PP are treated in a way to let them be hydrophilic. 'Sample 18' has values that are in the expected range for PC, however it should be expected that side 2 has a lower value that side 1 because of the greater roughness. Again, a possible explanation is that maybe the side 2 is treated in a way to let it be less hydrophilic than side 1.

Sample name	Contact angle ± standard deviation (degree)
FilmClean	102 ± 1
UltraClean	100 ± 4
PanelClean	102 ± 1
UTFClean	109 ± 5
NanoUClean	103 ± 3
NanoClean	113 ± 3
Sample 9 – side 1	71 ± 1
Sample 9 – side 2	73 ± 2
Sample 18 – side 1	50 ± 4
Sample 18 – side 2	88 ± 4
Sample 19 – side 1	78 ± 2
Sample 19 – side 2	78 ± 1
Sample 24 – side 1	82 ± 2
Sample 24 – side 2	77 ± 2
Sample 47 – side 1	84 ± 2
Sample 47 – side 2	82 ± 2

Table 5.17: Contact angles of Teknek's samples. Values are the average of ten runs of 200 measurements each.

Considering the contact values of all samples, the only hydrophobic samples are rollers, so their adhesion is not influenced by relative humidity; all the other samples may show a change in adhesion with hydrophilic particles according to the humidity of the environment in which they are.

5.3 Adhesion measurement

As seen before, most of Teknek's samples are very rough and with specific features on their surfaces. Because these features may have an influence on adhesion, adhesion measurements were done in the form of force maps, where, in addition to the adhesion map, a map showing heights of each collected point is simultaneously collected. Of course, force maps were acquired over a 10 x 10 μm^2 area as the greatest scan size used in the morphological analysis in order to have a better understanding of features that can be on these surface (that are often quite large) and the same scale of the morphological study. Thus, together with adhesion, for each measurement, also the corresponding RMS roughness will be reported. The absolute value of the latter should not be compared with the values reported in the morphology study because they will be certainly different because they are now acquired with a colloidal probe of 5 μm radius and so with a curvature ~300 times greater than that of a tapping mode AFM tip: actually it is a measurement of how an 'ideal' particle of 10 μm of diameter feels the surface. So, the RMS roughness values collected with the force map must be used only as comparison among them and for adhesion discussion.

Adhesion was collected using two different types of colloidal probes with the same shape and dimensions but made of different materials: one is hydrophilic (borosilicate glass) and the other is hydrophobic (PS probe) to test if these surfaces show differences.

Because of the variability shown by the features of these surfaces, average values of adhesion will be presented for each collected run (two) and not as average of all runs. These because this way of exposition of results represents better how these surfaces are.

As for the morphology study, the exposition of results will be done for elastomers and plastic sheets separately.

5.3.1 Rollers

Rollers adhesion will be reported respecting the couples indicated by Teknek as already done for the morphology section. Because rollers are all hydrophobic and so their adhesion is not sensitive to relative humidity, this was not collected during measurements.

5.3.1.1 FilmClean/UltraClean

FilmClean and UltraClean adhesion results together with the corresponding RMS roughness values are reported in Table 5.18 and in Table 5.19, respectively. Adhesion and height maps of both the two runs with the PS and borosilicate probes of FilmClean and UltraClean are reported in Figures 5.17, 5.18 and 5.19, 5.20, respectively.

	FilmClean	
Run/probe	Adhesion ± standard deviation (μN)	RMS roughness (nm)
1/PS	1.9 ± 0.2	59.1
2/PS	2.0 ± 0.1	38.9
1/Borosilicate	2.0 ± 0.2	33.2
2/Borosilicate	2.0 ± 0.2	28.5

Table 5.18: FilmClean average adhesion and RMS roughness as collected with PS and borosilicate colloidal probes (two runs for each probe).

	UltraClean	
Run/probe	Adhesion ± standard deviation (μN)	RMS roughness (nm)
1/PS	2.0 ± 0.7	158
2/PS	1.6 ± 0.6	204
1/Borosilicate	1.7 ± 0.9	208
2/Borosilicate	1.4 ± 0.6	125

Table 5.19: UltraClean average adhesion and RMS roughness as collected with PS and borosilicate colloidal probes (two runs for each probe).

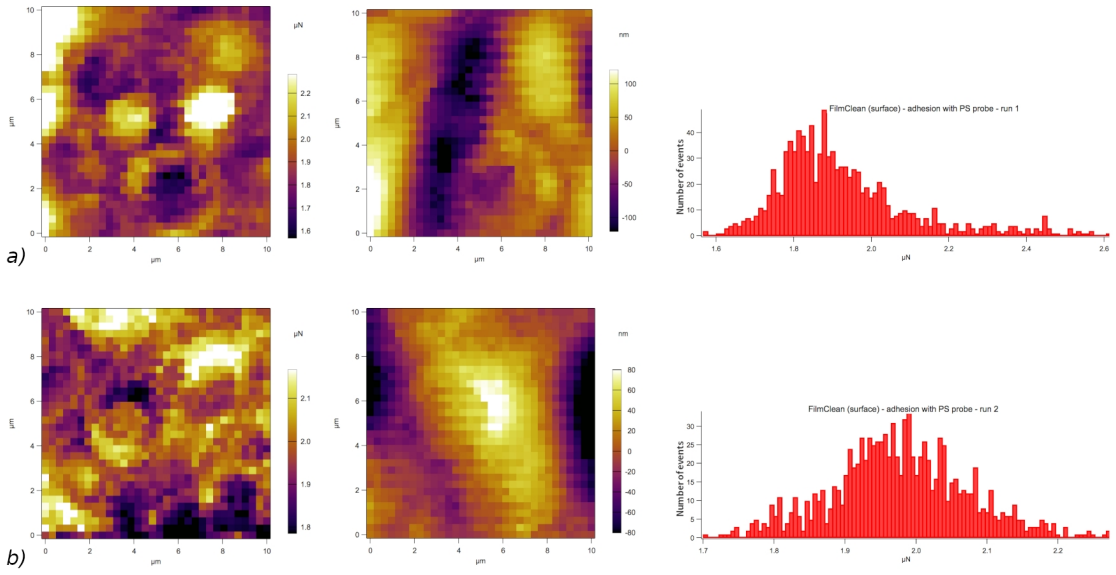

Figure 5.17: Adhesion maps, height maps and adhesion distributions of FilmClean with the PS probe in run 1, in panel (a), and in run 2 in panel (b).

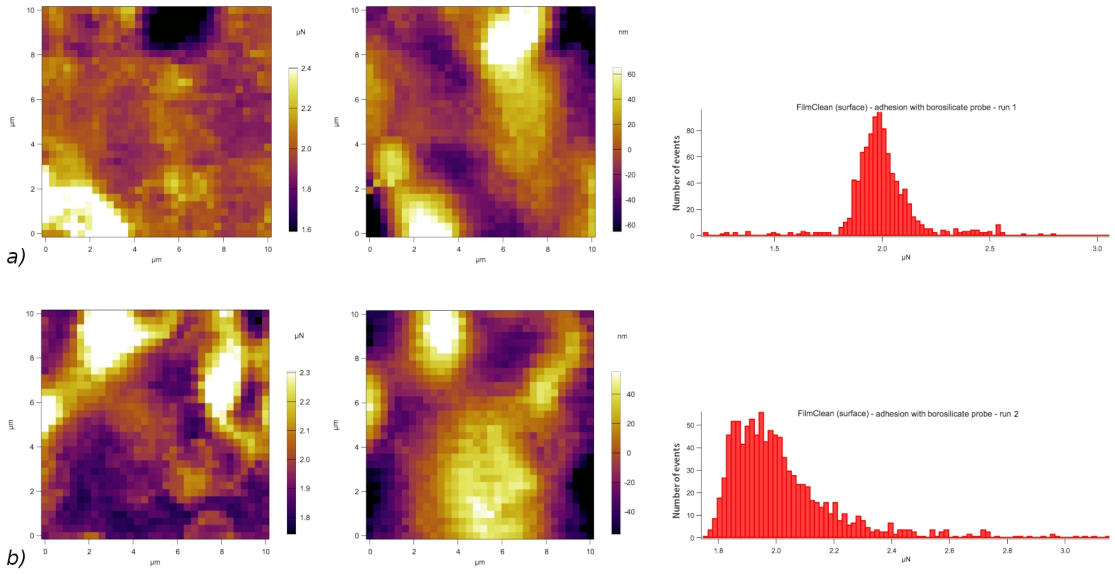

Figure 5.18: Adhesion maps, height maps and adhesion distributions of FilmClean with the borosilicate probe in run 1, in panel (a), and in run 2 in panel (b).

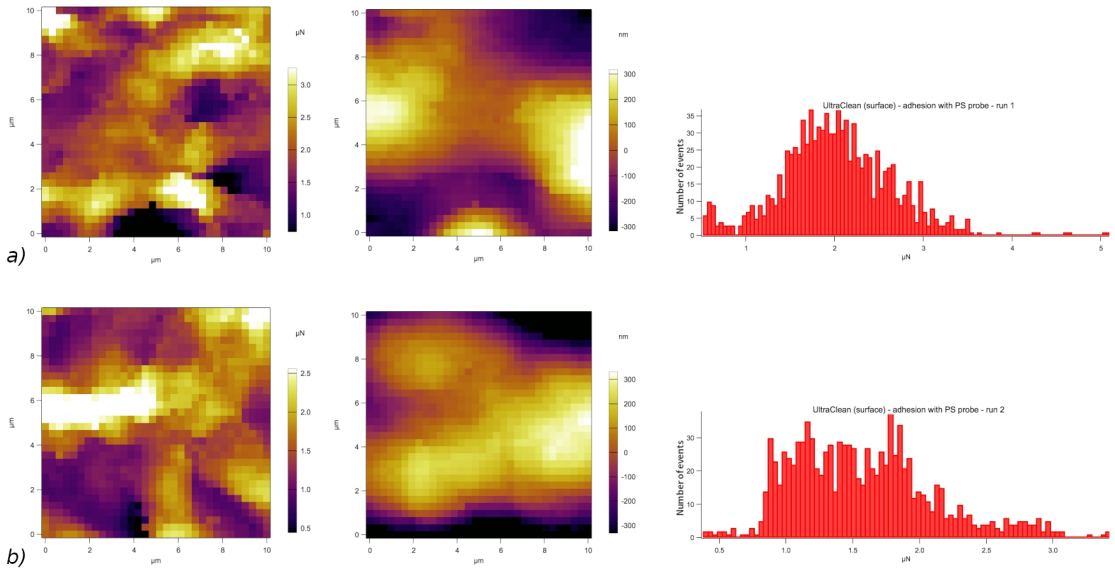

Figure 5.19: Adhesion maps, height maps and adhesion distributions of UltraClean with the PS probe in run 1, in panel (a), and in run 2 in panel (b).

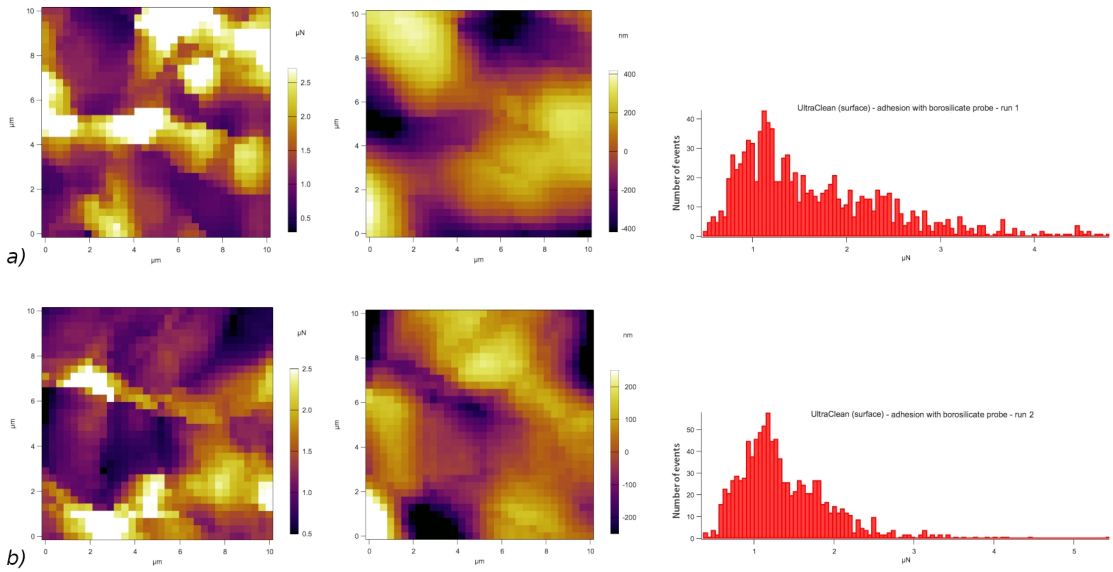

Figure 5.20: Adhesion maps, height maps and adhesion distributions of UltraClean with the borosilicate probe in run 1, in panel (a), and in run 2 in panel (b).

Adhesion values show that FilmClean has a similar adhesion for both probes, ranging around 2 μN, while UltraClean has probably a greater adhesion toward the PS probe (however, the dispersion of adhesion values of UltraClean does not allow to reach a precise conclusion about it). In any case, there is not a big difference in adhesion between the two samples. Looking at the adhesion maps, height maps and histograms of Figures 5.17 – 5.20 it is possible to note that adhesion data of UltraClean have a higher dispersion than those of FilmClean, mostly due to the specific features that are present on its surface.

What it is probably more interesting is to find a correlation, if possible, among regions with different adhesion and the corresponding morphology. Starting from FilmClean, it is possible to note that for both probes, usually, the greatest adhesion regions corresponds to the walls of high features of the surface if they are not to steep, and to some of the gorges among them if they are not too deep and their walls are not too far away each other. Even if in some parts of the maps seem that there is a correspondence between the greatest adhesion and the tops of high features (like, for example in Figure 5.18), in reality, a closer look changing the

colour scale or considering the unflattened height map, reveals that the greatest adhesion is near the tops of the features and corresponds to some slowly descending parts of them (not showed here). Lowest adhesion regions usually correspond to steep walls or too narrow or deep valleys. Looking at the height maps of UltraClean (Figures 5.19 and 5.20) it is clear that greatest adhesion corresponds to the grooves and the lowest adhesion to the tops of the highest features. And because this surface is quite irregular with high regions next to low regions, also adhesion shows suddenly changes, with values that spread on a greater range rather than in FilmClean, where the surface is less irregular.

An explanation of why FilmClean and UltraClean have a similar but not the same behaviour of adhesion with respect to surface features can be that in FilmClean the valleys are larger than in UltraClean where grooves are narrower especially in the lowest parts (please consider the different range of roughness of the two rollers). With this in mind, the adhesion behaviour between the two rollers is not so different: they both have the greatest adhesion values in the regions where there is a larger contact between the surface and the probe.

In conclusion, if the greater roughness does not affect so much the average value of the adhesion, that with a lower or greater dispersion is quite similar, it influences its distribution letting UltraClean have larger distribution of adhesion often centred on lower values than FilmClean, but also have quite high adhesion regions that are not present on the FilmClean surface.

5.3.1.2 PanelClean/UTFClean

Adhesion and RMS roughness values of PanelClean and UTFClean are listed in Table 5.20 and Table 5.21, respectively. Adhesion and height maps of both the two runs with the PS and borosilicate probes of PanelClean and UTFClean are reported in Figures 5.21, 5.22 and 5.23, 5.24, respectively. In the experiments of adhesion between PanelClean and the PS probe, a long range attractive force, probably the electrostatic one, acted as seen for PDMS-6K, increasing the adhesion force of

about 0.2 μN: data reported below have been already corrected, removing this positive bias.

PanelClean		
Run/probe	Adhesion ± standard deviation (μN)	RMS roughness (nm)
1/PS	2.1 ± 0.2	26.2
2/PS	2.4 ± 0.2	44.8
1/Borosilicate	2.0 ± 0.3	76.8
2/Borosilicate	1.9 ± 0.3	69.6

Table 5.20: PanelClean average adhesion and RMS roughness as collected with PS and borosilicate colloidal probes (two runs for each probe).

UTFClean		
Run/probe	Adhesion ± standard deviation (μN)	RMS roughness (nm)
1/PS	1.3 ± 0.7	454
2/PS	1.2 ± 0.6	464
1/Borosilicate	1.4 ± 0.9	599
2/Borosilicate	1.7 ± 0.9	347

Table 5.21: UTFClean average adhesion and RMS roughness as collected with PS and borosilicate colloidal probes (two runs for each probe).

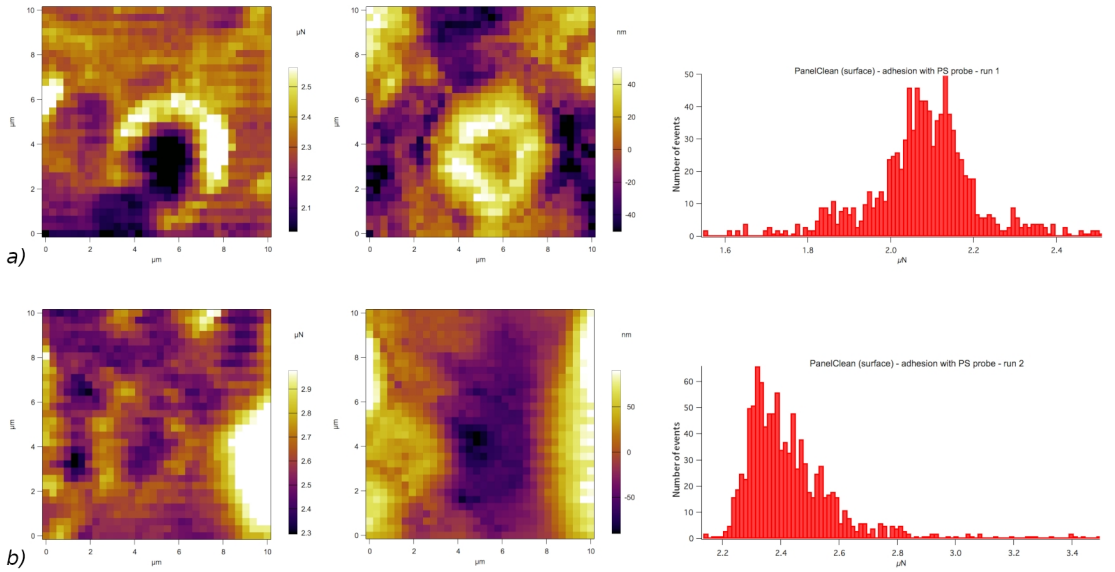

Figure 5.21: Adhesion maps, height maps and adhesion distributions of PanelClean with the PS probe in run 1, in panel (a), and in run 2 in panel (b).

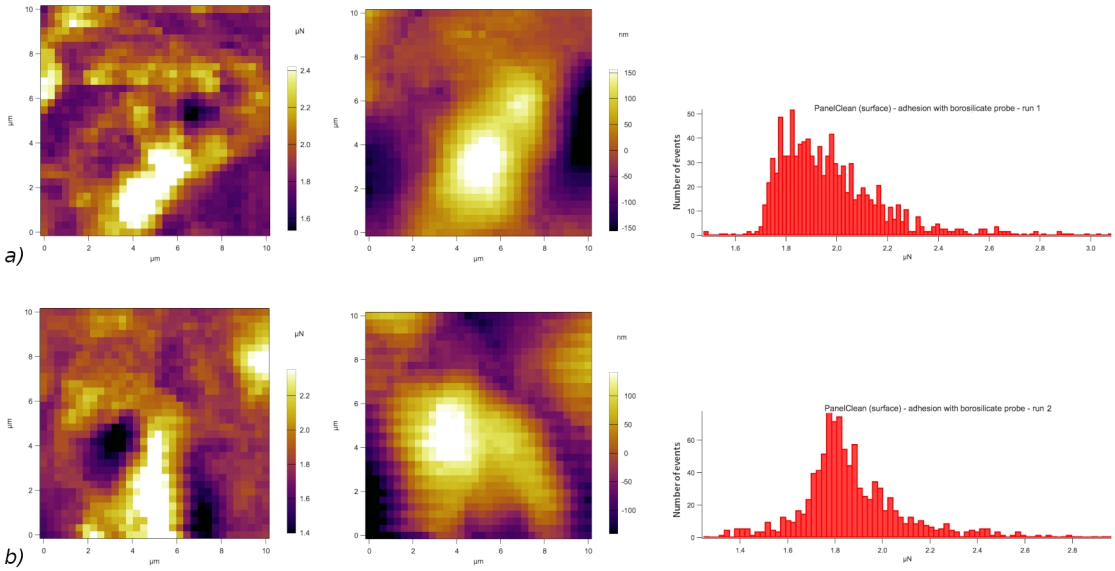

Figure 5.22: Adhesion maps, height maps and adhesion distributions of PanelClean with the borosilicate probe in run 1, in panel (a), and in run 2 in panel (b).

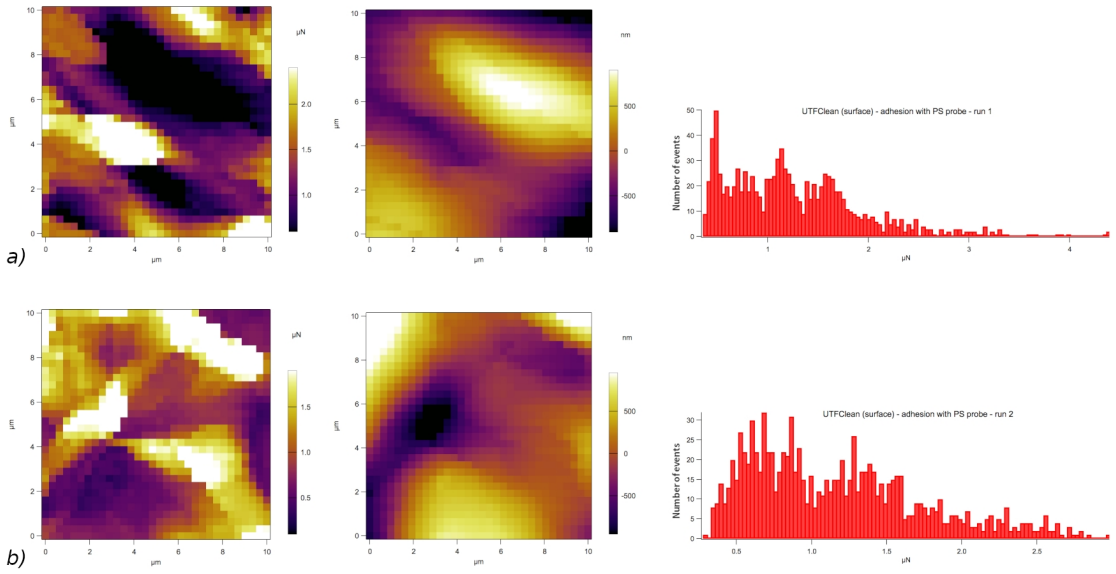

Figure 5.23: Adhesion maps, height maps and adhesion distributions of UTFClean with the PS probe in run 1, in panel (a), and in run 2 in panel (b).

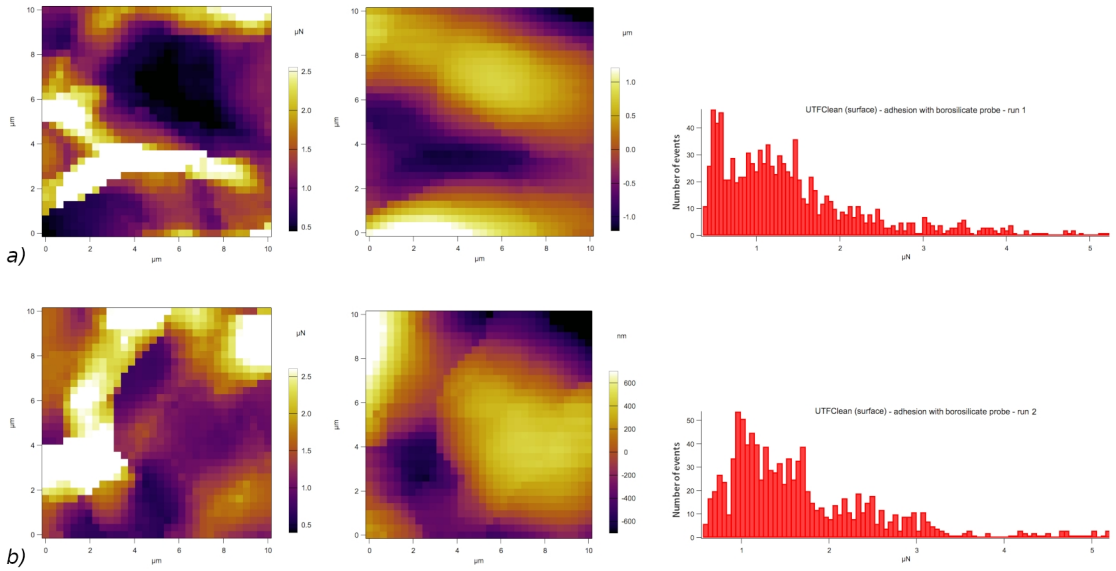

Figure 5.24: Adhesion maps, height maps and adhesion distributions of UTFClean with the borosilicate probe in run 1, in panel (a), and in run 2 in panel (b).

Looking at the adhesion values reported in Tables 5.20 and 5.21, both samples do not seem to show differences according to the used probe: PanelClean has an average value of 2 μN for both probes, UTFClean has probably a lower value but with a higher dispersion. On average, PanelClean seems to have a greater adhesion

than UTFClean, but this cannot be stated surely because of the greater dispersion of UTFClean adhesion data. Because both these rollers are made of the same material and the only difference among them is the surface grounding treatment of UTFClean, it is not surprising that they have similar values and adhesion behaviour toward the two probes: the greater dispersion of adhesion data is foreseeable from the greater roughness of UTFClean.

Again, it is probably more interesting to look at the adhesion and height maps of these samples: like in the FilmClean/UltraClean couple also in this case the highest adhesion is mostly located along non steep walls of high features in PanelClean and in the grooves between high features in UTFClean. Highest features, instead, usually correspond to low or to the lowest adhesion regions of the maps. The more variability of the UTFClean surface has a consequence that very high and very low adhesion regions are next each others while in PanelClean the transition among regions with different adhesion is milder.

Again, the fact that higher adhesion regions in PanelClean usually correspond to walls of valleys while in UTFClean they are located in the grooves can be explained with the bigger contact area of those parts of surface features. In fact, if the differences in the roughness range are taken into consideration, valleys that are on PanelClean surface are less narrow than gorges that are on UTFClean surface, especially in their lowest parts.

Looking at the histograms, as for FilmClean/UltraClean, also in this case the increase of roughness due to the grounding process of UTFClean shows a higher dispersion of adhesion data that are centred on lower values than PanelClean, but, at the same time, adhesion spreads also toward the highest values for this couple of rollers.

5.3.1.3 NanoUClean/NanoClean

Adhesion values and RMS roughness of NanoUClean and NanoClean for both the borosilicate and PS probes are listed in Table 5.22 and Table 5.23, respectively.

Adhesion and height maps of both the two runs with the PS and borosilicate probes of NanoUClean and NanoClean are reported in Figures 5.25, 5.26 and 5.27, 5.28, respectively.

	NanoUClean	
Run/probe	Adhesion ± standard deviation (μN)	RMS roughness (nm)
1/PS	1.1 ± 0.4	69.0
2/PS	1.1 ± 0.4	115
1/Borosilicate	0.27 ± 0.07	77.1
2/Borosilicate	0.3 ± 0.2	153

Table 5.22: NanoUClean average adhesion and RMS roughness as collected with PS and borosilicate colloidal probes (two runs for each probe).

	NanoClean	
Run/probe	Adhesion ± standard deviation (μN)	RMS roughness (nm)
1/PS	0.8 ± 0.6	212
2/PS	0.5 ± 0.3	306
1/Borosilicate	0.8 ± 0.7	617
2/Borosilicate	0.4 ± 0.4	738

Table 5.23: NanoClean average adhesion and RMS roughness as collected with PS and borosilicate colloidal probes (two runs for each probe).

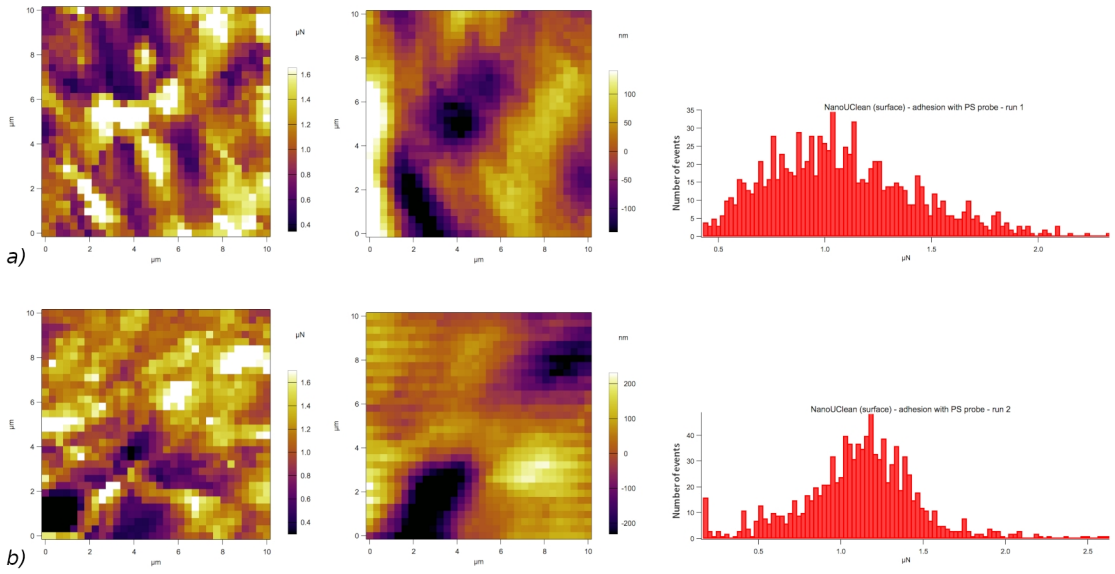

Figure 5.25: Adhesion maps, height maps and adhesion distributions of NanoUClean with the PS probe in run 1, in panel (a), and in run 2 in panel (b).

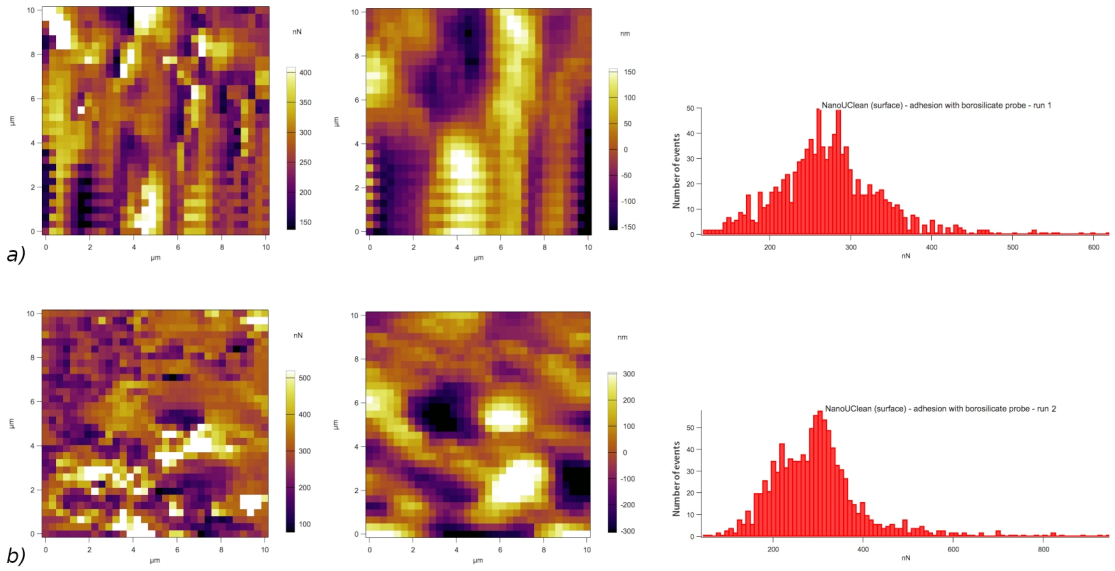

Figure 5.26: Adhesion maps, height maps and adhesion distributions of NanoUClean with the borosilicate probe in run 1, in panel (a), and in run 2 in panel (b).

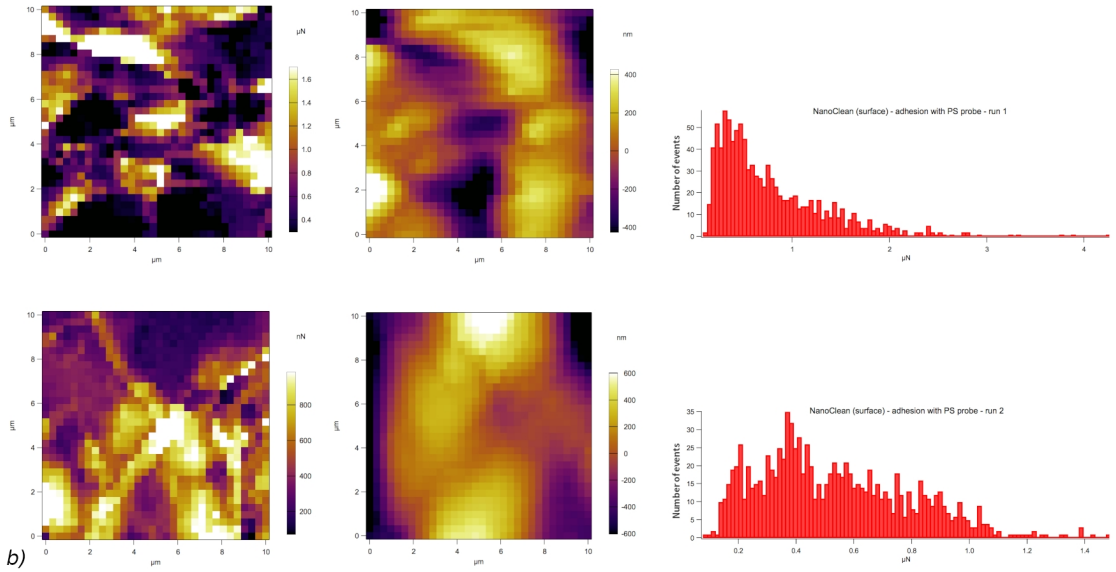

Figure 5.27: Adhesion maps, height maps and adhesion distributions of NanoClean with the PS probe in run 1, in panel (a), and in run 2 in panel (b).

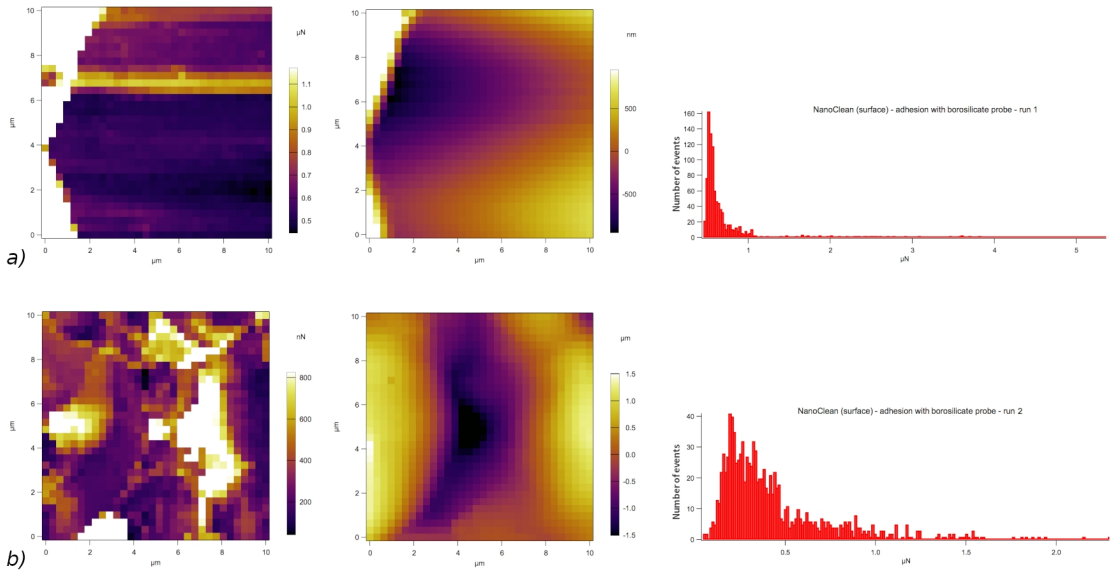

Figure 5.28: Adhesion maps, height maps and adhesion distributions of NanoClean with the borosilicate probe in run 1, in panel (a), and in run 2 in panel (b).

Adhesion data show that NanoUClean has a difference in adhesion between the two probes, with the highest adhesion for the PS one. This difference is not observable in the ground sample NanoClean, where adhesion values are similar for both probes. It may be possible that the low adhesion value of NanoUClean toward

the borosilicate probe can be ascribed to the particular regions investigated. In fact, also the second run of NanoClean with the borosilicate probe shows a such low similar value of adhesion, and this suggests that NanoUClean and NanoClean may be formed by regions with quite different values of adhesion greater than 10 x 10 μm^2. This is not so improbable, considering that from the morphological analysis these two samples have the less homogeneous surface features at this scan size.

A comparison among adhesion and height maps reveals that the greatest adhesion is usually related to some walls of valleys, but mostly to gorges among high regions. Differently from the other couples of rollers, in this case, for both NanoUClean and NanoClean, the greatest adhesion is usually in correspondence of the deepest parts of the gorges; while the lowest adhesion usually corresponds to the tops of the highest features. Thus, in this couple of rollers there is not the slight different behaviour seen for the previous rollers. This may be due to the roughness: NanoUClean has RMS roughness values that are greater than those of the other non ground samples. This suggests that with the increase of the roughness all the elastomers have the same behaviour, with the greatest adhesion corresponding to the gorges; only where RMS roughness is lower, regions with the highest contact areas are not located in gorges but along walls of valleys.

Looking at the histograms, it is easy to note that the increase of roughness or surface features from NanoUClean to NanoClean also increases the dispersion of adhesion data and again, as seen for the other rollers, the ground process allows NanoClean to have some regions with a quite significant higher adhesion in comparison to NanoUClean.

If the three couples of rollers are considered, it is possible to note that FilmClean/UltraClean and PanelClean/UTFClean show similar adhesion values and behaviours. That likely because they are made of the same material with differences in the elastic modulus (that for what seen in the previous chapter do not influence adhesion, if samples are elastic) and in roughness, that modifies adhesion

values distribution as just described above. Thus, roughness just spreads adhesion values but cannot totally change them. Different adhesion values are those of the last couple, NanoUClean/NanoClean with lower values towards both the probes: this can be ascribed mainly to their different material because their adhesion does not show a different modulation because of roughness from what seen for the other two couples.

5.3.2 Plastic sheets

Adhesion on plastic sheets was collected with the same procedure used with elastomers and so with force and height maps. However, because these samples are more standard than rollers for AFM analysis, the following discussion will be only about adhesion values without considering surface roughness. For the same reason, roughness of the height maps will be not reported; in place of that, the collected relative humidity will be indicated (also because these samples could all show an adhesion dependence on it for the hydrophilic probe).

Height maps will be reported: however, it may be that flattening algorithms are not able to work well, causing more distortions and artefacts than improving the quality of the images. It is noted that the height maps that show more problems are those of flat or with non well defined surface features. This may be due to the lower resolution of height maps with respect to the images collected for the morphology, linked to whether the probe size or the lower numbers of points that composed a height map. In addition, if raw height maps of these surfaces have edges that do not belong to the same plane, flattening will lead to unreliable results. In these cases, a non processed or a just flattened height map is shown and commented only for the parts that can be correlated with the corresponding adhesion map.

5.3.2.1 Sample 9

Adhesion values for both the borosilicate and PS probes of the two sides of 'Sample 9' are listed in Table 5.24 and Table 5.25 for side 1 and 2, respectively.

'Sample 9 – side 1' shows a significant standard deviation for both the probes. This can be explained with the large spread of the adhesion values that can be seen in the histograms of Figures 5.29 and 5.30. Considering the low precision of the measurements it is not possible to decide if this side has a greater adhesion for one of the two probes, even if data in the histograms may suggest that adhesion may be greater with the borosilicate probe. Sample 9 – side 2 shows more precise adhesion data than side 1 (Figures 5.31 and 5.32), with quite similar adhesion values for both the two probes, so this side does not show a preference for the hydrophilic or the hydrophobic probe. From these data it does not seem that there are significant differences in adhesion between the two sides.

Especially height maps of the side 2 are difficult to process in a way that can be coherent with the corresponding force maps and the shown morphology: only the height map of the first run with the PS probe could be processed in a satisfactory way. Of the remaining three maps of this side, the one of the second run with the borosilicate probe is flattened, but is likely to be distorted, while the others are shown as collected or with minimal post-processing. Comparing the height maps with the adhesion maps of both the two sides, it is possible to note that usually there is a correspondence between the tops of high features and the low adhesion regions (this is more evident in those regions where there are significant features, for example in both the first runs of 'Sample 1 – side 1' and in the first run with PS probe of 'Sample 9 – side 2'). It is more difficult to correlate high adhesion regions with specific features of these surfaces, however, it possible to note that the more extended high adhesion regions correspond to some gorges or walls of high features for both sides.

Sample 9 – side 1		
Run/probe	Adhesion ± standard deviation (μN)	Relative humidity (%)
1/PS	0.8 ± 0.4	33.4
2/PS	0.4 ± 0.1	33.1
1/Borosilicate	2 ± 2	30.5
2/Borosilicate	0.5 ± 0.2	30.2

Table 5.24: 'Sample 9 – side 1' average adhesion and relative humidity as collected with PS and borosilicate colloidal probes (two runs for each probe).

Sample 9 – side 2		
Run/probe	Adhesion ± standard deviation (μN)	Relative humidity (%)
1/PS	0.29 ± 0.07	32.6
2/PS	0.23 ± 0.07	32.1
1/Borosilicate	0.27 ± 0.03	30.5
2/Borosilicate	0.30 ± 0.04	29.6

Table 5.25: 'Sample 9 – side 2' average adhesion and relative humidity as collected with PS and borosilicate colloidal probes (two runs for each probe).

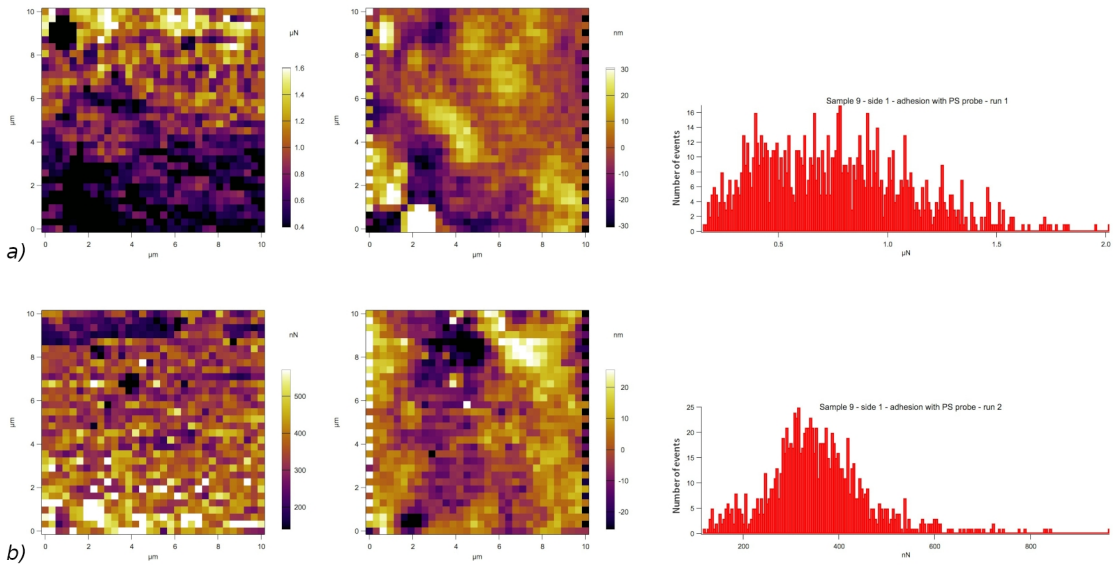

Figure 5.29: Adhesion maps, height maps and adhesion distributions of 'Sample 9 – side 1' with the PS probe in run 1, in panel (a), and in run 2 in panel (b).

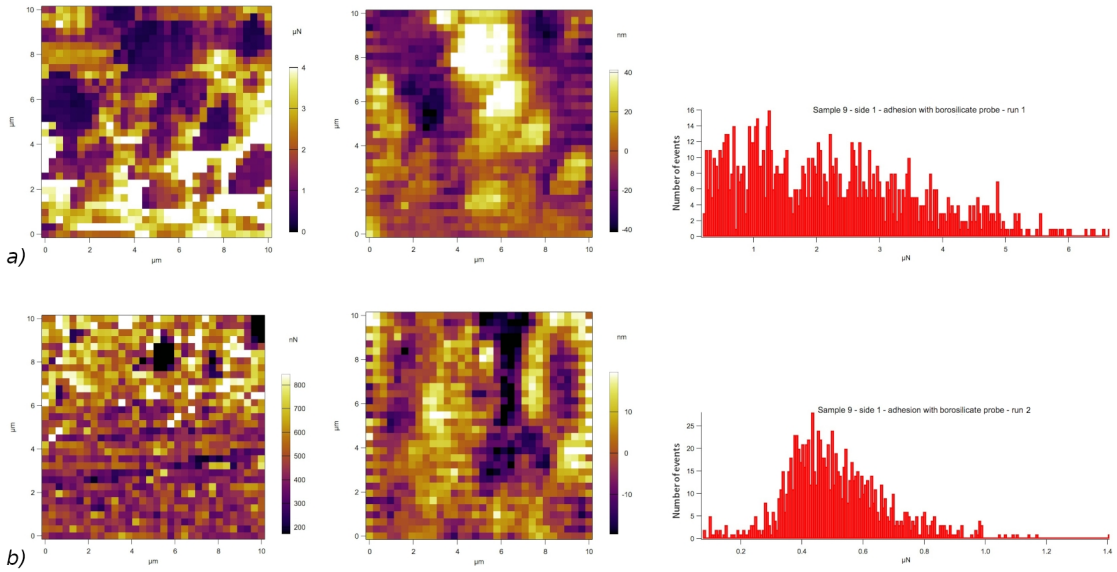

Figure 5.30: Adhesion maps, height maps and adhesion distributions of 'Sample 9 – side 1' with the borosilicate probe in run 1, in panel (a), and in run 2 in panel (b).

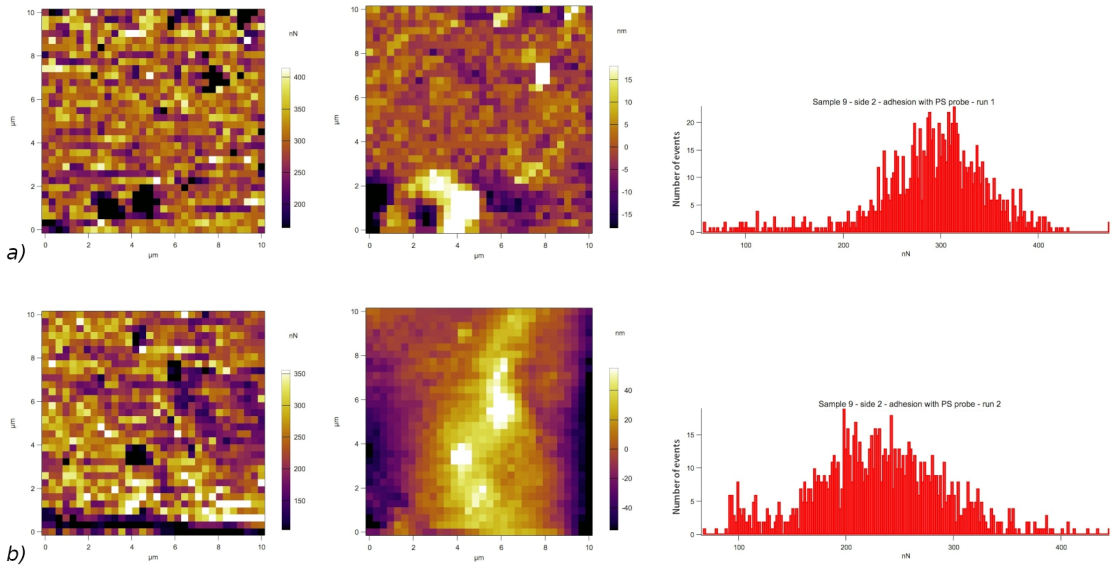

Figure 5.31: Adhesion maps, height maps and adhesion distributions of 'Sample 9 – side 2' with the PS probe in run 1, in panel (a), and in run 2 in panel (b).

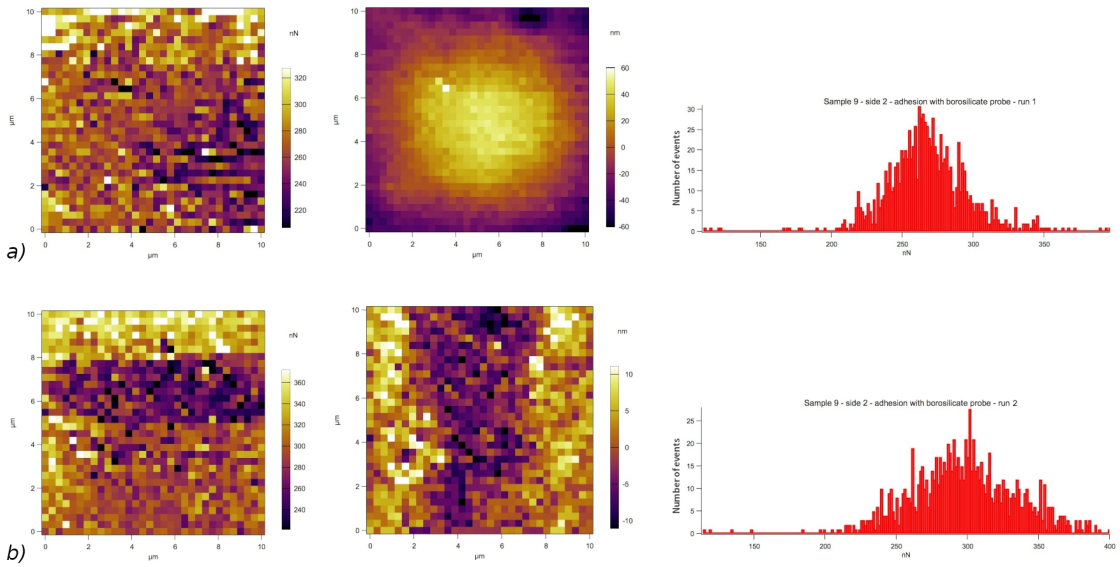

Figure 5.32: Adhesion maps, height maps and adhesion distributions of 'Sample 9 – side 2' with the borosilicate probe in run 1, in panel (a), and in run 2 in panel (b).

5.3.2.2 Sample 18

Adhesion and relative humidity collected for 'Sample 18' are listed in Table 5.26 and Table 5.27 for side 1 and side 2, respectively. Side 1 has a large standard deviation due to the fact that its values distributions for both probes have long (usually left) tails. However, the greatest part of the measurements is between 1 μN and 1.5 μN for the PS probe and around 2.5 μN for the borosilicate probes. Thus, it is possible to say that this side has a greater adhesion for the borosilicate probe, according to its hydrophilic nature as revealed by the contact angle. Side 2 shows lower values for both probes and, even if the dispersion of the adhesion values is lower than side 1, adhesion data are not always centred around some specific values but mostly spread from 0 to about 0.8-1 μN. Even if cautiously, it possible to say that side 2 may have a lightly higher adhesion toward the borosilicate probe than the corresponding side 1.

Looking at the height maps and comparing them with the adhesion maps it is possible to see that in 'Sample 18 – side 1' all the lowest adhesion regions

correspond to the asperities in the height maps. In fact, the adhesion maps of this side show quite homogeneous values in the majority part except for the locations corresponding to the highest features. Remembering that the morphology of this side is quite flat and smooth, except for some little asperities, it is possible to consider that the adhesion of this material toward the two probes is represented by the values that are in the peaks of the distributions shown in Figures 5.33 and 5.34. The long left tails are due to the small adhesion regions of the asperities. Differently from the other samples seen before, there is not an increase of adhesion along the walls of these asperities. This can be ascribed to the fact that these asperities are not very tall and they descend quickly toward the base: the bigger colloidal probe cannot be in intimate contact when it touches them in such a 'lateral' way, so the contact area is less than that of a normal contact and, consequently, also adhesion is reduced.

'Sample 18 – side 2' shows a different situation where the greatest adhesion is mostly on the tops of its big spots, while a reduction of adhesion is seen along the walls and the gorges among them (Figures 5.35 and 5.36). This behaviour is the opposite of what has been observed until now. However, it should be remembered that the dimensions and shapes of the spots in 'Sample 18 – side 2' are (or can be) more or less in the same scale of the colloidal probes. Moreover, lateral walls show a steep slope as seen in the morphology and the spots are quite next to each other, while the tops of the spots are quite large and flat. That means that, probably, for this surface, the contact area is greater in the flattest regions (in this case the tops of the spots) and lower along the walls because the slope of the surface in these parts and, more probably, the vicinity of other spots does not let the probe touch the surface completely. Proof of that can be seen in the maps of the second runs with the borosilicate probe: this is the only case where the greatest adhesion regions do not correspond to the highest features. However, in that location, right and left spots are quite far and in the middle of them there is another quite flat spot: thus, the central high adhesion region can be considered the top of a lower spot rather than a gorge. And the other left-hand side high adhesion region of the

map corresponds to the least steep and the smoothest descending wall of the spot. In conclusion, also on this surface the highest adhesion regions are due to the greatest contact area between the surface and the probes, however, the particular shape and scale of the features of this side cause that, differently from the previous samples, the tops of the spots are the locations where the contact areas are usually greater.

In conclusion, on the opposite of the other samples, in the case of 'Sample 18' roughness and features let adhesion spread toward lower values: all their distributions of adhesion values can be seen as the sum of two distributions centred on different values of adhesion: a higher value corresponding to the flattest regions and a lower one due to the suddenly changing parts of the surface. The extensions and the weights of these two distributions can be more significant or not according to the extension of the two types of regions and the spread of the adhesion values in each of them.

Sample 18 – side 1		
Run/probe	Adhesion ± standard deviation (μN)	Relative humidity (%)
1/PS	1.0 ± 0.4	31.8
2/PS	1.3 ± 0.4	32.0
1/Borosilicate	2.1 ± 0.6	29.2
2/Borosilicate	2.1 ± 0.8	29.2

Table 5.26: 'Sample 18 – side 1' average adhesion and relative humidity as collected with PS and borosilicate colloidal probes (two runs for each probe).

Sample 18 – side 2		
Run/probe	Adhesion ± standard deviation (μN)	Relative humidity (%)
1/PS	0.3 ± 0.2	46.8
2/PS	0.3 ± 0.2	46.8
1/Borosilicate	0.5 ± 0.3	28.0
2/Borosilicate	0.4 ± 0.3	27.0

Table 5.27: 'Sample 18 – side 2' average adhesion and relative humidity as collected with PS and borosilicate colloidal probes (two runs for each probe).

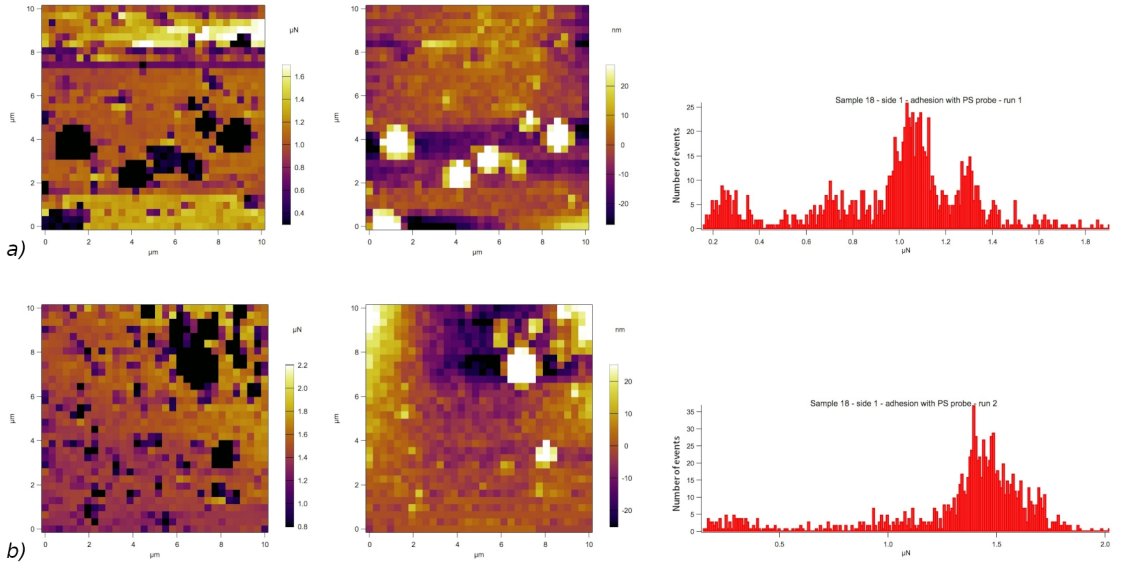

Figure 5.33: Adhesion maps, height maps and adhesion distributions of 'Sample 18 – side 1' with the PS probe in run 1, in panel (a), and in run 2 in panel (b).

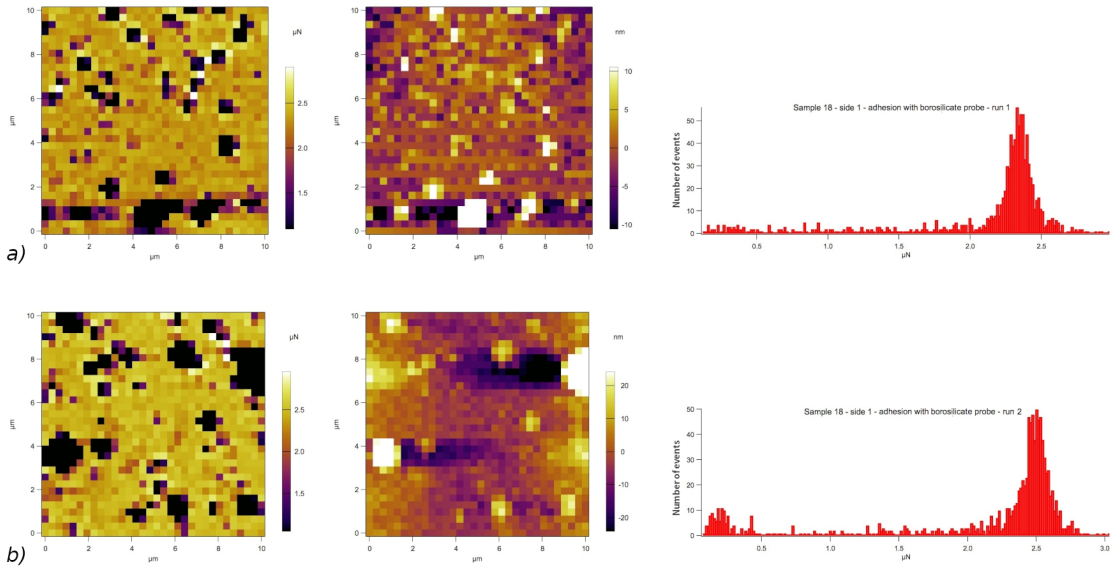

Figure 5.34: Adhesion maps, height maps and adhesion distributions of 'Sample 18 – side 1' with the borosilicate probe in run 1, in panel (a), and in run 2 in panel (b).

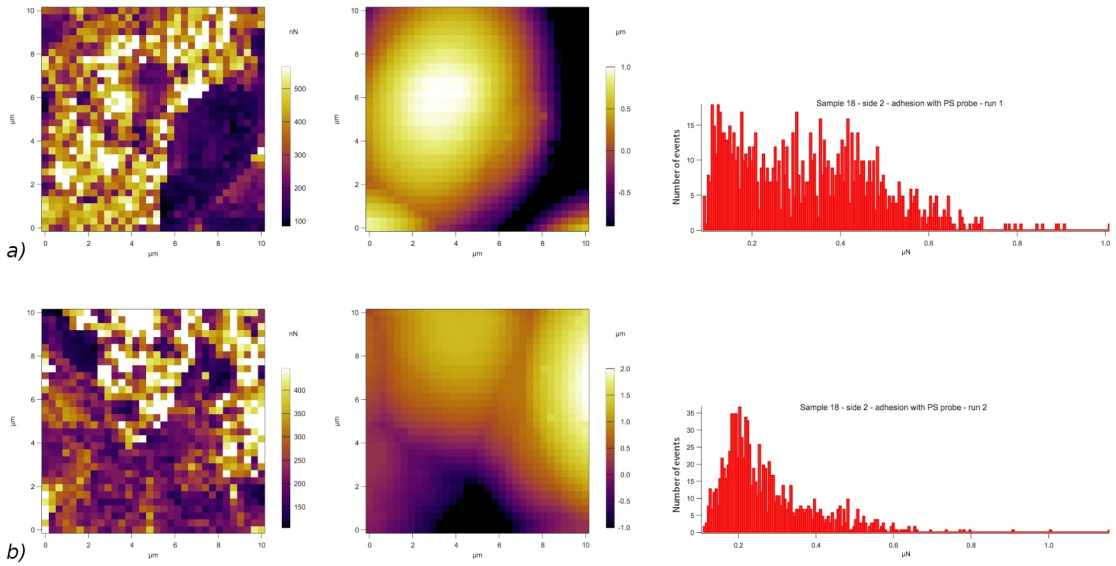

Figure 5.35: Adhesion maps, height maps and adhesion distributions of 'Sample 18 – side 2' with the PS probe in run 1, in panel (a), and in run 2 in panel (b).

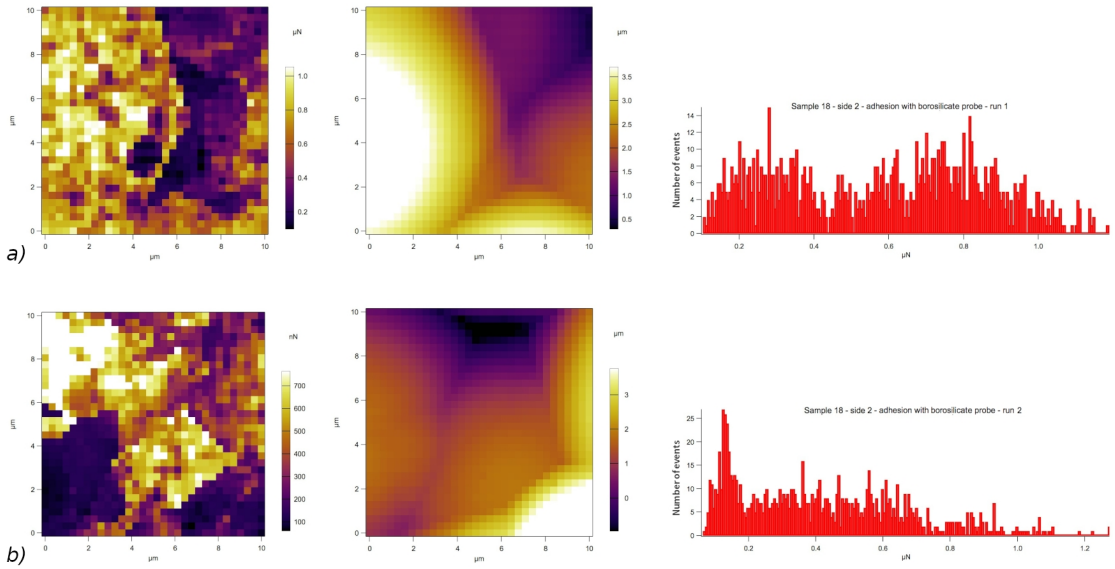

Figure 5.36: Adhesion maps, height maps and adhesion distributions of 'Sample 18 – side 2' with the borosilicate probe in run 1, in panel (a), and in run 2 in panel (b).

5.3.2.3 Sample 19

'Sample 19' adhesion and relative humidity during the measurements are listed in Table 5.28 and Table 5.29 for side 1 and side 2, respectively. In this case, both sides of 'Sample 19' show similar behaviours toward the probes: they have a greater adhesion for the borosilicate probe with the greatest part of measurements with values comprised between 1 μN to 2 μN according to the run. Adhesion for the PS probe, instead, has the greatest part of values below 1 μN for both sides.

Comparison among the height and adhesion maps of 'Sample 19 – side 1' shows that low adhesion regions correspond to small asperities, to some of the tops of the highest asperities, to some walls (those with the steepest descending slope) and to some very narrow gorges (Figures 5.37 and 5.38). On the contrary, high adhesion regions are located on the less steep descending walls of the big asperities. It is quite difficult to comment 'Sample 19 – side 2' because three of the four height maps could not be successfully processed (Figures 5.39 and 5.40). Also in the case of the morphological analysis, this sample was heavily processed in order to

highlight the fine features (lines) and deformations due to the flattening step were evident. Attempts to flatten the low resolution height maps could only show some of the highest asperities (the peaks seen in the morphology): the remaining parts of the maps were heavily distorted by algorithms and do not have any meaning. Where it is possible to find a correlation between adhesion and height, greater adhesion is linked to gorges, lower adhesion with the tops of features. In the second run acquired with the borosilicate probe, it is possible to note in the adhesion map the presence of one or two coupled lines: it or they show low adhesion in comparison with the next regions. It may be that on the edges of this (or these) line(s) the contact area is reduced because they are very narrow and the comparably large colloidal probe cannot penetrate inside them.

Sample 19 – side 1		
Run/probe	Adhesion ± standard deviation (μN)	Relative humidity (%)
1/PS	0.5 ± 0.3	31.2
2/PS	0.5 ± 0.3	31.2
1/Borosilicate	1.1 ± 0.6	27.0
2/Borosilicate	1.3 ± 0.6	27.0

Table 5.28: 'Sample 19 – side 1' average adhesion and relative humidity as collected with PS and borosilicate colloidal probes (two runs for each probe).

Sample 19 – side 2		
Run/probe	Adhesion ± standard deviation (μN)	Relative humidity (%)
1/PS	0.6 ± 0.4	31.2
2/PS	0.8 ± 0.3	31.8
1/Borosilicate	1.3 ± 0.5	27
2/Borosilicate	1.9 ± 0.6	27.3

Table 5.29: 'Sample 19 – side 2' average adhesion and relative humidity as collected with PS and borosilicate colloidal probes (two runs for each probe).

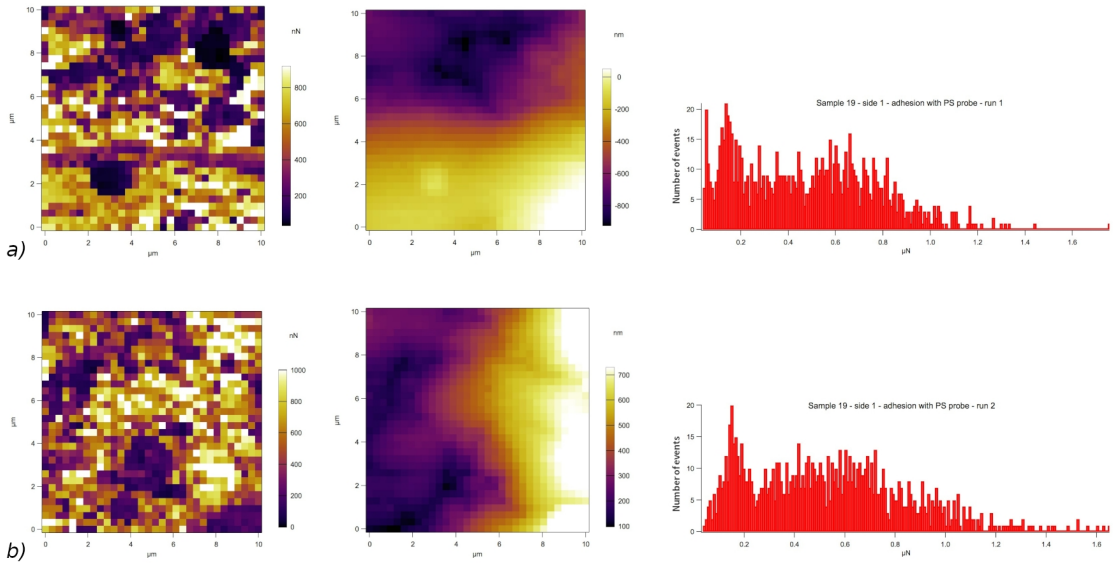

Figure 5.37: Adhesion maps, height maps and adhesion distributions of 'Sample 19 – side 1' with the PS probe in run 1 in panel (a), and in run 2 in panel (b).

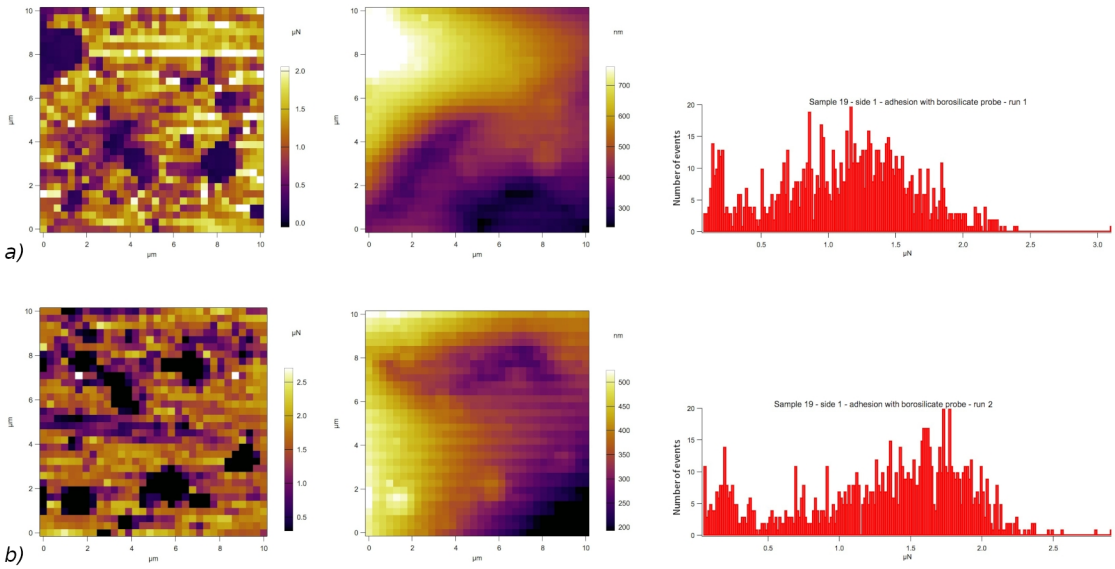

Figure 5.38: Adhesion maps, height maps and adhesion distributions of 'Sample 19 – side 1' with the borosilicate probe in run 1 in panel (a), and in run 2 in panel (b).

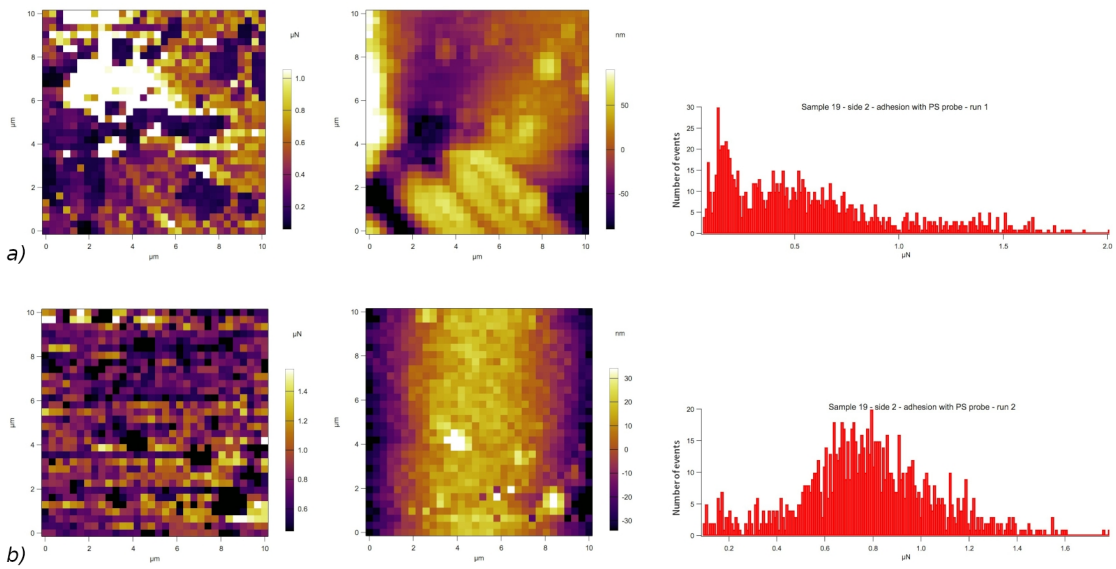

Figure 5.39: Adhesion maps, height maps and adhesion distributions of 'Sample 19 – side 2' with the PS probe in run 1 in panel (a), and in run 2 in panel (b).

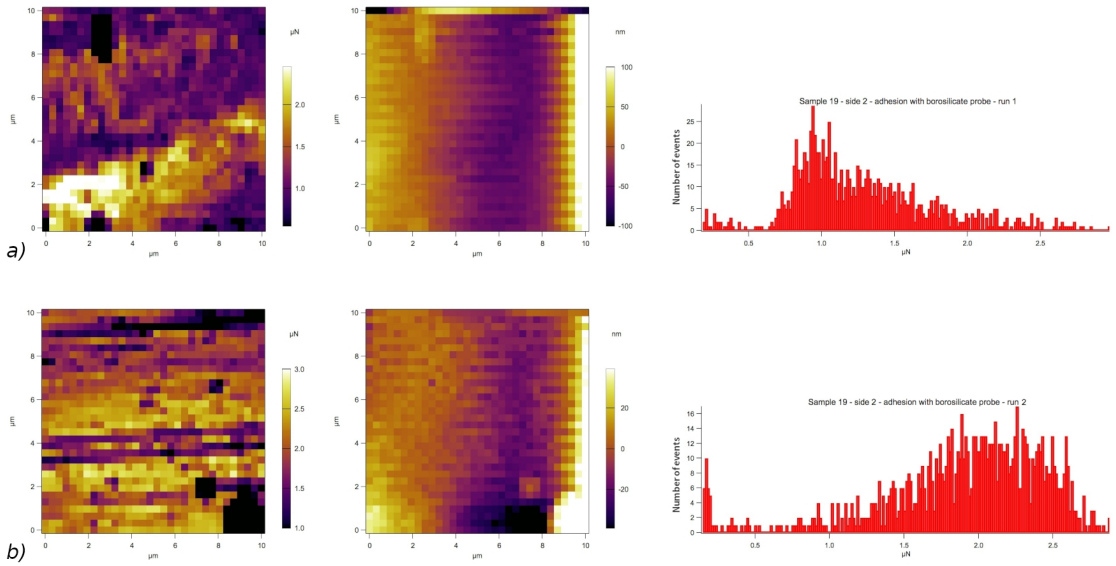

Figure 5.40: Adhesion maps, height maps and adhesion distributions of 'Sample 19 – side 2' with the borosilicate probe in run 1 in panel (a), and in run 2 in panel (b).

5.3.2.4 Sample 24

Results of the adhesion and relative humidity measurements for both side 1 and side 2 of 'Sample 24' are listed in Table 5.30 and Table 5.31, respectively.

Looking at adhesion values and histograms in Figures 5.41 – 5.44 it is clear that the two sides of 'Sample 24' have different behaviours. 'Sample 24 – side 1' shows quite a large spread in the adhesion values; despite of this, it is possible to see that the greatest part of adhesion values are around 1 μN for the PS probe and between 1.5 – 2 μN for the borosilicate probe: it is not surprising that this side has a greater adhesion toward the hydrophilic probe (as also the contact angle suggests). 'Sample 24 – side 2' shows a lower precision in the adhesion than the side 1, with a standard deviation in the same order or slightly lower than the measured adhesion. A look to the histograms shows that the greatest part of the adhesion values are below 0.5 μN (and below or around 0.25 μN). However, the remaining part of values is spread over a quite large range and this reduces the precision of the measurements. In any case, it does not seem that this surface has different adhesion according to the type of probe.

It can be surprising to see that 'Sample 24 – side 1', that is the flattest sample can show a so large spread of adhesion values. The spread of data is greater toward lower values and looking at the adhesion maps it is possible to note that the only regions that show a different and lower adhesion correspond to regions that resemble straight lines. Height maps of this side are shown as collected because the use of flattening algorithms put in evidence the fine features but together with the scanner artefacts and the overall effect is less comprehensible than the original maps. Looking at the height maps carefully, it is possible to confirm that the low adhesion lines correspond to the lines seen in morphological analysis. As for 'Sample 19 – side 2' space between the edge of these lines is very narrow and the probe can only sit on the top of them without come between them and so the contact area is less than in the flat parts of the surface.

The height maps of 'Sample 24 – side 2' appear to be similar to those of 'Sample 18 – side 2' with high rounded spots arising from the surface. However, differently from 'Sample 18 – side 2' where the tops of the spots usually correspond to the highest adhesion regions, in the case of 'Sample 24 – side 2' tops of asperities show the lowest adhesion while the high adhesion regions are gorges among spots. The strange shape of these spots that appear to be rounded, even if the morphological analysis shows that this sample has irregular shaped features with quite well defined and sharp edges, is an artefact deriving from the use of a spherical tip: the colloidal probe is much bigger than the scale of the details of the edges of the features of this surface and cannot catch so fine details, but only follow their profiles and revealing them as 'rounded'. The differences in the high adhesion regions of this sample with respect to 'Sample 18 – side 2' can be explained with the more space among the high feature that let the probe to have a bigger contact area. The fact that the high features show less adhesion than gorges is an additional indirect proof that on the tops of the spots the contact area is much less because, in reality, those high features do not have a hemispherical shape but an irregular and much reduced surface. And because this side has, in reality, a such irregular surface, adhesion is generally low except for the some small regions of the gorges that let the distribution have so long right tails.

Sample 24 – side 1		
Run/probe	Adhesion ± standard deviation (μN)	Relative humidity (%)
1/PS	0.9 ± 0.3	30.9
2/PS	0.9 ± 0.2	30.5
1/Borosilicate	1.5 ± 0.6	27.6
2/Borosilicate	1.5 ± 0.5	27.3

Table 5.30: 'Sample 24 – side 1' average adhesion and relative humidity as collected with PS and borosilicate colloidal probes (two runs for each probe).

Sample 24 – side 2		
Run/probe	Adhesion ± standard deviation (μN)	Relative humidity (%)
1/PS	0.7 ± 0.7	29.9
2/PS	0.5 ± 0.6	30.2
1/Borosilicate	1 ± 1	27.3
2/Borosilicate	0.5 ± 0.9	27.3

Table 5.31: 'Sample 24 – side 2' average adhesion and relative humidity as collected with PS and borosilicate colloidal probes (two runs for each probe).

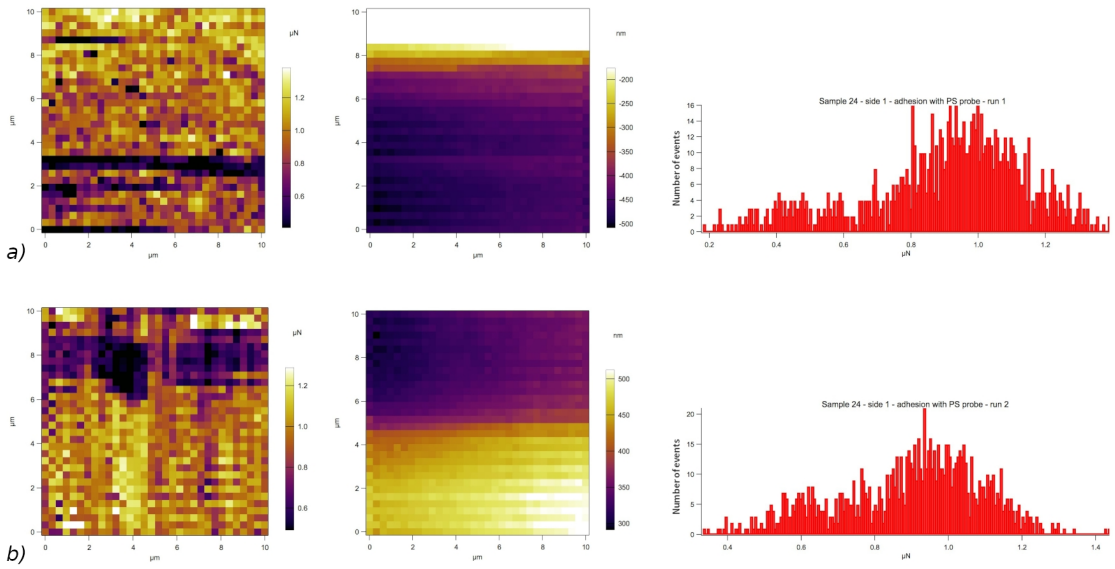

Figure 5.41: Adhesion maps, height maps and adhesion distributions of 'Sample 24 – side 1' with the PS probe in run 1 in panel (a), and in run 2 in panel (b).

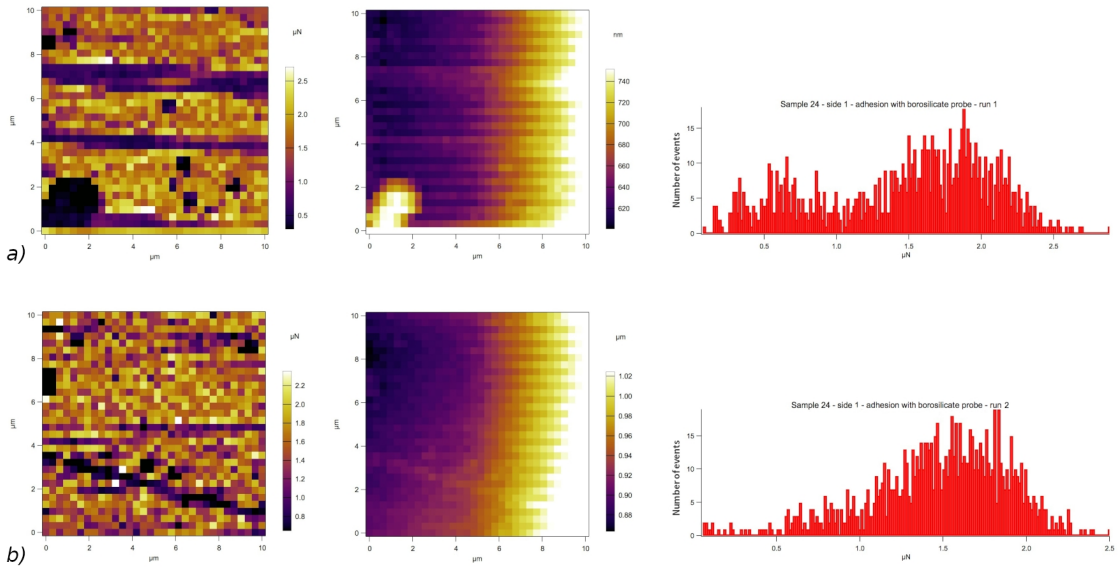

Figure 5.42: Adhesion maps, height maps and adhesion distributions of 'Sample 24 – side 1' with the borosilicate probe in run 1 in panel (a), and in run 2 in panel (b).

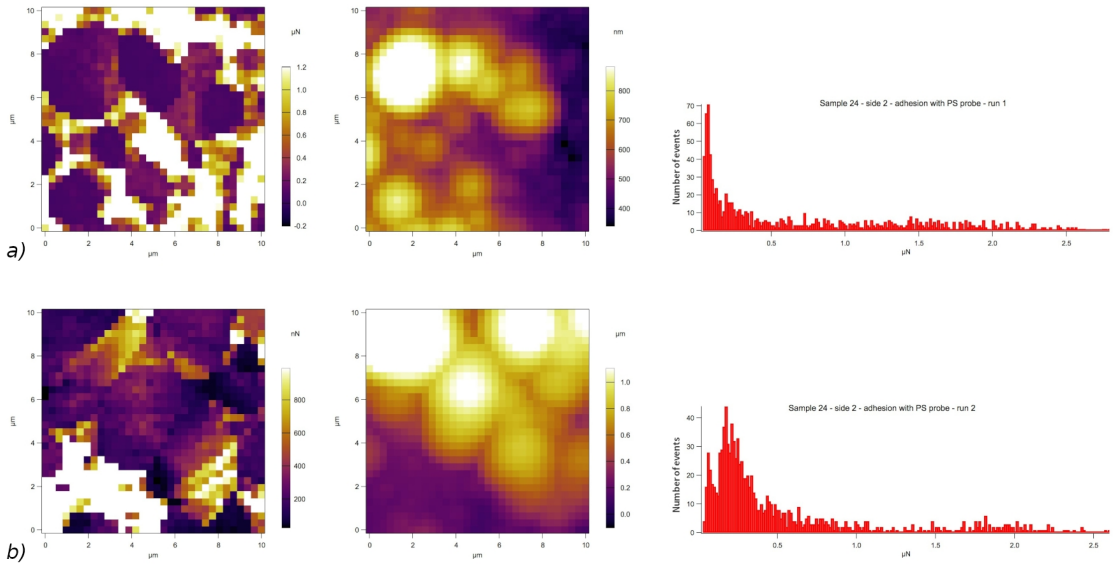

Figure 5.43: Adhesion maps, height maps and adhesion distributions of 'Sample 24 – side 2' with the PS probe in run 1 in panel (a), and in run 2 in panel (b).

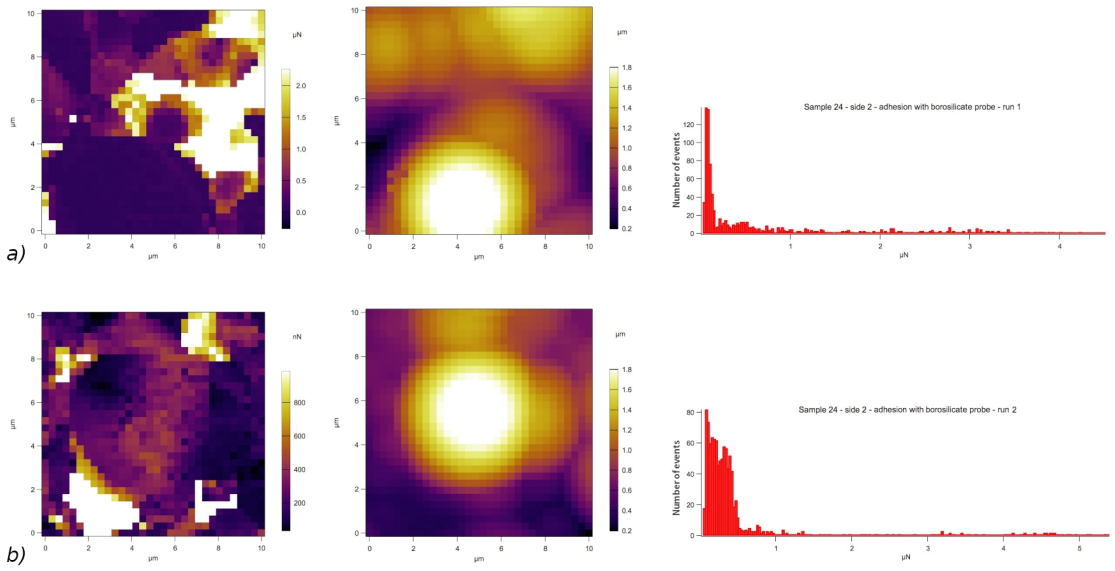

Figure 5.44: Adhesion maps, height maps and adhesion distributions of 'Sample 24 – side 2' with the borosilicate probe in run 1 in panel (a), and in run 2 in panel (b).

5.3.2.5 Sample 47

Adhesion and relative humidity values collected for 'Sample 47' are listed in Table 5.32 and Table 5.33 for side 1 and side 2, respectively. Looking at adhesion data and histograms, it is clear that 'Sample 47' do not show significant differences between the two sides and has similar values toward both probes. It is likely that such similar values and behaviour are mostly due to the surface features of the two sides of this sample that are relevant and similar for both the two sides.

Height maps reveal that, for both sides, higher adhesion usually corresponds to valleys, if they are large enough to let the probe come inside them, or, mostly, to walls of valley. Lower adhesion is connected with the tops of the characteristic lines of these surfaces and to the globular features seen in the morphological analysis.

Sample 47 – side 1		
Run/probe	Adhesion ± standard deviation (μN)	Relative humidity (%)
1/PS	0.3 ± 0.3	45.8
2/PS	0.5 ± 0.3	45.8
1/Borosilicate	0.26 ± 0.09	27.6
2/Borosilicate	0.25 ± 0.09	27.6

Table 5.32: 'Sample 47 – side 1' average adhesion and relative humidity as collected with PS and borosilicate colloidal probes (two runs for each probe).

Sample 47 – side 2		
Run/probe	Adhesion ± standard deviation (μN)	Relative humidity (%)
1/PS	0.4 ± 0.2	31.2
2/PS	0.4 ± 0.2	30.9
1/Borosilicate	0.3 ± 0.2	28.3
2/Borosilicate	0.5 ± 0.2	27.6

Table 5.33: 'Sample 47 – side 2' average adhesion and relative humidity as collected with PS and borosilicate colloidal probes (two runs for each probe).

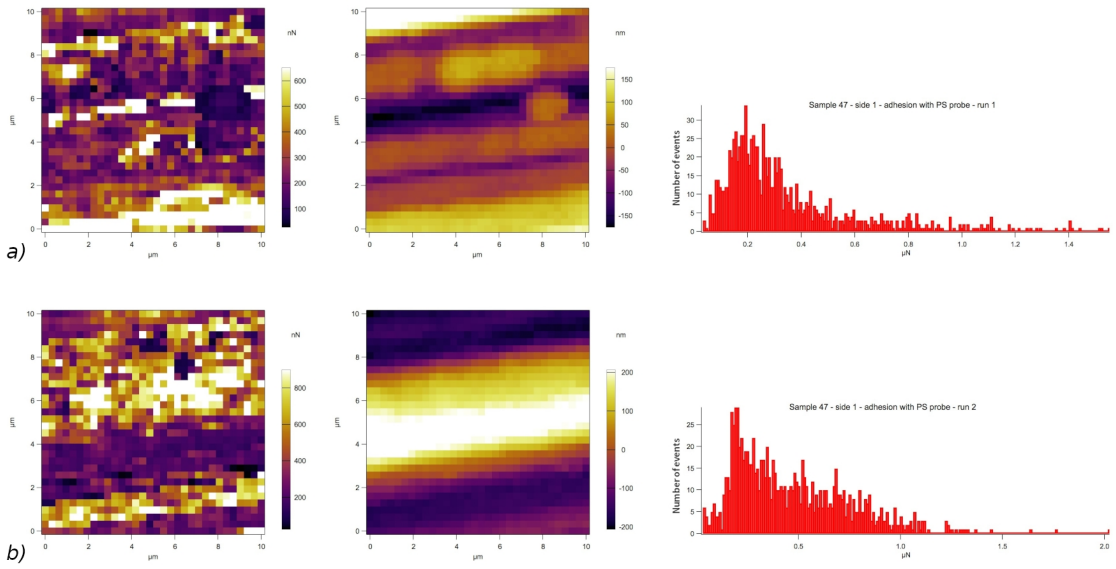

Figure 5.45: Adhesion maps, height maps and adhesion distributions of 'Sample 47 – side 1' with the PS probe in run 1 in panel (a), and in run 2 in panel (b).

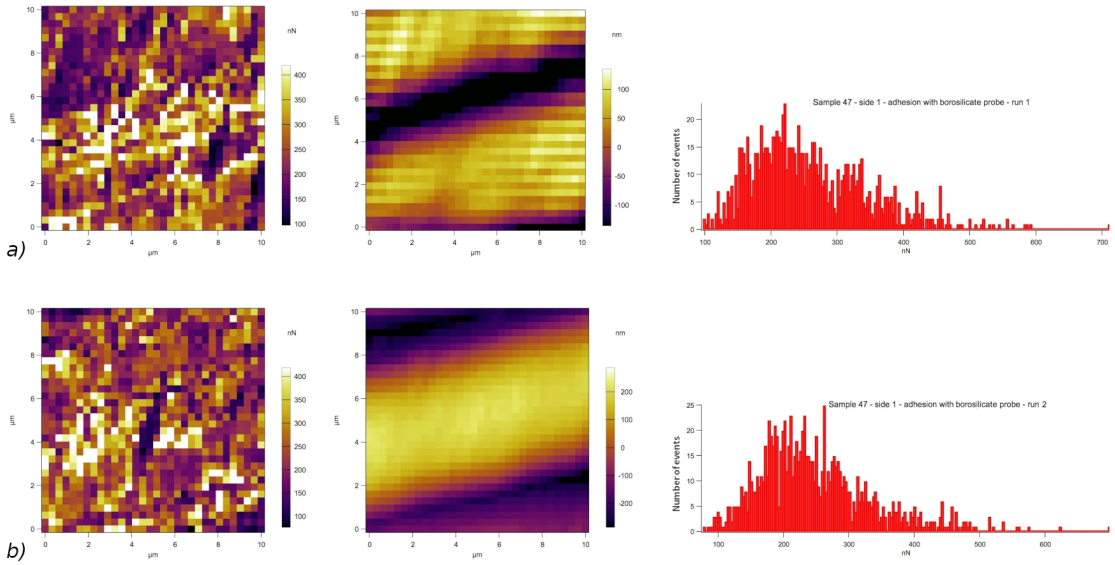

Figure 5.46: Adhesion maps, height maps and adhesion distributions of 'Sample 47 – side 1' with the borosilicate probe in run 1 in panel (a), and in run 2 in panel (b).

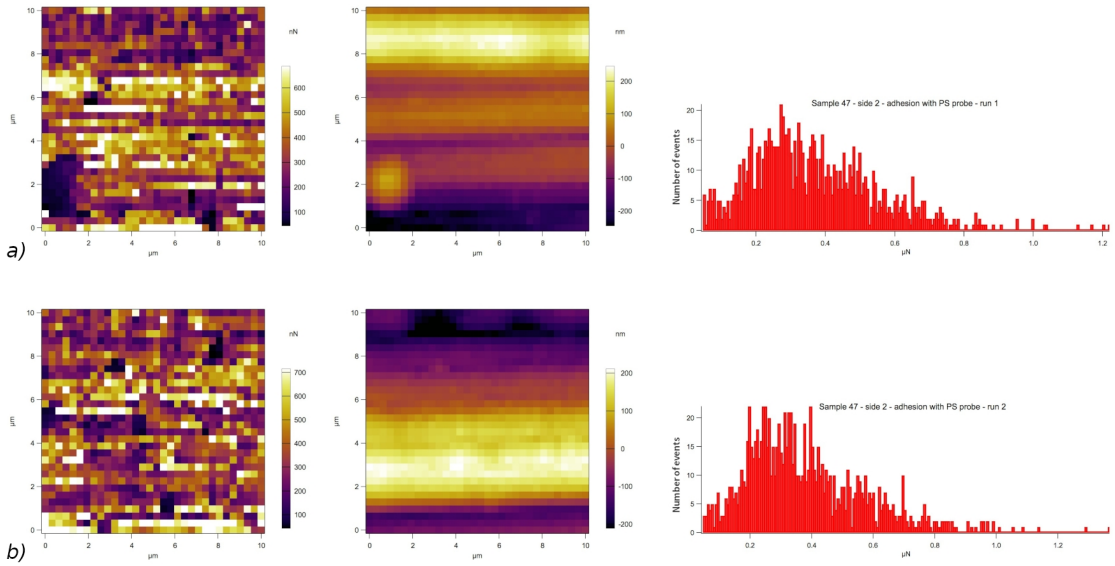

Figure 5.47: Adhesion maps, height maps and adhesion distributions of 'Sample 47 – side 2' with the PS probe in run 1 in panel (a), and in run 2 in panel (b).

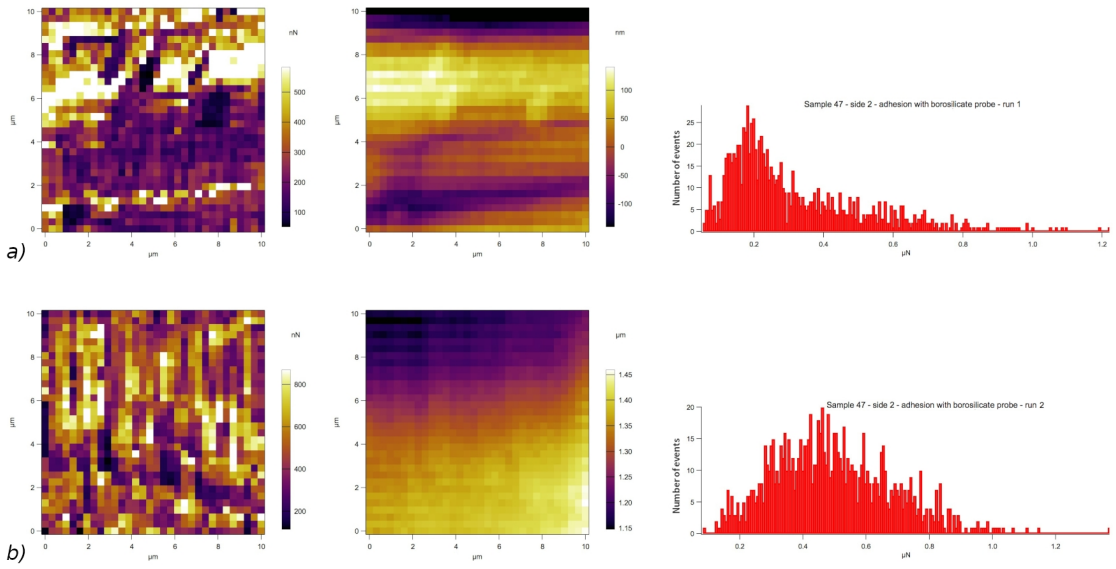

Figure 5.48: Adhesion maps, height maps and adhesion distributions of 'Sample 47 – side 2' with the borosilicate probe in run 1 in panel (a), and in run 2 in panel (b).

5.3.3 Discussion and adhesion comparison about samples

The adhesion data previously reported show that these samples can show a wide range of 'adhesion behaviours' that reflects their differences and this allows a more comprehensive awareness of roughness effects on adhesion. Because samples are so different, the next discussion will firstly consider rollers and plastic sheets separately and then comprehensive conclusions will be drawn. Discussions will start trying to find a link between surface features and adhesion and then will move to consider effects of features on adhesion distribution. Then, final conclusions on the cleaning skills of rollers with remarks will be provided. An initial remark should be done: in this system, the contaminant particle is exemplified by the colloidal probes, that differently from real dust particles, have a regular shape of defined size (in this case of 10 μm of diameter). Thus, validity of numerical results and conclusions should be intended only for systems with similar characteristics. In fact, for example, a change in the diameter of the particle may lead to completely different conclusions, maybe with a roller with a higher adhesion because it has features in the same scale of the particle.

Rollers show adhesion behaviour that is connected to their surface features in a different way according to the characteristics of those features. Quite flat samples (FilmClean and PanelClean) show the greatest adhesion in some parts of gorges, where they are not too deep and not too large, but mostly along walls of high features and valleys, if they do not have too steep slope. In the specific case of these two rollers, some high adhesion regions are quite near to the tops of the high features. All ground samples have a different behaviour, with the greatest adhesion corresponding to gorges and some parts of the walls of their features and the lowest adhesion connected to the tops of high features. Actually, the height maps of ground samples can be superimposed on the respective adhesion maps revealing that there are strictly correspondences between features and adhesion regions. This is not always the case of FilmClean and PanelClean. NanoUClean, instead, shows an adhesion behaviour that is in the middle between the one of the other two non ground samples and the ground samples. Even if, also in the NanoUClean there is a correspondence of the gorges with the greatest adhesion regions and of the tops of high features with the lowest adhesion values, a superimposition of the respective adhesion and height maps does not show an as close correspondence as in the case of ground samples. This is because in NanoUClean, greater adhesion is also connected to some walls of high features like in FilmClean and PanelClean. As already noted in the morphological analysis, also the roughness and surface features sizes of NanoUClean are in the middle among those of the other two non ground rollers and those of the ground samples. This allows to conclude that, for rollers, adhesion behaviour can be linked to roughness in this way: for the flattest samples, with roughness values in the range of FilmClean and PanelClean and with features with similar characteristics to those of these two rollers, adhesion is greater mostly along non too steep walls and some not too deep and large valleys; for intermediate roughness and surface features like in NanoUClean, a mixed adhesion behaviour is revealed, where the greatest adhesion is linked both to some gorges or to some walls; for higher roughness values and significant surface characteristics like those of ground samples,

adhesion is directly connected to surface features with strict correspondence of high adhesion regions with gorges and low adhesion regions with tops of high features.

It may be interesting to provide hypotheses about the observed adhesion dependence from roughness. Because greater adhesion is linked to greater contact area, it is possible to say that, according to roughness and interfacial features, the greatest contact among surfaces and probes happens in different regions of these surfaces. For rollers like FilmClean and PanelClean, whose surfaces are smooth, mildly wavy, with some little holes and asperities that do not interrupt the pattern of these surfaces, greater contact areas are achieved where curvature of the surface can well match the shape of the probe and where the surface waviness draws 'valleys' of a size comparable to those of the probes. This actually happens along some walls, sometimes near the tops of high feature (it should be note that these tops are blunt and do not have sharp edges) and in the narrowest parts of valleys, especially if there are also not to deep. This can be imagined as a lateral contact with one side of the probe for walls, and with both sides of the probe for narrow valleys. Where the curvature of the surface does not match exactly the probe a partial lateral contact, where the contact area is less than the contact area on the flat part of the sample, leads to a lower adhesion. When roughness and surface features become more relevant, like in NanoUClean, where the surface can be still considered smooth but it is wavier with a higher height range, greater contact area is reached in different regions. Sometimes along walls, like for FilmClean and PanelClean and very likely with the same contact geometry, sometimes inside gorges, if the size of gorges allows a both sides lateral contact to happen. Again, if the lateral contact is reduced because of the non perfect strictly match among the slope of a wall or the size of a valley with the probe shape, a reduction of adhesion is observed. When roughness increases, with sudden changes in surface features, tops of high regions become smaller and more irregular, while valleys become deeper. In the case of these ground rollers, because their valleys are deeper but not larger than those of non ground samples, it should

be concluded that there are quite narrow in their lowest parts. That is why the greatest contact area among these surfaces and the probes is reached in the lowest parts of gorges where the contact likely involves both the two (and sometimes three) lateral sides of the probe (and probably also the lowest part of the probe itself). In the case of NanoClean, where it happens that features overcome the 10 x 10 μm^2 scan size, the greatest contact area can still be reached along walls because of the lateral contact. In all the ground samples, the lowest adhesion usually corresponds to the tops of the high features. The morphological analysis of these high features has shown that they have irregular shape and edges: contact area between the probe and these non-smooth surfaces can only be partial and so also adhesion is lower.

In this framework, it is easy to explain also adhesion values and the variation among samples. In the case of the flattest samples FilmClean and PanelClean values dispersion is less than that of the other samples. This is because the contact area is often similar on the flat parts of these surfaces with tails due to regions with increased or reduced lateral contact. The larger dispersion of adhesion values of NanoUClean is connected with the more variability of its surface and so with more regions where a larger or reduced lateral contact happens. The greatest dispersion of adhesion values of the ground samples is actually due to the presence of regions with quite large contact area (lowest parts of gorges, where the contact can also be all around the lateral part of the probe) and regions where the contact is less than that of a flat surface. This also clarifies why ground surfaces have adhesion distributions often centred on lower values than the respective non ground samples but spread on highest adhesion values: in fact, surface roughness reduces the average contact area, but, inside gorges where the probe should be imagined almost surrounded by the walls of the high features, contact area is much larger than in non ground samples and so also adhesion has greater values. When features that allow probes to have a greater contact are suddenly next to regions where the adhesion is reduced, as in the case of ground rollers, adhesion maps show that usually there is not a gradual transition from high adhesion to low

adhesion: in these samples values of adhesion force are strictly linked to the specific features of their surfaces, as well as success in removing or not a particle.

When the greatest parts of adhesion values of distributions are considered rather than the average adhesion value, rollers usually show similar adhesion to both the hydrophilic and hydrophobic probes. The only exception is NanoUClean with higher values towards the PS probe but this may be ascribed to the size of surface features that is larger than the 10 x 10 μm^2 scan size, as previously discussed.

On this basis, hypotheses on how these rollers work can be done. It is likely that flat samples are able to remove particle from a surface mainly because they have an adhesion force toward it greater than that of the surface. Even if they are flat, they are also soft, especially FilmClean and PanelClean, so they can adapt themselves to the cleaning surface and catch particles also from samples that have intermediate roughness. A possible explanation of how ground samples can work may be that they act as 'traps' for the particle. Rolling these elastomers over a surface with at least the load of their weights can let the particle be settled in such features and so be removed from the surface. The choice of soft materials can help in this process because they can deform under the load, catch the particle, and, when the load is removed and the elastomers recover their original shape, they can retain the particle stronger. This can also avoid that the particle can leave the elastomer surface when it touches again the dirty surface. An evidence of that mechanism for the ground samples can be seen in Figure 5.49 which is the AFM image of a trapped particle on the UTFClean surface. The particle is the highest feature on the right-hand side of the images in Figure 5.49 and is actually trapped in a gorge among two high walls.

Thus, while flat rollers should have enough force to remove a particle, ground rollers, in addition to the attractive force may also help their cleaning performances with this 'trapping system', that probably lets them be efficient even if their overall adhesion can be lower than the respective flat roller.

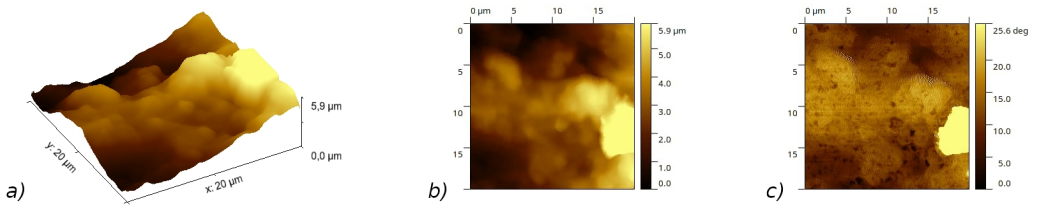

Figure 5.49: A particle trapped on the UTFClean surface: 3D rendering in panel (a), height image in panel (b) and phase image in panel (c).

Considering the values of the greatest parts of the adhesion distributions of rollers, rather than the average values, it is possible to see that, except for the couple NanoUClean/NanoClean, they show significant adhesion (mostly in the range of 1-1.5 μN). Only NanoUClean and NanoClean have lower adhesion, usually less than 1.5 μN. This may be due to the specific material of these two rollers, that is different from that used for the others, but it may also be ascribed by the more rigid material and their different ground patterns with respect to the other elastomers. It could be that they are designed for specific applications, where a less soft material is required and probably target particles to be removed have different characteristics. In fact, their surface features are often greater of the 10 μm scale used in this work.

Different kinds of adhesion behaviours can be noted also in the plastic sheets, with some samples that show the highest adhesion on the tops of high features, others that have higher adhesion inside valleys and finally some samples with the lowest adhesion in correspondence of straight lines. However, also in the case of plastic sheets, all these differences can be explained with the greater or smaller contact area between the surface and the colloidal probe. For example, samples with the flattest surfaces and small asperities or thin lines on them (like 'Sample 9 – side 2', 'Sample 18 – side 1', 'Sample 19 – side 2' and 'Sample 24 – side 1') show adhesion maps mainly where the flat regions have constant or small variations in adhesion, while regions where the small asperities and thin lines are present have the lowest adhesion. It can be assumed that in the flat part of the surface, the contact area is 'regular', that should be if the sample is flat, and adhesion values referred to these parts of the maps can be considered as 'reference' values for

adhesion. Small asperities like in 'Sample 9 – side 2' and 'Sample 18 – side 1' are too small and have walls with too steep slope to let the probe have a greater contact area than on the flat parts: it is very likely just a partial lateral contact. In the case of thin lines like in 'Sample 19 – side 2' and 'Sample 24 – side 1', very likely the probe just touches the edges and cannot come inside the gorge that lines drawn on the surface and so, again, its contact area with the surface is lower than that of the flat regions. Samples with intermediate size roughness and features, like 'Sample 9 – side 1', 'Sample 19 – side 1' and 'Sample 24 – side 2', show an adhesion behaviour similar to those seen for non ground sample, NanoUClean and ground rollers, respectively. In fact, in these samples, asperities have a larger scale and can let the probe have larger lateral contact area than in the flat regions or can create gorges where the probe can be surrounded by the surface. The special case of 'Sample 18 – side 2' is unique because it shows big round features just next each other. Tops of these spots have a small curvature, while lateral parts have a quite steep slope. In addition, these spots are quite near each other with small space among them. All these characteristics let this sample have a different adhesion behaviour, with the greatest adhesion on the tops of the spots and lower adhesion along the lateral walls. However, also this behaviour can be explained with the greater or lower contact area: the difference is that in this sample, the contact area is greater on the top of the spots that have the least curvature. Only when spots are not so near each other and the probe can be in contact with their walls, the lateral contact area becomes greater that the one on the tops of the spots and adhesion increases. A final remark on lines: 'Sample 47' in both its sides has lines, or maybe better, straight gorges much larger and deep than lines seen in 'Sample 19 – side 2' and 'Sample 24 – side 1': in this case, adhesion is greater when the gorge dimensions allow the probe to come in, otherwise high adhesion regions are usually on the initial part of walls that define gorges, where the lateral contact area is increased. This is also an indirect proof that the explanation used for 'Sample 19 – side 2' and 'Sample 24 – side 1' can hold, falling these two samples in the case of small space between the two walls of lines.

Adhesion values of plastic sheets and their dispersion can be quite different and are strictly dependent on surface features. It is interesting to note that, if there is a different adhesion towards the two probes, the borosilicate one is that that have the greatest adhesion, as expected from the hydrophilic nature of these samples.

A comparison of adhesion data of elastomers and plastics sheets versus the same type of probe allows to know if a specific roller is able to clean a surface or not. As introduced in previous chapters, the surface that will show the highest value of adhesion toward one of the probe is the surface that will catch or retain the particle. Success or failure of rollers in removing particles from the plastic sheets is described by condition 2.1: because of the great dispersion of adhesion values, the comparison is done considering $F_{\mathrm{adh\,PS}}$ and $F_{\mathrm{adh\,PR}}$ in a qualitative way, that means under which values the greatest parts of values of adhesion distributions are. If condition 2.1 is respected there is success in cleaning; if the two distributions of $F_{\mathrm{adh\,PS}}$ and $F_{\mathrm{adh\,PR}}$ are similar there is a competitive adhesion (the surface may or may not be cleaned); if condition 2.1 is not respected there is a failure in cleaning. Results are summarised in Table 5.34 and Table 5.35 for the PS and borosilicate probes, respectively.

5 Teknek's samples

	FilmClean	UltraClean	PanelClean	UTFClean	NanoUClean	NanoClean
Sample 9 side 1	Y	Y	Y	Y	≈	≈
Sample 9 side 2	Y	Y	Y	Y	Y	≈
Sample 18 side 1	Y	Y	Y	Y	≈	X
Sample 18 side 2	Y	Y	Y	Y	Y	Y
Sample 19 side 1	Y	Y	Y	Y	Y	≈
Sample 19 side 2	Y	Y	Y	Y	Y	≈
Sample 24 side 1	Y	Y	Y	Y	Y	≈
Sample 24 side 2	Y	Y	Y	Y	Y	Y
Sample 47 side 1	Y	Y	Y	Y	Y	≈
Sample 47 side 2	Y	Y	Y	Y	Y	≈

Table 5.34: Success (Y), failure (X) and competitive adhesion (≈) of rollers in cleaning surfaces from hydrophobic particles. Data comparison is done among the distributions of adhesion values of all samples towards the PS probe.

	FilmClean	UltraClean	PanelClean	UTFClean	NanoUClean	NanoClean
Sample 9 side 1	X	≈	X	≈	X	X
Sample 9 side 2	Y	Y	Y	Y	≈	≈
Sample 18 side 1	X	≈	X	≈	X	X
Sample 18 side 2	Y	Y	Y	Y	X	≈
Sample 19 side 1	Y	Y	Y	Y	X	X
Sample 19 side 2	≈	Y	≈	Y	X	X
Sample 24 side 1	≈	Y	≈	Y	X	X
Sample 24 side 2	Y	Y	Y	Y	≈	≈
Sample 47 side 1	Y	Y	Y	Y	≈	≈
Sample 47 side 2	Y	Y	Y	Y	X	≈

Table 5.35: Success (Y), failure (X) and competitive adhesion (≈) of rollers in cleaning surfaces from hydrophilic particles. Data comparison is among the distributions of adhesion values of all samples towards the borosilicate probe.

As reported in Table 5.34, rollers are quite effective in removing the hydrophobic PS particle from plastic sheets. Some difficulties or failures are linked to NanoUClean and NanoClean that have the lowest $F_{\mathrm{adh\,PR}}$ toward the PS probe among rollers. The situation is more complex in the case of the hydrophilic borosilicate probe, where there are surfaces that may be cleaned only by UltraClean and UTFClean with some difficulties, but not by the other rollers (Table 5.35). This is because 'Sample 9 – side 1' has a great dispersion in adhesion with values that can spread until 5 μN in some locations (as in the first run with the borosilicate probe); while 'Sample 18 – side 1' has the great part of adhesion values around 2.5 μN. Some other samples can be cleaned only by UltraClean and UTFClean, such as 'Sample 19 – side 2', 'Sample 24 – side 1' because their adhesion is near 5 μN or slightly above it. The remaining samples can be successfully cleaned by all the

rollers except for NanoUClean and NanoClean. Actually NanoUClean and NanoClean are not able to clean any of these surfaces from the borosilicate particle; in some cases they can both show a competitive adhesion and in some other cases only NanoClean perhaps may have success. Because relative humidity during adhesion measurements with the borosilicate probe ranges between 27% and 30%, it may be that it has a role in increasing $F_{\mathrm{adh\,PS}}$: however, the range of its variability is so small that, if there is a contribution of the capillary force, this should be similar for most of the samples.

It should be remarked again that previous conclusions are drawn on comparison of where the great part of adhesion values are in the distributions: it should not be forgotten that, especially for very rough surface and ground rollers, adhesion values are strictly connected to the position of surface features. It means that success or failure in cleaning a surface is also linked to the probability that the particle is caught by the right location of the roller surface.

5.4 Conclusions

The study of so many different samples for materials and surface features leads to a comprehensive qualitative picture of effects of surface features on adhesion. Adhesion and surface features are shown to be strictly connected, with the greatest adhesion where the geometry of the contact allows the probe to have a larger contact area, usually with one or more lateral contacts. In order to have this increase in adhesion, it is important that the surface features and the probe are in similar ranges of dimensions and shape: when features become too small, or they have too steep walls or finally they are too near each other, the contact area is less than on the corresponding flat surface and the adhesion is decreased. In the case of ground rollers, in addition to adhesion force, probably also a 'trapping' system of the particle may help in its removal.

Also data distributions and dispersions, that for some samples are really large, are connected to surface features: if the surface is quite flat with few asperities or

holes, values vary in a small range; while when the surface has a lot of features that can increase or decrease the contact area, then data dispersion may be quite large. If a surface (roller included) has features bigger than the studied scan size, this is reflected in adhesion values and distributions that can also be quite different from a location to another.

Cleaning performances of rollers are shown to be quite good for the hydrophobic particle, while more difficulties can arise with a hydrophilic particle. All the plastic sheets are hydrophilic and this explains why some of those can have a quite large adhesion, competitive with those of rollers for the hydrophilic particle. In some other cases, it is the spread of adhesion values or specific regions that can lead to an overall adhesion higher or in the same range of those of rollers. NanoUClean and NanoClean have low chances of efficiently removing a hydrophilic particle from these hydrophilic surfaces because of their low adhesion values toward the borosilicate probe. A contribution of the capillary force in increasing the adhesion between the plastic sheets and the hydrophilic probe cannot be excluded: however, considering that relative humidity during measurements was quite low, probably the contribution of the capillary force to the adhesion force is not the most important.

Rollers are made of hydrophobic material and usually show similar adhesion values toward the two types of probes. This is surely an advantage and indicates a wise choice of the type of the materials: rollers' performances are so similar to both hydrophobic and hydrophilic particles, with no influence of relative humidity on their adhesion. The ground process is able to create regions with higher adhesion: this spreads adhesion values on a larger range than the corresponding non ground sample, even if the data distribution may be centred on lower values. The ground process also creates high adhesion next to low adhesion features, with usually non gradual changes. This causes adhesion to be strictly connected to surface features: the success or the failure in removing a particle is also a matter of where the particle touches the roller and not only of the overall adhesion value. So, if to ground a sample can lead to the advantage that with a unique chemistry, the range

of adhesion can be modulate, the main disadvantage is that, together with high adhesion regions, also low adhesion regions are created and so the performance in cleaning also depends on the position where the particle to be removed is touched: if it is in contact with a high adhesion region it will be removed, otherwise it may happen that it will remain on the surface. A way to reduce the probability that this latter unpleasant event could happen it may be to use a roller twice on the same surface or to use two in series rollers: in this way the probability that a particle cannot be removed is reduced by the second roller. This way may also be interesting in the case of very dirty surfaces that may 'saturate' the first used roller. Another way may be to increase the load of the roller on the surface: because rollers are soft, this could let them deform and better collect particles from the surface. However the applied load should be carefully studied taking into account the characteristics of the target surface because if the load is too much, the roller may drag the surface (for example in the case of thin and adhesive films). Also different speeds can be evaluated for materials that show a light viscoelasticity, always with care to avoid damages to particular surfaces, like, again, thin films.

It is not possible to conclude with a well defined and unique recipe for contact cleaning: this is an introductory work revealing the main physical mechanisms of the adhesion and to go into details, a better knowledge of target surfaces, particles to remove and (why not?) industrial machineries design is required.

As final remark on this work; it is underlined once more that these results are strictly linked to the conditions and the geometry used in the experiments: a different particle size and shape can lead to different results. Each roller is specifically designed for specific purposes: for example, NanoUClean and NanoClean that in this work show to be the least efficient in cleaning surfaces from particles with a diameter of 10 μm may work better than the others in the specific field for which they are designed.

As future study, it may be of interest to try different particle shapes and dimensions to see how adhesion behaviour changes, maybe with choices that are more connected to the real application of rollers and more information about

rollers and reference surfaces (this is actually a blind study as wanted by Teknek). Another interesting study may be related to the ground process: considering that roughness is able to modulate adhesion, specific ground pattern can be tried and studied on purpose. It is also possible to think to use different techniques (like stylus profilometry of confocal microscopy) for the morphological characterization of samples, if surface features could have greater sizes than those analysed in this work.

6 Summary, conclusions and future work

Adhesion is not an easy topic to investigate, especially if the roles of different properties must be taken into account. It can be influenced both by bulk or surface characteristics, such as crosslink density, viscoelasticity and roughness.

Five PDMS samples were synthesised in a similar manner in order to get samples with similar surface features and network bulk properties gradually changing from an ideal elastomer to a light viscoelasticity. Surprisingly, those networks were all almost elastic even if the yields of the crosslink reactions ranged between 80% and 60%.

On the flat PDMS network, crosslink density does not show any effect on adhesion, mostly because the used experimental conditions were studied to be 'light' and so to not affect the bulk of the polymer. This explain why, on the contrary, in some nanoindentation studies where the probe has a different geometry and the maximum load is greater, an effect of the crosslink density on adhesion was reported.

On the contrary, on the same samples, viscoelasticity which was revealed by the macroscopic technique DMA is also observed to have an influence on adhesion. This influence is observable only at the highest AFM head speeds with an increase in the adhesion force. In order to check if the energy release rate follows the most common dependence with the crack speed, a new strategy for the evaluation of the contact radius was developed. In fact, because none of the already known methods work properly in the experimental used conditions (they were developed for lower or greater loads than those used in this thesis), a direct calculation of the contact radius at the adhesion point and the points just before and after it was done. Crack speed was calculated with the forward finite difference between the radii of the adhesion point and the following point and the energy release rate showed the known dependency with it with an exponent ranging around 0.6. In addition, this approach of calculation of the contact radius allowed to have an interesting insight

in the detachment mechanism of PDMS at the nanoscale: observations about the contact radii before and after the adhesion point allow to think that the debonding mechanism could be similar to that seen at the macroscale, with a regular (or absent) reduction of the crack radius until the adhesion point where fingering processes become predominant.

The described method for the calculation of the contact radius also requires the knowledge of the elastic modulus: even if this information was available from the bulk measurements it was chosen to determined it from the first (linear) part of the retraction curves, as already done by other authors. It appears that these 'surface' Young's moduli are different from the bulk ones as sometimes noted in literature: this is a proof that the studied conditions were suitable for a study addressed only to surfaces. Moreover, it is also interesting to note that a surface can have a different modulus from the bulk.

Thus, in studying surface properties care should be taken in both the choice of experimental set-up and in the use of values taken from bulk properties.

Roughness was studied on commercial samples provided by Teknek, together with the test of efficacy of its cleaning elastomers. Because roughness of these samples is very significant, all the differences in adhesion are ascribed to it. It is shown how, with the changes in the types and scale of surface features, adhesion can be changed (or be modulated in the case of rollers).

The study of the plastic sheets shows how adhesion increases when the features that are present on the surface have a scale and a geometry that let the probes increase its contact area by means of a 'lateral' contact. If this is not the case (features too small or, usually, with the steepest walls), the contact area is reduced and adhesion is lower.

Similar behaviour is seen also on the rollers, with the roughest elastomers showing the greatest spreads of adhesion values with respect to the flattest samples, together with a decrease of the centre (average) of adhesion data distributions. In addition to that, because rollers are made of elastic materials, they

can deform and catch particles better; ground elastomers can also improve their performances with an additional 'trapping' system of a particle inside their valleys.

Cleaning efficiency is good for the hydrophobic particles for the couples FilmClean/UltraClean and PanelClean/UTFClean, while in the couple NanoUClean/NanoClean, the latter can show difficulties in cleaning most of the surfaces. This may due to the fact that probably is designed for specific cleaning tasks that are different from those of the other rollers (for examples, for greater particles). None of the rollers was able to clean all the surfaces from the hydrophilic particle (and the capillary force can have a role in that), with the couples FilmClean/ UltraClean and PanelClean/UTFClean having similar performances and the couple NanoUClean/NanoClean hardly being efficient (and again, this may due to the different purposes from which this couple is probably designed).

Further investigations on surface elastomer properties that may influence adhesion can be done changing the model networks to see if also other materials may have similar behaviours. The use of new materials can be also a nice test for the new strategy proposed for the calculation of the contact radius and to have an insight of the detachment process at the nano-microscale. The use of different materials other than PDMS can also allow to synthesise samples with a more pronounced viscoelasticity without increasing surface stickiness too much (very low reaction yields in the PDMS crosslink reaction lead to sample too much sticky to be analysed by AFM, without considering that in these cases chain extraction, and so, contamination of the probe, becomes possible).

Other efforts may be dedicated to study how to increase the cleaning efficiency of the roller, with considerations about materials, weight (or applied load), speed and ground process.

Index of Figures

Index of Tables

References

[1] F. Corrado, R. Egan, G. Larsen and R. Sweet, *Contact Cleaner Roll Cleaning System* US Patent 5 251 348, October 12, 1993.

[2] F. Zhang and A. Busnaina, Appl. Phys. A. **69**, 437 (1999).

[3] A. A. Busnaina, H. Lin, and N. Moumen, *Surface Cleaning Mechanisms and Future Cleaning Requirements.* 2000 IEEE/SEMI Advanced Semiconductor Manufacturing Conference and Workshop. ASMC 2000 (IEEE, New York, 2000).

[4] A. A. Busnaina et al., IEEE Transactions on Semiconductor Manufacturing. **15**(4), 374 (2002).

[5] D. M. Mattox, Thin Solid Films. **53**(1), 81 (1978).

[6] R. G. Musket, et al., Applications of Surface Science. **10**(2), 143 (1982).

[7] E. Pedemonte, *Fondamenti di struttura, proprietà e tecnologia dei polimeri*, (Edizioni Nuova Cultura, Roma, 2011).

[8] D. J. Hu, *Shape Memory Polymers and Textiles*, (CRC Press, Boca Raton, 2007).

[9] K. P. Menard, *Dynamic Mechanical Analysis: a Pratical Introduction,* (CRC Press, London, 2008).

[10] E. M. James, (Ed.) *Physical Properties of Polymers Handbook*, (Springer, New York, 2007).

[11] P. J. Flory, and Jr, J. Rehner, J. Chem. Phys. **11,** 521 (1943).

[12] G. B. McKenna, K. M. Flynn, and Y. Chen, Polymer. **31**, 1937 (1990).

[13] J. L. Valentín et al., Macromolecules. **41**, 4717 (2008).

[14] L. A. Belfiore, *Physical Properties of Macromolecules,* (John Wiley & Sons, Inc., Hoboken, New York, 2010).

[15] D. Berti and G. Palazzo, (Ed.) *Colloidal Foundations of Nanoscience,* (Elsevier, Amsterdam, 2014).

[16] N. Schuld and B. A. Wolf, J. Polym. Sci. B Polym Phys. **39**, 651 (2001).

[17] J. C. Salamone, (Ed.) *Polymeric Materials Encyclopedia,* (CRC Press, Boca Raton, 1996).

[18] F. M. Fowkes, Ind. Eng. Chem. **56,** 40 (1964).

[19] D. Owens and R. Wendt, J. Appl. Polym. Sci. **13,** 1741 (1969).

[20] S. Wu, J. Polym. Sci., C Polym. Symp. **34**(1), 19 (1971).

[21] G. Bracco and B. Holst, (Ed.) *Surface Science Techniques,* (Springer Berlin Heidelberg, Heidelberg, 2013).

[22] H. W. Hao, A. M. Baró and J. J. Sáenz, J. Vac. Sci. Technol. B. **9**, 1323 (1991).

[23] J. N. Israelachvili, *Intermolecular and Surface Forces,* (Elsevier Inc., San Diego, 2011).

[24] H. -J. Butt, and M. K. Kappl, *Surface and Interfacial Forces,* (Wiley-VCH Verlag GmbH & Co. KGaA, Weinheim, 2010).

[25] F. Sir William Thomson, Phil. Mag. 4. **42**, 448 (1871).

[26] H. Butt, et al., Soft Matter **6**(23), 5930 (2010).

[27] H. -J. Butt, and M. Kappl, Adv. Colloid Interface Sci. **146**(1-2), 48 (2009).

[28] X. Xiao, and L. Qian, Langmuir. **16**(21), 8153 (2000).

[29] F. L. Leite, and P. S. P. Herrmann, J. Adhesion Sci. Technol. **19**(3-5), 365 (2005).

[30] J. Jang, G. C. Schatz, and M. A. Ratner, J. Chem. Phys. **120**(3), 1157 (2004).

[31] E. Hsiao, M. J. Marino, and S. H. Kim, J. Colloid Interface Sci. **352**(2), 549 (2010).

[32] B. Bhushan and H. Liu, Phys. Rev. B. **63**, 245412-1 (2001).

[33] N. Garoff and S. Zauscher, Langmuir. **18**(18), 6921 (2002).

[34] E. -S. Yoon, S. H.Yang, H.-G. Han and H. Kong, Wear **254**(10), 974 (2003).

[35] K. L. Johnson, *Contact Mechanics,* (Cambridge University Press, Cambridge, 1985).

[36] K. L. Johnson, K. Kendall and A. D. Roberts, Proc. Roy. Soc. A. **324**, 301 (1971).

[37] D. E. Packham, (Ed.) *Handbook of Adhesion*. (John Wiley & Sons, Ltd, Chichester, 2005).

[38] R. S. Bradley, Philos. Mag. **13**, 853 (1932).

[39] K. L. Johnson and J. A. Greenwood, J. Colloid Interface Sci. **192**(2), 326 (1997).

[40] K. L. Johnson**,** Br. J. App. Phys. **9**(5), 199 (1958).

[41] J. A. Greenwood and K. L. Johnson, Phil. Mag. A. **43**(3), 697 (1981).

[42] B. Derjaguin, V. Muller and Y. Toporov, J. Colloid Interface Sci. **53**(2), 314 (1975).

[43] B. Derjaguin, Kolloid-Zeitschrift **69**, 155 (1934).

[44] V. Muller, B. Derjaguin and Y. Toporov, Colloids Surfaces. **7**, 251 (1983).

[45] M. D. Pashley, Colloids Surfaces. **12**, 69 (1984).

[46] D. Maugis, J. Colloid Interface Sci. **150**(1), 243 (1992).

[47] D. Tabor, J. Colloid Interface Sci. **58**(1), 2 (1977).

[48] V. M. Muller, V. S. Yushenko and B. V. Derjaguin, J. Colloid Interface Sci. **77**(1), 91 (1980).

[49] J. A. Greenwood, Proc. R. Soc. A: Math. Phys. Eng. Sci. **453**(1961), 1277 (1997).

[50] J. Q. Feng, J. Colloid Interface Sci. **238**(2), 318 (2001).

[51] P. Attard, Langmuir **17**(14), 4322 (2001).

[52] P. Attard, J. Phys. Chem. B. **104**(45), 10635 (2000).

[53] M. Barquins and D. Maugis, J. Adhesion. **13**(1), 53 (1981)

[54] E. Barthel and S. Roux, Langmuir. **16**(21), 8134 (2000).

[55] J. Nase, O. Ramos, C. Creton,and A. Lindner, Eur. Phys. J. E. **36**(9), 1 (2013).

[56] Y. Sun and G. C. Walker, Langmuir. **21**(19), 8694 (2005).

[57] R. Buzio et al., Langmuir. **23**(18), 9293 (2007).

[58] I. U. Vakarelski, A. Toritani, M. Nakayama and K. Higashitani, Langmuir. **17**(16), 4739 (2001).

[59] J. A. Greenwood and K. L. Johnson, J. Colloid Interface Sci. **296**(2), 284 (2006).

[60] S. Hunter, J. Mec. Phys. Solids. **8**(4), 219 (1960).

[61] T. C. T. Ting, J. Appl. Mech. **33**(4), 845 (1966).

[62] Bhushan, B. (Ed.) *Handbook of Micro/Nano Tribology,* (CRC Press, Boca Raton, 1999).

[63] H. Kesari et al., Philos. Mag. Lett. **90**(12), 891 (2010).

[64] P.-G. de Gennes, C. R. Acad. Sci. Ser. IIb **320**(4), 193 (1995).

[65] E. Geissler, J. Polym. Sci. Polym. Phys. Ed. **13**(7), 1301 (1975).

[66] A. Zosel, J. Adhes. **34**(1-4), 201 (1991).

[67] G. Y. Choi, W. Zurawsky and A. Ulman**,** Langmuir **15**(24), 8447 (1999).

[68] J. Chen, K. E. Wright and M. A. Birch, Acta Mech. Sin. **30**(1), 2 (2014).

[69] F. Carrillo et al., J. Mat. Res. **20**(10), 2820 (2005).

[70] R. N. Wenzel, Ind. Eng. Chem. **28**(8), 988 (1936).

[71] A. Cassie, Discuss. Faraday Soc. **3**, 11 (1948).

[72] M. Miwa et al., Langmuir **16**(13), 5754 (2000).

[73] A. Marmur, Langmuir **19**(20), 8343 (2003).

[74] E. Bormashenko, J. Colloid Interface Sci. **360**(1), 317 (2011).

[75] P. Roach, N. J. Shirtcliffe and M. I. Newton, Soft Matter **4**(2), 224 (2008).

[76] E. Bormashenko, Adv. Colloid Interface Sci. **222**, 92 (2015).

[77] C. Dorrer and J. Rühe, Langmuir. **23**(7), 3820 (2007).

[78] A. Méndez-Vilas, M. L González-Martín, L. Labajos-Broncano and M. J. Nuevo, J. Adhes. Sci. Technol. **16**(13), 1737 (2002).

[79] B. Cappella, *Mechanical Properties of Polymers Measured through AFM Force-Distance Curves* (Springer Nature, Switzerland, 2016).

[80] H. Rumpf, (Ed.) *Particle technology,* (Chapman and Hall, London, 1990).

[81] H. -J. Butt, B. Cappella, and M. Kappl, Surf. Sci. Rep. **59**(1-6), 1 (2005).

[82] Y. I. Rabinovich et al., J. Colloid Interface Sci. **232**(1), 10 (2000).

[83] Y. I. Rabinovich et al., J. Colloid Interface Sci. **232**(1), 17 (2000).

[84] K. Cooper, N. Ohler, A. Gupta and S. Beaudoin, J. Colloid Interface Sci. **222**(1), 63 (2000).

[85] K. N. G. Fuller and D. Tabor, Proc. R. Soc. A: Math. Phys. Eng. Sci. **345**(1642), 327 (1975).

[86] S. Eichenlaub, A. Gelb and S. Beaudoin, J. Colloid Interface Sci. **280**(2), 289 (2004).

[87] J. C. Lötters, W. Olthuis, P. H. Veltink and P. Bergveld, J. Micromech. Microeng. **7**(3), 145 (1997).

[88] J. E. Mark, Acc. Chem. Res. **37**(12), 946 (2004).

[89] E. Delebecq and F. Ganachaud, ACS Appl. Mat. Interfaces **4**(7), 3340 (2012).

[90] J. E. Mark, J. Inorg. Org. Polym. Mater. **22**(3), 560 (2012).

[91] J. R. Falender, G. S. Y. Yeh and J. E. Mark, Macromolecules. **12**(6), 1207 (1979).

[92] J. R. Falender, G. S. Y. Yeh and J. E. Mark**,** J. Am. Chem. Soc. **101**(24), 7353 (1979).

[93] W. Oppermann and G. Rehage, Colloid Pol. Sci. **259**(12), 1177 (1981).

[94] S. R. Cohen and E. Kalfon-Cohen, Beilstein J. Nanotechnol. **4**, 815 (2013).

[95] S. Mani, P. Cassagnau, M. Bousmina and P. Chaumont, Macromolecules. **42**(21), 8460 (2009).

[96] J. Herz, A. Belkebir-Mrani and P. Rempp, Eur. Polym. J. **9**(11), 1165 (1973).

[97] J. R. Falender, G. S. Y. Yeh and J. E. Mark, J. Chem. Phys. **70**(11), 5324 (1979).

[98] M. Llorente and J. Mark, Macromolecules **13**(3), 681 (1980).

[99] T. Suzuki and T. Okawa**,** Polymer **29**(11), 2095 (1988).

[100] C. Rouf-George et al., Macromolecules **30**(26), 8344 (1997).

[101] J. L. Braun, J. E. Mark and B. E. Eichinger, Macromolecules **35**(13), 5273 (2002).

[102] D. W. Chung and T. G. Kim, J. Ind. Eng. Chem. **13**(4), 571(2007).

[103] J. E. Mark and J. L. Sullivan, J. Chem. Phys. **66**(3), 1006 (1977).

[104] X. He, J. Widmaier, J. Herz and G. Meyer, Eur. Polym. J. **24**(12), 1145 (1988).

[105] X. He, J. Widmaier, J. Herz and G. Meyer, Polymer **30**(2), 364(1989).

[106] F. Normand, et al., Eur. Polym. J. **25**(4), 371 (1989).

[107] S. Clarson, Z. Wang and J. Mark, Eur. Polym. J. **26**(6), 621 (1990).

[108] P. Xu and J. E. Mark, Polymer **33**(9), 1843 (1992).

[109] M. Sharaf, J. Mark and Z. A. Hosani, Eur. Polym. J. **29**(6), 809 (1993).

[110] X. Zhang, G. Lin, S. R. Kumar and J. E. Mark, Polymer **50**(23), 5414 (2009).

[111] J. Stein, L. N. Lewis, Y. Gao and R. A. Scott, J. Am. Chem. Soc. **121**(15), 3693 (1999).

[112] P. B. Hitchcock, M. F. Lappert and N. J. W. Warhurst, Angew. Chem., Int. Ed. Engl. **30**(4), 438 (2003).

[113] A. G. Bejenariu, J. Ő. Poulsen, A. L. Skov and L. C. Henriksen, Annual Transactions Of The Nordic Rheology Society **17**, 269 (2009).

[114] J. A. Chalk and J. F. Harrod**,** J. Am. Chem. Soc. **87**(1), 16 (1965).

[115] F. Faglioni, M. Blanco, W. A. G. Goddard and D. Saunders, J. Phys. Chem. B. **106**(7), 1714 (2002).

[116] L. Lewis and N. Lewis, J. Am. Chem. Soc. **108**(23), 7228 (1986).

[117] L. N. Lewis, J. Am. Chem. Soc. **112**(16), 5998 (1990).

[118] A. Onopchenko and T. E. Sabourin, J. Org. Chem. **52**(18), 4118 (1987).

[119] J. Stein, L. N. Lewis, K. A. Smith and K. X. Lettko, J. Inorg. Organomet. Polym. **1**(3), 325 (1991).

[120] T. Simpson, B. Parbhoo and J. Keddie, Polymer **44**(17), 4829 (2003).

[121] A. Esteves et al., Polymer 50(16), 3955 (2009).

[122] L. Lewis, R. Colborn, Y. Gao and J. Dong, J. Organomet. Chem. **521**(1-2), 221 (1996).

[123] B. Marciniec, Silicon Chem. **1**(1), 155 (2002).

[124] M. J. Owen and P. R. Dvornic, (Ed.), *Silicone Surface Science,* (Springer, Netherlands, 2012).

[125] A. Koh, G. Gillies, J.Gore and B. R. Saunders, J. Colloid Interface Sci. **227**(2), 390 (2000).

[126] Q. Zhang et al., Water Resour. Res. **50**(23), 7677 (2014).

[127] A. N. Falcao, J. S. Pedersen and K. Mortensen, Macromolecules **26**(20), 5350 (1993).

[128] J. E. Mark, (Ed.) *Polymer Data Handbook,* 1st Ed. (Oxford University Press, Oxford, 1999).

[129] M. R. Ramli, M. B. H Othman, A. Arifin and Z. Ahmad, Polym. Degrad. Stab. **96**(12), 2064 (2011).

[130] S. K. Patel et al., Macromolecules **25**(20), 5241 (1992).

[131] W. Chassé, M. Lang, J.-U. Sommer and K. Saalwächter, Macromolecules. **45**(2), 899 (2012).

[132] E. Charrault, C. Gauthier, P. Marie and R. Schirrer, Langmuir **25**(10), 5847 (2009).

[133] I. Franta, (Ed.) *Elastomers and Rubber Compounding Materials: Manufacture, Properties and Applications,* 1st Ed. (Elsevier, New York, 1989).

[134] K. Ravindranath and R. Mashelkar, Chem. Eng. Sci. **41**(9), 2197 (1986).

[135] V. Jankauskaite, G. Macijauskas and R. Lygaitis**,** Mater. Sci. Medziagotyra **14**(2), 119 (2008).

[136] F. Welle, Resour. Conserv. Recycl. **55**(11), 865 (2011).

[137] S. Wu, *Polymer Interface and Adhesion,* (Marcel Dekker, New York, 1982).

[138] J. J. Pireaux, P. Bertrand and J. L. Brédas, *Polymer-solid interfaces: proceedings of the First International Conference, Namur, Belgium, 2-6 September 1991*. (Institute of Physics, Bristol, 1992).

[139] L. Dauginet, A.-S. Duwez, R. Legras and S. Demoustier-Champagne, Langmuir **17**(13), 3952 (2001).

[140] D. -J. Liaw et al., Prog. Pol. Sci. **37**(7), 907(2012).

[141] Abadie, M. (Ed.) *High Performance Polymers - Polyimides Based*, (Intech, Croatia, 2012).

[142] L. Matienzo and F. Egitto, Polym. Degrad. Stab. **35**(2), 181 (1992).

[143] J. Brandrup and E. H. Immergut, (Ed.) *Polymer handbook,* (Wiley, New York, 1989).

[144] I. A. Ronova and M. Bruma, Struct. Chem. **21**(5),1013 (2010).

[145] J. Dann, J. Colloid Interface Sci. **32**(3), 302 (1970).

[146] R. Sanetra, B. N. Kolarz and A. Wlochowicz, Polymer 26(8), 1181 (1985).

[147] J. He et al., Polymer 49(18), 3993 (2008).

[148] R. Hurt et al., *Am. Chem. Soc., Div. Fuel Chem*. *Preprint* **47**(2), 422 (2002).

[149] S. Alvo, P. Lambert, M. Gauthier and S. Régnier, J. Adhes. Sci. Technol. **24**(15-16), 2415 (2010).

[150] J. Drelich and K. L. Mittal, (Ed.) *Atomic Force Microscopy in Adhesion Studies,* (CRC Press, New York, 2005).

[151] K. R. Spring and M. W. Davidson, *Introduction to Fluorescence Microscopy*, WWW Document, (https://www.microscopyu.com/techniques/fluorescence/introduction-to-fluorescence-microscopy).

[152] V. V. Tsukruk and S. Singamaneni, *Scanning Probe Microscopy of Soft Matter: Fundamental and Practices,* (Wiley-vch, Weinheim, 2012).

[153] P. Eaton and P. West, *Atomic Force Microscopy,* (Oxford University Press, Oxford, 2010).

[154] Marulanda, J. M., (Ed.) *Electronic Properties of Carbon Nanotubes,* (InTech, Croatia, 2011).

[155] K. C. Neuman and A. Nagy, Nat. Methods. **5**(6), 491 (2008).

[156] V. Bellitto, (Ed.), *Atomic Force Microscopy - Imaging, Measuring and Manipulating Surfaces at the Atomic Scale,* (InTech, Croatia, 2012).

[157] H. Czichos, T. Saito and L. Smith, (Ed.) *Springer Handbook of Materials Measurement Methods,* (Springer Berlin Heidelberg, Berlin, 2006)

[158] B. Cappella and G. Dietler, *Force-Distance Curves by Atomic Force Microscopy*, Surf. Sci. Reports **34**(1-3), 1 (1999)

[159] T. R Albrecht, S. Akamine, T. E. Carver and C. F. Quate, J. Vac. Sci. Technol. A. **8**, 3386 (1990)

[160] J. P. Cleveland, S. Manne, D. Bocek and P. K. Hansma, Rev. Sci. Instrum. **64**(2), 403 (1993).

[161] C. Gibson, G. Watson and S. Myhra, Nanotechnology **7**(3), 259 (1996).

[162] J. L. Hutter and J. Bechhoefer, Rev. Sci. Instrum. **64**(7), 1868 (1993).

[163] J. E. Sader, J. W. M. Chon and P. Mulvaney, Rev. Sci. Instrum. **70**(10), 3967 (1999).

[164] L. C. Sawyer, D. T. Grubb, G. F. Meyers, (Ed.) *Polymer Microscopy,* (Springer, New York, 2008).

[165] W. N. Sharpe, (Ed.) *Springer Handbook of Experimental Solid Mechanics,* (Springer, New York, 2008).

[166] P. Attard, J. Phys.: Condens. Matter **19**, 1 (2007).

[167] Y. Sun, B. Akhremitchev and G. C. Walker, Langmuir **20**(14), 5837 (2004).

[168] C. Soussen, D. Brie, F. Gaboriaud and C. Kessler, Modeling of force-volume images in atomic force microscopy in *2008 5th IEEE International Symposium on Biomedical Imaging: From Nano to Macro,* (IEEE, Paris, 2008).

[169] E. Valles and C. Macosko, Macromolecules **12**(4), 673 (1979).

[170] N. R. Langley and J. D. Ferry, Macromolecules **1**(4), 353 (1968).

[171] N. A. Peppas and E. W. Merrill, J. Appl. Polym. Sci. **21**(7), 1763 (1977).

[172] C. A. Tweedie et al., Adv. Mater. **19**(18), 2540 (2007).

[173] J. M. Torres, C. M Stafford, and B. D. Vogt, ACS Nano **3**(9), 2677 (2009).

[174] D. Hoffman, I. Miskioglu, K. E. Aifantis and J. Drelich, J. Adhes. Sci. Technol. **26**(8-9), 1201 (2012).

[175] E. Kroner, R. Maboudian and E. Arzt, Adv. Eng. Mater. **12**(5), 398 (2010).

[176] H. Kesari and A. J. Lew, J. Mech. Phys. Solids. **59**(12), 2488 (2011)

[177] D. Baek, P. Hemthavy, S. Saito and K. Takahashi, Appl. Adhes. Sci. **5**(1), 1 (2017)

[178] J. D. Andrade, (Ed.) *Surface and Interfacial Aspects of Biomedical Polymers,* (Springer, Boston, 1985).